Assessment of High-burnup LWR Fuel Response to Reactivity-Initiated Accidents

by

Wenfeng Liu

B.E., Engineering Physics,
Tsinghua University, P.R.China (1997)

Submitted to the Department of Nuclear Science and Engineering
in partial fulfillment of the requirements for the degree of

Doctor of Philosophy

at the

MASSACHUSETTS INSTITUTE OF TECHNOLOGY

September 2007

Author .....
Department of Nuclear Science and Engineering
August 20, 2007

Certified by .....
Mujid S. Kazimi
TEPCO Professor of Nuclear Engineering
Thesis Supervisor

Certified by .....
Jacopo Buongiorno
Assistant Professor of Nuclear Science and Engineering
Thesis Reader

Accepted by .....
Jeffrey A. Coderre
Chairman, Department Committee on Graduate Students

Assessment of High-burnup LWR Fuel Response to Reactivity-Initiated Accidents

by

Wenfeng Liu

Submitted to the Department of Nuclear Science and Engineering
on August 20, 2007, in partial fulfillment of the
requirements for the degree of
Doctor of Philosophy

Abstract

The economic advantages of longer fuel cycle, improved fuel utilization and reduced spent fuel storage have been driving the nuclear industry to pursue higher discharge burnup of Light Water Reactor (LWR) fuel. A design basis accident, the Reactivity Initiated Accident (RIA), became a concern for further increase of burnup as simulated RIA tests revealed lower enthalpy threshold for fuel failure associated with fuel dispersal, which may compromise the core coolability and/or cause radiological release should this happened in LWRs. Valuable information on the behavior of high burnup fuel during RIA are provided by the simulation tests. However atypical design and operating conditions in simulated tests limited the application of experimental data directly to evaluate the failure potential of LWR fuels. To better interpret the experimental results and improve the capability of the fuel performance codes to predict high burnup fuel behavior, this thesis developed mechanistic models of high burnup fuel during an RIA and implemented models in a transient fuel performance code FRAPTRAN 1.3.

Fission gas release (FGR) and swelling were systematically modeled to quantify gaseous loading effects. The grain boundary fission gas inventory is simulated prior to the transient using a diffusion model in FRAPCON 3.3 code. The restructuring of high burnup fuel in rim region is described in terms of porosity, pore size distribution, fission gas concentration, and pore overpressure.

The model assumes the fragmentation of fuel upon the separation of grain boundary or when a threshold temperature is exceeded in the rim region. The fission gas in fragmented fuel is assumed to release instantaneously to the free volume when the fuel expansion and swelling creates sufficient pellet-clad gap. The relaxation of rim pore at rapid temperature increase and the thermal expansion of fission gas in fragmented fuel are considered as additional loads on the cladding besides the contact force due to fuel thermal expansion. An analytical approximation is made to calculate the clad radial displacement subjected to fission gas expansion accounting for the constraint of the cladding on the fission gas which would otherwise be neglected in a rigid pellet model FRACAS-I in the FRAPTRAN code.

In comparison to the measured FGR from CABRI, NSRR and BIGR test facilities, this mechanistic model can reasonably predict fission gas release fraction for most of the test cases covering a burnup range of 26-64 MWd/kgU and enthalpy deposit of 37-200 cal/g. It reveals the effects of burnup and enthalpy deposit on the fission gas release: burnup is an important parameter affecting fission gas inventory and fuel micro-structure evolution during base irradiation; enthalpy deposit is directly connected to the availability of fission gas release via the grain boundary separation by the intergranular bubble over-pressurization.

Analysis of the fission gas radial profile is made with the aid of the neutronic code MCODE to validate the fission gas release from the rim of UO_2 fuel. The analysis indicates fission gas release is partly from the rim region and the majority of fission gas release is from grain boundaries for burnup up to 50 MWd/kgU. Fission gas induced hoop strain is predicted to be less than 0.3% in the early phase of RIA with peak fuel enthalpy less than 145 cal/g. Given the fact that the concerned failure mode is the PCMI failure at low energy deposit, the pellet thermal expansion is still considered as effective in analyzing the PCMI failure.

However at high level of enthalpy deposit, when clad yield strength is decreased at escalated temperature due to film boiling, the fission gas either released into the plenum or retained in the fuel pellet might strain more the cladding. This is observed in the large deformation of the cladding in some test cases in NSRR and BIGR due to pressure load.

A new set of heat transfer correlations were selected and implemented in the FRAPTRAN code to model the cladding-coolant heat transfer of high burnup fuel at room temperature and atmospheric pressure condition. This new set of correlations addressed the effects of subcooling and oxiation on the heat transfer characteristics at pool boiling conditions. They reflect the increase of rewetting temperature and increase of Critical Heat Flux (CHF) due to subcooling. They account for oxidation effects on the transition and film boiling regime and heat conduction through thick oxide as the oxidation is considered as a prominent feature of surface condition change of high burnup fuel.

In addition to high burnup fuels tested in NSRR, several fresh fuel tests with different degree of subcooling and a few separate-effects RIA tests are also included to validate the applicabilty of this set of correlations. For fuel enthalpy up to 190 cal/g and oxidation up to 25 micron, the predicted peak cladding temperature (PCT) and duration of DNB achieves generally good agreement with the experimental data.

The analysis of high burnup fuel heat transfer reveals that the surface oxidation could cause an early rewetting of high burnup fuel or suppression of DNB. Surface oxidation can delay the heat conducting to the surface while keeping the surface heat transfer in the effective nucleate boiling regime. It also raises the miniumum stable film boiling temperature by lowering the interface temperature during liquid-solid contact resulting from vapor breaking down.

Also modeled was Pellet-Cladding Mechanical Interaction (PCMI) failure of irradiated and hydrided cladding. The hydride rim accumulated at outer clad is assumed to cause the crack initiation. The fracture toughness of irradiated and hydrided cladding is obtained by fitting experimental data at different temperature range. The

model sets forth a simple criterion for failure associated with crack growth based on the J integral approach. The simplification is that for the thin clad, failure is assumed to occur at the onset of crack tip growth.

In comparison to CABRI and NSRR test results and other failure models, the model shows a good capability to separate the failure cases from non-failure cases. These models have been applied to LWR conditions to determine the failure potential of high burnup fuel. It shows that, at high burnup (and therefore high hydride levels in the cladding), the failure enthalpy is smaller than at low burnup. The pulse width is an important parameter in the burnup up to 50 MWd/kg, but starts to become less important for higher burnup with highly corroded cladding.

Thesis Supervisor: Mujid S. Kazimi
Title: TEPCO Professor of Nuclear Engineering

Thesis Reader: Jacopo Buongiorno
Title: Assistant Professor of Nuclear Science and Engineering

Acknowledgments

I am grateful to my advisor, Professor Mujid Kazimi, for his patient guidance and generous support in the past four years. He revised numerous versions of my papers and thesis, encouraged me to go further in research, and gave me helpful suggestions on many aspects of my study at MIT. Also thanks to my thesis reader, Professor Jacopo Buongiorno for his comments and suggestions to improve the thesis.

Many thanks to Dr. Antonino Romano at ENUSA who had been working with me at the starting stage of the work and help present my work at conferences when I was not able to attend. Special thanks to Dr. Chan Bock Lee at Korea Atomic Energy Research Institute (KAERI) for many discussions during his visit at MIT. Thanks to Dr. Yun Long at Westinghouse for his guidance when I entered into this field.

I benefited a lot from my colleagues: Dr. Pavel Hejzlar, Dr. Yi Yuan, Dr. Zhiwen Xu, Dr. Edward E. Pilat, and Dr Pradip Saha on various aspects of the work.

I would like to express my gratitude to Mr. Harold Scott at Nuclear Regulatory Commission (NRC), Dr. Beyer and Mr. Kenneth Geelhood at Pacific Northwest National Laboratory (PNNL), Dr. Rashid and Mr. Robert Montgomery at ANATECH Corp. for their comments and/or help.

I am greatly indebted to my mother-in-law, Shuxia Zhang. This work would not have been completed without her help taking care of my daugher, Yao Pei Liu, Finally, thanks to my wife, Lei Zheng, who stimulated me to finish the thesis.

This work has been partially funded by the Nuclear Regulatory Commission.

Contents

List of Figures

List of Tables

Chapter 1

Introduction

1.1 Motivation

The economic advantages of longer fuel cycle, improved fuel utilization and reduced spent fuel storage have been driving the nuclear industry to pursue a higher discharge burnup for the LWR fuel.

This has been largely achieved by increasing the reload UO_2 enrichment and by technical improvement of the cladding alloy. Nevertheless, owing to the already long duty in LWR environment, it is becoming more challenging to increase the burnup of current LWR fuel and especially to accommodate transient conditions.

At high burnup, corrosion and irradiation degrades the mechanical properties of the cladding, the gaseous fission products released into the free volume increase the fuel plenum pressure, the gaseous and solid fission products contained in the ceramic pellet cause swelling of the pellet, imposing a displacement loading during pellet cladding gap closure. These issues raise concerns of fuel failure and consequent radiological release during operational transients or postulated accident conditions. One specific concern is the Reactivity-Initiated Accident (RIA) as fuel failures in simulation tests indicate it might be a constraint for further increasing burnup.

In spite of the fact that many in-pile and out-of-pile experiments provide information on various aspects of high burnup fuel, prediction of the fuel performance by computer codes, especially for transient conditions, is still less satisfactory. Important

phenomena pertinent to high burnup fuel are often missed or not well addressed in fuel performance codes.

It is of important to accurately model the high burnup fuel behavior and phenomena identified in the transient tests to improve prediction of the thermal-mechanical response of the fuel pin, to evaluate the burnup limits for safe operation, and to provide insights on how to improve the fuel design.

1.2 Background

1.2.1 High burnup fuel issues

High burnup fuel is associated with either increased irradiation time or uprated power. In either case, detrimental effects can occur to the fuel element or the cladding enclosure. Typical issues associated with high burnup fuel are listed below:

- Oxidation

  The Zircaloy water reactions produce zirconia on the outer surface of the cladding. In PWRs, the corrosion tends to be uniform, while in BWRs, a nodular corrosion is more likely. Although the thickness of oxide layer varies significantly at a certain burnup, it does increase at high burnup. For example, in a PWR fuel rod with average burnup greater than 60 MWd/kg, at a coolant outlet temperature $\geq$ 327 °C, an oxide layer thickness can be greater than 100 microns [1]. A thick oxidation layer:

  - Degrades the cladding thermal conductivity,
  - Thins the metallic cladding wall,
  - Leads to formation of hydride blisters when spallation occurs.

  Another form of oxidation occurs at the inner side of the cladding surface. As burnup increases, the pellet cladding gap is closed due to swelling of pellet and creep down of cladding. After the gap closure, a chemical bonding is formed between the cladding inner surface and pellet outer surface. The full bonding

occurs at a fuel burnup of about 50 MWd/kg [2]. This bonding prevents the axial transport of fission gases in the fuel and induces severe pellet cladding mechanical interaction.

- Hydrogen pickup

  Hydrogen in the water loop is generated either by chemical reaction between the zirconium alloy and water coolant or by radiolytic decomposition of water. The released hydrogen, subsequently permeates through the porous oxide layer and migrates into the metallic cladding. Because of the low solubility of hydrogen in alpha phase zirconium, (50-100 ppm at 280-300 °C), the excess hydrogen precipitates as brittle hydrides in the metallic cladding. As a result, the ductility of the cladding is reduced.

- Crud deposition

  Depending on the water chemistry characteristics, crud is deposited on the outer surface of the cladding. Sometimes, the amount of deposition is a function of burnup [2]. The crud deposition may cause

  - Unexpected change in core power distribution.
  - Axial offset abnormality when boron is picked up in the crud.
  - Localized corrosion when the process is chemically favorable.
  - Dryout of fuel rod surface when the crud is thick.

- Irradiation hardening

  Both zirconium and its alloys show mechanical properties change under the irradiation environment. The defects clusters produced by fast fluence introduces a hardening mechanism to change the mechanical properties of the cladding:

  - Increases the yield strength and the ultimate tensile strength.
  - Decreases the rate of work hardening.
  - Decreases the ductile to brittle transition temperature.

- Fission gas release and swelling

  Fission gas release (FGR) results in the pressure increase of the fuel internal plenum. This has always been the safety concern of fuel design for its potential to lift off the cladding. At a burnup higher than 40-50 MWd/kg, fission gas release of UO_2 fuel tends to increase rapidly. This leads to high plenum pressure as well as deteriorate the gap gas heat transfer. Even worse, deterioration of gap heat transfer introduces a feedback mechanism to further increase fission gas release by increasing the fuel temperature.

  The gaseous products precipitated as intergranular or intragranular bubbles and solid fission products cause additional swelling of the pellet especially during transient condition.

- Formation of high burnup structure

  As the LWR fuel is irradiated at an average burnup of 40 MWd/kg , a typical high burnup structure is formed in the rim region of the UO_2 pellet that depends on temperature, fuel enrichment and neutron flux spectrum. This is due to the fact that U-238 neutron absorption is particularly higher near a surface exposed to water, thus leading to higher Pu-239 build up. Plutonium in turn has a high fission cross-section yielding a higher fission rate per unit volume at pellet surface when the pellet reaches high burnup. Post irradiation examination shows that this structure is characterized by:

  - Large sized pores
  - High porosity of about 10-20%
  - Formation of sub-micron grains
  - Depletion of fission gas from fuel matrix

  The high fission gas content and high porosity increases the potential for fission gas release and swelling.

- Degradation of thermal conductivity

  It is widely agreed that the thermal conductivity of UO_2 will degrade in the

irradiation environment. For example, at a linear power of 25 kW/m, the centerline temperature of UO_2 fuel with a burnup of 86 MWd/kg increases by 250 K over its initial value [3]. The thermal conductivity degradation can be attributed to:

- Build-up of solid and gaseous fission products
- Presence of radiation defects
- Formation of porosities

The degraded thermal conductivity raises the fuel temperature, increases the fission gas release and leads to a narrower margin to fuel melting.

- Other issues

  Beside these issues associated with cladding and pellet, fuel assembly growth and distortion under irradiation, grid-to-rod fretting wear from debris caught in assembly, and failure to full insertion of control rod are exacerbated at high burnup.

1.2.2 Reactivity initiated accidents

A reactivity initiated accident is a postulated accident. The design basis accident for PWRs is the control Rod Ejection Accident (REA): whereby the high system pressure is assumed to eject outside the core the control assembly at the failure of the control rod drive mechanism housing. The design basis accident for BWRs is the control Rod Drop Accident (RDA): the control blade is assumed to drop down below the core by gravity resulting from detachment from the rod drive.

The significance of the RIA lies in that if a reactivity insertion is greater than prompt critical, the power surge would only be limited by fuel temperature feedback, until eventually terminated by a reactor trip. Safety concerns over RIA are: whether the fuel can withstand such a transient without failure; whether the coolability of the core is compromised; whether the radiological release is acceptable in the event of fuel failure.

Based on the evaluation of early simulated RIA tests SPERT-CDC and TREAT in 1970s, the Nuclear Regulatory Commission (NRC) in the U.S. adopted two criteria. The first one is concerning the core coolability: the radial average peak fuel enthalpy can not exceed 280 cal/g. The second one is for evaluating radiological consequence due to fuel clad failure: cladding failure is assumed when Departure from Nucleate Boiling (DNB) occurs in PWR and critical heat flux is reached for BWR at high power condition and radial average fuel enthalpy exceeds 170 cal/g for BWR at zero and low power condition.

In 1980s, MacDonald reevaluated the early results from SPERT and TREAT as well as the new Power Burst Facility (PBF) test results conducted at the Idaho National Engineering Laboratory [4]. He concludes that a design limit of 230 cal/g might be chosen and a possible failure threshold of 140 cal/g has been identified for fuel rods irradiated up to a burnup of 4.6 MWd/kg, although the RIA will not pose a safety concern considering the low enthalpy deposit calculated in the event [4].

In 1990s, the nuclear industry continued its efforts to increase the burnup. Simulated tests conducted at CABRI and Nuclear Safety Research Reactor (NSRR) revealed that fuel rod failures can occur at an enthalpy level less than 70 cal/g [5] [6]. Moreover, fuel dispersal was found to be associated with most of the high burnup fuel failure [5]. Thus, this area has attracted attention from nuclear industry and regulatory authorities as it might impose a limitation for increase fuel burnup.

The simulated RIA tests can be categorized by test facilities:

- SPERT

  In 1970s, tests were conducted in the SPERT Capsule Driver Core (CDC) for the U.S. Atomic Energy Commission. Single rods were tested in an instrumented water-filled capsule at ambient conditions. The power pulse width was about 20 ms. The burnup was up to 32 MWd/kg.

- PBF

  During 1980s, simulated RIA tests were conducted in the Power Burst Facility (PBF) at Idaho National Laboratory. The reactor consisted of a driver core in

a water pool and a pressurized water loop that can provide a wide range of test conditions. The power pulse width was 15 ms.

- NSRR

  NSRR is a modified TRIGA-ACPR (Annular Core Pulse Reactor) with a dry space located in the center of the core. A single instrumented fuel rod in a water-filled capsule was placed in the center of the core and pulse irradiated in the simulated RIA test. About 1200 experiments have bee performed by the the test facility of NSRR to evaluate the thresholds, modes, and consequences of fuel rod failure in terms of fuel enthalpy, fuel burnup, coolant conditions and fuel design [7].

  Since 1989, many irradiated fuel have been tested in the NSRR. For PWRs, about twenty-nine tests, with burnup ranging from 38 to 79 MWd/kg, have been performed. Sixteen tests with BWR fuel have been performed with burnup of 26 to 61 MWd/kg. In recent tests, the integrity of advanced cladding alloy MDA and Zirlo under RIA have been investigated. All the irradiated tests were conducted at atmospheric pressure and most of them were at room temperature. NSRR features a very narrow power pulse about 5 ms.

- CABRI

  In 1993, the first high burnup test was performed in the CABRI facility led by Institute for Protection and Nuclear Safety (IPSN). It indicated failure of high burnup fuel can occur at a much lower enthalpy deposit than assumed thus far. The objective of the CABRI Rep-Na program was to investigate the high burnup effects on fuel behavior and to verify the RIA safety criteria. The driver core of the reactor is in a water pool while the test loop has sodium coolant at a pressure of 0.5 MPa at a temperature of 280 °C. Since the heat transfer characteristics of the sodium are different from the LWR conditions. It could only represent the fuel behavior in the early phase of RIA. Except for RepNa2, which is a rod irradiated in BR3, all the others have been cut from commercial rods and refabricated to fit the size of the CABRI reactor. In

addition to UO_2 fuel, tests of MOX fuel have also been conducted in CABRI reactor. In 2000, IRSN launched in a new international program called CABRI Water Loop, in which the tests would be conducted in a pressurized water loop, more representative of the thermal hydraulics conditions of LWRs. In reference tests CIP0 in 2002, advanced cladding alloy M5 and Zirlo have been tested in the sodium loop. After renovation with a water loop, six other test series are undergoing and planned: CIPQ, CIP1-CIP5.

- IGR

  During the 1980s and early 1990s, the Russian Research Centre "Kurchatov Institute"(RRC KI) conducted simulated RIA tests and post test examinations of more than 200 VVER fuel rods [8]. At the final stage of the program, refabricated fuel rods manufactured from commercially irradiated VVER fuel up to 50 MWd/kg were tested in IGR test reactor. Fresh fuel were tested at a power pulse from 0.14 to 1.5 second and coolant conditions varies from 0.1 to 16 MPa at 20 °C. High burnup fuel were tested at a power pulse from 0.6 to 0.8 second at room temperature and ambient conditions. Ballooning and subsequent burst has been identified as the failure mechanism with no appreciable difference between fresh fuel and high burnup fuel. The peak fuel enthalpy at failures of high burnup fuel takes approximately the same values as fresh fuel.

- BIGR

  To study the VVER high burnup fuel behavior in a wide range of peak fuel enthalpy generated by narrow power pulse, 12 test fuel rods refabricated from VVER 440 and VVER 1000 commercial fuel rods irradiated from 47-60 MWd/kg were tested at BIGR. The BIGR reactor is a fast pulse research reactor with a homogeneous uranium-graphite core. The Zr-1%Nb cladding shows again sufficient ductility during the RIA tests. The failure occurs at an peak fuel enthalpy level around 170 cal/g similar as the tests results in IGR [9] [10].

The fuel failure observed in the simulated RIA tests above can be illustrated by Figure 1-1. Depending on the cladding temperature and the nature of loading

force, the failure modes are characterized as brittle fracture, ballooning and melting failure. The failure of high burnup fuel in NSRR tests and CABRI tests belongs to the category of fracture. The high burnup VVER fuel in IGR and BIGR tests have failed by ballooning with less corrosion and higher fuel enthalpy deposit.

Among high burnup issues identified in section 1.2.1, oxidation and hydride are known as the reason for the fracture failure by reducing the ductility. This is further exacerbated with irradiation and transient loading.

The effects of fission gas release and swelling during an RIA are not well understood. Experimental programme for separate effects due to fission gas are still undergoing to further reveal its contribution and kinetics.

1.3 Objective

In view of the key high burnup issues identified for RIA scenario, this thesis aims at developing and improving mechanistic models to predict high burnup fuel response during RIA. Modeling efforts are directed towards:

- Modeling fission gas release and swelling to quantify the effects due to fission gas loading systematically by accounting for the grain boundary fission gas accumulation and formation of high burnup structure.

- Modeling Pellet-Cladding Mechanical Interaction (PCMI) failure of irradiated and hydrided cladding to best differentiate the failure fuels from non-failure fuels.

- Modeling heat transfer of high burnup fuel by capturing effects of subcooling and oxidation to provide the basis of predicting cladding temperature to characterize the failure modes.

Models are assembled in an integrated fuel performance code FRAPTRAN and are validated by experimental data from international programme. Models are applied to LWR conditions to determine the failure conditions of high burnup fuels.

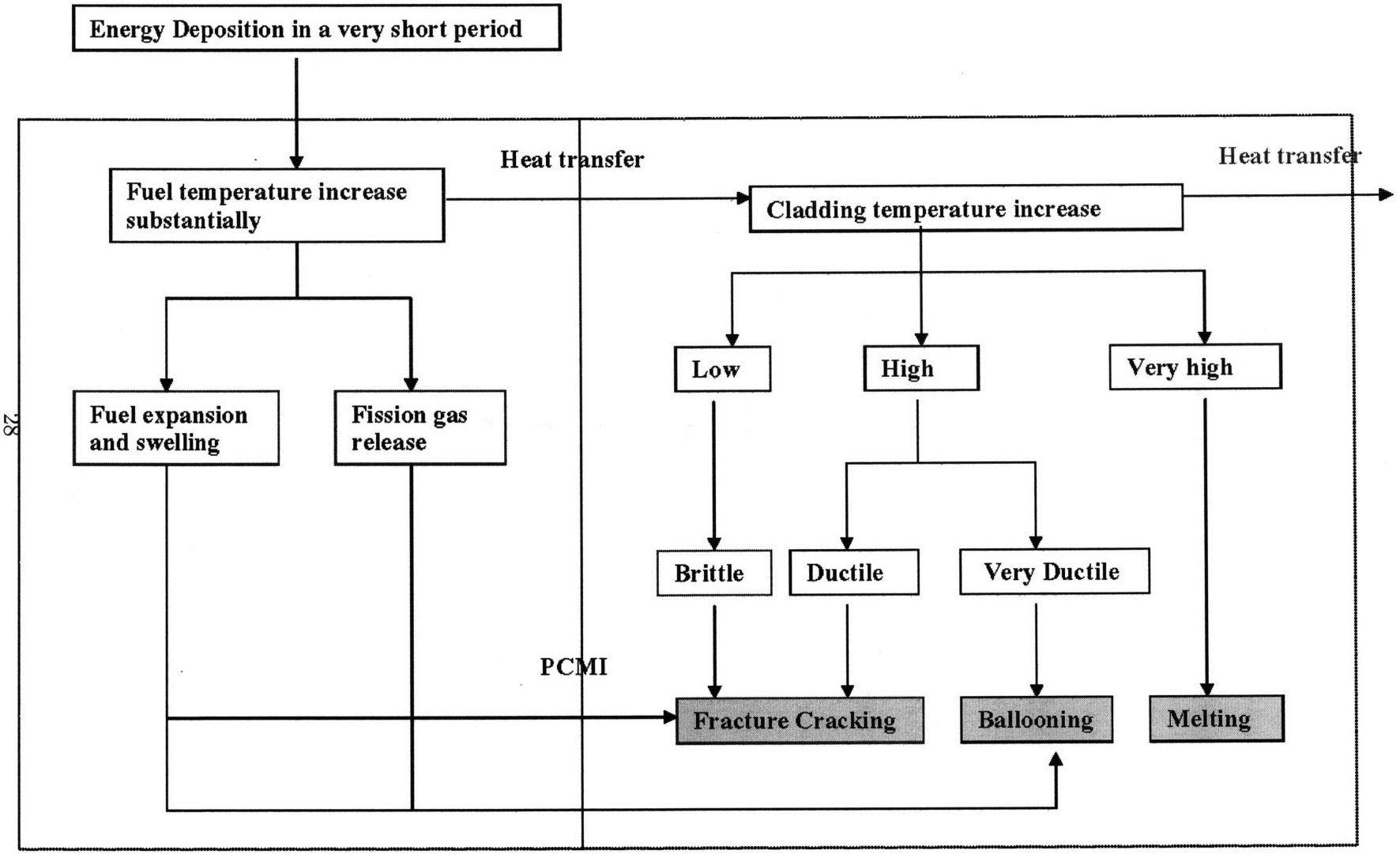

Figure 1-1: Illustration of RIA Mechanisms [11]

1.4 Model development

1.4.1 Analysis codes

Models are developed and integrated in existing fuel performance codes to analyze the burnup fuel behavior during RIA conditions, The analysis codes in this report are listed below.

- FRAPCON 3.3

  FRAPCON is a code developed by Pacific Northwest National Laboratory (PNNL) to model the fuel performance of UO_2 and MOX pellet with Zry-2 and Zry-4 cladding. The code calculates the temperature, pressure, and deformation of a fuel rod as functions of time-dependent fuel rod power and coolant boundary conditions. The phenomena modeled by the code include

  - Heat conduction through the fuel and cladding,
  - Cladding elastic and plastic deformation,
  - Fuel-cladding mechanical interaction,
  - Fission gas release,
  - Fuel rod internal gas pressure,
  - Heat transfer between fuel and cladding,
  - Cladding oxidation,
  - Heat transfer from cladding to coolant.

  The latest version 3.3 is used for base simulation in this work to provide pre-transient parameters. This version is also modified to provide parameters the fission gas release and swelling models applied to RIA.

- FRAPTRAN 1.3

  FRAPTRAN is a transient fuel performance code developed by PNNL to model LWR fuel behavior up to 65 MWd/kg [12]. Phenomenological models including heat conduction, rod internal gas pressure and cladding stress strain calculations

are coupled to predict the thermal and mechanical response under transient conditions. It features solving 1-D radial heat conduction through a composite cylinder including a pellet, a gap and a cladding by finite difference method. In the closed regime of a gap, mechanical deformation of the clad is modeled by the free thermal expansion of the pellet. In open regime of gap, the thin-walled theory is applied. The thermal and mechanical properties of Zircaloy cladding UO_2 fuel at temperatures ranging from room temperature to melting are defined in a material property package, MATPRO [13]. A modified version of MATPRO-11 Revision 2 is used in FRAPTRAN and FRAPCON to reflect the burnup dependency of material thermal and mechanical properties.

- MCODE 1.0

  MCODE is a core/fuel depletion code developed at MIT [14]. It couples the particle transport code MCNP4c3 and isotope generation/depletion code ORIGEN2.1. It is used to study the fission products generation profile within the fuel pellet.

1.4.2 Model diagram

The models implemented in the fuel codes are shown schematically in Figure 1-2. The transient fission gas release and swelling models are developed and applied in the FRAPTRAN code. A heat transfer incorporating the oxidation effects of high burnup fuel is implemented. A PCMI failure model based on fracture mechanics is applied in the FRAPTRAN code. FRAPCON code is modified and coupled with FRAPTRAN to generate fission gas inventory. MCODE 1.0 is used together with the fission gas release model in FRAPTRAN to calculate the Xe/Kr ratio. The thermal-mechanical parameters in CABRI UO_2 tests, NSRR tests, and BIGR tests are used to validate the models.

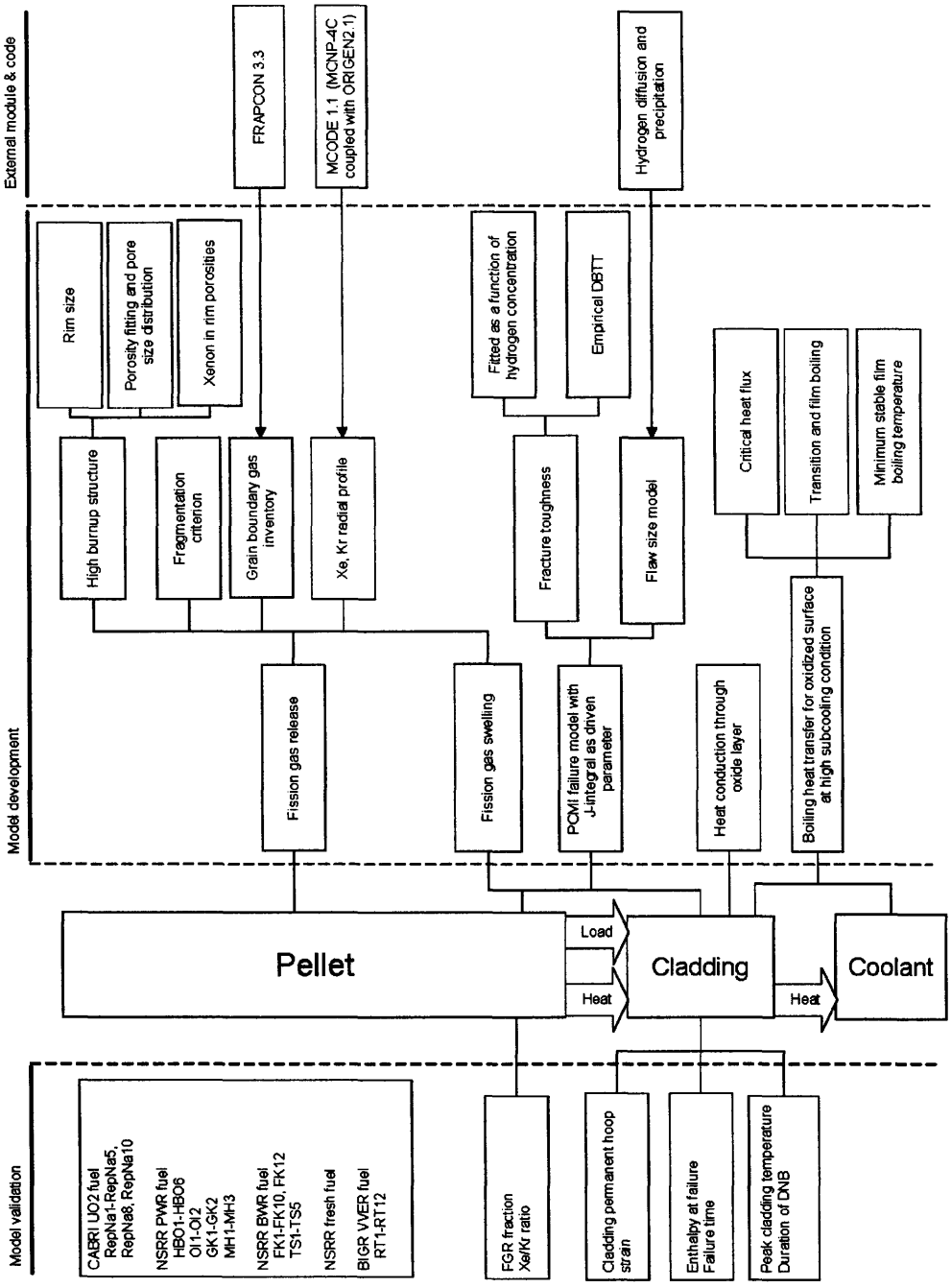

Figure 1-2: Diagram of models implementation and validation

1.5 Thesis organization

This reports consists of six chapters.

This chapter (Chapter 1) provides an introduction to the issues of high burnup fuel behavior during RIA conditions, and to describe the motivation, objectives, and analysis tools used in the thesis.

Chapter 2 then describes fission gas release and swelling models.

Chapter 3 presents the development of heat transfer models during reactivity initiated accident conditions.

Chapter 4 presents a model for the PCMI failure of the high burnup fuel in most test conditions.

Chapter 5 are the applications of the models to LWR conditions. The two conditions representing the reactivity insertion are the Hot Zero Power (HZP) condition of a PWR and the Cold Zero Power (CZP) condition of a BWR.

In chapter 6, the work is summarized, concluding remarks and recommendations for future work are made.

Chapter 2

Modeling fission gas release and swelling

2.1 Introduction

This chapter describes fission gas release and swelling models developed for high burnup UO_2 fuel during RIA and their implementations in the FRAPTRAN and FRAPCON codes.

The fission gas inventory prior to an RIA transient is systematically established. Fission gas at the grain boundaries and in fuel matrix are provided by simulating the base irradiation of each test case by FRAPCON code. The fission gas in the rim pores is calculated based on a new high burnup structure model accounting for the depletion of fission gas from fuel matrix.

A new method is developed in the thesis to couple the fission gas induced deformation of pellet under the constraint of cladding with the existing fuel thermal expansion model, FRACAS-I, in FRAPTRAN. Gaseous swelling accounts for both the rim pore relaxation and fission gas thermal expansion.

All models are validated by extensive database covering simulated RIA tests from NSRR, CABRI and BIGR.

2.2 Fission gas release

Due to the insolubility of gaseous fission products in UO_2 the fission gas is either trapped into the natural or irradiation induced defects or released to a free volume like cracking, open porosity, and fuel surface. The fission gas can precipitate in the fuel matrix in the form of intragranular bubbles or at the grain boundary as intergranular bubbles.

Gaseous fission products such as Xe and Kr released into plenum could increase the internal pressure of the fuel rod and degrade the heat transfer. Therefore, fission gas release is a very important parameter affecting fuel performance.

For high burnup, the fission gas inventory is increased at grain boundaries and in the rim region where there is high fission gas content due to local radial power peaking. As burnup is above 40–50 MWd/kgU, fractional fission gas release tends to increase rapidly. During a transient condition, thermal shock entailed cracking or fuel fragmentation promotes additional release path connecting the free volume to the grain boundary fission gas. For example, post irradiation examination (PIE) of simulated RIA indicates a large fraction of fission gas is released (5 to 30%). They contribute additional pressure loading on the cladding besides filling gas, and increase the possibility to fail the cladding.

2.2.1 Mechanism of steady state fission gas release

The generally accepted mechanisms for fission gas release in LWR fuels are:

- Athermal release

  After a nuclear fission reaction, fission fragments are born with significant kinetic energy. They, as heavy charged particles, will generally be stopped in the fuel matrix via the Coulomb forces of the electrons. If this process happens near a free surface within the range of fission fragments motion of around 10 μm gaseous products in the fragments might be released directly to the free volume.

  The elastic collisions between lattice atoms and fission fragments or neutrons

will displace atoms from the lattice. These displaced atoms, called primary-knock-ons, can further collide with other atoms to produce a cascade of collision. Any gaseous atoms in the fuel matrix might be knocked out in a collision and be released to a nearby free volume if they obtain sufficient kinetic energy.

Both of the recoil and knockout process are independent of temperature. They are the dominating mechanisms of fission gas release at low temperature (less than 600 °C). They generally contribute a small fraction of fission gas release unless high open porosity are available to increase the specific surface of open porosity.

When burnup increase, high porosity and grain subdivision are formed in the rim region, which gives additional surface, thus increasing the possibility of fission gas release. This athermal release had been modeled by some research work to explain the enhanced fission gas release of high burnup [15] [11].

However there is an argument that pore coalescence and initial channeling of porosities will not take place at the outermost rim until local burnup is very high (> 150 MWd/kgU) [16]. By Monte Carlo simulation according to porosity and pore size distribution in the rim region, Koo concluded that above a threshold porosity of 24%, the number of rim pores forming release channel increases rapidly [17]. Spino pointed out that 24% is too low considering the experimental results and supporting evidence from 3-D pore-reconstruction technique [18].

An alternative explanation of the enhanced fission gas release of high burnup fuel is that a restructured rim serves as an added thermal resistance of the fuel, thus increasing fission gas release via the thermal diffusion mechanism by raising fuel temperature.

- Thermal diffusion controlled release

  An increase of fuel temperature causes an increase of mobility of gas atoms due to lattice diffusion as illustrated by a typical diffusion coefficient shown in Figure 2-1. Gas atoms are able to migrate along a temperature gradient to a favorable sink like grain boundaries. Precipitated gas bubbles may further grow

via the incoming atoms and vacancies. At a certain point, when bubbles touch a free surface like open porosities or cracks, the fission gas would be released to the free volume. The classic model is Booth's diffusion model [20], in which the

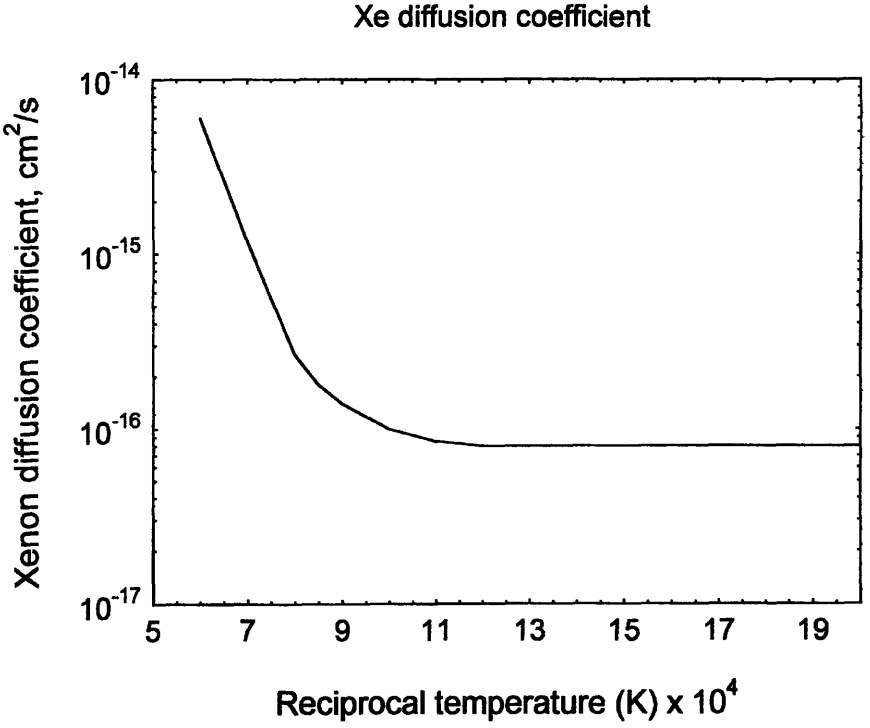

Figure 2-1: Xenon diffusion coefficient at a fission rate of 36 W/g [19]

fuel grains are assumed to be spherical and a perfect sink is set as the boundary condition at a grain boundary.

$$\frac{\partial C}{\partial t} = \frac{1}{r^2} D \frac{\partial}{\partial r} r^2 \frac{\partial}{\partial r} C(r,t) + \beta(t) \tag{2.1}$$

Initial condition:

$$C(r,0) = 0$$

Boundary condition:

$$C(a,t) = 0$$

$$\frac{\partial C}{\partial r}|_{r=0} = 0$$

An analytic solution for the fractional fission gas release is thus obtained by solving the diffusion equation:

$$F_{release} = 1 - \frac{6a^2}{90Dt} + \frac{6a^2}{\pi^4 Dt}\sum_{n=1}^{\infty}\frac{1}{n^4}\exp(-n^2\pi^2 Dt/a^2) \tag{2.2}$$

An approximation for $F_{release} < 57\%$ is:

$$F_{release} = \begin{cases} 4(\frac{Dt}{\pi a^2})^{1/2} - 3\frac{Dt}{2a^2} & for \quad \frac{\pi^2 Dt}{a^2} \leq 1, \\ 1 - \frac{0.43a^2}{\pi^2 Dt} - \frac{6(e^{-1}-e^{-\pi^2 Dt/a^2})a^2}{\pi^4 Dt} & for \quad \frac{\pi^2 Dt}{a^2} \geq 1, \end{cases} \tag{2.3}$$

where D is the gas diffusion coefficient in m^2/s, a is the grain radius in meters and t is the time in seconds. $\beta(t)$ is the gas production rate. Along the same line, many mechanistic models have been developed. Speight proposed a model to account for the trapping of intragranular bubble and irradiation induced resolution [21]. White and Tucker developed a model with an elaborate tunnel network accounting for the gas transfer through an intermittent open grain-edge tunnel network [22]. Forsberg and Massih developed a model with grain boundary saturation as the condition for fission gas release from grain boundary to the free volume [23]. Kim theoretically analyzed a two stage release accounting for lattice diffusion as well as grain boundary diffusion and demonstrated that the model can explain the burnup enhancement of fractional fission gas release [24]. Koo proposed a model consisting of two module: grain face and grain edge, the interlinkage of fission gas at the grain edge by swelling is a prerequisite condition for fission gas release [25]. Given the simplicity and computational efficiency, Massih's model had been adopted in FRAPCON. Accounting for the resolution of intergranular bubbles, Forsberg and Massih changed the boundary condition to

$$C(a,t) = b(t)\lambda N(t)/2D \tag{2.4}$$

where N = surface gas concentration, λ = resolution layer depth and b = resolution rate. They use an approximation of the integration kernel K to

express the fission gas accumulation at the grain boundary and in the fuel grain.

$$\int_0^a 4\pi r^2 C(r,t)dr = \int_0^\tau K(\tau-\tau_0)\beta_c(\tau_0)d\tau_0 \tag{2.5}$$

$$\beta_c = \beta/D$$

$$\tau = Dt$$

$$K = 8a^3/\pi \sum_{n=1}^{\infty} \exp(-n^2\pi^2\tau/a^2)/n^2$$

In a new published paper [26], a four-term approximation of the integration kernel is made. This is used in FRAPCON 3.3 [27]. In FRAPCON, the resolution rate is treated as an adjustable parameter. The partition of fission gas is defined as:

$$\Delta G_{Resolved} = \Delta G_B^o F/(1+F) \tag{2.6}$$

$$\Delta G_B = \Delta G_B^o/(1+F) \tag{2.7}$$

where, F is an adjustable multiplier, ΔG_B^o is the originally calculated fission gas at grain boundary, ΔG_B is the grain boundary fission gas after resolution. The resolved fission gas at grain boundary as well as the fission gas in intergranular bubbles is also treated to be released when the saturation criterion is met. The saturation criterion in Massih's model is determined by an assumed intergranular bubble size and critical surface fractional coverage:

$$N_{sat} = \frac{4r_b f(\theta) f_c}{3k_B T \sin^2\theta}\left(\frac{2\gamma}{r_b} + p_H\right) \tag{2.8}$$

where

γ is surface tension of the bubble = 0.6 N/m^2

r is bubble radius = 0.5 micron

k_B is Boltzmann constant

T is the temperature in K

p_H is the hydrostatic pressure in Pa

f_c is the fractional coverage of grain boundary at saturation = 0.25

θ is the dihedral half-angle = 50 °

$f(\theta) = 1 - 3\cos\theta/2 + \cos^3\theta/2$.

This model has been validated by 28 steady state cases with a standard deviation of 2.8% FGR and 18 power ramp cases with a standard deviation of 5.3% FGR [28]. Before the saturation criterion is reached, the gas accumulation at the

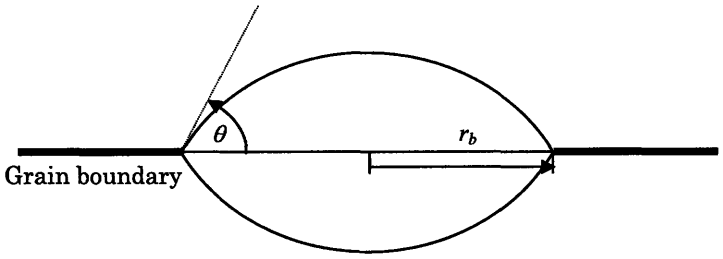

Figure 2-2: Illustration of intergranular bubble

grain boundary can be calculated by the Massih model. This provides a fission gas inventory available for the transient burst release discussed in Section 2.2.2. Thus the FRAPCON code had to be modified in our work to provide in the output the pre-transient parameters characterizing the fission gas inventory for RIA analysis.

2.2.2 Mechanisms of transient fission gas release

In post irradiation thermal annealing experiments, an initial rapid release has been observed followed by release kinetics controlled by thermal diffusion [29]. This burst release of fission gas from polycrystalline UO_2 is believed to be the venting of fission gas accumulated at grain boundaries. Analogous to thermal annealing and other temperature transients, an RIA transient leads to a very high heating rate at 10^5 K /sec. Thus the burst release process should be the same as for the other. However due to the short duration of a power pulse, bulk thermal diffusion is unlikely to be activated. Micrographs from TEM shows that for a previously irradiated fuel held at

1500 °C for 6 hr, no evidence of large amounts of gas collected at grain boundaries [30]. Kashibe's work also confirmed that the diffusional release is estimated to be less than 1% during the 1500 °C and 6 hr annealing [31]. Given a power pulse duration of only from 5 milliseconds to a few hundred milliseconds in simulated tests, even at a higher temperature, a simple estimation based on diffusion theory can rule out the bulk diffusion effects on fission gas release. Mechanisms of burst release involve two possible pathways [32]:

- Interlinkage of bubbles by the growth of bubbles from the arrival of the vacancies and gas atoms.
- Micro-cracking along the grain boundary due to the stress exerted by the over-pressure of intergranular bubbles.

Both approaches or the combination of the above mechanisms have been adopted in modeling transient fission gas release [32]. The nature of fast heating during an RIA enables the cracking along grain boundary to be the more likely mechanism. This is also evidenced by extensive fuel fragmentation observed in most of the RepNa tests and in the NSRR tests [33].

2.2.3 Burst release model

Calculating the micro-cracking along the grain boundary requires detailed information of bubble distribution and the stress field. This is often empirically modeled [25][34]: the entire grain boundary gas inventory is assumed to be vented out instantaneously as the linear power level changes and temperature exceeds a certain value.

In modeling fission gas release during RIA in the SCANAIR code [33], Lemoine used the following condition for grain boundary separation:

$$p > p_s + \frac{p_H}{f} + (\frac{1-f}{f})\sigma_r \tag{2.9}$$

where f is the grain surface gas coverage fraction, p_s is the surface tension pressure in Pa and σ_r is the fuel fracture stress in Pa. Some estimation of the GB gas content

as a function of burnup in irradiated UO_2 and MOX have been made based on few microprobe results [33].

We also use Eq 2.9 as the criterion for grain boundary separation. Recognizing that the fission gas content in grain boundary depends largely on the irradiation history, we use the Massih model in FRAPCON code to provide this fission gas inventory. The grain surface gas coverage is also determined from the code calculation instead of setting a constant value. For the rim region, in which the grain boundary information is quite different from the central region of the fuel pellet, a threshold temperature is set for fragmentation of the fuel. From the SILENE experiments, the temperature threshold of fragmentation can be 2300-2400 K [35]. It is clearly lower in PWR fuel $\leq$ 1500 K [35] and it is possible to obtain grain boundary cracking at a lower temperature (around 900 to 1000 °K) [33]. In fact, the high burnup fuel disc experiment indicates some fragmentation when temperature increases [36]. This can be rationalized by the fact that high porosity appears in the rim region: increasing the porosity of UO_2 from 5 to 16% causes a 70% reduction in fracture strength [29]. In our model, the threshold temperature is set as 1400 K.

Therefore, transient fission gas release is assumed to occur as long as the fragmentation occurs. Once the grain boundary is separated, fission gas would be released through the grain boundary edges, faces, and corners as they are connected to free volume of fuel. Neglecting the gas flow in the porous media, a simultaneous release is assumed in this process.

So far, fission gas release during RIA tests has been measured by the rod puncture, in which gas are collected with determination of total volume, interior void and composition of the collected gas. PIE analysis using Electron Probe Micron-Analysis (EPMA) provide additional information about the distribution of fission gas. But no information concerning the kinetics of fission gas release is available.

A program of separate effects of fission gas release, SILENE, is undergoing to obtain a better quantification of the kinetic aspects of fission gas under RIA transients [35]. Our model can be further improved if such information becomes available.

2.3 Swelling during transients

2.3.1 Modeling of high burnup structure

As an LWR fuel pin is irradiated to an average burnup of 40 MWd/kgU and a local rim burnup range of 70-80 MWd/kgU, a typical high burnup structure is formed in the rim region of the fuel pellet that depends on the fuel enrichment and neutron flux spectrum. Post irradiation examination shows that this structure is characterized by large micrometer sized pores that contribute a porosity of 10–20% in the rim region of the fuel, and by formation of fine grains of the size of fractions of micrometers.

It is generally agreed that this micro-structure is due to the combination of high burnup and low operating temperatures. It can be characterized by parameters such as thickness of rim, porosity, pore size distribution and xenon gas depletion.

- Thickness of the rim region

  The thickness of the rim region is generally correlated with the burnup. A simple model based on the average burnup can be deduced from Ref. [37]:

  $$w_{rim} = 7.02 BU_{avg} - 178 \tag{2.10}$$

  where BU_{avg} is the fuel radial average burnup in MWd/kgU and w_{rim} is the thickness of the rim in μm

- Xenon depletion

  The xenon depletion observed by EPMA indicates that the majority of the fission gas produced during fuel irradiation is contained in the large rim pores. A correlation for the amount of xenon is [38]:

  $$Xe_c = \dot{c} - \dot{c}(\frac{1}{a} + (BU_0 - \frac{1}{a}\exp(-a(BU - BU_0))) \tag{2.11}$$

  where Xe_c is the xenon concentration in %wt. $\dot{c}$ is the xenon production rate in %wt /BU, BU_0 is a threshold burnup for the xenon depletion measured in MWD/kgU and a is a constant measured in the reciprocal of BU units related

to the xenon equilibrium concentration.

- Porosity

  The porosity is correlated to the radial position in the fuel by an exponential formula:

$$P(r/r_0) = a_1 + \exp(a_2 + a_3(r/r_0)) \tag{2.12}$$

  where r_0 is the fuel radius and a_1, a_2, and a_3 are burnup dependent parameters as follows:

$$a_1 = 0.001144 BU_{avg} - 0.02287 \tag{2.13}$$

$$a_2 = 1.05 BU_{avg} - 100.6 \tag{2.14}$$

$$a_3 = -1.057 BU_{avg} + 99.01 \tag{2.15}$$

  It is fitted with experimental specimen for UO_2 initially with 3-5% U-235 and covering burnup 40 MWd/kgU to 67 MWd/kgU and average linear heat from 170 to 230 W/cm as shown in Figure 2-3.

- Pore size distribution

  According to Ref. [39], the pore size follows the lognormal distribution in the rim region except for the very outermost fuel region. The probability $f(r_p)dr_p$ that the pore radius is within r_p and $r_p + dr_p$ is given as:

$$f(r_p)dr_p = \frac{1}{\sqrt{2\pi}\sigma r_p} \exp(-\frac{(\ln r_p - \mu)^2}{2\sigma^2})dr_p \tag{2.16}$$

  where the pore size r_p is in m, μ and σ^2 are the statistical mean and variance for $\ln r_p$ respectively. To determine the parameters μ and σ, the pore size distribution of a 40.3 MWd/kgU sample is used [39]: $r_{p,min} = 0.25$ μm $r_{p,max} = 2.0$ μm and $r_{p,mode} = 0.55$ μm. Since:

$$\ln r_{p,max} = \mu + 3\sigma \tag{2.17}$$

$$\ln r_{p,mode} = \mu - \sigma^2 \tag{2.18}$$

We can get: μ = -14.27, σ^2 = 0.1457.

To verify the assumption that the pore size distribution can be represented by the same set of parameters, consider the dependence of porosity, P, on pore number density, N. The porosity would depend linearly on pore size number density if the pore size distribution is not dependent on burnup and radial position. Therefore:

$$P(r/r_0) = \bar{V}(r_p)N(r/r_0) \tag{2.19}$$

Where $\bar{V}$ is the average volume of each pore in m^3:

$$\bar{V} = \int_0^\infty \frac{4\pi}{3} r_p^3 f(r_p) dr_p \tag{2.20}$$

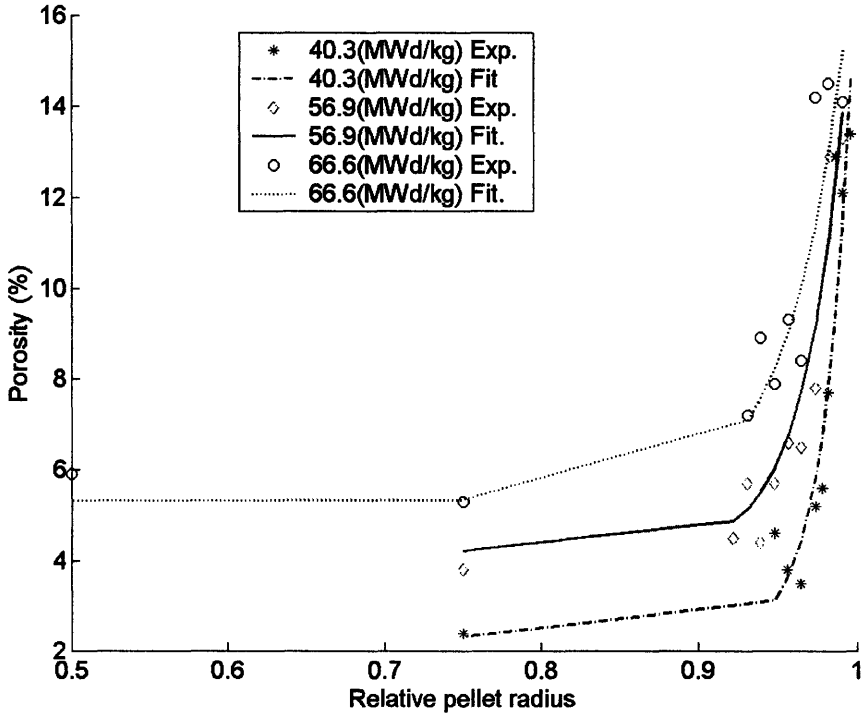

Figure 2-3: Fitting of porosity in the rim region

Since we have:

$$\begin{aligned}
&\int_{r_{p,min}}^{r_{p,max}} x^n \exp(-\frac{(\ln x-\mu)^2}{2\sigma^2})dx \\
&= -\sigma \exp(\frac{(1+n)(2\mu+\sigma^2+n\sigma^2)}{2}) \\
&\sqrt{\frac{\pi}{2}}(\text{erf }(\frac{\mu+\sigma^2+n\sigma^2-\ln(r_{p,max})}{\sqrt{2}\sigma}) - \text{erf }(\frac{\mu+\sigma 2+n\sigma^2-\ln(r_{p,min})}{\sqrt{2}\sigma}))
\end{aligned} \tag{2.21}$$

The average volume of pores is obtained as:

$$\begin{aligned}
\bar{V}(r_p) = -\frac{4\pi}{3}\sigma \exp(\frac{3(2\mu+3\sigma^2)}{2})\sqrt{\frac{\pi}{2}} \\
(\text{erf }(\frac{\mu+3\sigma^2-\ln(r_{p,max})}{\sqrt{2}\sigma}) - \text{erf }(\frac{\mu+3\sigma^2-\ln(r_{p,min})}{\sqrt{2}\sigma}))
\end{aligned} \tag{2.22}$$

Figure 2-4 plots the experimental porosity versus pore number density at a certain radial position for burnup from 40.3–67 MWd/kgU. As can be seen, the above parameters can reasonably represent the pore size distribution.

- Thermal conductivity of high burnup fuel

  It is generally accepted that the thermal conductivity of UO_2 will degrade in the irradiation environment. This can be attributed to:

  - Build-up of solid and gaseous fission products
  - Presence of radiation defects
  - Formation of porosity

  At a temperature below 1900 K, the elementary theory of conductivity of a solid UO_2 describes the lattice vibration as the mechanism of heat transport in the ionic solid [29]. This is usually described by:

$$K = \frac{1}{A+BT} \tag{2.23}$$

where A and B are coefficients accounting for phonon-defects and phonon-

phonon scattering respectively. At a higher temperature above 1900 K, an electronic conduction may dominate. This contribution is reflected by adding another term $\frac{C}{T^2}exp(-\frac{D}{T})$.

For high burnup fuel, attempts have been made accounting for each separative effect due to irradiation defects, fission products solutions and precipitates in the thermal conductivity model [40][41]. However, the complexity of irradiation environment and the difficulties in the measurement often obscure distinctions among each separative effect. Other semi-empirical models are developed to fit the experimental data. [3, 42, 27]. The current thermal conductivity model developed by PNNL in FRAPTRAN and FRAPCON code was modified on the basis of NFI model [42]. Thermal conductivity of UO_2 calculated by the model in FRAPCON for a burnup up to 150 MWd/kgU is shown in Figure 2-5. None of the above models address explicitly the rim structure, although in the range of burnup where the model is validated, the rim structure should have appeared.

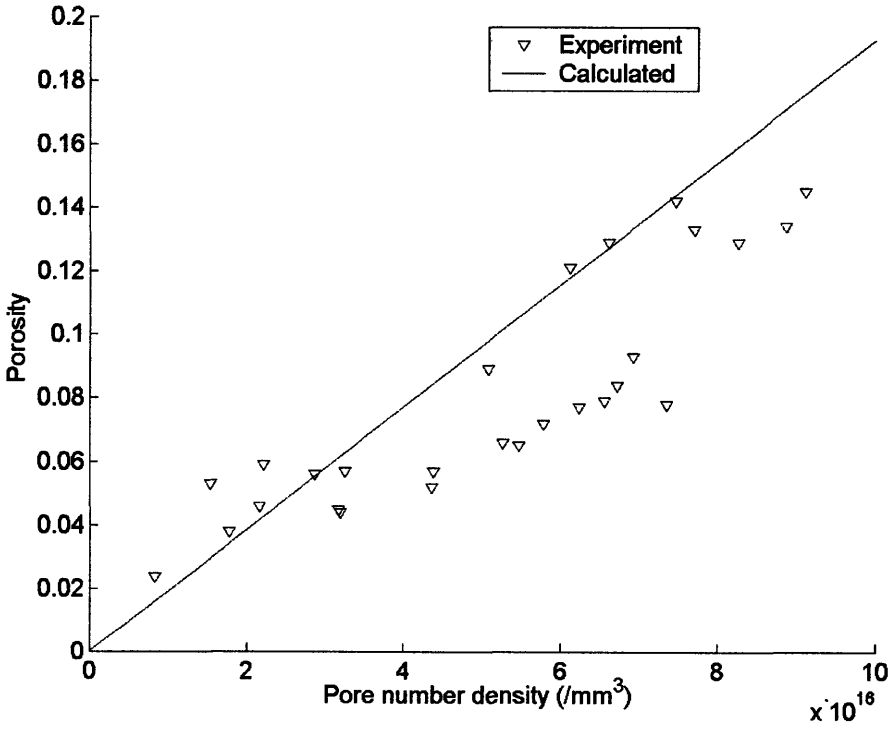

Figure 2-4: Porosity vs. pore number density

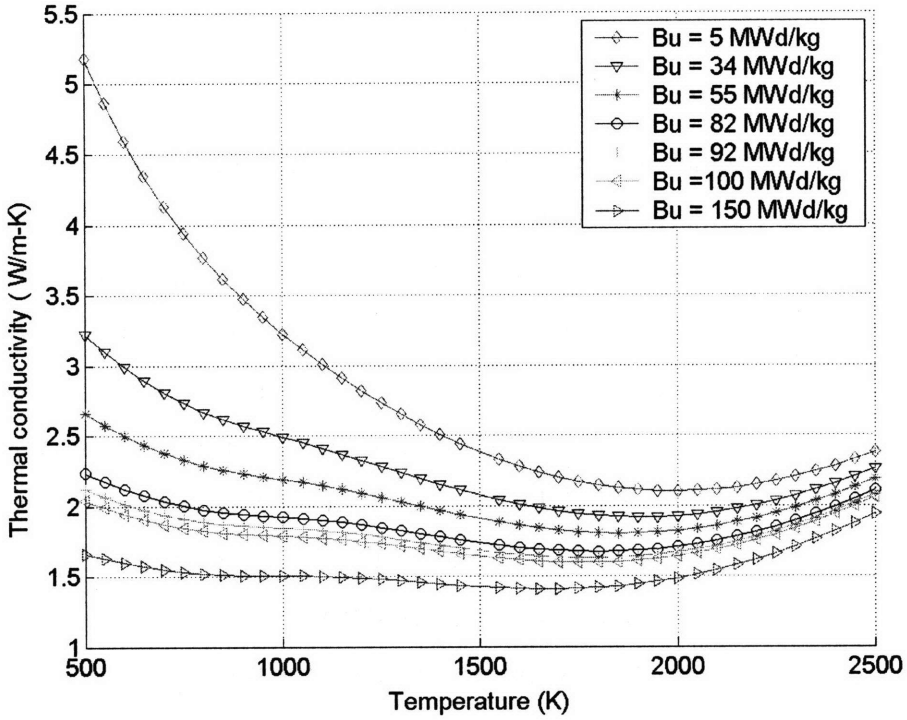

Figure 2-5: Thermal conductivity calculated by FRAPCON model

It is recognized that the high porosity in the rim structure could contribute to further degradation of thermal conductivity [40]. Accounting for this effect, Koo presents a model showing additional 20% reduction of thermal conductivity in Halden's thermal conductivity model [43]. However measurement of thermal conductivities of both high burnup disc and PWR fuel up to 100 MWd/kg indicate that the thermal conductivity degradation at the rim is not so severe as it would have been without the rim structure [36, 41, 44]. This may be explained as damage recovery [44] or removal of fission gas from the fuel matrix [36].

To verify the applicability of the PNNL model, the data for thermal conductivity of high burnup structure listed in Table 2.1 are used to compare with the model calculation.

The data from ref. [36] is normalized to 95% theoretical density by the the equation below [41].

$$K_{95}(T) = \frac{1 - 0.05f(T)}{1 - Pf(T)} K(T)$$

where $f(T) = 2.6 - 0.5T/100$, and P is the porosity. Prediction of the thermal conductivity at 95% theoretical density by the PNNL model and Halden model compared with the experimental data are shown in Figure 2-6 and Figure 2-7 respectively. PNNL model shows 5% under-prediction of the thermal conductivity at a typical operating temperature of rim around 800 K. Halden model under predicts the thermal conductivity by 10%. Thus in the analysis of RIA, we have adopted the PNNL model.

2.3.2 Modeling of rim pore relaxation

A Transmission electron microscopy (TEM) observation was made on the rim of a BWR fuel pellet with an average burnup of 49 MWd/kgU by Nogita and Une [45]. The micrograph of the surface of gas pores shows extremely high density of dislocations, which suggests that they contain fission gas at high pressure. For a spherical bubble,

Table 2.1: Thermal conductivity of high burnup fuel

T (K)	Tirr[a] = 700 K [b] Bu = 82 MWd/kg	Tirr = 730 K Bu = 96 MWd/kg	Tirr = 973 K [c] Bu = 92.2 MWd/kg	Tirr = 873 K Bu = 99.8 MWd/kg
490	–	–	1.72	1.67
500	2.18	2.06	–	–
550	2.16	2.04	–	–
600	2.14	2.03	–	–
650	2.12	2.01	–	–
700	2.10	1.99	–	–
750	2.08	1.97	–	–
800	2.07	1.95	–	–

[a]Tirr is the irradiation temperature.
[b]Data in columns 2-3 are normalized to 95% theoretical density [41].
[c]Data in columns 4-5 are not normalized [36].

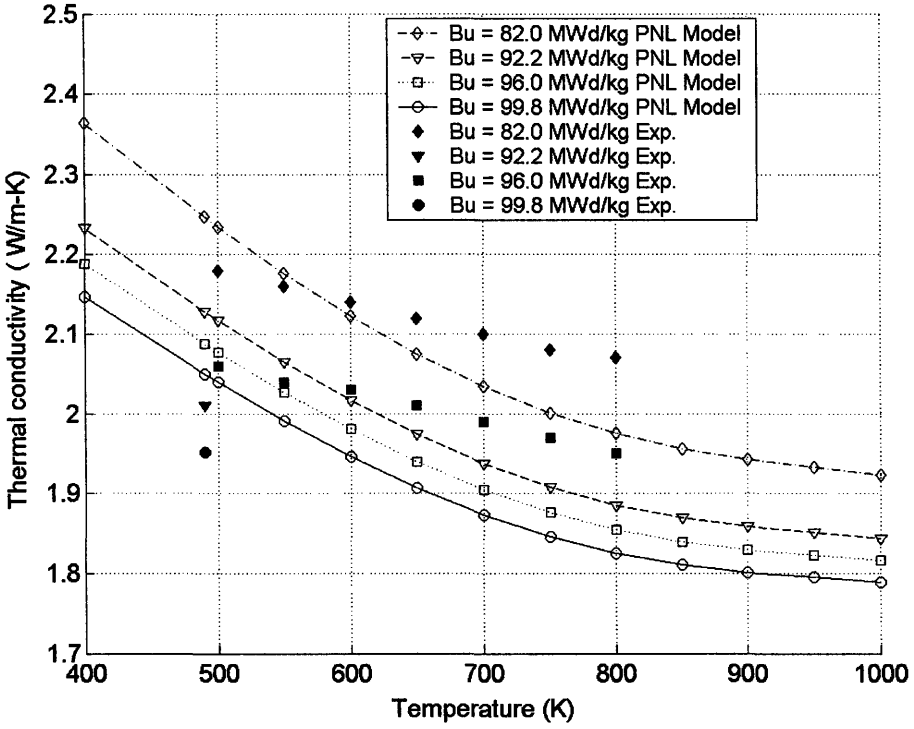

Figure 2-6: Comparison of FRAPCON model with experimental thermal conductivity

the criterion of onset of dislocation punching is:

$$p_{ex} = \mu b/r \tag{2.24}$$

where, p_{ex} is the excess pressure above equilibrium, μ is shear modulus, r is the radius of bubble and b is the Burgers vector (the parameter characterizes the slip of dislocation lines in crystalline solids). $b = 0.39$ nm for UO_2 [29].The pressure is estimated to be 194 to 48 MPa for bubbles in 0.5 to 2 μm using Eq 2.24 [45].

Assuming that the xenon depletion in the rim is equal to the fission gas of the pores, Koo quantitatively estimated the pressure is 477 MPa in a pore with radius 0.5 μm using the data from Spino's experiment [37]. This pressure seems unrealistically high as compared to the pressure that can induce plastic flow of the surrounding fuel matrix.

To evaluate swelling of the pores under transient condition, we re-evaluate the

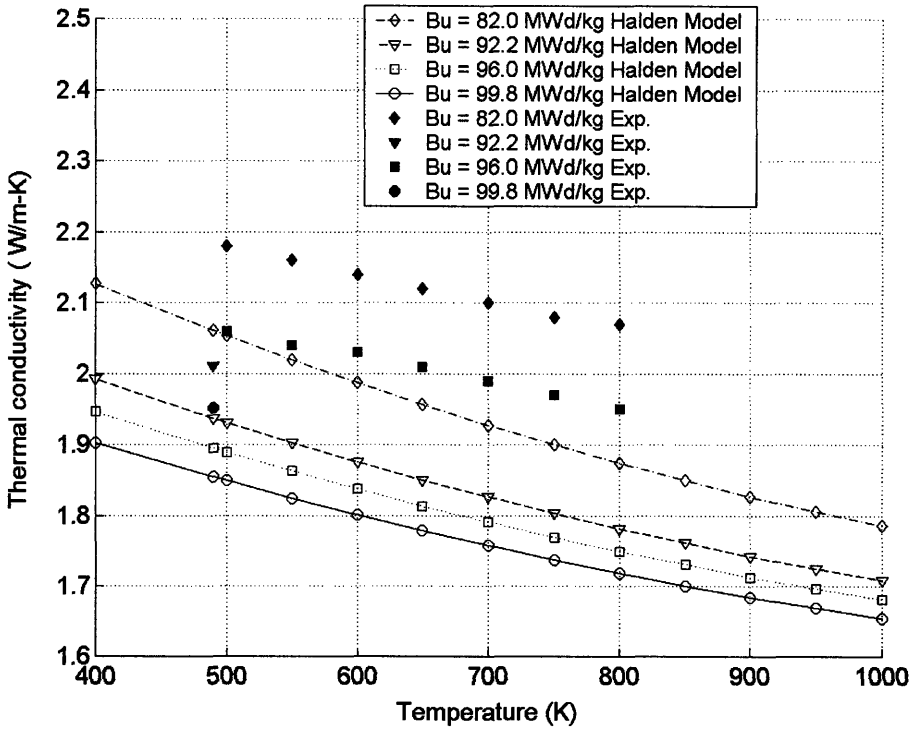

Figure 2-7: Comparison of Halden model with experimental thermal conductivity

excess pressure of rim pores. By equating fission gas in the rim to the pores, we get:

$$Xe_c(r/r_0)\rho_f(\frac{N_{AV}}{M_{Xe}}) = (\frac{P(r/r_0)}{\bar{V}})\int_0^\infty \frac{4\pi}{3} r_p^3 f(r_p)(\frac{p}{pB + k_B T})dr_p \tag{2.25}$$

where ρ_f is the fuel density in kg /m^3, N_{AV} is Avogadro's number and M_{Xe} is the Xe atomic mass in kg /mole.

Neglecting hydrostatic pressure, the pressure in the rim pore is expressed as:

$$p = \frac{C}{r_p} \tag{2.26}$$

where C is a function of temperature and burnup in N/m. Plugging the above equation into Eq 2.25, we obtain:

$$\int_0^\infty (\frac{Cr_p^3}{CB + k_B T r_p}) \exp(-\frac{(\ln r_p - \mu)^2}{2\sigma^2}) d\ln r_p = \sqrt{\frac{9\sigma}{8\pi}(\frac{Xe}{P})(\frac{N_{AV}}{M_{Xe}})}\rho_f \bar{V} \tag{2.27}$$

At a certain burnup, the integral on the left hand side is evaluated by the adaptive Simpson method over a range of (-3σ, 3σ) of the pore size distribution for a given C. By changing the initial guess value of C, the integral is obtained as a function of C. Comparing the calculated integral with the right hand side of the equation, the C that satisfies above equations is determined by a numerical interpolation. This numerical procedure however is less favorable to be implemented into a fuel code. Thus an analytical approximation is obtained in the following way: given the fact that the pore size follows a log normal distribution, the function

$$r_p \frac{\exp(-(\ln r_p - \mu)^2/2\sigma^2)}{\sqrt{2\pi}\sigma} \tag{2.28}$$

is approximated by a δ function

$$\delta(r_p - r_{p,0}) \int_{r_{p,min}}^{r_{p,max}} r_p \frac{\exp(-(\ln r_p - \mu)^2/2\sigma^2)}{\sqrt{2\pi}\sigma} dr_p \tag{2.29}$$

where, $r_{p,0}$ satisfies:

$$\frac{d}{dr_p}[r_p \frac{\exp(-(\ln r_p - \mu)^2/2\sigma^2)}{\sqrt{2\pi}\sigma}] = 0 \tag{2.30}$$

$$r_{p,0} = \exp(\mu + \sigma^2) \tag{2.31}$$

Plug Eq 2.29 into Eq 2.27, we get:

$$\begin{aligned} &\frac{4\pi C}{3BC/r_{p,0} + 3kT} \int_{r_{p,min}}^{r_{p,max}} r_p \frac{\exp(-(\ln r_p - \mu)^2/2\sigma^2)}{\sqrt{2\pi}\sigma} dr \\ =& -\frac{4\pi C}{3BC/r_{p,0} + 3kT} \sigma \exp(2\mu + 2\sigma^2) \sqrt{\frac{\pi}{2}} \\ &(\text{erf}\ (\frac{\mu + 2\sigma^2 - \ln(r_{p,max})}{\sqrt{2}\sigma}) - \text{erf}\ (\frac{\mu + 2\sigma^2 - \ln(r_{p,min})}{\sqrt{2}\sigma})) \end{aligned} \tag{2.32}$$

Given the value of right hand side of Eq 2.27, C can be easily determined by Eq 2.32. Both the analytical solution and the numerical solution are listed in Table 2.2. As can be seen, this approximation gives very reasonable agreement with the numerical evaluation. The excess pressure as a function of burnup and pore radius is plotted in Figure 2-8. It is slightly lower than Nogita's analysis. This pressure is more realistic

since Nogita's analysis actually gives an upper bound of the excess pressure.

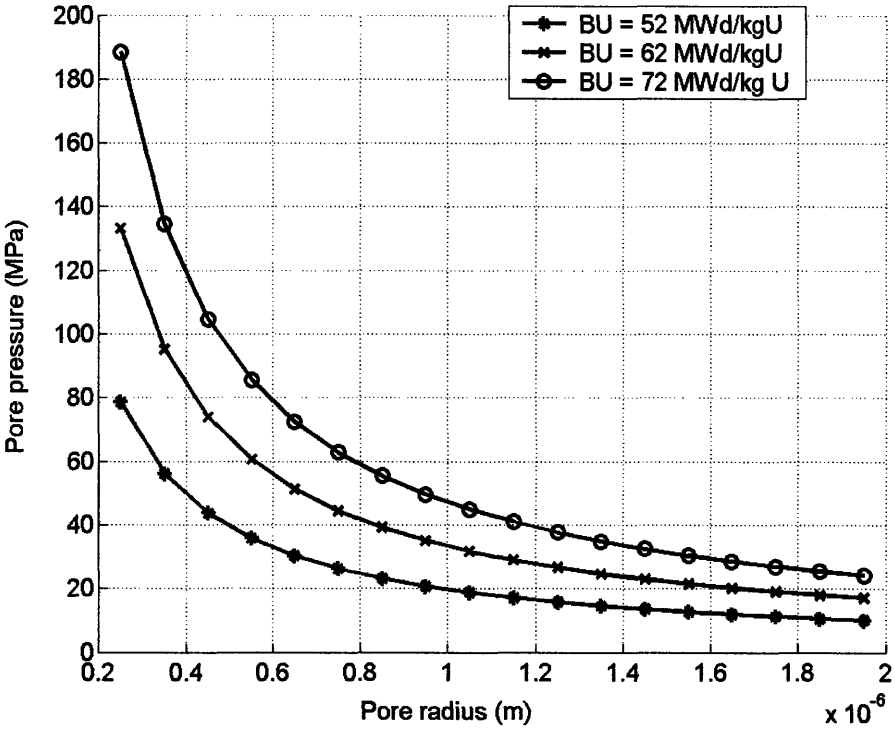

Figure 2-8: Pore pressure vs. pore radius at different burnup

The driving force for swelling can be either influx of vacancies or internal pressure inside the pores. Because of the starvation of vacancies in the rim regions where the pore is already over-pressurized. The mechanism of swelling is more likely due to the driving pressure. When the pressure exceeds the yield strength of the surrounding matrix, it pushes a dislocation into the matrix [19]. Thus we propose a mechanical equilibrium model described as follows: during the transient, as the local rim temperature increases, the pore pressure is first calculated using the xenon state equation.

Table 2.2: Coefficient of excess pressure of rim pores

BU (MWd/kgU)	C (N/m) Numerical	C(N/m) Analytical.
52	19.74	19.66
62	32.8	33.32
72	45.5	47.11

If the pore pressure exceeds the equilibrium condition:

$$p > \frac{C}{r_p} + p_H \tag{2.33}$$

where p_H is the hydrostatic pressure. The pore relaxation is assumed to occur by induction of the local plasticity in the fuel surrounding the pore (by punching dislocation loop). The pore volume increases by $\pi r^2 b$ [19]. The new radius of the pore, after pushing a dislocation, is

$$r_{p,new} = r_{p,old}(1 + \frac{3b}{4r_{p,old}})^{1/3} \tag{2.34}$$

where, $b = 0.39$ nm is the Burgers vector for UO_2. The volume increase continues until the equilibrium condition (2.35) is reached.

$$p = \frac{C}{r_p} + p_H \tag{2.35}$$

At the pellet radius r, the volume change due to the pore relaxation is then:

$$\Delta V(r/r_0) = N_V(r/r_0) \int_0^\infty \frac{4\pi}{3}(r_{p,new}^3 - r_p^3) f(r_p) dr_p \tag{2.36}$$

The fuel swelling due to the rim pore relaxation is added to the fuel thermal expansion term and affect the cladding deformation by imposing that the clad outward radial displacement follows that of the fuel during PCMI.

2.3.3 Coupling with FRACAS-I model in FRAPTRAN

The intergranular bubbles are assumed to be in the lenticular form in equilibrium status as described in the Forsberg-Massih model. During a short transient, influx of vacancies and diffusion of gas bubbles from interior grain are unlikely to happen, thus the growth of intergranular bubbles is negligible.

After grain boundary separation, the grain boundary fission gas is assumed to mix in the porous fuel medium. subjected to a hydrostatic pressure if the P/C gap is still

closed. Thermal expansion of the grain boundary fission gas contributes to the load on the cladding.

The FRACAS-I mechanical deformation model in the FRAPTRAN code assumes no resistance to the fuel deformation occurs during the PCMI. For a strong PCMI which induces high interface pressure, it is necessary to consider the constraint by the cladding on fission gas expansion.

Therefore, we develop a two step method in the FRAPTRAN code to couple our fuel swelling model with the existing mechanical deformation model FRACAS-I:

1. Predict the state of stress and strain of the cladding due to thermal expansion of the pellet by the FRACAS-I rigid pellet model.

2. Correct the above solution by calculating the incremental displacement due to fission gas by linearizion of the Generalized Hook's law and Prandtl flow rule.

This method admits that fuel thermal expansion is the primary force during PCMI and the fission gas thermal expansion contributes the secondary loading. At each time step, when deformation of the cladding is calculated by the FRACAS-I model, an incremental displacement is given by the fission gas thermal expansion. This solution must satisfy the stress and strain of cladding due to any displacement loading as well as the gas state equation. It is schematically illustrated in Figure 2-9.

Neglecting the radial stress, the generalized Hooke's law is written in the following form:

$$\varepsilon_\theta = \frac{1}{E}(\sigma_\theta - \nu\sigma_z) + \varepsilon_\theta^p + d\varepsilon_\theta^p + \varepsilon_T \tag{2.37}$$

$$\varepsilon_z = \frac{1}{E}(\sigma_z - \nu\sigma_\theta) + \varepsilon_z^p + d\varepsilon_z^p + \varepsilon_T \tag{2.38}$$

$$\varepsilon_r = -\frac{\nu}{E}(\sigma_\theta + \sigma_z) + \varepsilon_r^p + d\varepsilon_r^p + \varepsilon_T \tag{2.39}$$

where, θ, z and r refer to the hoop, axial and radial direction respectively. ε^p is the accumulated plastic strain. $d\varepsilon^p$ is the increment of plastic strain. ε_T is the thermal strain of cladding. All variables except ε^p refers to the current time step following the same convention as used in Ref. [12] in describing the FRACAS-I model.

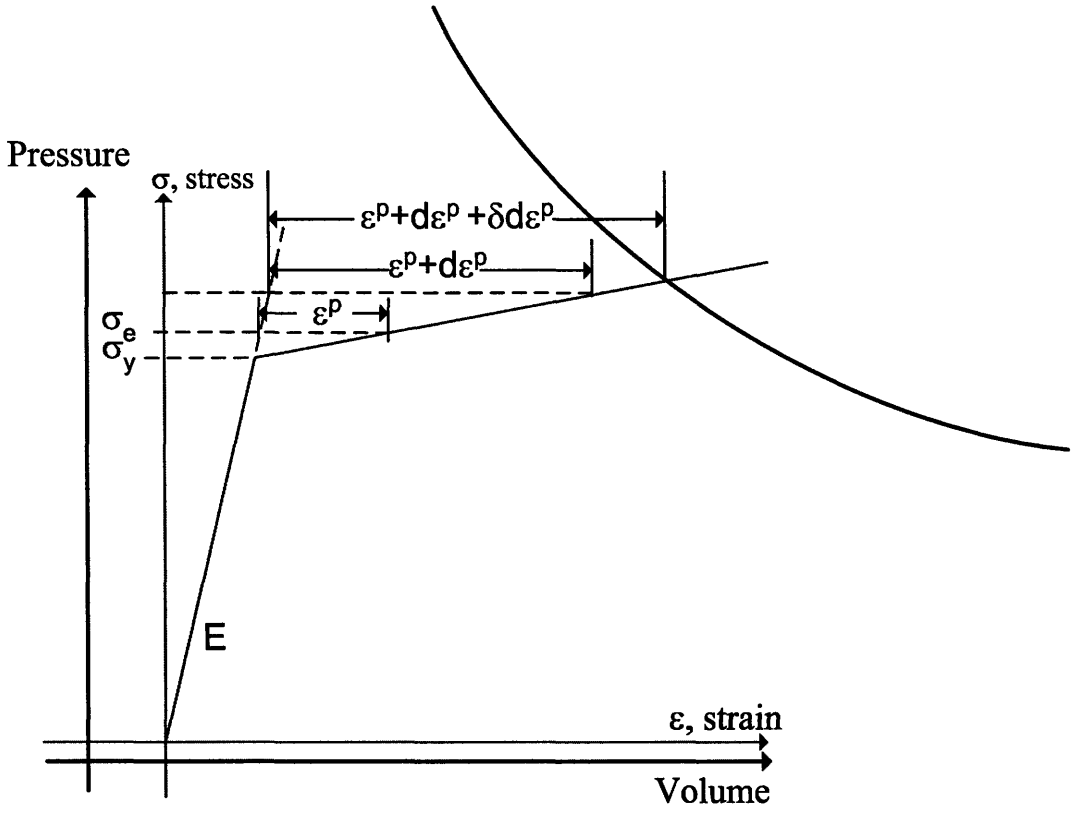

Figure 2-9: Illustration of fission gas induced deformation

Displacement of the cladding inner surface is:

$$u(r_i) = \bar{r}\varepsilon_\theta - \frac{t}{2}\varepsilon_r \tag{2.40}$$

where, t is the thickness of cladding and $\bar{r}$ is the average radius of cladding. Plugging Eq 2.37–Eq 2.39 into Eq 2.40 we obtain:

$$\frac{u(r_i)}{\bar{r}} = \frac{1}{E}(\sigma_\theta - \nu\sigma_z) + \varepsilon_\theta^p + d\varepsilon_\theta^p + \varepsilon_T \tag{2.41}$$

Given axial strain at the cladding inner surface, we can calculate the stress as:

$$\begin{bmatrix} A_{11} & A_{12} \\ A_{21} & A_{22} \end{bmatrix} \begin{bmatrix} \sigma_\theta \\ \sigma_z \end{bmatrix} = \begin{bmatrix} B_1 \\ B_2 \end{bmatrix} \tag{2.42}$$

where

$$\begin{aligned} A_{11} &= 1 + \frac{\nu}{2}\frac{t}{\bar{r}} \\ A_{12} &= \nu(\frac{t}{2\bar{r}} - 1) \\ A_{21} &= -\nu \\ A_{22} &= 1 \\ B_1 &= E\frac{u(r_i)}{\bar{r}} + \frac{Et}{2\bar{r}}(\varepsilon_r^p + d\varepsilon_r^p + \varepsilon_T) - E(\varepsilon_\theta^p + d\varepsilon_\theta^p + \varepsilon_T) \\ B_2 &= E(\varepsilon_z - \varepsilon_z^p - d\varepsilon_z^p - \varepsilon_T) \end{aligned}$$

Hoop and axial stresses can be obtained explicitly as:

$$\sigma_\theta = \frac{B_1A_{22} - B_2A_{12}}{A_{11}A_{22} - A_{12}A_{21}} \tag{2.43}$$

$$\sigma_z = \frac{B_2A_{11} - B_1A_{21}}{A_{11}A_{22} - A_{12}A_{21}} \tag{2.44}$$

The variation of hoop and axial stress is

$$\delta\sigma_\theta = \frac{\delta B_1 A_{22} - \delta B_2 A_{12}}{A_{11}A_{22} - A_{12}A_{21}} \tag{2.45}$$

$$\delta\sigma_z = \frac{\delta B_2 A_{11} - \delta B_1 A_{21}}{A_{11}A_{22} - A_{12}A_{21}} \tag{2.46}$$

Assume $\delta\varepsilon_z = 0$, we obtain

$$\delta B_1 = \frac{E}{\bar{r}}\delta u(r_i) + \frac{Et}{2\bar{r}}\delta d\varepsilon_r^p - E\delta d\varepsilon_\theta^p \tag{2.47}$$

$$\delta B_2 = -E\delta\varepsilon_z^p \tag{2.48}$$

Following the Prandtl-Reuss flow rule, we have:

$$d\varepsilon_\theta^p = \frac{3}{2\sigma_e}(\sigma_\theta - \frac{1}{3}(\sigma_\theta + \sigma_z))d\varepsilon^p \tag{2.49}$$

$$d\varepsilon_z^p = \frac{3}{2\sigma_e}(\sigma_z - \frac{1}{3}(\sigma_\theta + \sigma_z))d\varepsilon^p \tag{2.50}$$

$$d\varepsilon_r^p = -(d\varepsilon_\theta^p + d\varepsilon_z^p) \tag{2.51}$$

With von-Mise yield criterion, the effective stress is:

$$\sigma_e = \sqrt{\frac{(\sigma_\theta - \sigma_z)^2 + \sigma_\theta^2 + \sigma_z^2}{2}} \tag{2.52}$$

Correspondingly, the variation of effective stress, and plastic strains are as follows:

$$\delta\sigma_e = \frac{3}{2\sigma_e}(S_\theta\delta\sigma_\theta + S_z\delta\sigma_z) \tag{2.53}$$

$$\delta d\varepsilon^p = \frac{\delta\sigma_e}{E_2} \tag{2.54}$$

where S_θ and S_z are deviatoric stresses in hoop and axial directions respectively. E_2 is the plastic modulus.

Since during the loading in the closed-gap regime, the ratio of hoop to axial stress is close to 1.0 and radial stress is negligible, we can assume the variation of the ratio

of deviatoric stress to effective stress is negligible and get equations below:

$$\delta d\varepsilon_\theta^p = \frac{3}{2\sigma_e} S_\theta \delta d\varepsilon^p \tag{2.55}$$

$$\delta d\varepsilon_z^p = \frac{3}{2\sigma_3} S_z \delta d\varepsilon^p \tag{2.56}$$

$$\delta d\varepsilon_r^p = -(\delta d\varepsilon_\theta^p + \delta d\varepsilon_z^p) \tag{2.57}$$

Let

$$\begin{aligned}
\lambda_1 &= A_{22}/(A_{11}A_{22} - A_{12}A_{21}) \\
\lambda_2 &= A_{12}/(A_{11}A_{22} - A_{12}A_{21}) \\
\mu_1 &= A_{11}/(A_{11}A_{22} - A_{12}A_{21}) \\
\mu_2 &= A_{21}/(A_{11}A_{22} - A_{12}A_{21})
\end{aligned}$$

Then we get

$$\begin{bmatrix} C_{11} & C_{12} \\ C_{21} & C_{22} \end{bmatrix} \begin{bmatrix} \delta\sigma_\theta \\ \delta\sigma_z \end{bmatrix} = \begin{bmatrix} \lambda_1 E/\bar{r} \\ -\mu_2 E/\bar{r} \end{bmatrix} \delta u(r_i) \tag{2.58}$$

where

$$\begin{aligned}
C_{11} &= 1 + \lambda_1(\frac{Et}{2\bar{r}} + E)\frac{1}{E_2}(\frac{3S_\theta}{2\sigma_e})^2 + (\lambda_1\frac{Et}{2\bar{r}}\frac{1}{E_2} - \lambda_2\frac{E}{E_2})(\frac{3\sigma_\theta}{2\sigma_e})(\frac{3\sigma_z}{2\sigma_e}) \\
C_{12} &= \lambda_1(\frac{Et}{2\bar{r}} + E)\frac{1}{E_2}(\frac{3S_\theta}{2\sigma_e})(\frac{3S_z}{2\sigma_e}) + (\lambda_1\frac{Et}{2\bar{r}}\frac{1}{E_2} - \lambda_2\frac{E}{E_2})(\frac{3\sigma_z}{2\sigma_e})^2 \\
C_{21} &= -\mu_2(\frac{Et}{2\bar{r}} + E)\frac{1}{E_2}(\frac{3S_\theta}{2\sigma_e})^2(-\mu_2\frac{Et}{2\bar{r}}\frac{1}{E_2} + \mu_1\frac{E}{E_2})(\frac{3\sigma_\theta}{2\sigma_e})(\frac{3\sigma_z}{2\sigma_e}) \\
C_{22} &= 1 - \mu_2(\frac{Et}{2\bar{r}} + E)\frac{1}{E_2}(\frac{3S_\theta}{2\sigma_e})(\frac{3S_z}{2\sigma_e})(-\mu_2\frac{Et}{2\bar{r}}\frac{1}{E_2} + \mu_1\frac{E}{E_2})(\frac{3\sigma_z}{2\sigma_e})^2
\end{aligned}$$

We can get the variation of hoop stress as:

$$\delta\sigma_\theta = \frac{\lambda_1 C_{22} + \mu_2 C_{12}}{C_{11}C_{22} - C_{12}C_{21}} \frac{\delta u(r_i)E}{\bar{r}} \tag{2.59}$$

The interface pressure is given by:

$$P = \frac{t\sigma_\theta + r_o P_o}{r_i} \tag{2.60}$$

We have:

$$\delta u(r_i) = \frac{1}{K}\delta P \tag{2.61}$$

where:

$$K = \frac{Et}{r_i \bar{r}} \frac{\lambda_1 C_{22} + \mu_2 C_{12}}{C_{11}C_{22} - C_{21}C_{12}}$$

On the other hand, the fission gas in the fragmented zone follows the ideal gas law. In a cylindrical pellet with unit height, the volume of fission gas is:

$$V_{gas} = \int_0^1 \int_0^{r_f} \frac{2n(r)RT\pi r}{P} dr dz \tag{2.62}$$

Where r_f is the radius of pellet. The swelling strain due to fission gas is:

$$\varepsilon_{swl} = \frac{V_{gas}}{3\pi r_f^2} \tag{2.63}$$

Radial displacement due to fission gas is:

$$\delta u(r_i) = \frac{\int_0^{r_f} 2n(r)RTrdr}{3Pr_f^2} \tag{2.64}$$

The displacement due to fission gas thus is:

$$\delta u = -\frac{P}{2K} + \frac{1}{2K}\sqrt{P^2 + \frac{4K\int_0^{r_f} 2n(r)RTrdr}{3r_f}} \tag{2.65}$$

Therefore by assuming:

- the variation of axial stress due to fission gas effect is zero, and
- the ratio of deviatoric stress to the von-Mise stress remains unchanged

an analytical solution for the incremental displacement due to fission gas is obtained in Eq 2.65. Then with the correction of fission gas induced displacement, the FRACAS-I

model predicts the state of stress and strain accounting for this incremental displacement.

2.4 Gas release and fuel swelling model implementation

2.4.1 Model validation

Test cases used for comparison with the model include irradiated UO_2 fuel in CABRI, NSRR and BIGR simulated RIA tests. When the model was being developed, only the data from CABRI and NSRR were available from literature. This set of test cases from CABRI and NSRR has been subdivided into two groups: one group for model parameter fitting and the other for model validation. Later on, the data from BIGR simulated RIA became available and were used for further validating the model.

The FGR predictions by the modified FRAPTRAN for the NSRR and CABRI test cases are shown in Figure 2-10. The fuel code gives good agreement with the experimental data except for large under-prediction of HBO2, HBO3 and HBO4. The absolute error of FGR is 4.9% for the fitting cases and 5.6% for the validation cases. BIGR test data serves as another set of independent data to compare the models. The prediction by our model in FRAPTRAN 1.3_MIT as well as a modified version of FRAPT-6 [9] are compared with the measured FGR in Figure 2-11. Although FRAPTRAN1.3_MIT generally underpredicts FGR it still gives a standard error not exceeding the validation cases in Figure 2-10.

One uncertainty comes from the fission gas inventory prediction during steady state. This involves more detailed comparison of the radial fission gas distribution calculated by the Massih Model in FRAPCON with PIE analysis. Only one segment rod GE-2 in the Third RISØ Fission Gas Release Project is compared at a terminal ramped power of 41 kW/m in the FRAPCON code. Given that the standard error for the steady-state cases is 2.8% FGR, and the standard deviation for the power ramp cases is 5.3% FGR [27], we can see this prediction during RIA transient is

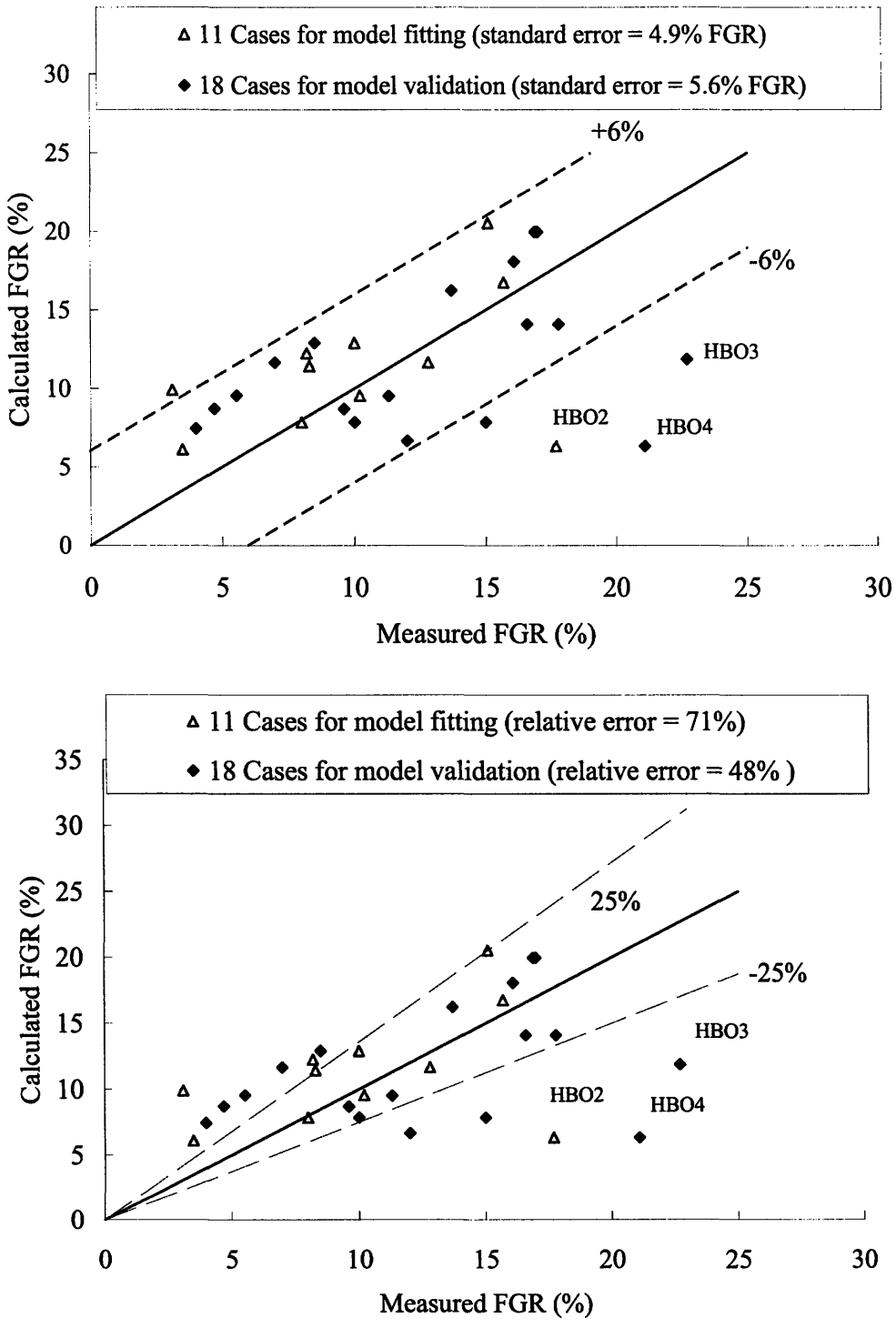

Figure 2-10: Prediction of fission gas release for CABRI and NSRR cases

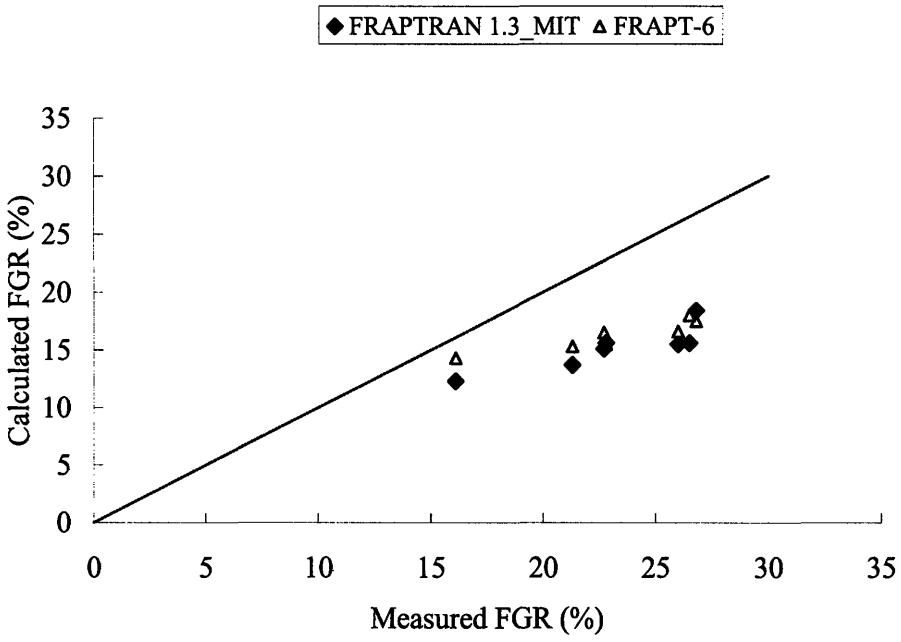

Figure 2-11: Prediction of fission gas release for BIGR cases

reasonable. The model assumes that the fragmentation in the rim region will also contribute to the prompt fission gas release. To verify this assumption and to validate the fission gas distribution in detail. The Xe to Kr ratio is also calculated to compare with the measured one. Since the ratio of Xe/Kr from fission of plutonium isotopes is higher than uranium isotopes, this ratio has generally been considered as an indicator to track fission gas release from the rim structure where there is a high content of plutonium isotopes.

A calculation by the MCODE 1.0 [14], which couples the particle transport code MCNP 4c3 and isotope generation and depletion code ORIGEN 2.1, has been performed to generate the radial profile of Xe/Kr ratio for PWR fuel and BWR fuel tested in NSRR. A single pin cell model shown in Figure 2-12 has been employed to perform the calculation by MCODE 1.0. Since the test rods in NSRR are short refabricated rods and have uniform axial burnup profiles, the 2-D pin cell model is able to represent the isotope generation and depletion in such rods. Figure 2-13 and Figure 2-14 give the Xe/Kr ratio in rim region as well as in the whole cross section as

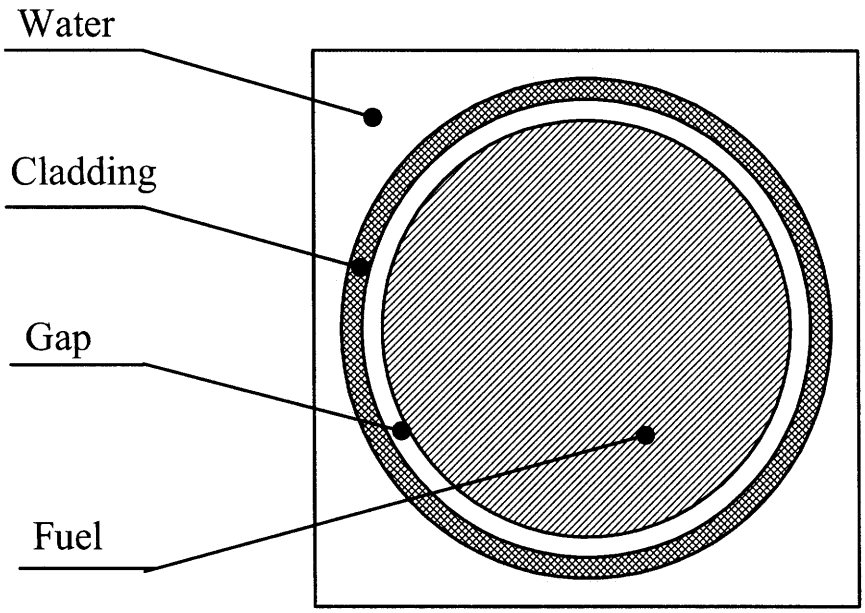

Figure 2-12: Illustration of pin cell model [14]

a function of radial average burnup. Range of enrichment of test cases is from 2.6% to 4.5%. The measured Xe/Kr ratios are also plotted on the figures. Most of the data are bounded by the rim region curve and whole cross section curve ("total" on the plots in Figure 2-13 and Figure 2-14) except for some BWR fuel: TS5, FK5 and FK7.

The formula to calculate the Xe/Kr of released fission gas is given as follows:

$$Xe/Kr = \frac{\sum_{i=1}^{N} n_i/(1+(Xe/Kr)_i)}{\sum_{i=1}^{N} n_i(Xe/Kr)_i/(1+(Xe/Kr)_i)} \tag{2.66}$$

where n_i is the quantity of total fission gas released at the $i-th$ radial node, $(Xe/Kr)_i$ the Xe/Kr ratio at radial node i. n_i is predicted by the FGR model in the FRAP-TRAN code. The Xe/Kr radial profile is calculated by MCODE 1.0. The Xe/Kr ratio is compared with that obtained from rod punctures in NSRR tests as shown in Figure 2-15 and Figure 2-16.

Analysis of the Xe/Kr ratio of HBO2–HBO4 indicates that the large under-prediction of fission gas release in Figure 2-10 is partially due to the under-prediction of the fission gas release from the rim region. Figure 2-16 shows more clearly there

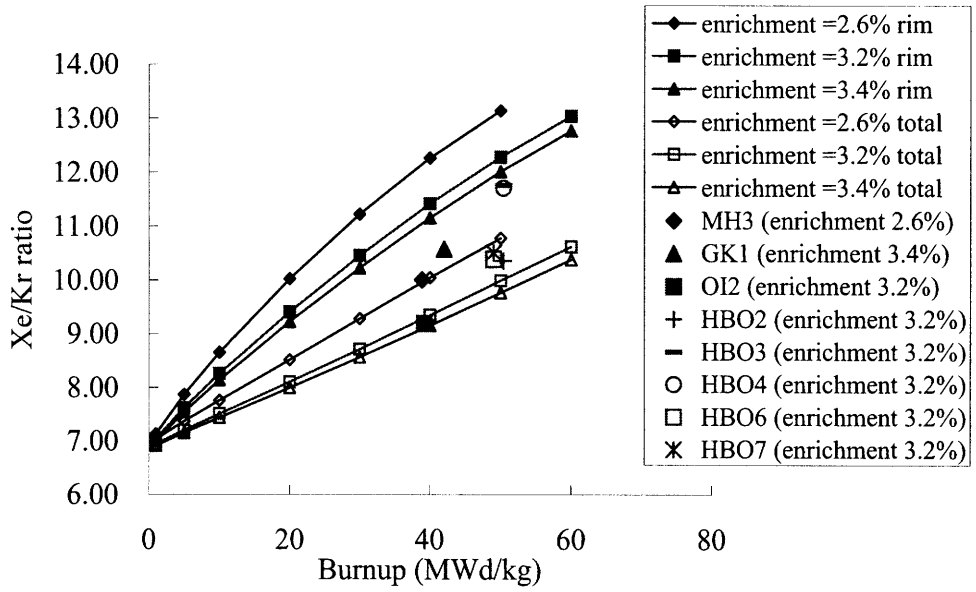

Figure 2-13: Xe to Kr ratio for PWR fuel vs. burnup

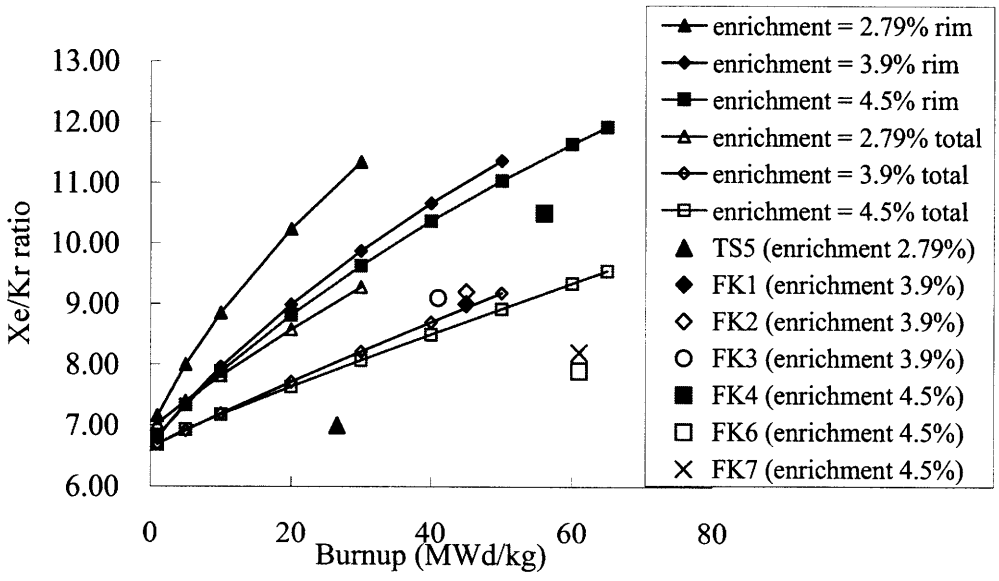

Figure 2-14: Xe to Kr ratio for BWR fuel vs. burnup

is an over-prediction of Xe/Kr for TS5, FK6 and FK7. As shown in Table A.4, all of these cases have larger FGR during base irradiation. This may lead to more uncertainty in fission gas distribution prior to RIA transients.

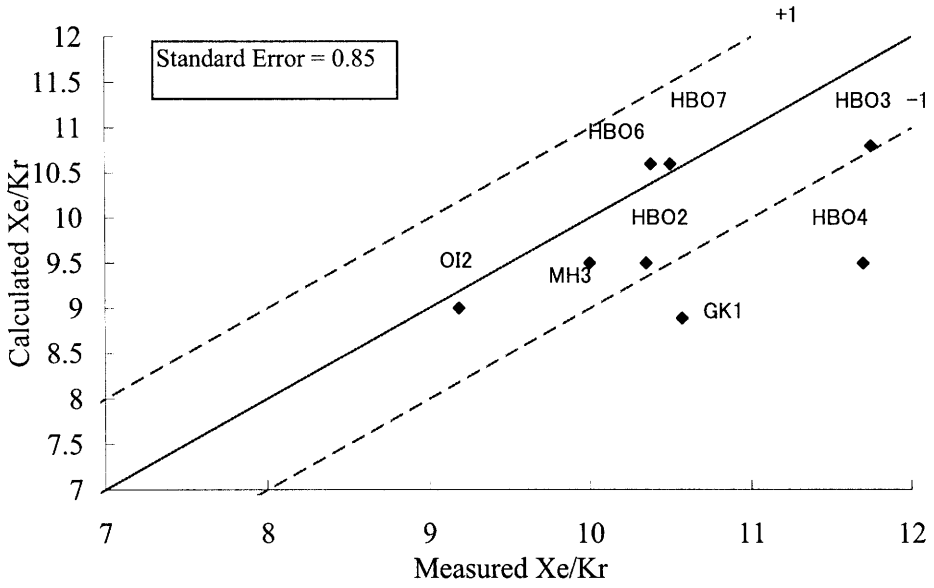

Figure 2-15: Validation of Xe to Kr ratio for PWR fuel

Figure 2-17 gives predictions of the permanent hoop strains by the modified FRAPTRAN code. The large scattering of these data points is largely due to the lack of detailed pre-transient state of the test fuel rod. Ref. [46] states that some preconditioning may lead to the fuel chips in the P/C gap, which effectively decrease the gap thickness. Ref. [47] shows that the frictional model is missing in the fuel code.

To reveal the effects due to fission gas, the prediction of the permanent hoop strain by the modified code as compared to the original FRAPTRAN code is given in Figure 2-18. The model predicts the fission gas induced hoop strain during PCMI is less than 0.3%, much smaller than that due to the thermal expansion of the pellet. The only large improvement of GK1 however is found in the high temperature phase. Figure 2-18 gives the peak value of measured permanent hoop strain. Since the uniform axial power profile in NSRR cases can't produce the local ballooning type

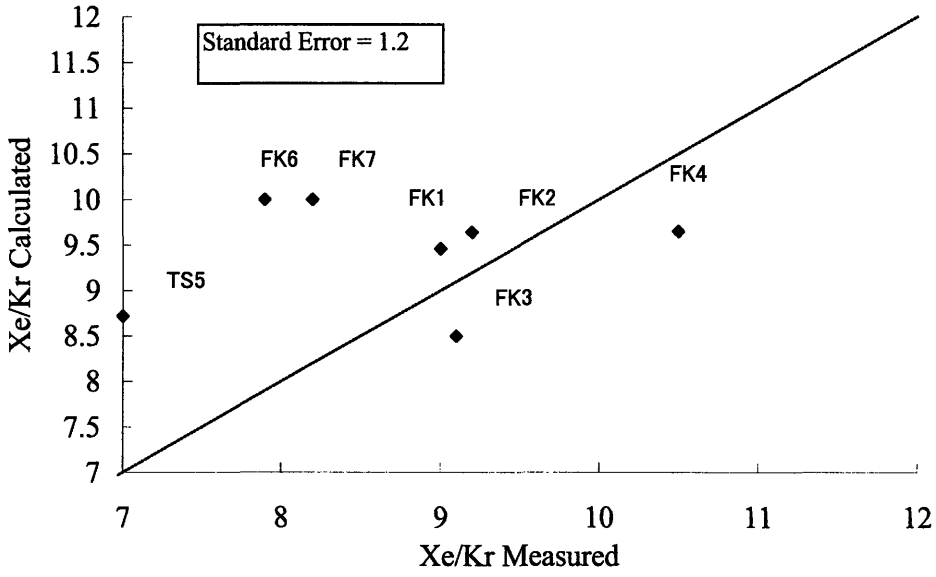

Figure 2-16: Validation of Xe to Kr ratio for BWR fuel

deformation. This might be the reason of the large under-prediction of OI2.

Figure 2-19 gives the prediction of average permanent hoop strain by the FRAP-TRAN 1.3_MIT and the calculation by Russian codes [9]. Table 2.3-Table 2.14 list detailed calculation results. These BIGR cases generally have larger enthalpy deposition and more ductile cladding to survive the PCMI phase. Thus the large deformations are mainly due to the pressure loading.

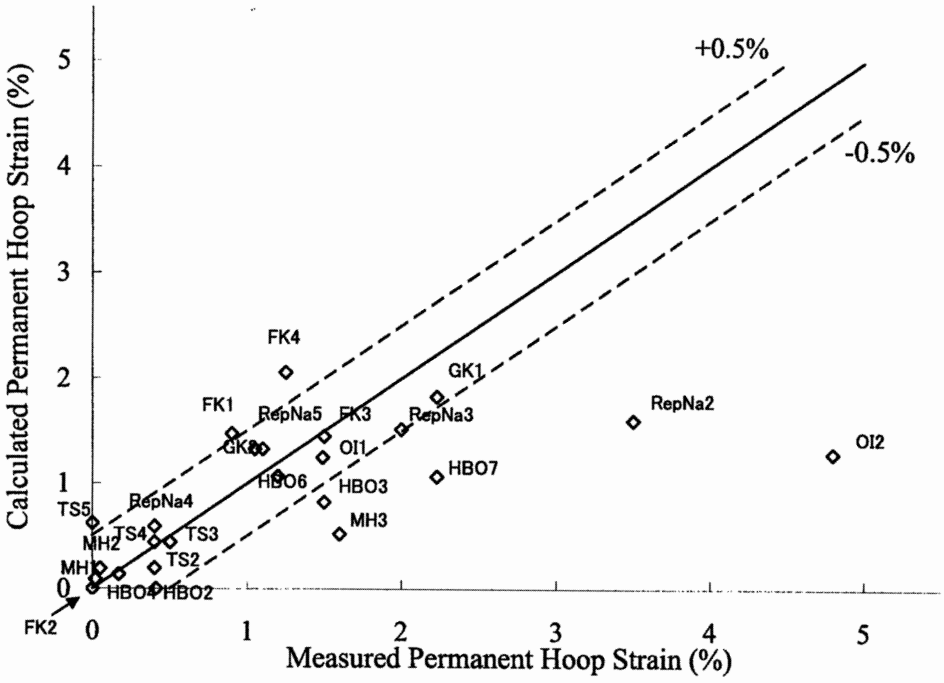

Figure 2-17: Prediction of permanent hoop strain for CABRI and NSRR cases

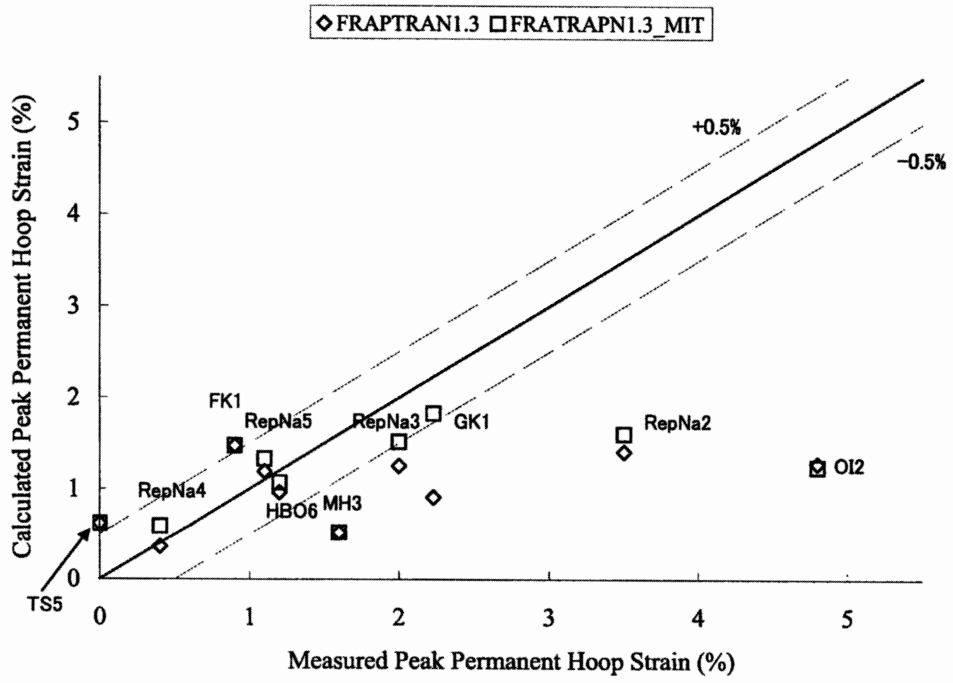

Figure 2-18: Prediction of permanent hoop strain by FRAPTRAN 1.3 and FRAPTRAN 1.3_MIT

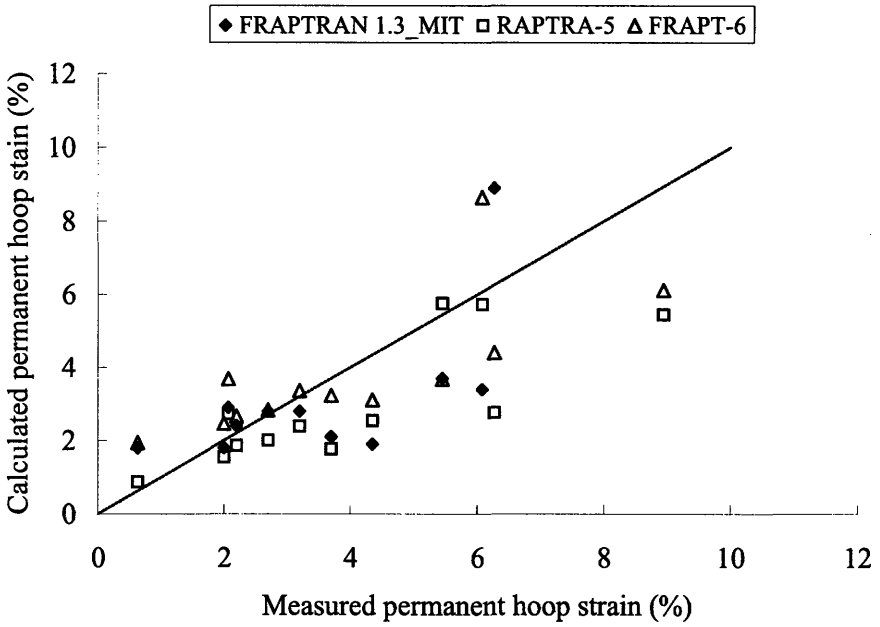

Figure 2-19: Prediction of permanent hoop strain for BIGR cases

Table 2.3: Test Results for fuel rod RT1

Parameter	Measured	Calculated		
		FRAP–T6	RAPTRA–5	FRAPTRAN1.3_MIT
Bunrup (MWd/kg)	48.3	-	-	-
Base FGR (%)	2.85	-	-	1.36
Initial Gas Pressure (MPa)	2.1	2.1	2.1	2.1
Peak Fuel Enthalpy (cal/g)	-	142.9	141.6	142.3
Fuel Maximum Temperature(K)	-	2323	2327	2102
Peak Cladding Temperature (K)	-	1111	1162	1347.6
Permanent Hoop Strain (%)	2.20	2.66	1.86	2.41
Fission Gas Release (%)	22.8	15.5	-	15.61 (2.2% from rim)
Rim size (micron)	60	-	-	60
Fuel Failure	Unfailed	Unfailed	Unfailed	Unfailed

Table 2.4: Test Results for fuel rod RT2

Parameter	Measured	Calculated		
		FRAP–T6	RAPTRA–5	FRAPTRAN1.3_MIT
Bunrup (MWd/kg)	48.0	-	-	-
Base FGR (%)	2.85	-	-	1.32
Initial Gas Pressure (MPa)	2.1	2.1	2.1	2.1
Peak Fuel Enthalpy (cal/g)	-	114.3	116.2	115.5
Fuel Maximum Temperature (K)	-	1963	2011	1825.6
Peak Cladding Temperature (K)	-	982	1019	1232.9
Permanent Hoop Strain (%)	0.63	1.94	0.88	1.81
Fission Gas Release (%)	16.1	14.3	-	12.3 (0.0% from rim)
Rim size (micron)	60	-	-	60
Fuel Failure	Unfailed	Unfailed	Unfailed	Unfailed

Table 2.5: Test Results for fuel rod RT3

Parameter	Measured	Calculated		
		FRAP–T6	RAPTRA–5	FRAPTRAN1.3_MIT
Bunrup (MWd/kg)	47.5	-	-	-
Base FGR (%)	2.85	-	-	1.2
Initial Gas Pressure (MPa)	2.1	2.1	2.1	2.1
Peak Fuel Enthalpy (cal/g)	-	138.6	137.2	133.6
Fuel Maximum Temperature (K)	-	2266	2279	2030.8
Peak Cladding Temperature (K)	-	1104	1127	1296.5
Permanent Hoop Strain (%)	2.00	2.46	1.55	1.85
Fission Gas Release (%)	21.3	15.3	-	13.7 (0.8% from rim)
Rim size (micron)	60	-	-	60
Fuel Failure	Unfailed	Unfailed	Unfailed	Unfailed

Table 2.6: Test Results for fuel rod RT4

Parameter	Measured	Calculated		
		FRAP–T6	RAPTRA–5	FRAPTRAN1.3_MIT
Bunrup (MWd/kg)	60.1	-	-	-
Base FGR (%)	2.82	-	-	2.23
Initial Gas Pressure (MPa)	2.1	2.1	2.1	2.1
Peak Fuel Enthalpy (cal/g)	-	125.3	123.9	126.2
Fuel Maximum Temperature (K)	-	2099	2126	1967.2
Peak Cladding Temperature (K)	-	1110	1099	1037.1
Permanent Hoop Strain (%)	3.70	3.23	1.77	2.11
Fission Gas Release (%)	-	17.1	-	18.1 (8.3% from rim)
Rim size (micron)	175	-	-	175
Fuel Failure	Unfailed	Unfailed	Unfailed	Unfailed

Table 2.7: Test Results for fuel rod RT5

Parameter	Measured	Calculated		
		FRAP–T6	RAPTRA–5	FRAPTRAN1.3_MIT
Bunrup (MWd/kg)	48.6	-	-	-
Base FGR (%)	4.46	-	-	1.18
Initial Gas Pressure (MPa)	2.1	2.1	2.1	2.1
Peak Fuel Enthalpy (cal/g)	-	146.4	145.6	146.2
Fuel Maximum Temperature (K)	-	2353	2379	2151.5
Peak Cladding Temperature (K)	-	1125	1175	1358.2
Permanent Hoop Strain (%)	2.70	2.83	2.01	2.84
Fission Gas Release (%)	26	16.6	-	15.5 (2.6% from rim)
Rim size (micron)	60	-	-	60
Fuel Failure	Unfailed	Unfailed	Unfailed	Unfailed

Table 2.8: Test Results for fuel rod RT6

Parameter	Measured	Calculated		
		FRAP–T6	RAPTRA–5	FRAPTRAN1.3_MIT
Bunrup (MWd/kg)	47.8	-	-	-
Base FGR (%)	2.41	-	-	0.5
Initial Gas Pressure (MPa)	2.1	2.1	2.1	2.1
Peak Fuel Enthalpy (cal/g)	-	152.5	152.7	152.5
Fuel Maximum Temperature (K)	-	2421	2459	2213.8
Peak Cladding Temperature (K)	-	1157	1207	1406.9
Permanent Hoop Strain (%)	3.20	3.36	2.39	2.86
Fission Gas Release (%)	26	18	-	15.6 (2.4% from rim)
Rim size (micron)	60	-	-	60
Fuel Failure	Unfailed	Unfailed	Unfailed	Unfailed

Table 2.9: Test Results for fuel rod RT7

Parameter	Measured	Calculated		
		FRAP–T6	RAPTRA–5	FRAPTRAN1.3_MIT
Burnup (MWd/kg)	60.3	-	-	-
Base FGR (%)	1.15	-	-	2.2
Initial Gas Pressure (MPa)	2.0	2.0	2.0	2.0
Peak Fuel Enthalpy (cal/g)	-	131.7	136.4	140.3
Fuel Maximum Temperature (K)	-	2183	2251	2110.9
Peak Cladding Temperature (K)	-	1146	1126	1223.2
Permanent Hoop Strain (%)	2.07	3.68	2.73	2.9
Fission Gas Release (%)	26.8	17.5	-	18.4 (9.1% from rim)
Rim size (micron)	-	-	-	175
Fuel Failure	Unfailed	Unfailed	Unfailed	Unfailed

Table 2.10: Test Results for fuel rod RT8

Parameter	Measured	Calculated		
		FRAP–T6	RAPTRA–5	FRAPTRAN1.3_MIT
Burnup (MWd/kg)	60.2	-	-	-
Base FGR (%)	2.82	-	-	2.26
Initial Gas Pressure (MPa)	2.0	2.0	2.0	2.0
Peak Fuel Enthalpy (cal/g)	-	162.3	166.4	162.4
Fuel Maximum Temperature (K)	-	2514	2580	2327
Peak Cladding Temperature (K)	-	1219	1265	1440.5
Permanent Hoop Strain (%)	6.08	8.64	5.73	2.47
Fission Gas Release (%)	-	19.1	-	16.0 (5.3% from rim)
Rim size (micron)	175	-	-	175
Fuel Failure	Failed	-	-	Unfailed

Table 2.11: Test Results for fuel rod RT9

Parameter	Measured	Calculated		
		FRAP–T6	RAPTRA–5	FRAPTRAN1.3_MIT
Burnup (MWd/kg)	59.9	-	-	-
Base FGR (%)	2.82	-	-	2.34
Initial Gas Pressure (MPa)	2.0	2.0	2.0	2.0
Peak Fuel Enthalpy (cal/g)	-	162.4	167.5	171.5
Fuel Maximum Temperature (K)	-	2524	2584	2446.3
Peak Cladding Temperature (K)	-	1164	1249	1213.3
Permanent Hoop Strain (%)	6.27	4.41	2.77	1.25
Fission Gas Release (%)	-	19.3	-	12.1 (0.0% from rim)
Rim size (micron)	175	-	-	175
Fuel Failure	Failed	-	-	-

Table 2.12: Test Results for fuel rod RT10

Parameter	Measured	Calculated		
		FRAP–T6	RAPTRA–5	FRAPTRAN1.3_MIT
Burnup (MWd/kg)	47.0	-	-	-
Base FGR (%)	2.08	-	-	1.22
Initial Gas Pressure (MPa)	2.0	2.0	2.0	2.0
Peak Fuel Enthalpy (cal/g)	-	162.5	165.9	162.8
Fuel Maximum Temperature (K)	-	2542	2578	2302
Peak Cladding Temperature (K)	-	1214	1251	1425.6
Permanent Hoop Strain (%)	8.94	6.12	5.45	3.60
Fission Gas Release (%)	-	18.4	-	31.2 (18.6% from rim)
Rim size (micron)	175	-	-	175
Fuel Failure	Failed	Failed	Failed	Unfailed

Table 2.13: Test Results for fuel rod RT11

Parameter	Measured	Calculated		
		FRAP–T6	RAPTRA–5	FRAPTRAN1.3_MIT [a]
Burnup (MWd/kg)	47.2	-	-	-
Base FGR (%)	2.08	-	-	1.17
Initial Gas Pressure (MPa)	2.0	2.0	2.0	2.0
Peak Fuel Enthalpy (cal/g)	-	188.4	186.7	184.9
Fuel Maximum Temperature (K)	-	2782	2774	2473.6
Peak Cladding Temperature (K)	-	1306	1333	1708.5
Permanent Hoop Strain (%)	5.45	3.68	5.76	3.7
Fission Gas Release (%)	-	22.0	-	15.5 (2.3% from rim)
Rim size (micron)	60	-	-	60
Fuel Failure	Failed	Failed	Failed	-

[a]Execution stopped when Tclad > 1738 K

Table 2.14: Test Results for fuel rod RT12

Parameter	Measured	Calculated		
		FRAP–T6	RAPTRA–5	FRAPTRAN1.3_MIT
Burnup (MWd/kg)	47.4	-	-	-
Base FGR (%)	2.08	-	-	1.17
Initial Gas Pressure (MPa)	0.1	0.1	0.1	0.1
Peak Fuel Enthalpy (cal/g)	-	154.7	154.9	152.5
Fuel Maximum Temperature (K)	-	2472	2466	2206.8
Peak Cladding Temperature (K)	-	1180	1249	1319.5
Permanent Hoop Strain (%)	4.35	3.11	2.54	1.93
Fission Gas Release (%)	-	16.5	-	15.1 (2.6% from rim)
Rim size (micron)	60	-	-	60
Fuel Failure	Unfailed	-	-	Unfailed

2.4.2 Discussion

Figure 2-20 and Figure 2-21 show the trend of fission gas release as a function of peak fuel enthalpy and burnup level. The general increase of FGR as peak fuel enthalpy increase is captured by the model prediction for burnup 26–42 MWd/kg. Above 45 MWd/kg, the rim structure gives additional contribution to the FGR. This is observed in both the measured and calculated trend. In the low enthalpy and high burnup range (HBO2–HBO4), however, the model gives large under-prediction. As mentioned in Section 2.4.1, this is partially due to under-prediction of the fission gas from the rim region. This trend is more likely to be an athermal process, in which the tensile thermal stress plays a more important role rather than the gas excess pressure alone in intergranular bubbles. A detailed characterization of the micro-structure and accurate calculation of the stress field would help to improve this prediction.

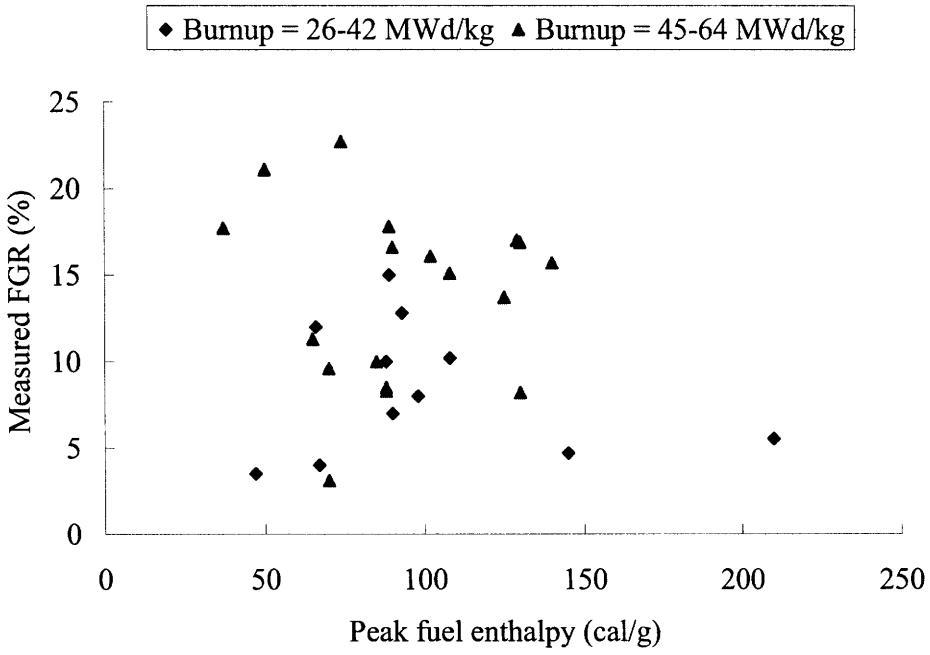

Figure 2-20: Measured FGR vs. enthalpy for CABRI and NSRR cases

Fission gas retention calculated by FGR model is compared with EPMA analysis in Figure 2-22 and Figure 2-23. The model is capable of predicting that the majority of the fission gas release takes place in the central region, but there are some limitations

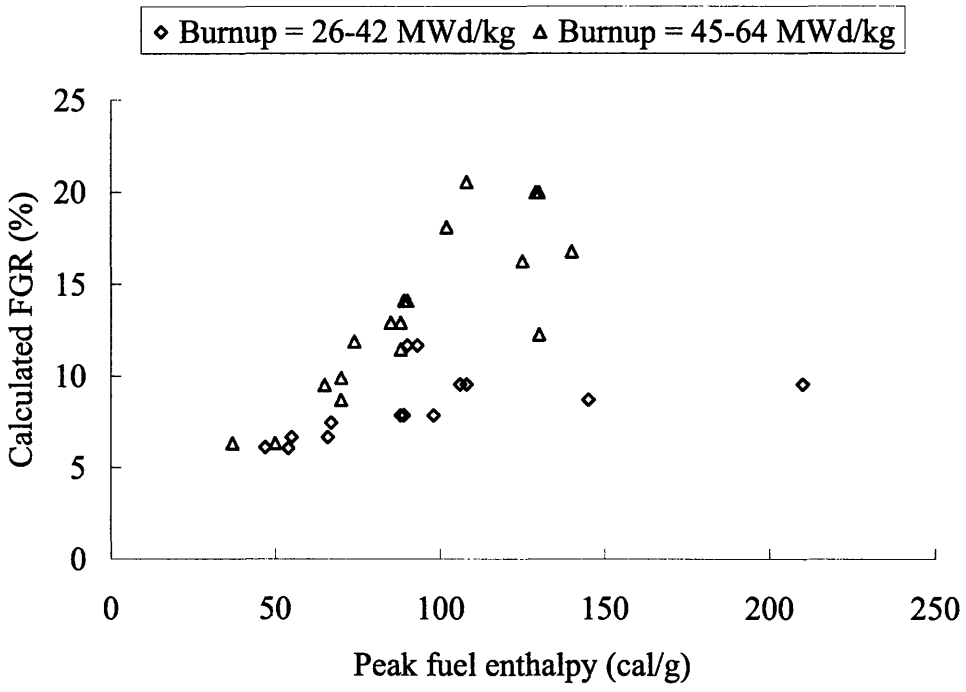

Figure 2-21: Calculated FGR vs. enthalpy for CABRI and NSRR cases

due to the assumption of complete grain boundary separation. In Optical Microscopy (OM) and Scanning Electron Microscopy (SEM) ceramographs carried out on test rod FK1 after RIA test, a weak separation of crystal grains was observed at the pellet center [48]. Therefore, there is a possibility that the grain boundary separation leading to a partial communication with the free volume.

By changing the power level, a sensitivity study of case OI2 is shown in Figure 2-24. When the peak cladding temperature is less than around 750 K, the deformation is determined by the PCMI in the early phase. When the peak cladding temperature is greater than 1100 K by further increasing the power, large deformation appears in the high temperature phase. Figure 2-25 gives the yield stress of Zry-4 calculated by the MATPRO in FRAPTRAN code. As can be seen in the early phase, the cladding yield strength is at least a few hundred MPas, due to the low temperature as well as strain hardening and strain rate hardening. When the temperature is above 1100 K, it drops down to a few tens of MPas. The fill gas and the fission gas released into the plenum makes the large deformation possible. Note that the End of Life (EOL)

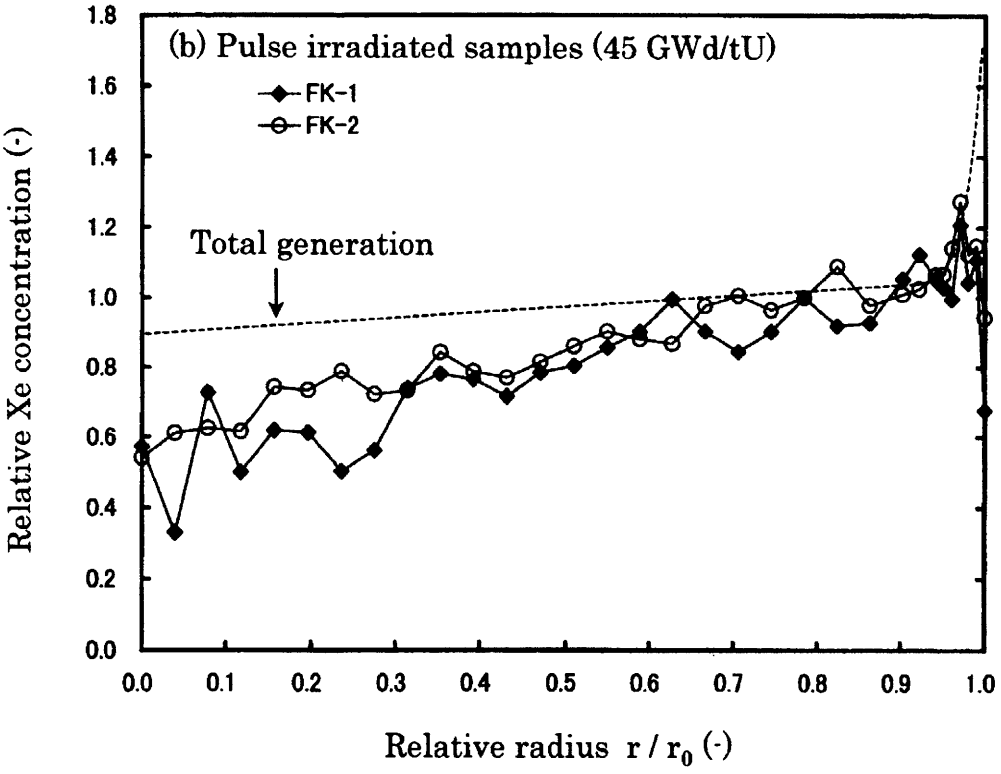

Figure 2-22: EPMA analysis of FK1-2 [49]

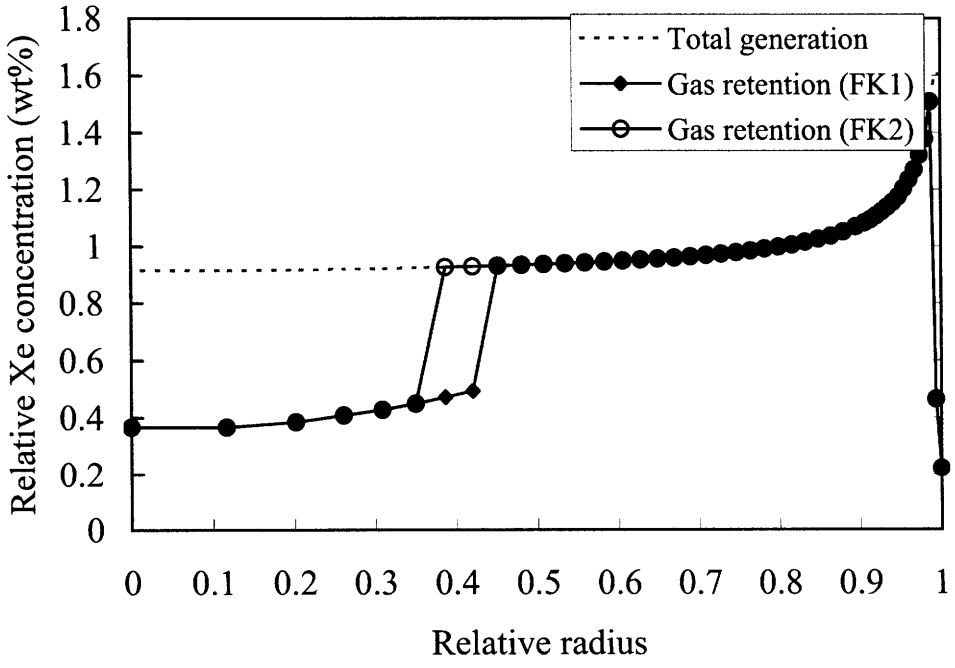

Figure 2-23: Prediction of gas retention for FK1-2

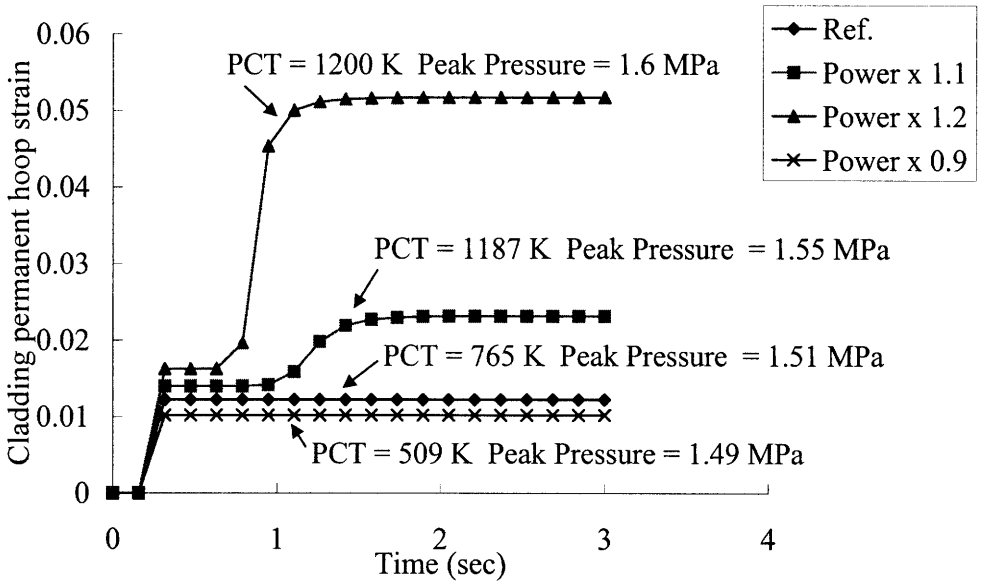

Figure 2-24: Sensitivity study of OI2

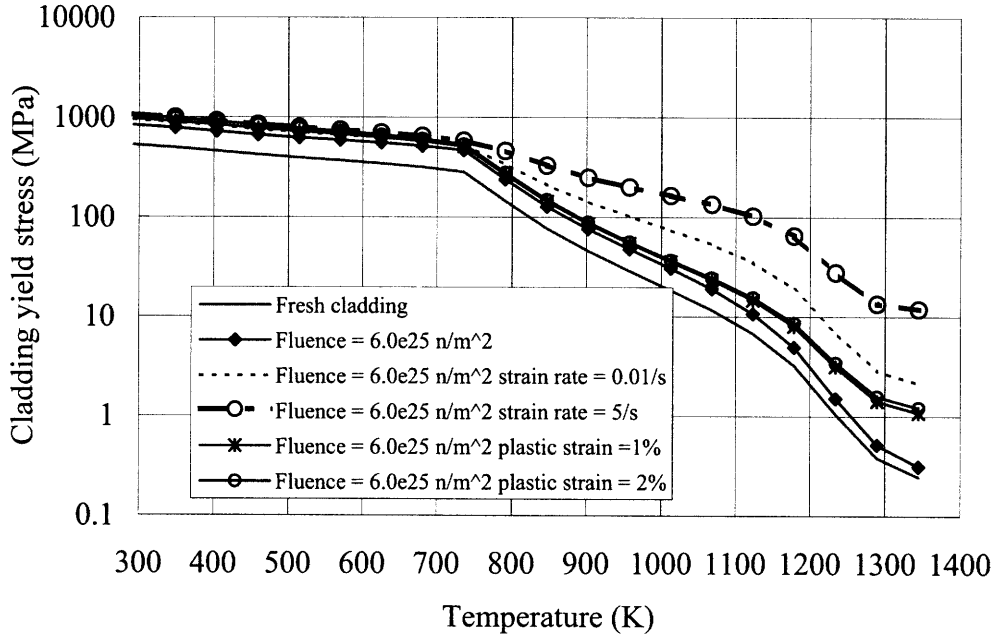

Figure 2-25: Yield stress of Zry-4 predicted by MATPRO

gap gas pressure could be higher in a commercial rod than in the test rod because the commercial rod has a relatively smaller plenum to fuel volume ratio than that of the test rod by a factor of 2 [50]. For a commercial rod, the DNB should be more of concern as the rod pressure is more likely to cause the ballooning of the fuel rod.

2.5 Summary and conclusions

This chapter summarizes the improved FRAPTRAN modeling of fission gas induced deformation during an RIA.

The Massih model in FRAPCON code is used to initialize the fission gas inventory at grain boundaries. A detailed modeling of micro-structure of the rim region is given in terms of porosity, pore size distribution, fission gas concentration and pore overpressure.

The model assumes the fragmentation of fuel upon the separation of grain boundary or when a threshold temperature is exceeded in the rim region. The fission gas in fragmented fuel is assumed to release instantaneously to the free volume when the fuel expansion and swelling creates sufficient pellet-clad gap. The relaxation of rim pore at rapid temperature increase and the thermal expansion of fission gas in fragmented fuel are considered as additional loads on the cladding besides the contact force due to fuel thermal expansion. A two step method is developed to couple the fission gas induced deformation with the rigid pellet model FRACAS-I in FRAPTRAN code.

The models are validated by NSRR, CABRI and BIGR simulation tests in terms of FGR, Xe/Kr, and permanent hoop strain. Fission gas induced hoop strain is predicted to be less than 0.3% in the early phase of RIA when the peak fuel enthalpy is less than 145 cal/g. This is attributed to the high interface pressure suppressing fission gas expansion. The fission gas induced deformation in the early phase of RIA is not significant as expected even in the presence of rim structure and large amount of fission gas at grain boundaries for high burnup fuel. Thus, a simple pellet expansion model is still considered as effective in analyzing the PCMI failure of fuel pins. However, with the increased amount of energy deposit, large deformation of

clad is possible due to decreased cladding strength at escalated temperature. Xe/Kr analysis indicates fission gas release is partly from the rim region and the majority of fission gas is released from the grain boundary for burnup up to 50 MWd/kgU. Validation by Xe/Kr shows the capability of the model to partition the fission gas release from rim and intergranular bubbles in central pellet.

Chapter 3

Modeling cladding-coolant heat transfer

3.1 Introduction

This chapter describes the choice and development of models for cladding-coolant heat transfer of high burnup fuel during a Reactivity-Initiated Accident (RIA) at atmospheric pressure and room temperature.

For a number of un-failed test rods at NSRR, escalation of cladding surface temperature has been observed and is believed to be associated with cladding coolant heat transfer in the film boiling regime. Such a phenomenon poses particularly interesting questions regarding the safety margin of high burnup fuel during RIA. On one hand, the temperature increase of the cladding could lead to an increase of its ductility, which may help avoid a brittle failure due to PCMI failure. On the other hand, decreased yield strength of zircaloy cladding at high temperature may allow ballooning and burst failure of the cladding with pressure loading due to fission gas release of high burnup fuel. An accurate prediction of the cladding temperature is required in the fuel performance code to provide the foundation to address these questions and to better quantify the safety margin.

The original FRAPTRAN code however doesn't have the capability to predict the cladding surface temperature using existing heat transfer packages. Therefore a new

set of heat transfer models have been implemented in the modified fuel performance code designated as FRAPTRAN 1.3_MIT. The minimum stable film boiling temperature, affected by subcooling and clad oxidation, is modeled by a modified Henry correlation. This accounts for the effects of thermal properties of the cladding surface on the transient temperature drop during liquid-solid contact. The transition boiling regime is described as the interpolation of the heat flux between two anchor points on the pool boiling curve: Critical Heat Flux (CHF) and minimum stable film boiling heat flux. The CHF correlation is the Zuber hydrodynamic model multiplied by a subcooling factor. Frederking correlation is chosen to model the film boiling regime. Heat conduction through the oxide layer of the cladding surface of high burnup fuel is calculated by solving the heat conduction equations with thermal properties of zirconia taken from MATPRO [13]. The heat transfer models are validated with the data from simulated RIA tests conducted at room temperature and atmospheric pressure condition in NSRR.

3.2 Model description

Simulated RIA tests at NSRR were conducted at room temperature and atmospheric pressure, which may best represent the cold zero power (CZP) condition of BWRs. In the simulated test, a single instrumented test rod was placed in a water filled capsule, and was pulse irradiated. In the early phase of an RIA test, the temperature of the pellet would increase rapidly as a result of the power burst and the gap was closed due to the thermal expansion and swelling of pellet. With sufficient heat transferred to the cladding and coolant, a vapor envelope developed around the cladding causing film boiling at the cladding outer surface. The sustained film boiling could lead to a high temperature of cladding. Later on, the gap was reopened due to mechanical deformation and reduced power, the cladding temperature would drop down slowly and eventually the rewetting temperature was met. Then the breakdown of the vapor film leads to rewetting of the cladding. Neglecting the increase of water temperature in the capsule, heat transfer from cladding to coolant may be characterized as pool

boiling conditions.

Ohnishi derived empirical correlations from inverse heat conduction calculation of the measured cladding surface temperature of fresh test fuel at subcooled boiling condition [51]. Application of these heat transfer correlations in the NSR-77 code, and similar empirical correlations in the DYN3D code [52], give good predictions of the cladding surface temperature history of fresh fuel. However, when the models for fresh fuel have been applied to the cases of high burnup fuel, prediction of cladding surface temperature and quenching behavior was far from matching the experimental data [53]. In fact, the observed cladding temperature is lower and duration of DNB is shorter for high burnup fuel than fresh fuel at similar enthalpy deposit [54]. From the results of simulated RIA tests of fresh fuel with pre-oxidized cladding, Sugiyama concluded that wettability change is the dominant factor in explaining the heat transfer of high burnup fuel [54]. Nevertheless no model was presented to account for the effect on heat transfer. Therefore, our modeling of the heat transfer is focused on capturing the effects due to oxidation, which is a distinctive feature of high burnup fuel. Other possible factors affecting heat transfer are also investigated to improve the prediction of cladding temperature of high burnup fuel during the RIA transient.

3.2.1 Oxidation effects

To model the oxidation effects, we consider two factors:

- Heat conduction through the oxide layer;
- Change of surface heat transfer characteristics by oxidation.

The former is modeled by solving the transient heat conduction equation through the oxide layer with thermal-physical properties obtained from MATPRO [13]. One radial node is meshed with thermal properties of zirconia in the numerical solution of the 1-D heat conduction problem.

The oxidation effect on surface heat transfer characteristics is modeled by taking into account the thermal-physical properties of the oxide layer instead of its wettability. The reasons are as follows:

- The experimental work on wettability change is usually done by oxidation of the surface, associated with the thermal-physical property change of a coating material [55]. It can not exclude the effect due to thermal property change.

- The influence of substrate material thermal properties on the pool boiling curve was demonstrated by the work of Westwater [56]

- Lack of measurement data of contact angle of zirconia to provide a good foundation for a wettability model.

Furthermore, this effect can be rationalized by Henry's postulate that liquid-solid contact resulting from the returning liquid after bubble detachment from the wall or breaking through the liquid could produce thermal transients in the solid wall and that these surface transients could then lead to the progressive breakdown of the film boiling regime [57]. Thus, the thermal properties of the surface material affecting the interface temperature during liquid-solid contact can significantly influence rewetting.

3.2.2 Subcooling effects

Due to a high degree of subcooling in NSRR simulated RIA tests, the boiling heat transfer would be greatly affected. The effect on CHF has been addressed by Ivey and Morris (1966) by experiment for horizontal wires with degree of subcooling from 0 to 70 °C and pressure 0.03 to 3.4 MPa for a wide range of coolants: water, ethyl alcohol, ammonia, carbon tetrachloride and isooctane [58]. A subcooling factor was given as follows:

$$f_{subc} = 1 + 0.1(\rho_f/\rho_g)^{0.75} c_{p,f}(T_{sat} - T_l)/h_{fg} \tag{3.1}$$

It is used in the heat transfer models to account for subcooling effects although it slightly exceeds the range of subcooling in the original experiment. In the transition and film boiling regime, simulated RIA tests on fresh fuel indicates subcooling also has a strong effect to enhance the heat transfer [51].

3.2.3 Transient effects

In nucleate boiling regime, the bubble dynamics are investigated as follows. The bubble size at departure is given by the Fritz equation, which is a function of liquid solid contact angle [59]. Bubble growth rate at atmospheric pressure is shown in Figure 3-1 using the analytical solution by Mikic. As superheat increases, the bubble growth time is decreased. As can be seen, the order of bubble growth time is in millisecond. After the bubble detach, the thermal boundary would be re-established. This period including both the bubble growth and the waiting time is given by the Malenkov correlation as a function of heat flux and contact angle [59] shown in Figure 3-2. Though it decreases with the increase of heat flux, at the critical heat flux, it is still 10 millisecond for the example at contact angle of 90°.

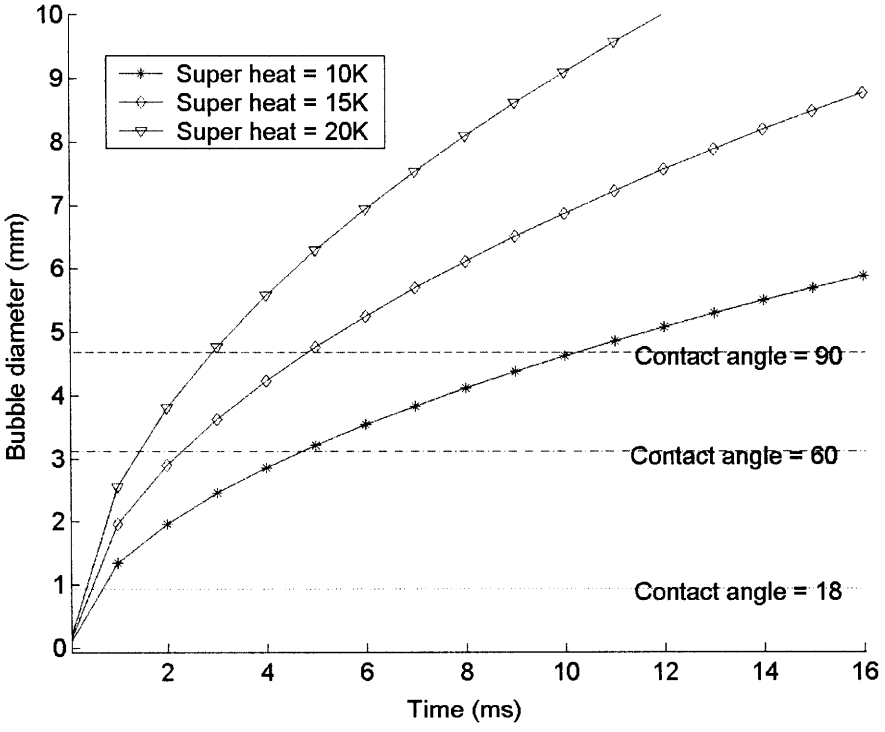

Figure 3-1: Bubble growth kinetics at different super heat

Therefore, the mechanism that describes the heat transfer at steady state may not be able to describe accurately the heat transfer in the early phase, as the power pulse width is comparable to the bubble growth and release time. On the other

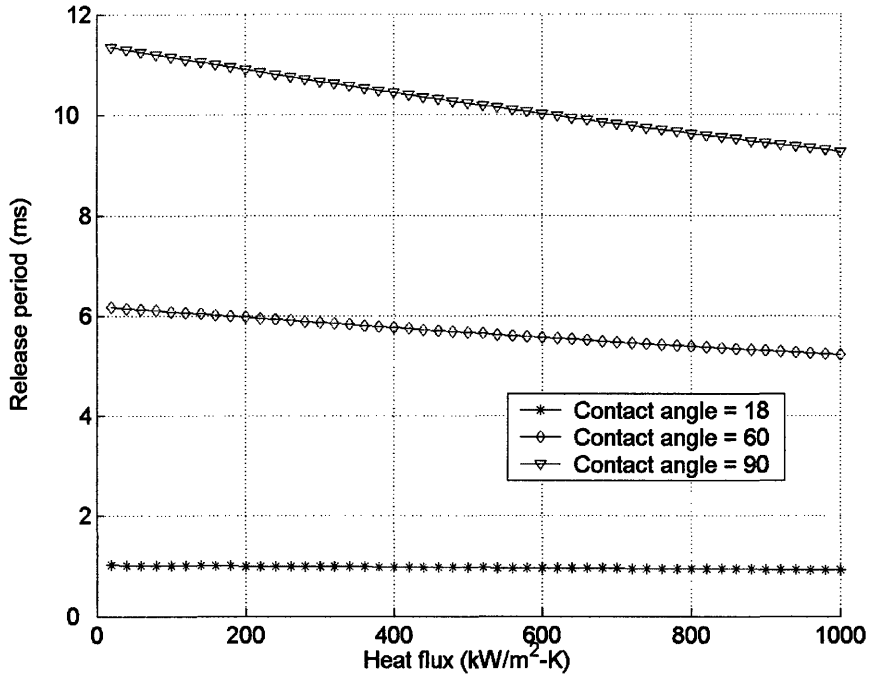

Figure 3-2: Bubble release period as a function of heat flux at different contact angles

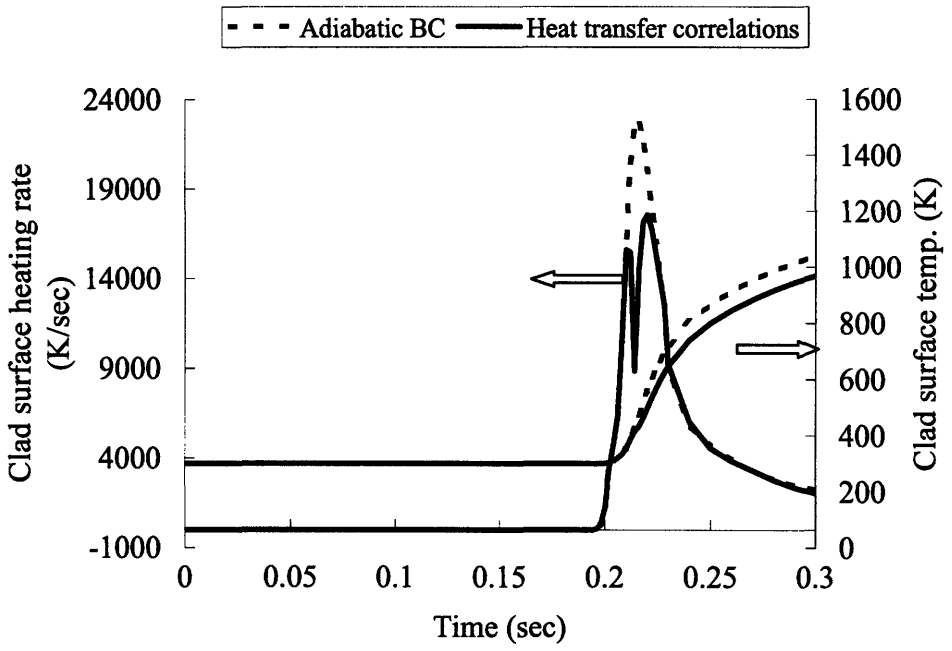

Figure 3-3: Cladding heating rate and temperature with adiabatic boundary condition

hand, the duration of the nucleate boiling regime is also very short. By setting two kinds of boundary conditions for test case FK3, the cladding surface heating rate is examined in Figure 3-3. One is a typical heat transfer correlation currently employed in FRAPTRAN code. The other one is an adiabatic boundary condition. The peak heating rate is caused by the high heat flux from the fuel surface during the closure of gap. The depression of the peak predicted by the heat transfer correlations is caused by encountering nucleate boiling. The time in the nucleate boiling regime is around 3 ms. This is comparable to the bubble growth time and less than the bubble release period. Thus the heat transfer is not as effective as that during steady state. Figure 3-3 also shows that the steady state heat transfer correlation doesn't lead to much difference from an adiabatic boundary condition. Therefore, in this regime a steady state heat transfer correlation is used as shown in the next section.

For CHF, power excursion tests in a pool boiling of water by Tachibana et. al found that the CHF increases as the power pulse time decreases [60]. This has also been confirmed by other work [60] showing a short burst of nucleate boiling at heat fluxes about 5 to 20 times the steady-state values with a power pulse width less than 1 ms. This was explained as due to an increase in the number of nucleation sites being activated simultaneously.

In the PATRICIA test program, the clad to coolant heat transfer was tested under very fast transients at PWR HZP condition: 15MPa and 280 °C. By heating up the clad by Joule effect with electrical power transients simulating the heat generated by the neutronic power transient, a range of pulse widths from 20 ms to 350 ms was applied. It led to the conclusion that a critical heat-flux of the order of 5-6 MW/m^2 can be reached when the clad outer temperature is around T_{sat} + 50 °C [61].

Given the high degree of subcooling at a cold zero power condition, it is doubtful that a transient effect can further increase the magnitude of CHF. Thus we still keep the assumption that the CHF is dominated by the subcooling effect.

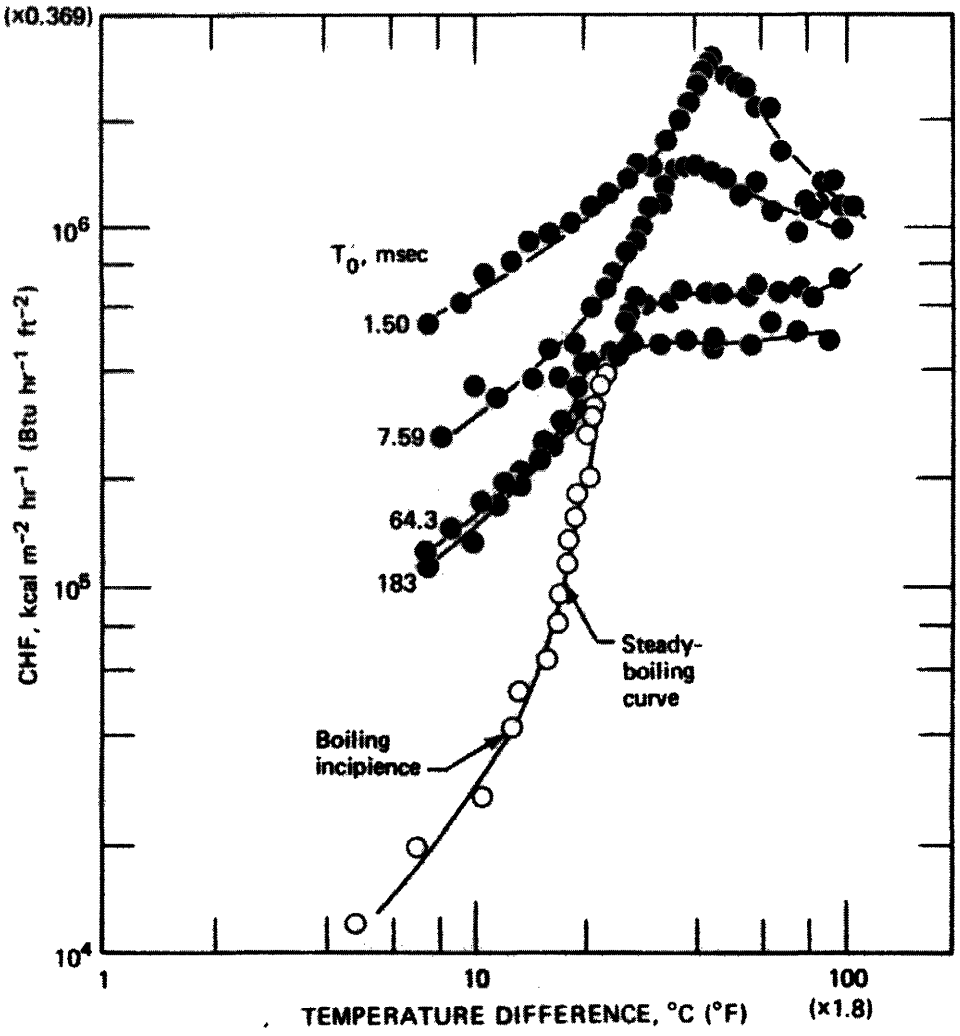

Figure 3-4: Pool boiling curve at power excursion (From Ref.[60])

3.2.4 Heat transfer models

During an RIA, heat transfer on the cladding surface is represented by the heat transfer correlations on a boiling curve to provide boundary conditions for the thermal models of the fuel rod in the fuel code.

Before the onset of nucleate boiling on the cladding surface, a natural convection correlation is applicable as follows.

$$h_n = \begin{cases} 0.59\frac{k_l}{D_h}(GrPr)^{0.25}, & 10^4 < (GrPr) < 10^9 \\ 0.10\frac{k_l}{D_h}(GrPr)^{0.333}, & 10^9 < (GrPr) < 10^{13} \end{cases} \tag{3.2}$$

$$Gr = \frac{g\beta(T_w - T_l)\rho_l^2 D_h^3}{\mu_l^2} \tag{3.3}$$

$$Pr = \frac{\mu_l c_{p,l}}{k_l} \tag{3.4}$$

During fast heat up of the fuel rod, a very short period of vapor bubbles nucleation, growth, and departure follows natural convection. The Rosenhow correlation is used to represent the heat transfer in this regime [62].

$$q = \mu_l h_{fg}[\frac{g(\rho_l - \rho_g)}{\sigma}]^{0.5}[\frac{c_{p,f}(T_w - T_{sat})}{0.013 h_{fg} Pr_f^{1.7}}]^3 \tag{3.5}$$

As evidenced by the results shown in Figure 3-3, the short duration of heat transfer in nucleate boiling and the relatively lower heat flux on the cladding surface as compared to that on the fuel surface could justify application of the above correlations.

The criterion for reaching critical heat flux would be more important as it judges whether DNB would occur. The CHF correlation is based on the Zuber hydrodynamic model corresponding to a well-wetted surface. To account for a high subcooling condition, a multiplication factor f_{subc} is introduced [63]. The final form of the critical heat flux correlation is

$$q_{chf} = 0.131 f_{subc} h_{fg} \rho_g^{0.5} (\sigma g(\rho_f - \rho_g))^{0.25} \tag{3.6}$$

As the cladding surface is fully covered with a vapor film, a heat transfer correlation for turbulent film boiling is chosen [64].

$$h_{film} = 0.2[\frac{k_v^2 g(\rho_f - \rho_v)h'_{fg}}{\rho_v(T - T_{sat})}]^{1/3} \tag{3.7}$$

where $h'_{fg} = h_{fg} + 0.5c_{p,g}(T_g - T_{sat})$ is the modified latent heat. Radiation heat transfer coefficient is given by:

$$h_r = \sigma_{SB}\frac{T_w^4 - T_l^4}{(1/\epsilon_w + 1/\epsilon_l - 1)(T_w - T_l)} \tag{3.8}$$

The total heat transfer coefficient thus is:

$$h_{tot} = f_{subc}h_{film} + h_r \tag{3.9}$$

In Eq 3.9 , f_{subc} is introduced to account for the subcooling effects. In the transition boiling regime, the heat flux is represented as an interpolation of the critical heat flux and minimum heat flux [65]

$$q = \zeta q_{chf} + (1 - \zeta)q_{min} \tag{3.10}$$

$$\zeta = (\frac{T_w - T_{min}}{T_{chf} - T_{min}})^2 \tag{3.11}$$

T_{chf} is determined by the critical heat flux and nucleate boiling heat transfer correlations. T_{min} is strongly affected by the surface condition as well as by the subcooling of the coolant. At high subcooling conditions, the following empirical correlations have been developed especially to address the heat transfer at cold zero power condition.

The Ohnishi correlation [51]:

$$T_{min} = T_{sat} + 350 + 5.1(T_{sat} - T_l) \tag{3.12}$$

The Gotoviskij correlation [52]:

$$T_{min} = T_{sat} + 100 + 8(T_{sat} - T_l) \tag{3.13}$$

Semi-theoretical Eq 3.14 by Henry accounts for the effect due to thermal-physical properties of surface material [65], but is less capable of representing heat transfer at a high degree of subcooling in comparison with the empirical correlations as evidenced in Figure 3-5.

$$T_{min} = T_{NH} + (T_{NH} - T_l)R^{1/2} \tag{3.14}$$

Where

$$R = \frac{k_l \rho_l c_{p,l}}{k_w \rho_w c_{p,w}}$$

$$\begin{aligned} T_{NH} = {} & 647.28 - (2.623 \times 10^2)(3203.6 - 0.000145P) \\ & + (1.328 \times 10^{-5})(3203.6 - 0.00145P)^2 \\ & - (3.2329 \times 10^{-9})(3203.6 - 0.00145P)^3 \end{aligned}$$

Therefore in the code application, the Henry correlation is modified by adding a term sensitive to the subcooling in Eq 3.15.

$$T_{min} = T_{NH} + (T_{NH} - T_l)R^{1/2} + C_{subc}(T_{sat} - T_l) \tag{3.15}$$

C_{subc} is an empirical parameter taken as 3.3 to best match the Ohnishi and Gotoviskij correlations at high subcooling conditions.

Table 3.2 describes the variables in Eq 3.2 to Eq 3.15. Table 3.3 summarizes various effects of surface conditions on the heat transfer characteristics according to open literatures.

Figure 3-6 shows the pool boiling curve of heat flux versus wall superheat with subcooling and oxidation effects, plotted in a log-log scale.

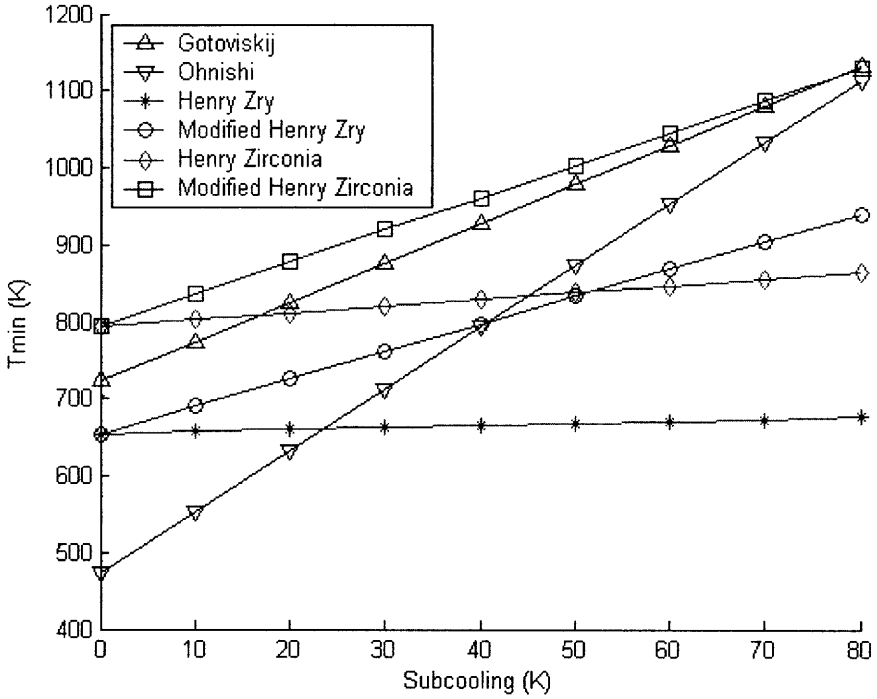

Figure 3-5: T_{min} correlation vs. subcooling at 0.1 MPa

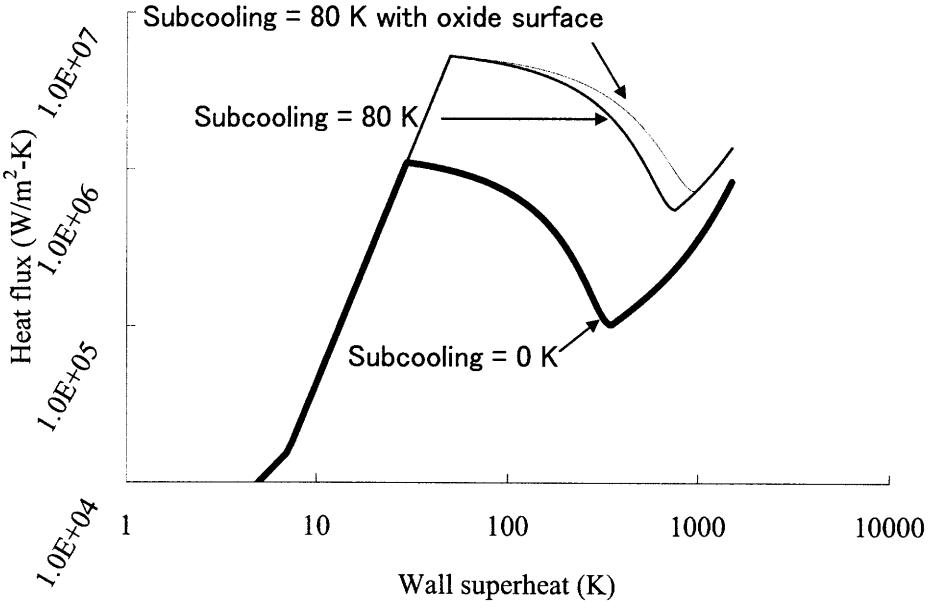

Figure 3-6: Pool boiling curve change due to subcooling and oxidation

Table 3.1: Nomenclature for Eq 3.2-Eq 3.15

Parameter	Description	Unit
c_{pf}	specific heat of liquid at saturated temperature	kJ/kg-K
c_{pg}	specific heat of vapor at saturated temperature	kJ/kg-K
c_{pl}	specific heat of subcooled liquid	kJ/kg-K
c_{pw}	specific heat of cladding wall	kJ/kg-K
f_{subc}	a factor to account for the subcooling effect	-
g	acceleration due to gravity	m/s^2
h_f	enthalpy of saturated liquid	kJ/kg
h_{fg}	latent heat of vaporization	kJ/kg
h'_{fg}	modified latent heat of vaporization	kJ/kg
h_{film}	film boiling heat transfer coefficient	W/m^2-K
h_g	enthalpy of saturated vapor	kJ/kg
h_n	natural convection heat transfer coefficient	W/m^2-K
h_{nb}	nucleate boiling heat transfer coefficient	W/m^2-K
h_r	radiation heat transfer coefficient	W/m^2-K
h_{tot}	heat transfer coefficient including film boiling and radiation	W/m^2-K
k_f	thermal conductivity of liquid at saturated temperature	W/m-K
k_g	thermal conductivity of vapor at saturated temperature	W/m-K
k_l	thermal conductivity of subcooled liquid	W/m-K
k_v	thermal conductivity of superheated vapor	W/m-K
k_w	thermal conductivity of cladding wall	W/m-K
q	heat flux	W/m^2
q_{chf}	critical heat flux	W/m^2
q_{min}	minimum heat flux	W/m^2
C_{subc}	fitting parameter in modified Henry correlation	-
D_h	heat diameter of fuel rod	m
Gr	Grashof number	-
P	pressure	Pa
Pr	Prandtl number	-
R	Ratio of the product of $k\rho c_p$ of liquid to that of wall	-
T_{chf}	temperature at critical heat flux	K
T_f	initial temperature in film boiling regime	K
T_{min}	minimal stable film boiling temperature	K
T_{sat}	saturated temperature	K
T_w	wall temperature	K
T_l	bulk coolant temperature	K
T_{NH}	homogeneous nucleation temperature	K
β	thermal expansion coefficient	-
ϵ_l	emissivity of liquid	-
ϵ_w	emissivity of wall	-
ρ_f	density of liquid at saturated temperature	kg/m^3
ρ_g	density of vapor at saturated temperature	kg/m^3
ρ_l	density of subcooled liquid	kg/m^3

Table 3.2: Nomenclature for Eq 3.2-Eq 3.15 (continued)

Parameter	Description	Unit
ρ_v	density of super heated vapor	kg/m^3
ρ_w	density of cladding wall	kg/m^3
σ	surface tension energy at saturated temperature	N/m
σ_{SB}	Stefan-Boltzman constant	W/m^2-K^4
μ_f	liquid viscosity at saturated temperature	Pa-s
μ_l	viscosity of subcooled liquid	Pa-s

Table 3.3: Various effects on pool boiling heat transfer

	Nucleate boiling	Critical heat flux	Transition boiling	T_{min}
Surface roughness ↑	↑	↑ and shifted to lower wall superheat [66].	↓ [66] Not strongly affected as in nucleate boiling [55]	
Surface thermal property			Boiling curve is shifted to the right as $\rho_w C_w k_w$ ↓ [59]	↑ as $\rho_w C_w k_w$ ↓ [57]
Surface wettability ↑		↑ [66][55][59]	↑ [55]	↑ [66]
Subcooling ↑		↑ [66]		↑ [65]
Heating rate ↑	↑ [60]	↑ but the superheat doesn't change remarkably [67] [60]		

3.3 Model implementation

To verify the applicability of the heat transfer model at RIA conditions, test cases covering both fresh fuel and high burnup fuel are validated in the FRAPTRAN code. All the test cases are taken from pulse irradiation tests at NSRR. The key parameters for each case are listed in Table 3.4.

Table 3.4: Key parameters for test cases to validate heat transfer models

Test No.	Burnup (MWd/kg)	Oxide thickness (μm)	Peak fuel enthalpy (cal/g)	Gap size (μm)	Subcooling (K)
TK3	50	10	99	10	80
FK1	45	22	130	95	80
FK2	45	22	70	95	80
FK3	41	25	145	95	80
FK4	56	15	140	43	80
FK5	56	15	70	43	80
NM	0	0	110	20	80
1M	0	1	110	20	80
NH	0	0	135	20	80
1H	0	1	135	20	80
Fresh01	0	0	190	82	80
Fresh02	0	0	190	82	40
Fresh03	0	0	190	82	10

3.3.1 Model validation

The PCT and the duration of DNB defined as the time from onset of DNB until complete rewetting of the fuel rod are selected as parameters to validate the model. Prediction for PCT and duration of DNB as compared to experimental data are plotted in Figure 3-7 and Figure 3-8. As can be seen in Figure 3-7, generally good results have been achieved by the code calculation except for two points FK1 and 1M. The code predicts no DNB for cases FK2, 5 and DNB for the others. It is consistent with the experimental results and demonstrates the capability of the fuel code to differentiate DNB cases from no DNB cases. From the analysis of Vickers hardness change (measured at four circumferential position 0, 90, 180 and 270 degree at selected axial

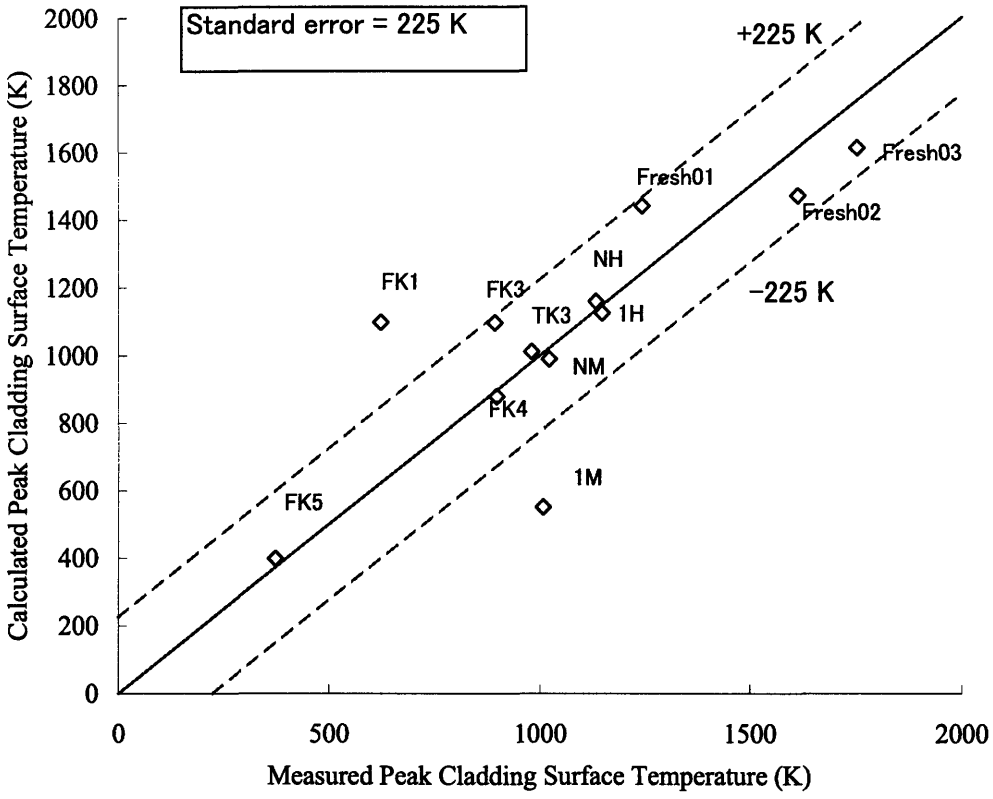

Figure 3-7: Comparison of calculated PCT and measured PCT

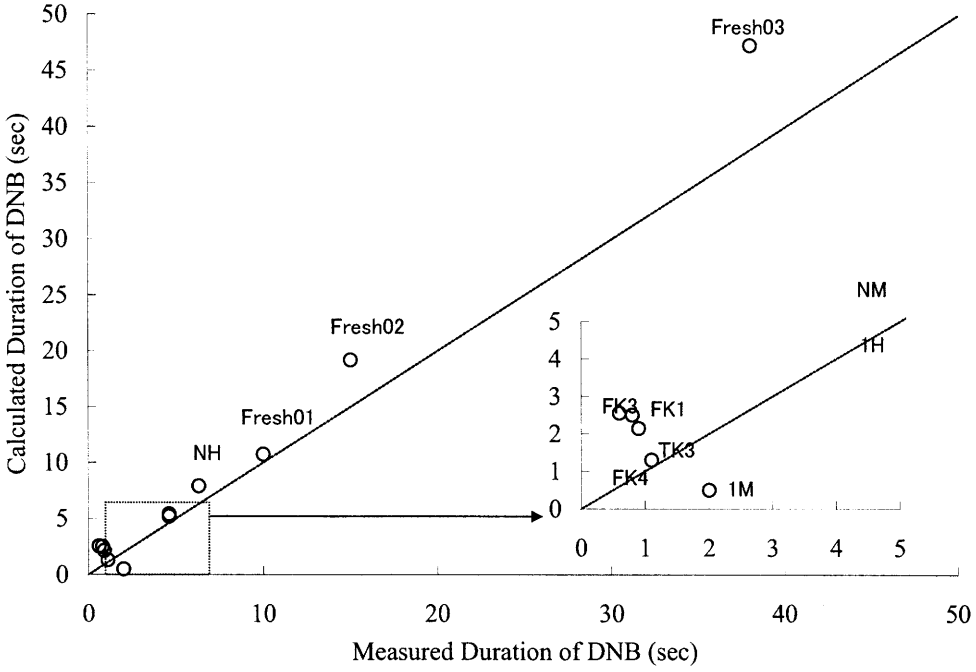

Figure 3-8: Comparison of calculated duration of DNB and experimental data

positions) due to high temperature annealing [68], the peak cladding temperature for both FK1 and FK3 should have reached around 550-600 °C [54], close to the temperature by thermal couple measurement for FK3 but far from that for FK1. The measurement of Vickers Hardness indicates a circumferential variation of temperature of high burnup fuel, but it is not reflected by the thermal couple measurement. Result for FK1 confirms the temperature derived from Vickers Hardness measurement, although it is still over-predicted. Figure 3-9 to Figure 3-15 give the prediction of cladding surface temperature history in comparison with the experimental data from various tests. Enthalpy deposits are similar for cases NH, 1H, FK3 and FK4. In comparison with the fresh fuel, the film boiling regime is less distinctive, and relatively lower PCT and shorter duration of DNB are found for high burnup fuel cases FK3 and FK4. For the fresh fuel with and without oxidation, the film boiling regime could be predicted by FRAPTRAN calculation. Nevertheless, the prediction for irradiated fuel still shows large uncertainty as can be seen from Figure 3-14. This implies that besides oxidation effect, other factors like gap conductance could play an important

role for high burnup fuel.

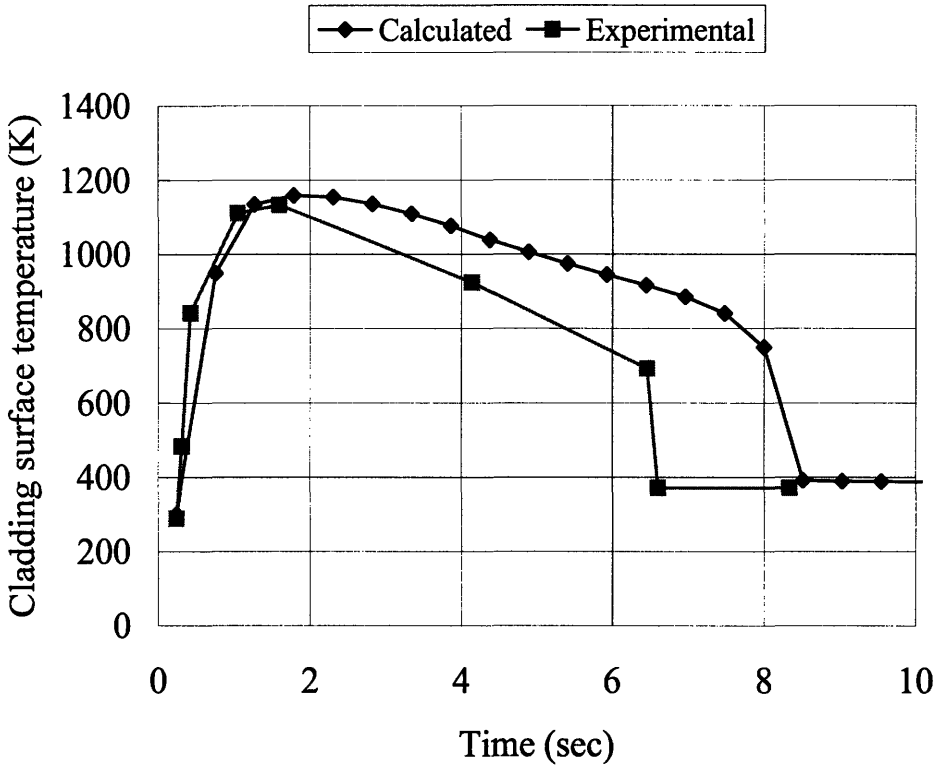

Figure 3-9: Prediction of Cladding Surface Temperature History for NH

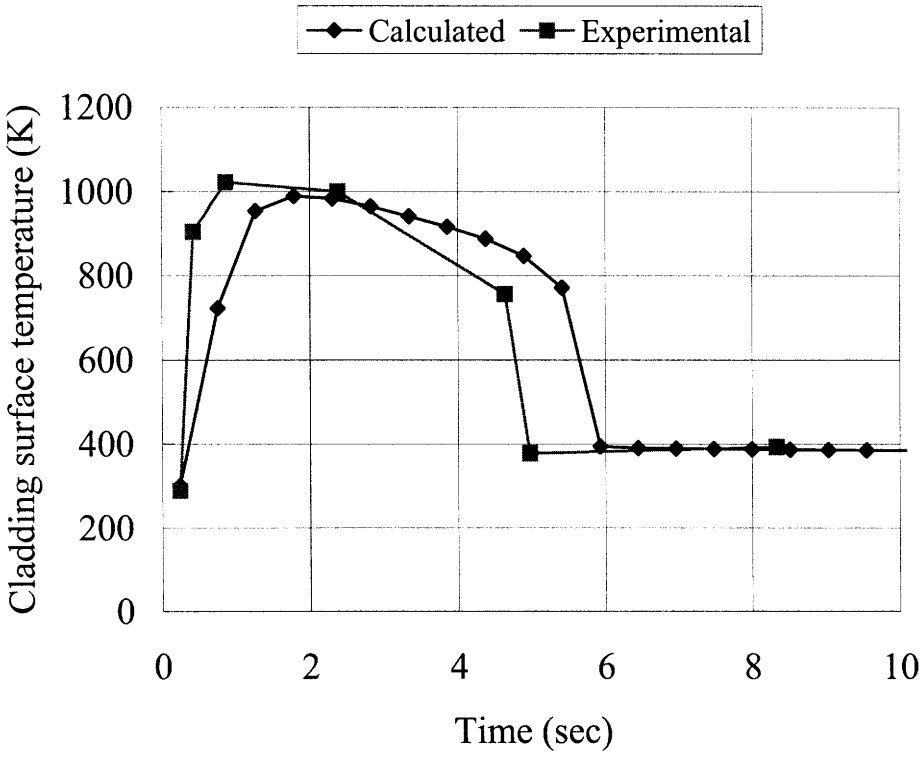

Figure 3-10: Prediction of Cladding Surface Temperature History for NM

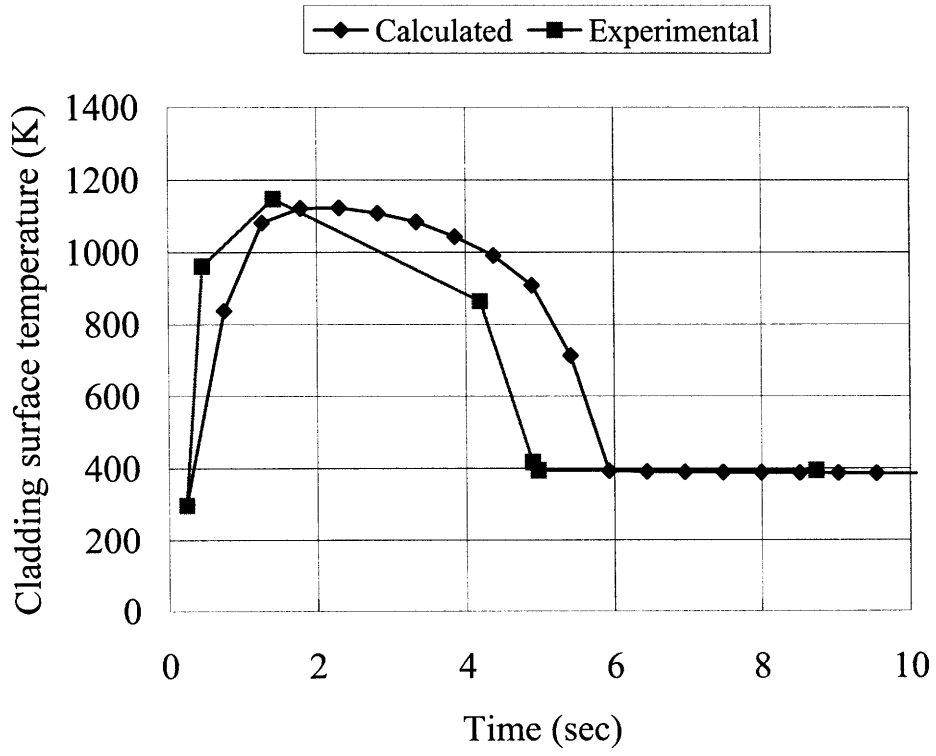

Figure 3-11: Prediction of Cladding Surface Temperature History for OH

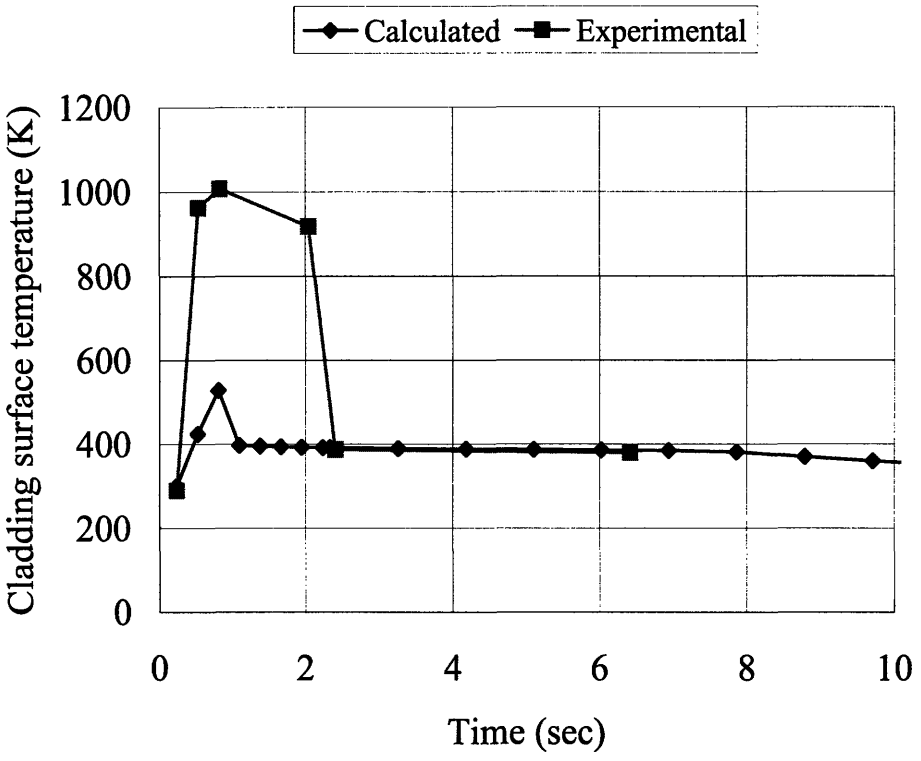

Figure 3-12: Prediction of Cladding Surface Temperature History for OM

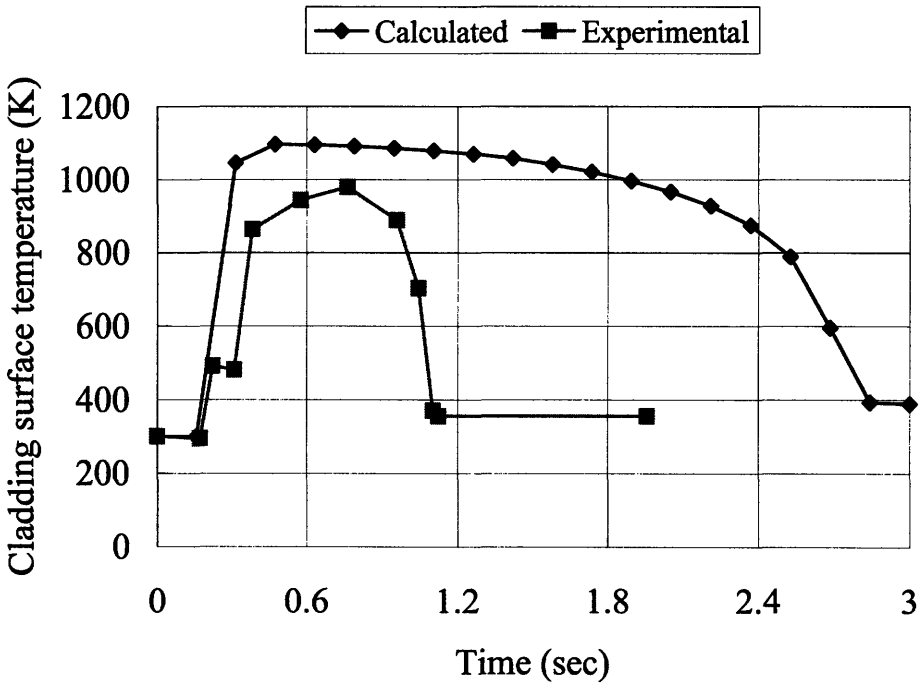

Figure 3-13: Prediction of Cladding Surface Temperature History for TK3

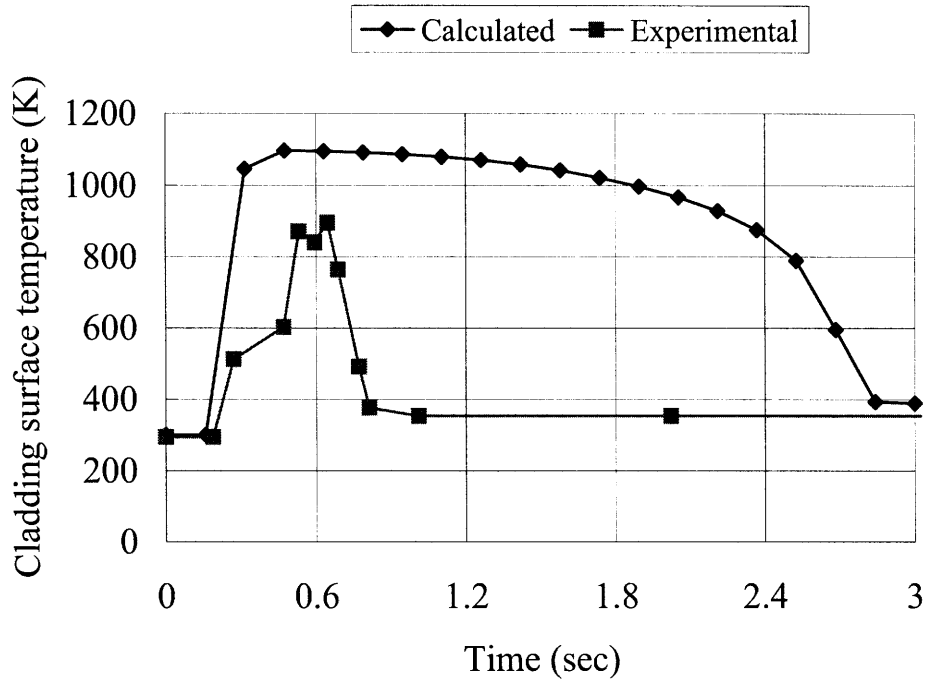

Figure 3-14: Prediction of Cladding Surface Temperature History for FK3

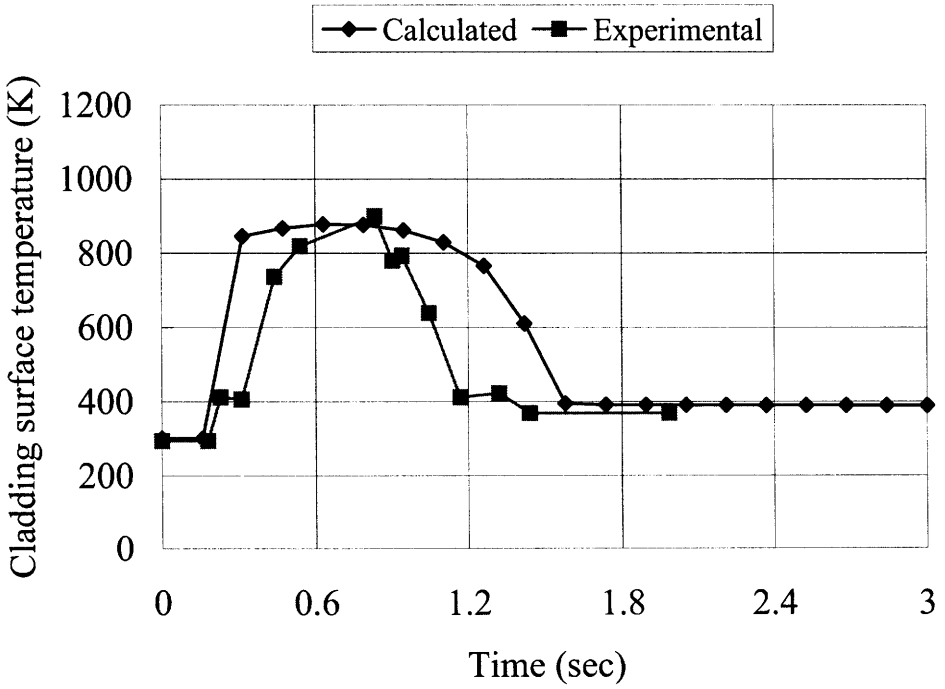

Figure 3-15: Prediction of Cladding Surface Temperature History for FK4

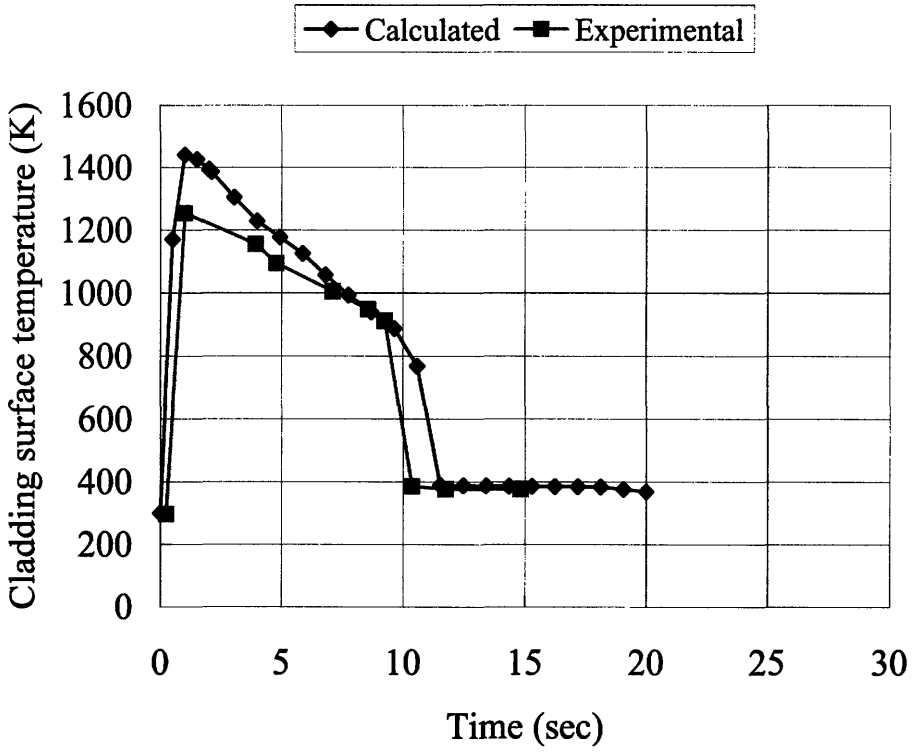

Figure 3-16: Prediction of Cladding Surface Temperature History for Fresh01

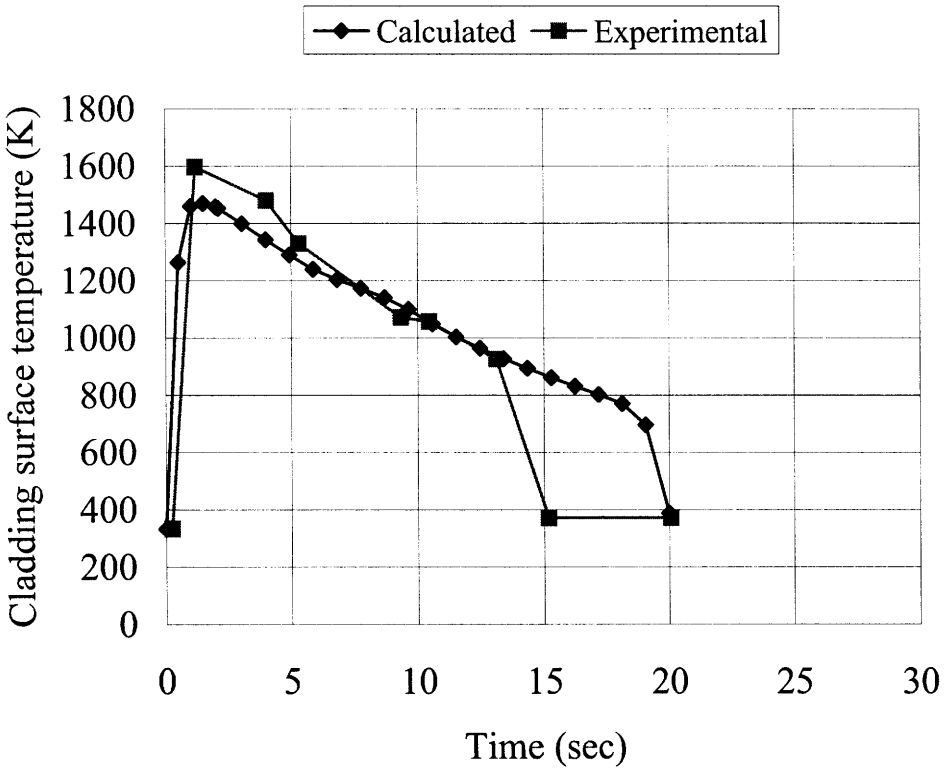

Figure 3-17: Prediction of Cladding Surface Temperature History for Fresh02

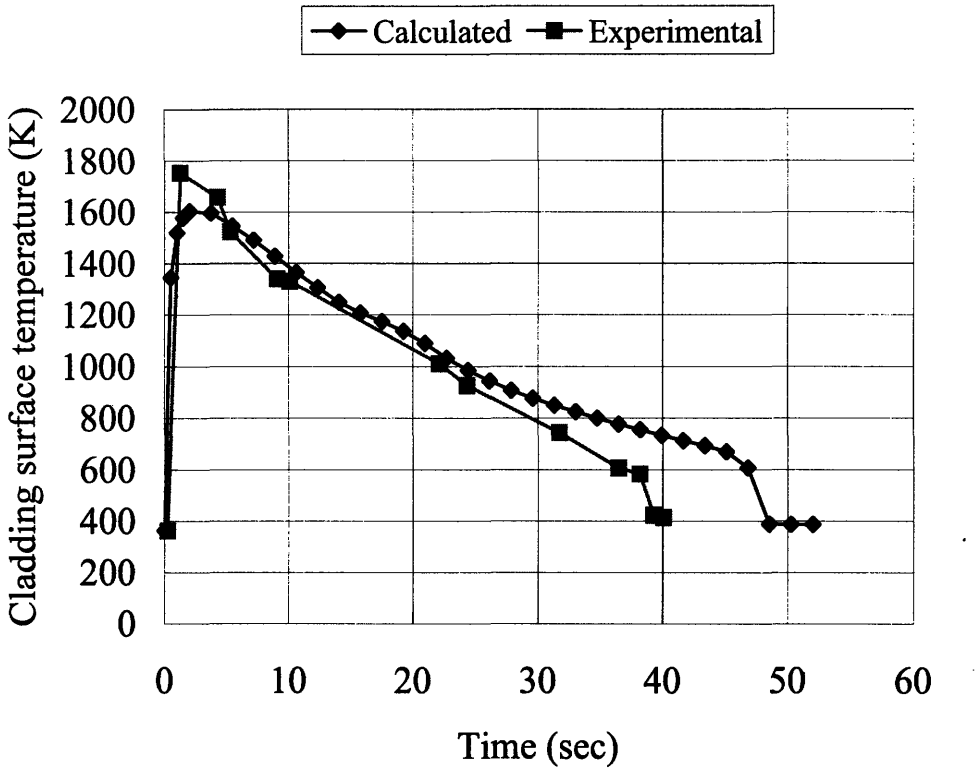

Figure 3-18: Prediction of Cladding Surface Temperature History for Fresh03

3.3.2 Discussion

- Oxidation effects

  Thermal properties of Zry and zirconia are plotted in Figure 3-19 and Figure 3-20. Because of the relatively smaller thermal conductivity and diffusivity of

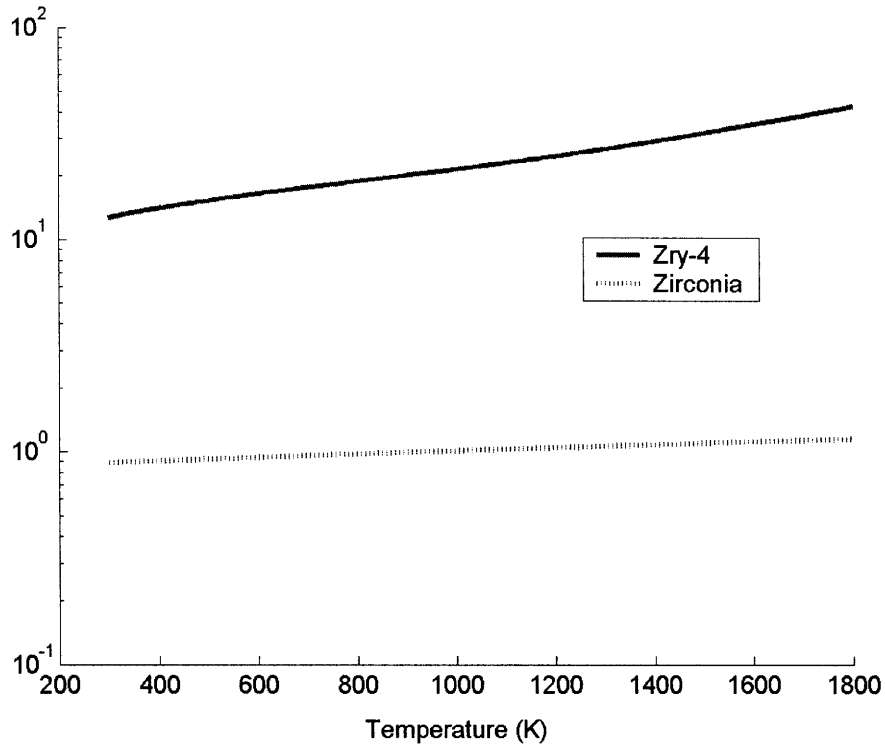

Figure 3-19: Thermal conductivity of Zry and zirconia

zirconia, a larger temperature drop across the oxide layer at steady state and a longer time to establish the temperature field during transient condition are expected.

By varying the oxide layer thickness while keeping the outer and inner diameters constant, the effect of oxidation on heat conduction is clearly observed in Figure 3-21. Without the thermal conduction through the oxide layer, the duration of DNB is longer. During the late phase of RIA, as the gap conductance decreases due to gap reopening, the temperature of cladding is mainly determined by the heat flux on the cladding surface. A thick oxide layer tends to

cause a larger temperature drop across the cladding and to lower the cladding surface temperature, thus making rewetting more easily. The surface oxidation may also delay the heat conducted to the cladding surface while keeping the surface heat transfer in the effective nucleate boiling regime. For a very thick oxide layer of 100 micron, DNB could even be suppressed as demonstrated by the result in Figure 3-21. Zirconia has a larger product of ρCk than Zry. This tends to increase the value of T_{min} for film boiling in accordance with Eq 3.14. As can be seen from Figure 3-5, there exists a shift of T_{min} around 150 K at the same degree of subcooling. By varying the minimal stable film boiling temperature, we can observe the influence on the cladding temperature in Figure 3-22. Without the shift of T_{min} due to oxidation, a much longer rewetting time would be predicted. In applying the Henry correlation, it should be recognized that the thickness of surface oxide coating is not reflected in the model. The one-dimensional model analysis of alumina overlaid on copper demonstrated that

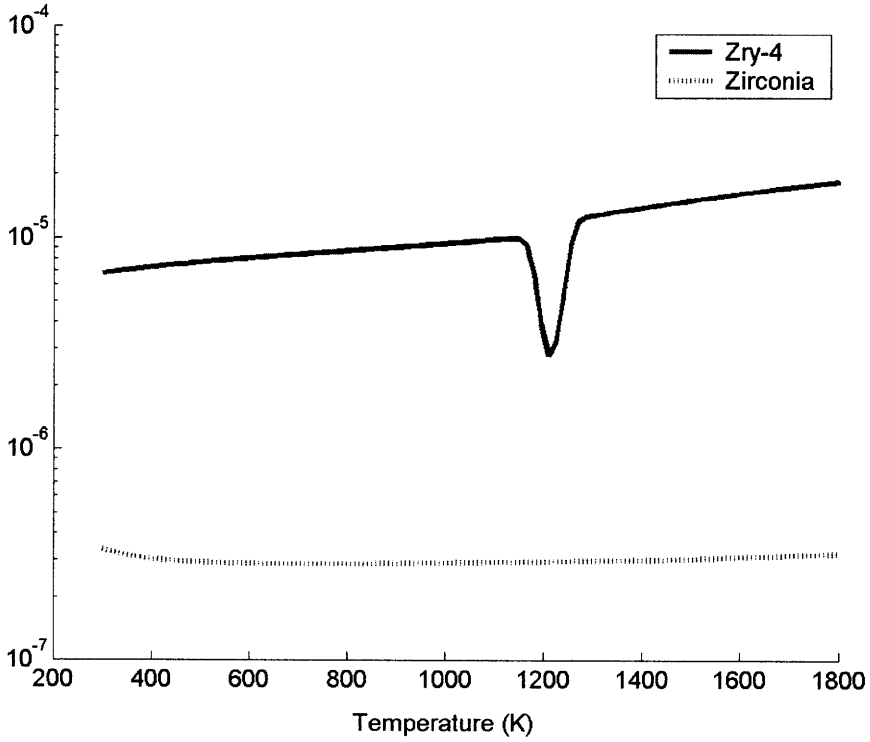

Figure 3-20: Thermal diffusivity of Zry and zirconia

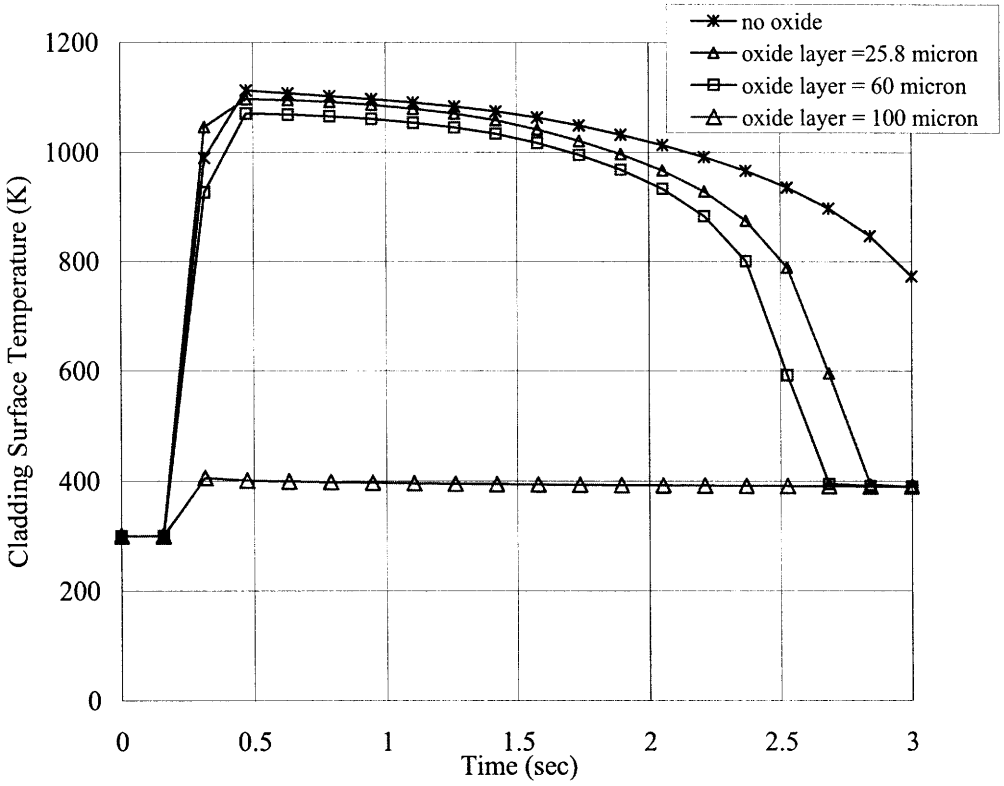

Figure 3-21: Cladding surface temperature dependence on oxide thickness for case FK3

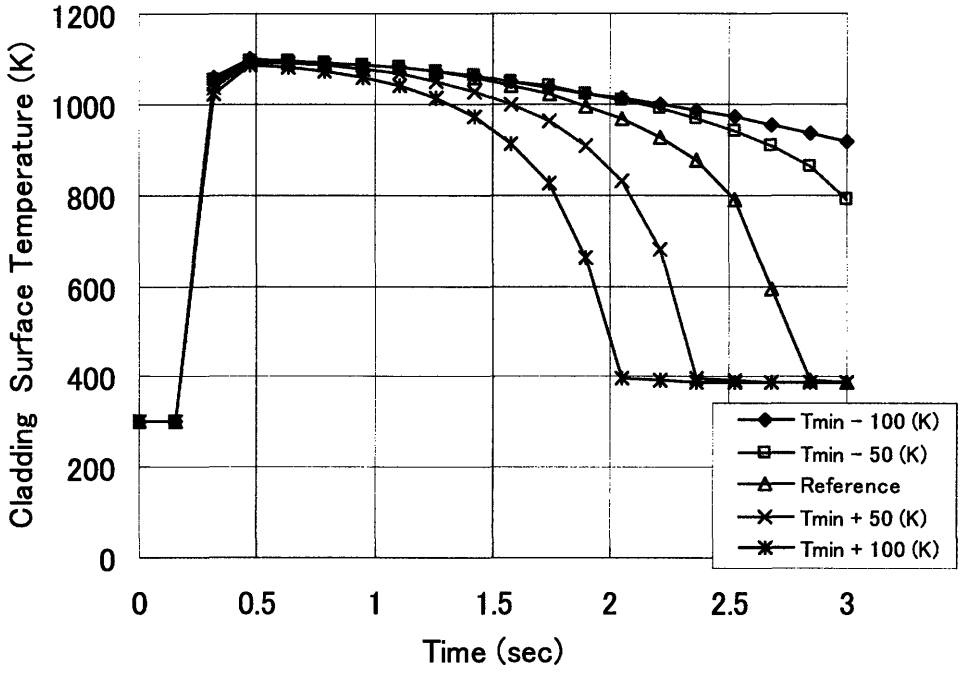

Figure 3-22: Cladding surface temperature dependence on T_{min} for case FK3

the interface temperature during liquid-solid contact could depend on the thickness of oxide layer, although the dependence is less distinctive as the oxide layer becomes thicker [69]. Pan's model gives interface temperature in Eq 3.16.

$$T_I = T_l + \frac{b_2(T_w - T_l)}{(1+b_2)} \sum_{n=0}^{\infty} \left[\frac{(1-b_1)(1-b_2)}{(1+b_1)(1+b_2)}\right]^n \text{erfc}\left(\frac{n\Delta}{\sqrt{\alpha_c t}}\right) + \frac{b_2(1-b_1)(T_w - T_l)}{(1+b_1)(1+b_2)} \sum_{n=0}^{\infty} \left[\frac{(1-b_1)(1-b_2)}{(1+b_1)(1+b_2)}\right]^n \text{erfc}\left(\frac{(n+1)\Delta}{\sqrt{\alpha_c t}}\right) \tag{3.16}$$

where:

$b_1 = (k\rho c_p)_c^{1/2} / (k\rho c_p)_h^{1/2}$

$b_2 = (k\rho c_p)_c^{1/2} / (k_{eff}\rho c_p)_l^{1/2}$

k_{eff} = effective thermal conductivity of liquid accounting for turbulent diffusivity (W/m-K)

t = time (sec)

T_I = interface temperature during liquid-solid contact(K)

α_c= thermal diffusivity of coating material (m^2/s)

Δ = thickness of coating material (m)

n = order of function erfc

Subscript c refers to coating, h refers to heater, l refers to liquid. Effective thermal conductivity taking into account the turbulent diffusivity of the liquid is

$$k_{eff} = k_l + C_{fit}(g\beta)^{1/2}[\frac{\sigma}{g(\rho_l - \rho_v}]^{3/4}\frac{(T_w - T_l)^2}{T_w^{3/2}}\rho_c c_{pl} \tag{3.17}$$

Using Pan's model with function erfc truncated at order 10, the interface temperature during transient contact between zirconia coating overlaid on zirconium and water at CZP condition is shown in Figure 3-23. It can be seen that as the oxide layer gets thicker, there is more time for the interface to reside at a relatively lower temperature. This may lead to breaking down of the vapor film more easily, essentially it increases the minimum film boiling temperature. Considering this thickness effect, we may expect that the prediction for case 1M and case 1H with only 1 micron oxide layer will not be accurate. The results in Figure 3-7 and Figure 3-8 shows the prediction for case 1M is poor as compared to that of case 1H. It seems that the oxidation effect on the surface heat transfer is exaggerated for the case 1M with moderate enthalpy deposit. The reason could be that high temperature oxidation cause different additional oxidation buildup at a different enthalpy level.

- Quench front movement

  Because of the finite length of the fuel rod, the heat may be conducted axially from the cladding in film boiling regime to any cold ends. The axial heat conduction essentially results in a moving quench front between the film boiling and nucleate boiling. Thus rewetting of the cladding may start at a temperature somewhat above T_{min} due to quench front movement. To investigate this effect, we calculate the quench front velocity u_q (m/s) in a simplified 1-D model in

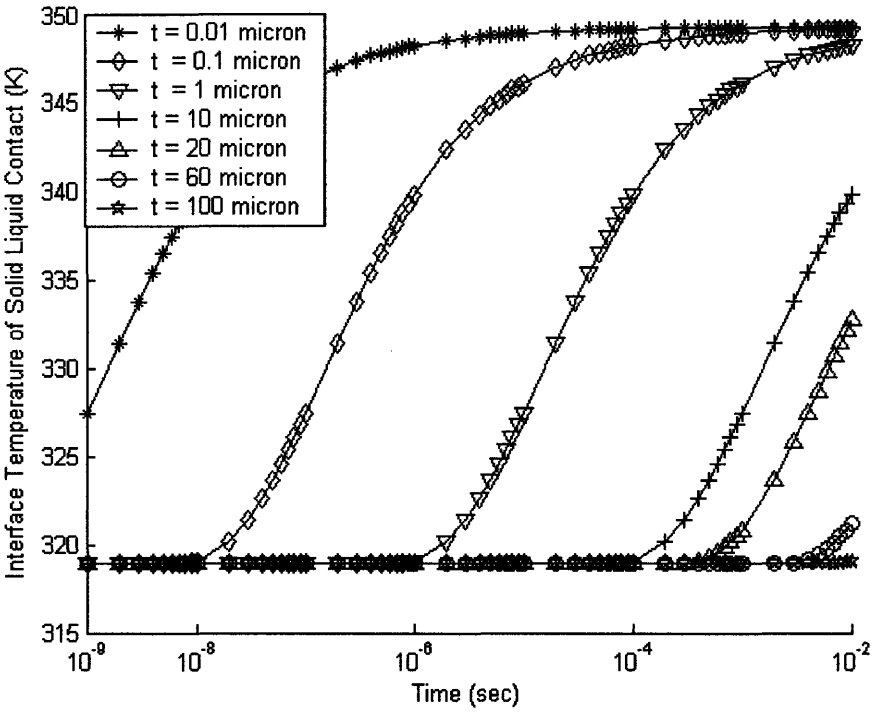

(a) Temperature of solid is 450 K

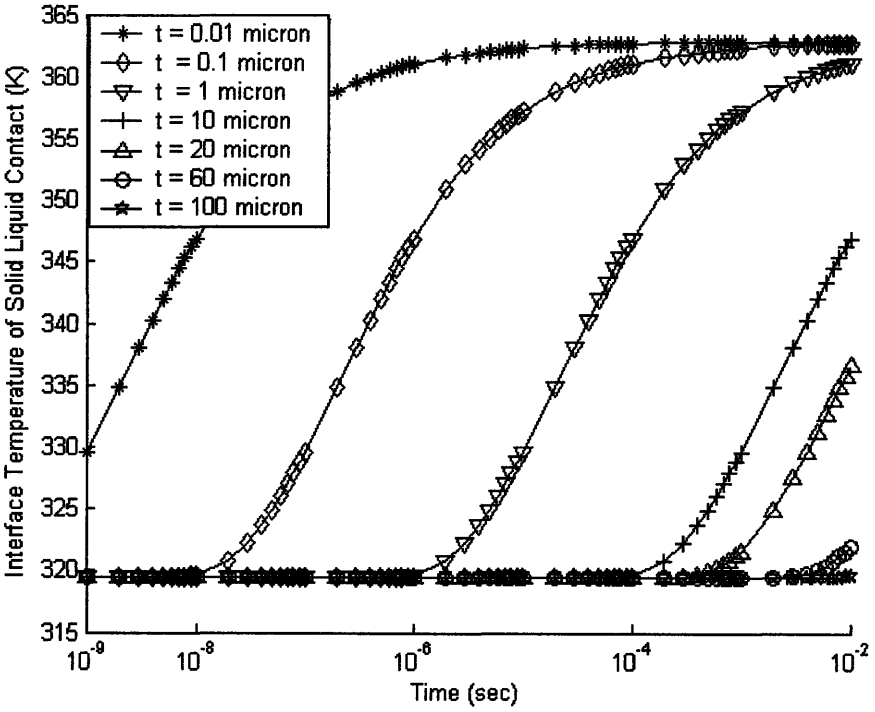

(b) Temperature of solid is 700 K

Figure 3-23: Effect of oxide layer thickness on interface temperature

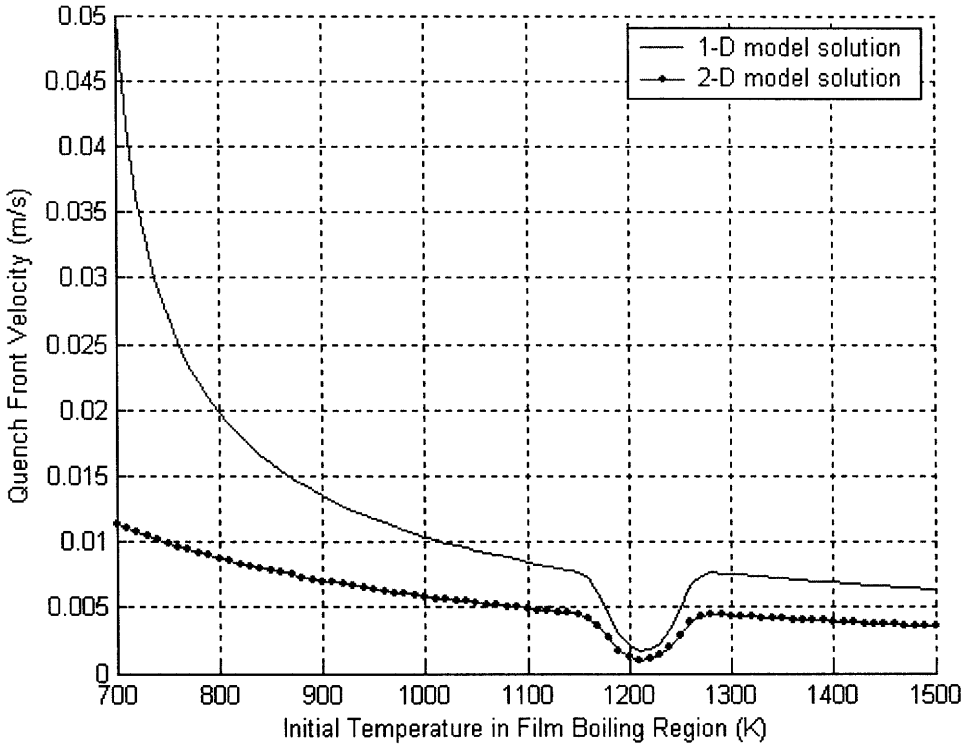

Figure 3-24: Quench front velocity vs. initial temperature in film boiling regime

Eq 3.18 [70]:

$$u_q = \frac{1}{\rho_w c_{pw}} \left(\frac{h_{nb} k_w}{\delta}\right)^{1/2} \frac{T_{min} - T_l}{(T_f - T_l)^{1/2}(T_f - T_{min})^{1/2}} \tag{3.18}$$

and a 2-D solution in Eq 3.19 [70]:

$$u_q = \frac{2h_{nb}}{\pi \rho_w c_{pw}} \frac{(T_{min} - T_l)}{(T_f - T_l)} \tag{3.19}$$

Taking the clad thickness δ = 0.86 mm, T_l = 298 K, T_{sat} = 373 K, a conservative estimate for h_{nb} is the heat transfer coefficient at critical heat flux, 40.4 kW/m^2-K. Cladding thermal properties are evaluated at T_f. Minimal film boiling temperature is evaluated by Eq 3.15. The quench front velocity calculated by Eq 3.18 and Eq 3.19 is shown in Figure 3-24 as a function of different initial temperatures in the film boiling regime. In the simulated RIA tests at NSRR, the length of a re-fabricated test rod is on the order of 10 cm. Given Figure 3-24, the order of time for quench front moving should be 10 seconds for the test rods. Therefore, the quench front movement may affect the heat transfer of fresh fuel at very high enthalpy deposit. As can be seen from Figure 3-8, this may explain the over-prediction of the duration of DNB for case Fresh02 and Fresh03. For high burnup fuel, this effect can be neglected as compared to the mechanism of simultaneous collapse of vapor film.

- Critical heat flux

  As discussed in Section 3.2.2 and Section 3.2.3 and shown in Table 3.3, critical heat flux can be strongly affected by subcooling, surface condition and transient heating effect. Figure 3-25 shows the sensitivity study for case FK3 by changing the critical heat flux. As can be seen, the prediction of peak cladding temperature is not sensitive to the change of the magnitude of CHF, although the rewetting time can be shortened at a higher CHF.

- Gap conductance

  As shown in Figure 3-26, in the early phase of RIA, at the tail of the power

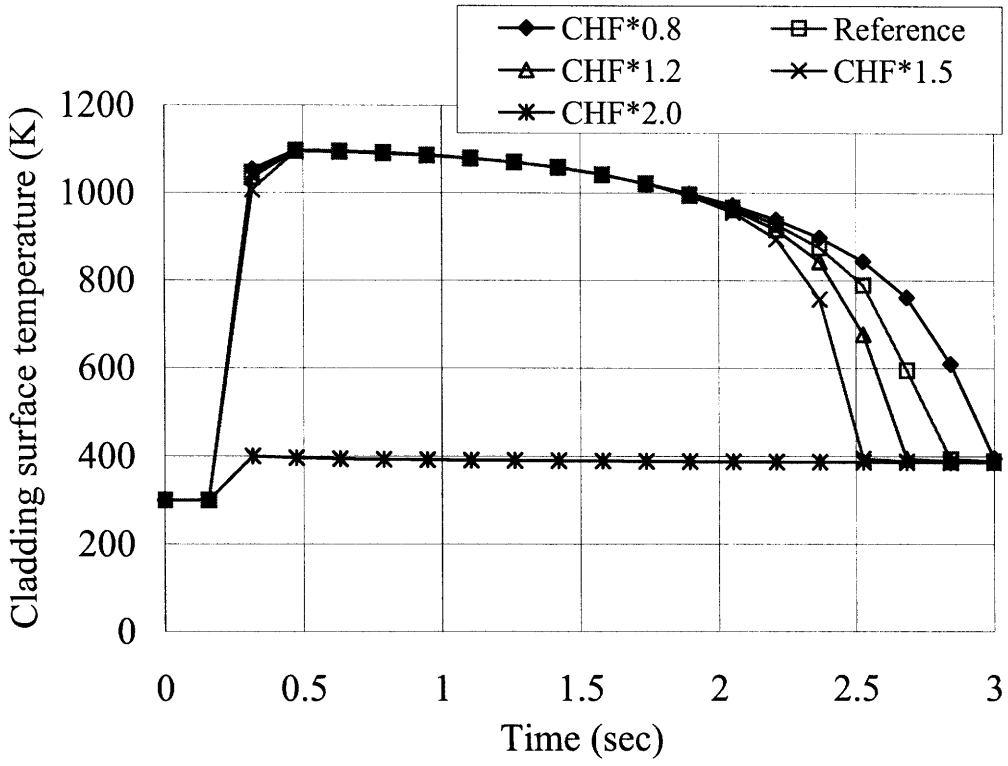

Figure 3-25: Cladding surface temperature dependence on CHF for case FK3

pulse, heat transfer moves from the nucleate boiling regime to the transition and film boiling regime. The fuel surface heat flux is orders higher than the cladding surface heat flux. The cladding temperature increase is dominated by the heat flux from the fuel surface.

Fuel surface heat flux depends largely on fuel surface temperature and gap conductance. For high burnup fuel, the radial power profile is edge-peaked due to self-shielding and accumulation of fissiles in the rim region. Under the circumstance of a narrow power pulse, the initial fuel surface temperature is expected to be higher than that of fresh or lower burnup fuel. Reduced gap size at high burnup would facilitate early closure of the gap between the pellet and cladding. The large gap conductance during the gap closure plus the high temperature of fuel surface may contribute to a higher cladding temperature. On the other hand reduced gap size would allow a strong PCMI, which may enable an earlier gap reopening, thus decrease the heat input to the cladding and result in a lower cladding temperature. Figure 3-27 suggests that PCMI is the dominant factor. Since the gap conductance is strongly affected by the mechanical deformation, this could introduce a larger uncertainty as compared to the fresh fuel. Figure 3-28 gives the effects of gap conductance on the cladding temperature. Low gap conductance favors early rewetting and even suppresses the DNB. In addition, the influences of inner oxidation of cladding, chemical bonding, fuel fragmentation, relocation and rim structure on the gap conductance are not well understood for high burnup fuel. These factors are not taken into account in the gap conductance model in FRAPTRAN. They also contribute to the uncertainty in calculating the heat flux from the fuel surface.

- Thermocouple measurement

  In the experiments, the thermocouples are welded on a local area of the cladding outer surface where oxide is removed. Thus the measured temperature might be higher than the cladding surface temperature calculated by the model. However, because of the fin cooling effects of long wire of thermal couple, the measured

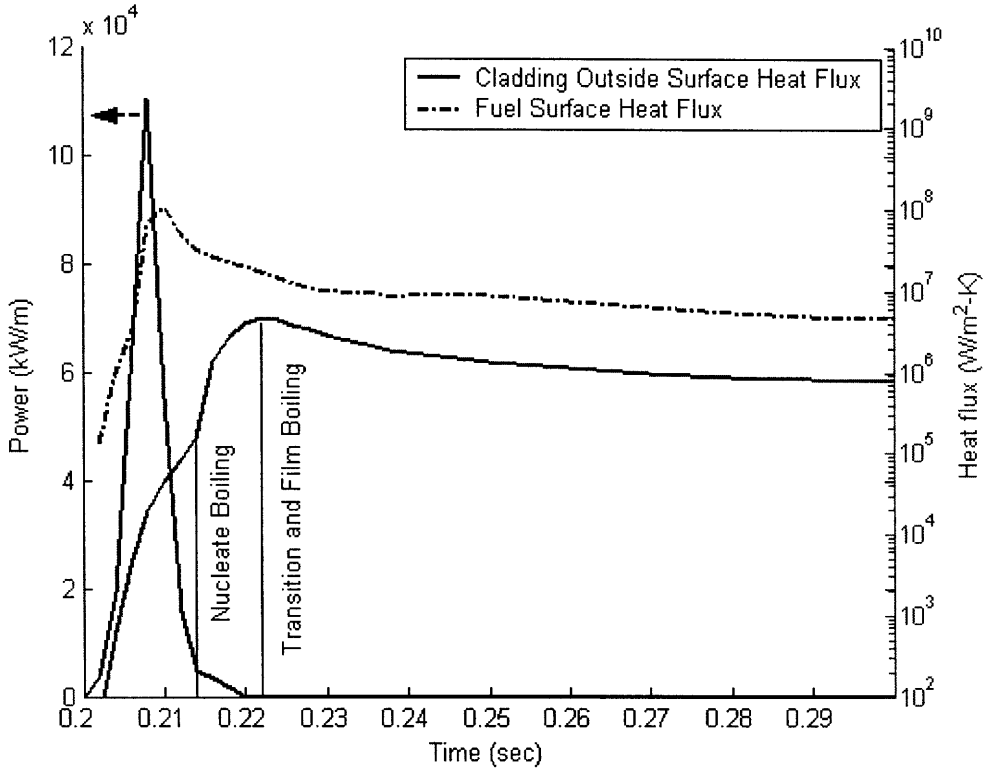

Figure 3-26: Power and heat flux calculated by modified FRAPTRAN for case FK3

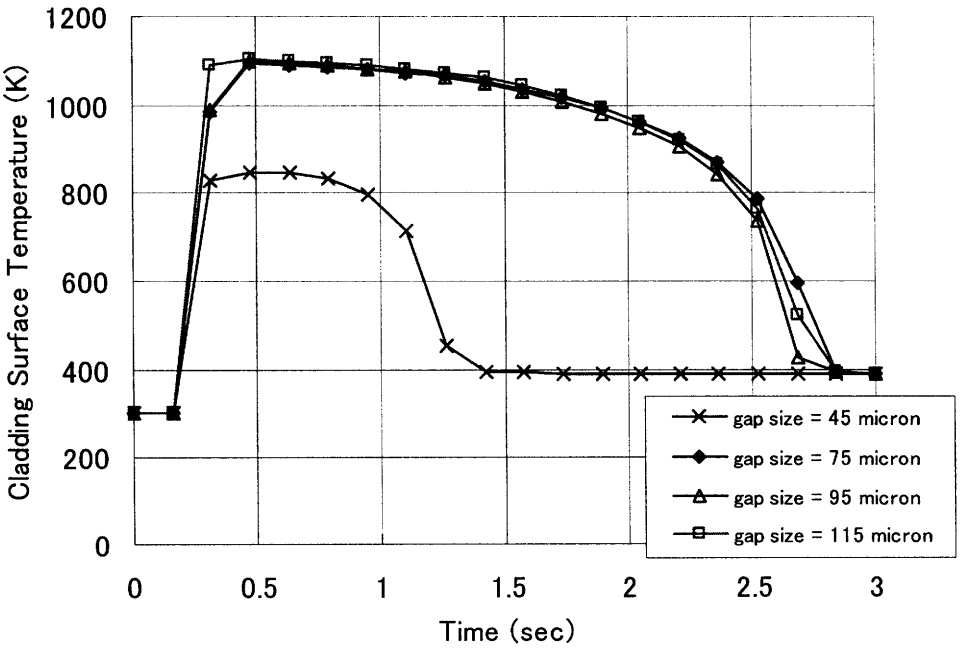

Figure 3-27: Gap size effect for case FK3

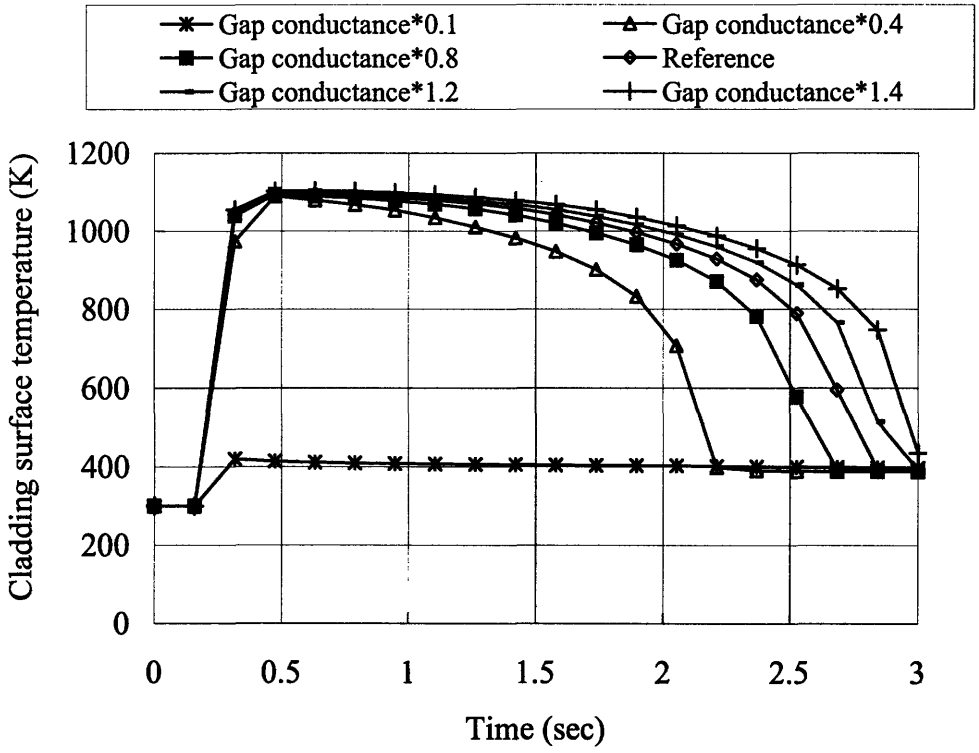

Figure 3-28: Gap conductance effect for case FK3

temperature could be lower than the average temperature on the interface between oxide and metal. A study by IRSN [71] indicates that the over-all effects for oxide thickness from 0 to 100 micron:

- Fin cooling effect lead to $T_{clad} - T_{TC}$= from 25 °C to -50 °C.
- Transient capacitive effects of thermal couple is lager, from 100 °C to -150 °C, but only limited in very early phase and not necessarily to affect peak cladding temperature measurement.

Therefore, peak cladding temperature prediction might shift at most 25 °C to the right in Figure 3-7 according to the study by IRSN. However, their analysis are only limited to cladding temperature up to 600 °C.

3.4 Summary and conclusions

A new set of heat transfer correlations has been implemented in FRAPTRAN to model the cladding-coolant heat transfer of high burnup fuel at CZP during RIA conditions. The minimum stable film boiling temperature affected by the subcooling and the oxidation is modeled by a modified Henry correlation, which accounts for the effects of thermal properties of the cladding surface on the transient temperature drop during liquid-solid contact. The transition boiling regime is described by the interpolation of the heat flux between two anchor points on the boiling curve: the critical heat flux and minimum stable film boiling. The CHF correlation is based on the Zuber hydrodynamic model multiplied by a subcooling factor. Frederking's correlation is chosen to model the film boiling regime. The heat conduction through the oxide layer of cladding surface of high burnup fuel is also calculated by solving heat conduction equations with thermal properties of zirconia taken from MATPRO [13].

The model has been validated in the FRAPTRAN code for both high burnup and fresh test fuel rods including the burnup level (0-56 MWd/kg), peak fuel enthalpy deposit (70-190 cal/g), degree of subcooling (0-80 °C) and extent of oxidation (0-25

micron). The modified code is capable of differentiating between the DNB and none-DNB cases. The predicted peak cladding temperature (PCT) and duration of DNB achieves generally good agreement with the experimental data.

With regard to high burnup fuel, this effort reveals that the surface oxidation could cause an early rewetting of high burnup fuel or suppression of DNB due to two factors:

1. The thick oxide layer may delay the heat conducting to the surface while keeping the surface heat transfer in the most effective nucleate boiling regime.

2. The transient liquid-solid contact resulting from vapor breaking down would cause a lower interface temperature for an oxidized surface. This effectively increases the minimum stable film boiling temperature.

Chapter 4

Modeling PCMI failure

4.1 Introduction and literature review

In the simulated RIA tests at the Power Burst Facility (PBF), failure of the fuel rod cladding was observed with short through wall cracks at a radial average peak fuel enthalpy of 140 cal/g for fuel irradiated up to a burnup of 4.6 MWd/kg [4]. The failure of cladding is primarily driven by the pellet cladding mechanical interactions (PCMI), thus is called PCMI failure.

In 1990s, simulated RIA tests conducted at CABRI and Nuclear Safety Research Reactor (NSRR) revealed that fuel rod failures occur at an enthalpy level less than 70 cal/g for LWR fuel irradiated above 50 MWd/kg. PCMI was still considered as the mechanism for failure. As high burnup fuel features reduced gap size, enhanced gaseous swelling and edge-peaked radial power profile, stronger PCMI may be caused during power transients for high burnup fuel. Failure of cladding tubes was observed with long axial splitting as shown in Figure 4-1. Micro-graph of the cross sectional area reveals that a through-wall crack may develop as shown in Figure 4-3 or a crack may form halfway in the cladding followed by a change of the direction of crack surface or ductile shear failure shown in Figure 4-2. The corrosion of high burnup fuel cladding with oxidation and hydride formation assists this process by decreasing the ductility of the cladding. The $\delta-$phase hydride precipitates, which preferentially accumulate at the outer surface, are found more detrimental to the embrittlement of

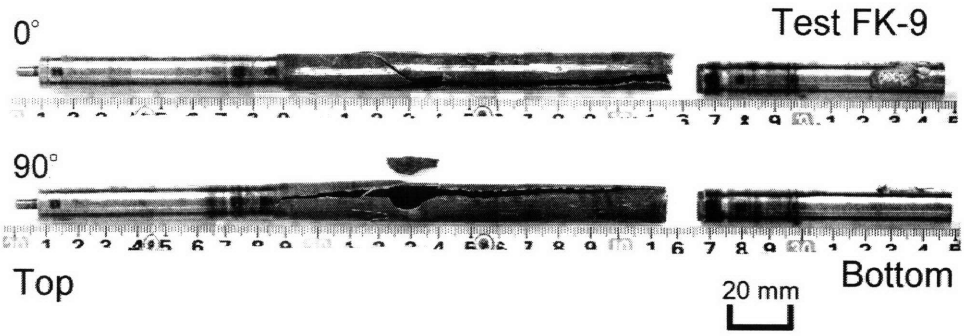

Figure 4-1: Failure morphology for FK9 [72]

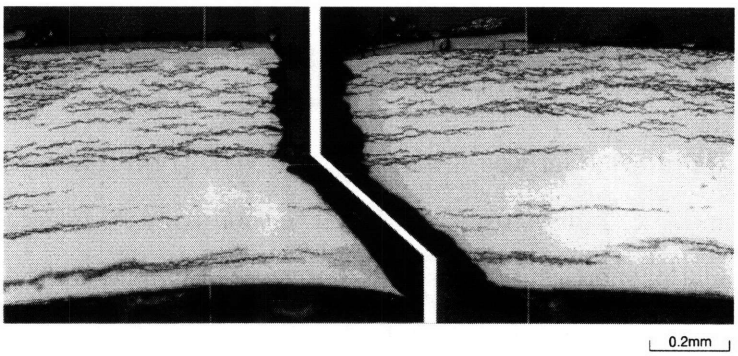

Figure 4-2: Failure morphology for HBO5 [73]

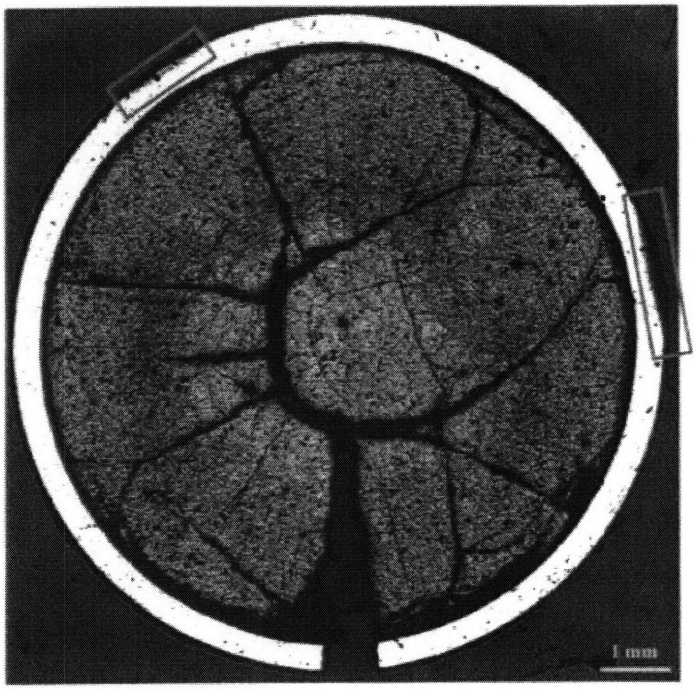

Figure 4-3: Failure morphology for RepNa10 [46]

cladding than zirconium oxide. This embrittlement is found in both the Zry-2 and Zry-4 alloy. The high strain rate of cladding during RIA can also deteriorate the ductility of cladding. As discussed in Section 1.2.2, both the NSRR and CABRI tests are not representative of the LWR conditions in terms of the coolant condition and power pulse width. Thus it is not appropriate to extrapolate directly the measured failure enthalpy from simulated RIA tests to LWR environments to determine the failure condition. Many models and analysis methods have been developed to explain the failure behavior and to set forth a failure criterion during RIA [46] [74] [75].

4.1.1 Strain based failure model

A strain based failure model was developed by PNNL [74]. Based on uniform elongation data from biaxial burst tests, and axial tension tests on irradiated cladding in PNNL mechanical properties database, an empirical model for uniform hoop elongation was proposed as a function of temperature and excess hydrogen in the cladding.

$$UE = \min(UE_0, UE_{Hex}) \tag{4.1}$$

where,

UE = uniform plastic elongation (%)

$UE_0 = 2.2\%$

$UE_{Hex} = AH_{ex}^{-p}\ H_{ex} > 0$

$UE_{Hex} = UE_0\ H_{ex} = 0$

$A = 1211\exp(-0.00927T)\ T < 700K$

$A = 1.840803\ T > 700K$

$p = 1.355231 - 0.001783T\ T < 700K$

$p = 0.107131\ T > 700K$

H_{ex} is the excess hydrogen in ppm, calculated by subtracting the solubility limit from the total hydrogen in the cladding. p is a dimensionless fitting exponent. A is fitting coefficient in $\text{ppm}^{\frac{1}{p}}$.

The total hydrogen is calculated in FRAPCON-3 from the oxide thickness and

a 15% hydrogen pickup fraction in PWRs and a 29% hydrogen pickup fraction in BWRs [74]. The solubility model to calculate the excess hydrogen concentration is as follows.

$$H_{sol} = 1.2 \times 10^5 \exp(\frac{-8550}{1.985887T}) \tag{4.2}$$

The rate of dissolution is:

$$f = \frac{7.8 \times 10^{-3}}{h} t^{1/2} \exp(\frac{-12440}{1.985887T}) \tag{4.3}$$

where h is a constant thickness of hydride rim: 0.25 micron. f is the fraction of hydride dissolved. Rate of hydride precipitation was modeled as:

$$H_p = \min[1.0, 1.18 \times 10^3 \exp(\frac{-35716}{8.314T})] \tag{4.4}$$

This model provides a slightly conservative estimation of failure conditions when applied to most of the RIA tests. But it was found not able to predict the failure of CABRI tests, which have an operating temperature of 280 °and have sodium coolant [74].

This model doesn't take into account the difference in loads between mechanical test and RIA condition. In a mechanical test, specimens with well characterized geometries undergo axial tension or pressure loading on an open-end or close-end cladding tube. In an RIA test, strong PCMI loading leads to a high axial to hoop stress ratio, which is different from all the mechanical tests.

The distribution of hydride is not accounted for in the strain based model. This will also affect the mechanical properties as high accumulation of hydride at the outer surface tends to cause failure more easily [76]. In an early RIA phase, the transient temperature distribution of cladding exhibits a colder outer surface, which tends to suppress the dissolution of the hydride. Thus the PNNL model with uniform dissolved hydrogen would be less conservative over-estimating the ductility change.

This model was already implemented into the FRAPTRAN code by PNNL. It

will be used to compare the results with the new failure analysis model developed in the thesis.

In Ref. [77], measured total elongation of cladding tube specimen is used to determine the failure strain. Recognizing that the failure depends on the hoop to axial stress ratio, the measured total elongation is converted to an equivalent critical hoop plastic strain, refereed to as failure strain:

$$\varepsilon_f = C_{Ri}\varepsilon_{te} \tag{4.5}$$

where C_{Ri} is a reduction factor empirically determined. Open end burst test data, closed end burst test data and axial tube tension test data are converted to an equivalent failure strain at PCMI condition. Note that total elongation is not a material property, it depends on the size and geometry of test specimen.

Strain based models neglect the effects of hydride distribution on the cladding without accounting for effects of surface flaw on the stress concentration.

4.1.2 SED and CSED model

Instead of using only hoop strain as a failure criterion, a stress-strain failure model uses strain energy density (SED) as driving force and critical strain energy density (CSED) as the criterion to judge the failure of high burnup fuel during RIA [75]. SED is calculated by the integral of the product of strain and strain.

CSED correlation is derived by fitting of RIA test data and mechanical test data of irradiated specimen. The critical strain energy density depends on temperature and the presence of an oxide layer as follows:

- Above 280 °C

  For non-spalled cladding:

$$U_c = 41.5\exp(-6.6R_{ox}) \quad 0.03 < Rox < 0.23 \tag{4.6}$$

For spalled cladding:

$$U_c = 0.371 R_{ox}^{-1.24} \quad 0.1 < R_{ox} < 0.23 \tag{4.7}$$

- Below 150 °C

  For non-spalled cladding:

$$U_c = 15.67 \exp(-7.19 R_{ox}) \tag{4.8}$$

Where,

U_c is the critical strain energy density in MJ/m^3

R_{ox} is the ratio of the outer surface zirconium oxide layer thickness to cladding thickness, i.e., the normalized oxide layer thickness

This CSED approach is claimed to be applicable for PWR Zry-4 cladding at CZP and HZP condition for burnup up to 64 MWd/kg [75]. To connect the oxidation to the burnup level of a fuel rod, a conservative correlation for oxide thickness was proposed as [75]:

$$Ox = 6 + 0.35BU - 0.0135BU^2 + 1.613BU^3 \tag{4.9}$$

where,

Ox is the bounding average maximum oxide thickness in micron,

BU is the rod average burnup in MWd/kgU.

At zero and low burnup regime, an empirical model for failure enthalpy is

$$H = 170 \quad \text{cal/g}, \quad BU < 36 \quad \text{MWd/kg} \tag{4.10}$$

$$H = 125 + 7058 \exp(-0.1409BU) \quad \text{cal/g}, \quad BU > 36 \quad \text{MWd/kg} \tag{4.11}$$

Although the normalized oxide layer thickness is used in deriving CSED, it is the

hydrides that more pronouncedly affect the ductility of cladding. As the hydrogen pickup is almost proportional to the oxidation, this parameter can represent the effects due to hydride. But for Zry-2 cladding, both the orientation of hydrides and total hydrogen pickup would change. This limits the application of the above correlations to Zry-2 cladding of BWR fuel.

4.1.3 Scaling analysis

Meyer [46] proposed a scaling analysis method to determine the failure enthalpy at PWR HZP conditions with the data from selected simulated failure tests. Scaling method consists of two steps:

1. Run FRAPTRAN and determine the state of stress or strain as failure stress or strain at the observed failure time.

2. Change the failure case to LWR conditions in terms of power pulse, coolant temperature and pressure, run FRAPTRAN a second time to determine the enthalpy at failure for failure stress or strain obtained from previous step.

Choosing the stress or strain as a failure criterion is judged by the analysis of the fuel rod at simulated RIA condition from FRAPTRAN calculation. Thus this method can be used to analyze a case given enough information is obtained at time of failure. Temperature change due to the change of power pulse and coolant condition is not well addressed. A simple "freezing" assumption is made to keep the material properties, fracture toughness and uniform elongation, as constant during the power pulse phase.

4.1.4 Fracture mechanics

Kuroda [76] modeled the failure of unirradiated hydrided cladding by a two-criteria approach based on Elastic Plastic Fracture Mechanics (EPFM). The failure assessment curve is:

$$K_r = S_r[\frac{8}{\pi^2}\ln\sec(\frac{\pi}{2}S_r)]^{1/2} \tag{4.12}$$

K_r and S_r are defined as:

$$K_r = K_I / K_{IC} \tag{4.13}$$

$$S_r = \sigma / \sigma_c \tag{4.14}$$

where σ is the applied stress and σ_C is the collapse stress. A more advanced assessment curve is J-based failure assessment curve:

$$K_r = \sqrt{J_r} = \sqrt{J_e / J} \quad for \quad L_r \leq L_r^{max} \tag{4.15}$$

$$K_r = 0 \quad for \quad L_r > L_r^{max} \tag{4.16}$$

$$L_r^{max} = \frac{\sigma_f}{\sigma_y} \tag{4.17}$$

where σ_f is the flow stress and σ_y is the yield stress. Failure occurs when the assessment points with coordinates (Lr,Kr) are beyond the failure assessment curve. Therefore when $L_r < L_r^{max}$, failure is assumed to be driven by cracking growth; when $L_r > L_r^{max}$, failure is assumed to be driven by plastic collapse. By setting a plastic collapse stress at 1.07 σ_y, Kuroda constructed the failure assessment curve and in analyzing the failure of hydrided cladding tube in burst test by finite element models, Kuroda [76] showed that the J integral and stress intensity factor for a plate with surface hydrides have higher values than that with uniform distribution, suggesting the stress concentration due to the distribution of hydrides in LWR cladding tubes.

This approach doesn't account for dynamic crack propagation, and was used for unirradiated specimens. No attempts have been made to analyze RIA tests with this method.

4.2 Model description

It is well recognized that brittle failure of test rods due to PCMI in the early phase of RIA is the limiting factor of high burnup fuel as it has low failure enthalpy.

Post irradiation examination of the cladding indicates that the hydrogen absorbed play an important role in the embrittlement of cladding via the formation of $\delta-$phase hydride. Therefore this failure process is also referred to as hydride assisted process.

Separate effects of hydrides on burst stress [76][78] shows that cladding with hydride rim accumulated near the outer surface is susceptible to failure compared to the cladding with a uniform hydride distribution. The hydride rim, dense distribution of the hydride near the outer surface of the cladding, is the initial cracking sites and causes stress concentration during PCMI. Moreover, when the oxide layer becomes very thick, the debonding of oxide layer from the cladding often occurs given the brittle nature of zirconia. A cold spot with better heat transfer would form at a location of cladding outer surface where oxide layer spallation happens. Hydride accumulated at this location forms a blister by migration along temperature gradient. These blisters can also serve as initial cracking sites. Hydride rims and hydride blisters are often observed in the zircaloy cladding of high burnup fuel and are confirmed to cause the initial cracking in simulated RIA tests.

Given these observations, we assume the physical process during PCMI loading is that cracks firstly initiated near the outer surface of the cladding with relatively dense hydride at a low stress. The cracking of the zirconia layer in the outermost region of the cladding is also assumed to be pre-existent. The cracks initiated at the dense hydride rim propagate axially as well as through the thickness of the cladding depending on the initial crack sizes, loading force and the fracture toughness of the cladding.

The model includes:

- Prediction of the flaw size due to hydride formation

- Fracture toughness model for hydrided irradiated cladding

- Failure criterion to compare the driving parameter of fracture with the critical value of fracture toughness

In this model we neglect the axial crack propagation and assume that a single crack perpendicular to the hoop direction, with a depth controlled by a pre-existed hydride rim.

4.2.1 Flaw size model

The reaction between the zirconium alloy and water coolant in a nuclear reactor could release hydrogen. Because of the porous and flaky nature of the post-transition oxide layer, for each molecule of water that reacts with zircaloy, about 16% of hydrogen atoms (produced from oxidation) permeate through the oxide layer and is absorbed in the zircaloy cladding. Hydrogen dissolved in zircaloy is in α phase. The solubility of α-Zr is only 50-100 ppm at 280-300 °C (decreases as temperature drops). Above the solubility limit, excess hydrogen precipitates as δ phase zirconium hydride in the cladding alloys.

At high burnup, enhanced corrosion of cladding leads to significant hydrogen absorption. Concentrations of 200-800 ppm are common in some Zry-4 cladding at fuel burnups around 60 MWd/kg. Embrittlement due to high hydrogen concentration can be illustrated by unirradiated Zry-4 tests at room temperature by Bai et al. [79]. The tensile elongation and reduction-in-area change abruptly for hydrogen content larger than 700 ppm.

A hydride rim between the oxide layer and the metal is observed, which greatly deceases the ductility of the cladding and may lead to its brittle failure.

As mentioned early, hydrogen atoms tend to migrate along the temperature gradient and accumulate at a cold spot. Thus a dense hydride rim is often observed at the outer region of the cladding wall underneath the oxide layer, especially when the spallation of oxide layer causes the accumulation of hydride as a blister. The distribution of hydride is primarily controlled by the temperature gradient across the cladding. Its orientation depends largely on the stress field and the texture of cladding alloy. Small

platelet $\delta-$phase hydride tends to orient circumferentially in the Zry-4 cladding. But the texture of Zry-2 cladding enables a considerable amount of radially oriented hydride platelet as seen in Figure 4-4. Therefore, the cladding of high burnup fuel can

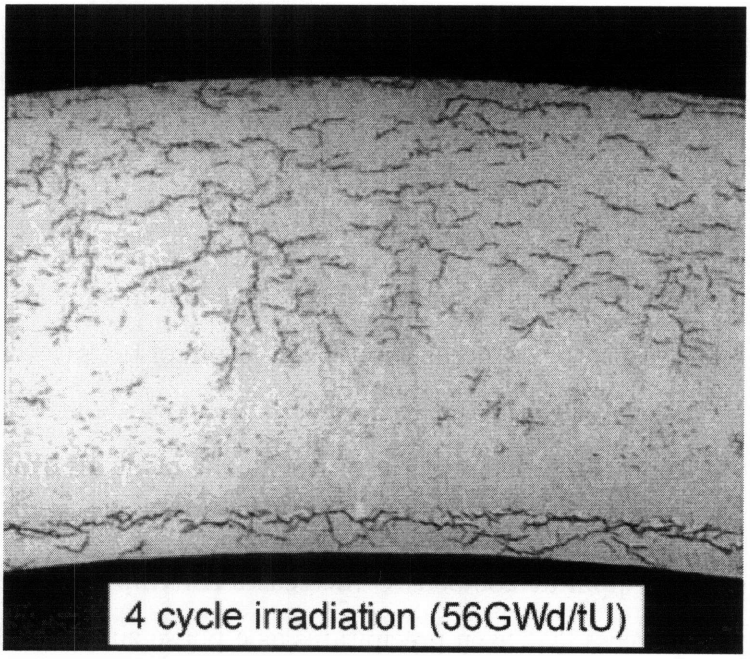

Figure 4-4: BWR Zry-2 cladding with radially orientated hydride [50]

be viewed as a composite consisting of a zirconia outer layer, hydride rim or blister underneath the oxide layer and metal with some precipitated hydrides and hydrogen dissolved in the zirconium alloy. The outer oxide layer is always cracked, even before the RIA transient. It doesn't have load-bearing capability [80]. Thus we need only consider how the hydride contributes to crack initiation. The measured fracture strength of $\delta-$phase hydride is very low: 18 MPa [81]. Therefore, we can assume the hydride rim or blister as a pre-existing cracks, which serves as the initial flaw size in a fracture failure model. However, analysis of the formation of hydride blister requires local knowledge concerning the oxide spallation. Thus, we only consider the continuous hydride rim as a flaw. The corrosion model in FRAPCON can predict the oxidation and the total hydrogen absorption by multiplication of hydrogen pickup ratio on the oxidation. A constant pickup ratio of 15% is set for PWR cladding. For BWRs, a model in MATPRO determines the pickup logic which gives lower pickup

fractions than for PWRs [1]. Given the total hydrogen absorbed, calculating the flaw size of continuous hydride rim can be viewed as a hydrogen redistribution problem. Neglecting the diffusion of $\delta-$phase hydride, the equations for hydrogen precipitation and diffusion are given as follows [82]

$$\frac{\partial C}{\partial t} = -\nabla(\nu_\alpha J_\alpha) \tag{4.18}$$

$$J_\alpha = -D_\alpha(C_\alpha + \frac{Q_\alpha C_\alpha}{RT^2}T) \tag{4.19}$$

$$C = \nu_\alpha C_\delta + \nu_\delta C_\delta \tag{4.20}$$

$$C_\alpha(r,t) = \min(C(r,t), TSS) \tag{4.21}$$

$$D_\alpha = D_0 \exp(-Q/RT) \tag{4.22}$$

where,

subscript α and δ denote α-phase and δ-phase respectively.

ν_α is volumetric fraction of α-phase.

ν_δ is volumetric fraction of δ-phase.

J_α is hydrogen flux in α-phase in ppm m/s.

C is the total concentration of hydrogen in ppm.

C_α is the concentration of hydrogen in α-phase in ppm.

C_δ =16000 ppm is the concentration of hydrogen in δ-phase.

R = 8.314 J/mol-K is the ideal gas constant.

D_0 = 0.27 mm$^2/s$ is diffusion coefficient of hydrogen [83].

Q = 35196 $\pm$ 1680 J/mol is activation energy for diffusion [83].

Q_α is heat of transport = 20930 J/mol [84].

$$TSS = \exp(-H/RT) \tag{4.23}$$

TSS is the terminal solid solubility of hydrogen in α-phase in ppm

H = 39060 J/mol is heat of mixing [85].

$K = 1.99 \times 10^5$ ppm is constant for terminal solid solubility [85].

Let us assume:

1. diffusion of hydride can be neglected,

2. precipitation and dissolution occurs instantly, and

3. thermodynamic equilibrium is achieved.

Following the above assumptions, hydrogen diffusion would be driven to the cold surface by temperature gradient, resulting in a continuum hydride rim formed at the cold surface. Since diffusion of δ-phase hydride is neglected, in the two phase (α+δ) region, the hydrogen flux from the α-phase must be zero at steady state. At the same time, the hydrogen concentration of α-phase must satisfy the terminal solid solubility. Thus the two phase region can only exist at the interface separating δ-phase hydride rim from the α-phase solid solution.

$$C_H(R_{Co}^2 - R_{Ci}^2) = C_\delta(R_{Co}^2 - (R_{Co} - t_H)^2) + \int_{R_{Ci}}^{R_{Co}-t_H} 2rC_\alpha(r)dr \tag{4.24}$$

$$C_\alpha(R_{Co} - t_H) = TSS(T(R_{Co} - t_H)) \tag{4.25}$$

$$\frac{dC_\alpha}{dt} + \frac{Q_\alpha C_\alpha}{RT^2}\frac{dT}{dr} = 0 \tag{4.26}$$

where,

C_H is total hydrogen pickup from the water side corrosion in (ppm).

t_H is the thickness of continuous hydride rim in (m).

R_{Co} is the outer radius of cladding in (m).

R_{Ci} is the inner radius of cladding in (m).

r is the radius from the centerline of pellet (m)

Given the cladding outside temperature and the temperature gradient across the cladding, which is determined by the average linear heat generation rate during the steady state, the temperature distribution is known. Plugging into the above equations, the thickness of the continuous solid hydride rim can be solved. Figure 4-5 shows schematically the process of hydrogen redistribution: Figure 4-5(a) stands for non-equilibrium condition from an initial uniform distribution. Figure 4-5(b) is equilibrium condition which has only two distinctive phases.

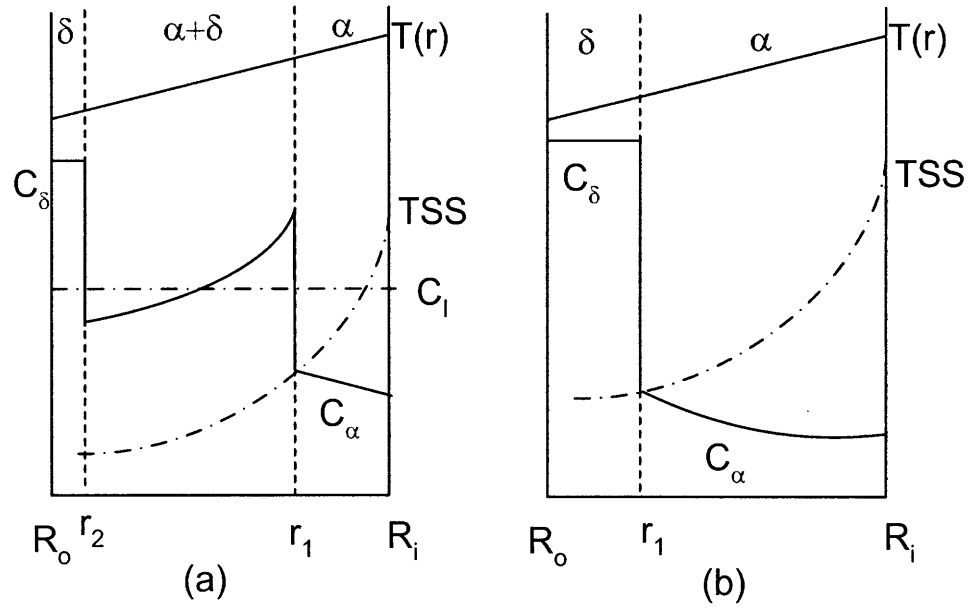

Figure 4-5: Hydrogen redistribution

Assume a linear distribution of temperature across the cladding, the temperature distribution can be obtained as:

$$T(r) = T_{Co} + \frac{q'(R_{co} - r)}{2\pi k R_{Co}} \tag{4.27}$$

where,

q' is the linear heat generation rate in (W/m)

k is the thermal conductivity of zircaloy (W/m-K)

T_{Co} is the clad outer temperature (K)

T_{Ci} is the clad inner temperature (K)

For linear heat generation rate from 15 kW/m to 35 kW/m, the temperature dis-

Table 4.1: Parameters for simulating hydride rim

Parameter	Unit	Value	
Clad thickness	mm	0.57	
Clad outer diameter	mm	9.5	
Clad outer temperature	K	573	700
Zry thermal conductivity	W/m-K	16.2	17.7

tribution is determined by the parameters in Table 4.1. Plugging the temperature distribution into Eq 4.24, the hydride rim can be calculated as shown in Figure 4-6 and Figure 4-7.

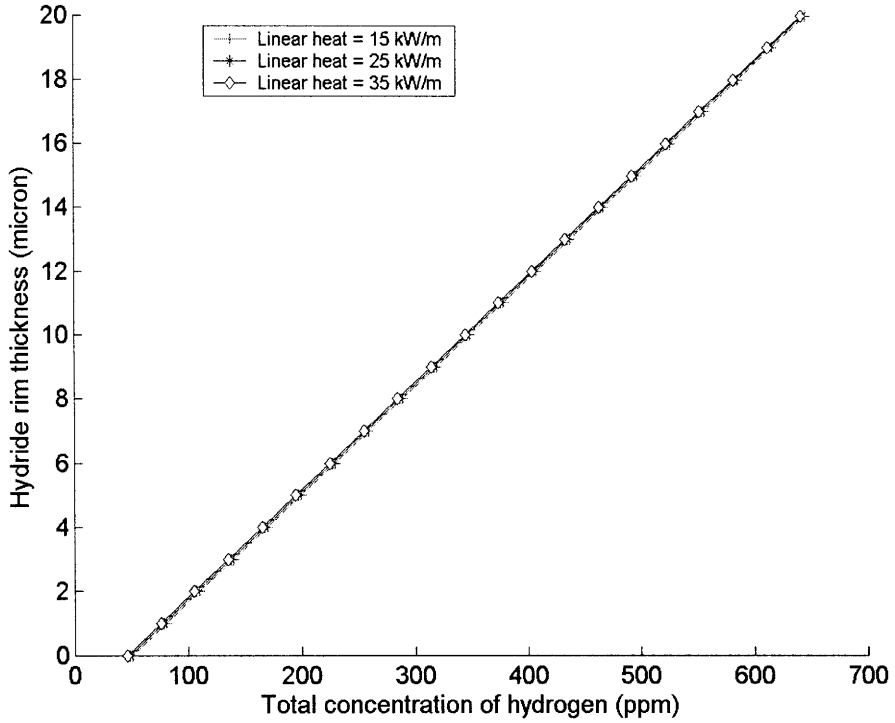

Figure 4-6: Hydride rim prediction with Tco = 573 K

As can be seen from Figure 4-6 and Figure 4-7, at the equilibrium condition, the hydride rim is not sensitive to the temperature gradient across the cladding as the majority of hydrogen accumulates as hydride precipitate. Due to the generally low solubility of hydrogen, we may neglect the effect of temperature distribution on the rim thickness. A simplified model for the hydride rim is given as:

$$t_H = R_{Co} - \sqrt{\frac{C_\delta - C_H}{C_\delta - TSS} R_{Co}^2 + \frac{C_H - TSS}{C_\delta - TSS} R_{Ci}^2} \tag{4.28}$$

Where, TSS is the terminal solid solubility of hydrogen in α-phase at the temperature of the cladding outer surface. The effective flaw size in [m] is set as:

$$a = \lambda t_H \tag{4.29}$$

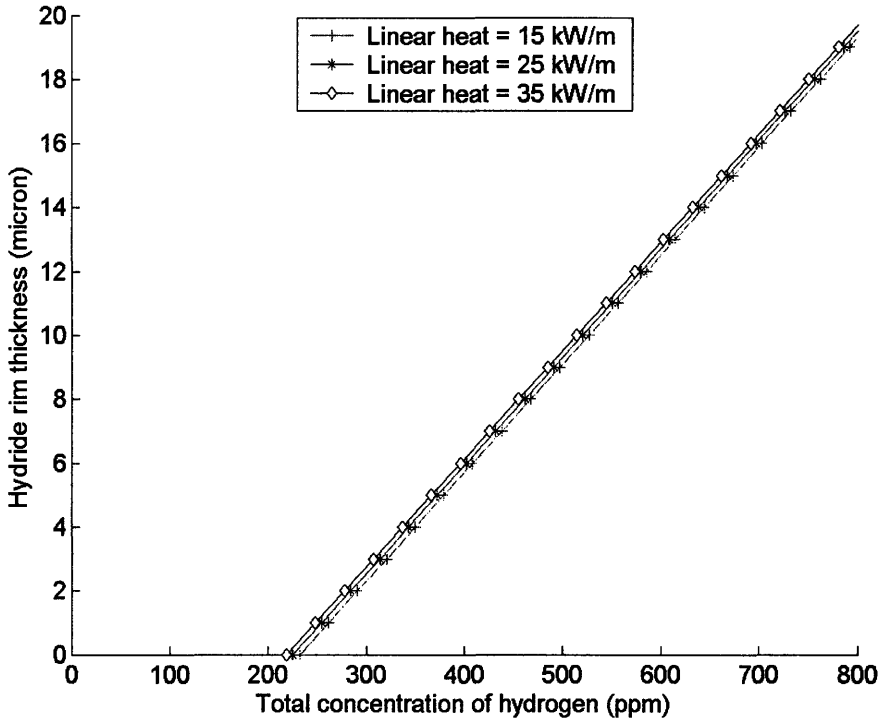

Figure 4-7: Hydride rim prediction with Tco = 700 K

where t_H is the thickness of hydride rim in [m] and λ is an empirical multiplication factor chosen based on fitting the experimental data.

$$\lambda = \begin{cases} 6.0 & for \quad PWR \quad Zry-4 \quad cladding \\ 11.0 & for \quad BWR \quad Zry-2 \quad cladding \end{cases}$$

The implication of this multiplication factor is to account for the stacking of hydride platelets. The larger value for BWR Zry-2 cladding is due to effects of radially orientated hydrides.

4.2.2 Fracture toughness

In general, the temperature, hydrogen content, hydride orientation, and fast fluence could modify the fracture toughness of the cladding at high burnup. However no single experiment could cover such a wide range of parameters. Axially notched ring

Zry-2 specimen cut from the cladding tube [86][87] and β-treated Zry-4 compact tension specimens tests [88]are selected for fitting the fracture toughness model. The data and fracture toughness model is shown in Figure 4-8. PL refers to pin loading. CT refers to compact tension.

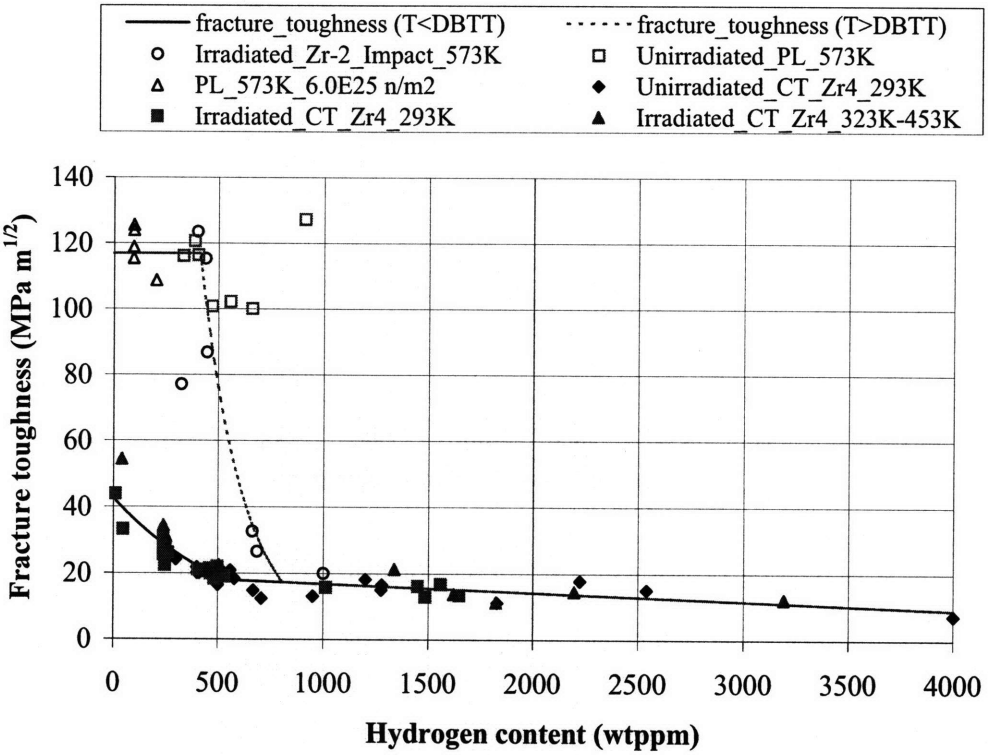

Figure 4-8: Fracture toughness

As seen from Figure 4-8, the fracture toughness for both the unirradiated and irradiated hydride specimens decreases as hydrogen content increases at room temperature. In comparison to the specimens at room temperature, the fracture toughness increases at 573 K for both the irradiated and unirradiated specimens. This increase could be best characterized by the a brittle to ductile transition. At 573 K, no major difference for the fracture toughness of the irradiated zircaloy is shown for hydrogen content up to 500 ppm. For unirradiated sample this cut-off hydrogen content could be even higher. These data are consistent with the conclusion that radiation damage controls ductility for hydrogen content up to 800 ppm at reactor operating temperature [84], although the cut-off hydrogen content is higher. Therefore, two curves

representing the fracture toughness at both room temperature and reactor operating temperature are fitted. The ductile to brittle transition temperature (DBTT) is introduced to differentiate the two curves for hydrogen content less than 1000 ppm.

$$T > DBTT$$

$$K_{IC} = \begin{cases} 116.9 - 0.00782C_H & 0 \leq C_H < 411.3 \quad \text{ppm} \\ 855.3\exp(-0.005C_H) & 411.3 \quad \text{ppm} \leq C_H < 806.1 \quad \text{ppm} \\ 19.38 - 0.00257C_H & 806.1 \quad \text{ppm} \leq C_H \end{cases} \tag{4.30}$$

$$T < DBTT$$

$$K_{IC} = \begin{cases} 42.64\exp(-0.001619C_H) & 0 \leq C_H < 532.4 \quad \text{ppm} \\ 19.38 - 0.00257C_H & 532.4 \quad \text{ppm} \leq C_H \end{cases} \tag{4.31}$$

DBTT is a function of hydrogen concentration, fast fluence and strain rate for irradiated cladding. DBTT is also a function of strain rate, [80] for highly irradiated cladding, DBTT is 473 K at a strain rate of 1.5 % /s, 573 K at a strain rate of 500 % /s. Given that the high strain rate measured during RIA is in an order of tens %/s [89], the DBTT is set as 500 K during the PCMI loading phase.

The fracture toughness is modeled by the hydrogen content and temperature being below or above DBTT. The non-uniformity of fracture toughness due to preferential accumulation of hydride at the outer region of the cladding is not particularly addressed in fitting the fracture toughness curve from the hydrided specimen. Instead, we consider it in the flaw size model to account for the non-uniform distribution of hydrides.

4.2.3 Failure criterion

To characterize the failure condition, J-integral is introduced as the parameter driving the fracture. J-integral is a parameter characterizing the stress-strain field at the tip of a crack by an integration path taken sufficiently far from the crack tip to be analyzed and then substituted for a path close to the crack tip region. For linear

elastic plane-strain conditions,

$$J_{IC} = \frac{(1-\nu^2)K_{IC}^2}{E} \tag{4.32}$$

where: J_{IC} is the critical toughness value at the initiation of crack growth, K_{IC} is the mode-I critical stress intensity factor, E is the elastic modulus, and ν is the Poisson ratio.

The line integral J is defined as:

$$J = \int_{\Gamma} W dy - T\frac{\partial \bar{u}}{\partial x} ds \tag{4.33}$$

where,

Γ = any counter-clockwise contour surrounding the crack tip.

W = loading work per unit volume or, the strain energy density for elastic bodies.

T = the traction vector at ds defined according to the outward normal n along Γ.

$\bar{u}$ = displacement vector at ds.

ds = arc length along contour Γ.

$T\frac{\partial \bar{u}}{\partial x} ds$ = the rate of work input from the stress field into the area enclosed by Γ.

J-integral has the advantage to describe the stress-field around a crack tip with certain amount of plasticity. Numerical calculation of J usually involves using finite element model to calculate the above parameters along a chosen line contour. Since the current mechanical deformation model in the FRAPTRAN code is not able to define a line contour to calculate J from its definition, an engineering approach is adopted as follows:

$$J = J_e + J_p \tag{4.34}$$

$$J_e = \frac{K_e^2(1-\nu^2)}{E} \tag{4.35}$$

$$K_e = F\sigma_\theta\sqrt{\pi a} \tag{4.36}$$

where F is given as [76]:

$$F = 1.12 - 0.231(\frac{a}{W}) + 10.55(\frac{a}{W})^2 - 21.72(\frac{a}{W})^3 + 30.39(\frac{a}{W})^4$$

a is the effective flaw size. W is the cladding wall thickness. Plastic component of J-integral is approximately given as [90]:

$$J_p = \frac{\varepsilon_p}{\varepsilon_e \sqrt{n}} J_e \tag{4.37}$$

ε_p and ε_e are the plastic and elastic hoop strain respectively. n is the strain hardening exponent. The failure criterion is set as:

$$J \geq J_{IC} \tag{4.38}$$

The process of fracture failure is schematically illustrated in Figure 4-9. The fracture of hydride platelets is assumed to form initial cracks. Onset of the crack growth corresponds to the condition of $J \geq J_{IC}$. The development of through-wall crack leads to failure of the cladding.

Therefore, it can be seen that Eq 4.38 is a conservative assumption for failure, since it only corresponds to blunting around the crack tip, the condition of the onset of crack growth rather than the condition of unstable crack propagation. The cladding tube should have certain resistance at each given initial flaw size. In summary, Eq 4.38 gives a necessary condition for failure. Since it neglects the crack growth in the ligament and in axial direction, it would generally under-estimate the enthalpy at failure.

Note that during the gap closure of RIA, the cladding is subjected to biaxial stress state. The J-integral methodology accounts for the effect of the hoop stress on the opening of cracks, which neglects the effect of axial stress on the crack growth. This effect is anticipated to be low as the axial stress is parallel to the crack surface, although the axial stress may tend to affect the plastic zone size around the crack tip.

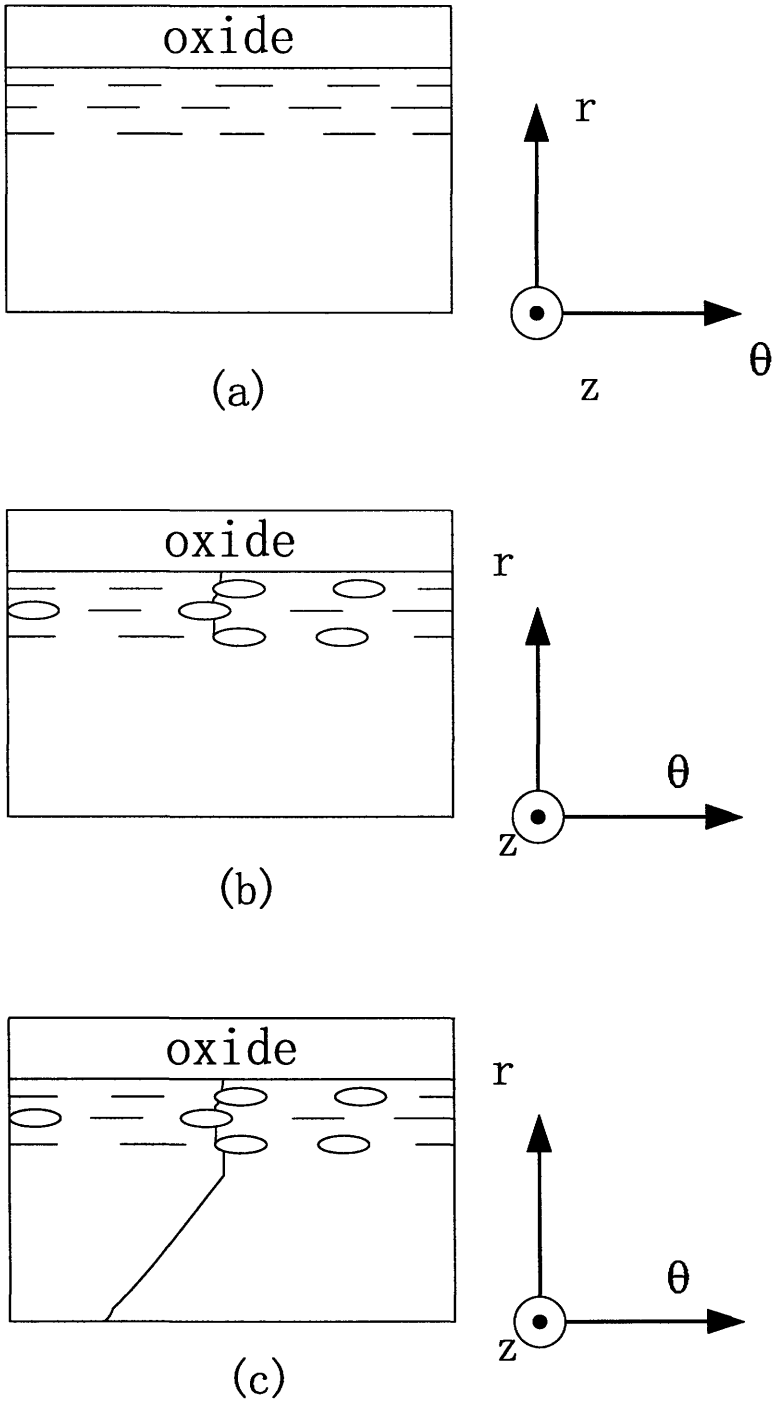

Figure 4-9: Illustration of fracture of hydrided cladding

4.3 Model implementation

4.3.1 Model validation

Results by application of the failure model are shown in Table 4.2-4.4. Strain-based failure model by PNNL and SED/CSED model by EPRI are also listed in the tables to compare with the failure model denoted as MIT model in the tables. As can

Table 4.2: Summary of failure prediction for CABRI tests

Test No.	Failure time (sec)				Enthalpy at failure (cal/g)			
	Measured	EPRI	PNNL	MIT	Measured	EPRI	PNNL	MIT
RepNa1	0.0740	0.0775	0.0817	0.0770	30	49.0	88.4	45.1
RepNa2	N	N	N	N	-	-	-	-
RepNa3	N	0.0952	N	N	-	124.8	-	-
RepNa4	N	N	N	N	-	-	-	-
RepNa5	N	N	N	N	-	-	-	-
RepNa8	0.5318	0.5091	N	0.5114	78	54.8	-	56.5
RepNa10	0.4560	0.4458	N	0.4531	79	56.5	-	69.5

Table 4.3: Summary of failure prediction for NSRR PWR fuel

Test No.	Failure time (sec)				Enthalpy at failure (cal/g)			
	Measured	EPRI	PNNL	MIT	Measured	EPRI	PNNL	MIT
HBO1	Failed	0.2016	0.2037	0.2017	60	53.9	70.2	54.5
HBO2	N	N	N	N	-	-	-	-
HBO3	N	0.2016	0.2037	0.2017	-	53.9	70.2	54.5
HBO4	N	0.2169	N	N	-	50.0	-	-
HBO5	Failed	0.2077	0.2091	0.2072	76.9	53.8	70.8	45.3
HBO6	N	0.2079	0.2103	N	-	60.2	83.6	-
HBO7	N	0.2079	0.2103	N	-	60.3	83.6	-
GK1	N	0.1987	N	N	-	86.8	-	-
GK2	N	0.1962	N	N	-	69.7	-	-
OI1	N	0.2022	N	N	-	69.5	-	-
OI2	N	0.2025	N	N	-	69.3	-	-
MH1	N	N	N	N	-	-	-	-
MH2	N	N	N	N	-	-	-	-
MH3	N	N	N	N	-	-	-	-

be seen from the above tables, our model is good at distinguishing failure cases from non-failure cases, with one wrong prediction for case HBO3. The uniform elongation model by PNNL gives six wrong predictions: RepNa8, RepNa10,FK4, HBO3, HBO6,

Table 4.4: Summary of failure prediction for NSRR BWR fuel

Test No.	Failure time (sec)				Enthalpy at failure (cal/g)			
	Measured	EPRI	PNNL	MIT	Measured	EPRI	PNNL	MIT
FK1	N	0.2062	N	N	-	91.3	-	-
FK2	N	N	N	N	-	-	-	-
FK3	N	0.2090	N	N	-	101.8	-	-
FK4	N	0.2037	0.2056	N	-	83.4	121.9	-
FK5	N	N	N	N	-	-	-	-
FK6	0.2440	0.2442	0.2444	0.2437	70	67.2	72.5	53.5
FK7	0.2443	0.2444	0.2446	0.2439	62	69.9	76.2	59.2
FK8	N	N	N	N	-	-	-	-
FK9	0.2692	0.2662	0.2666	0.2647	86	74.6	76.9	60.9
FK10	Failed	0.2654	0.2658	0.2647	80	75.98	79.2	67.9
FK12	Failed	0.2665	0.2666	0.2651	72	79.12	76.9	68.1
TS1	N	N	N	N	-	-	-	-
TS2	N	N	N	N	-	-	-	-
TS3	N	N	N	N	-	-	-	-
TS4	N	N	N	N	-	-	-	-
TS5	N	N	N	N	-	-	-	-

HBO7. For CABRI cases, both EPRI and MIT models give close results while PNNL model can't capture the failures except for case RepNa1. Test case CABRI RepNa1 is believed to have hydride redistribution in the welding process. It may change the fracture toughness greatly. Thus case RepNa1 have a very low value of enthalpy deposit. Microphone signal detected the crack initiation is at 44 cal/g for RepNa8. The enthalpy at failure predicted by our model is closer to this value than the failure enthalpy of 79 cal/g.

The calculation of SED however depends on the mechanical model used in the code. The SED and CSED failure criterion developed for the FALCON code may not be suitable in the FRAPTRAN code. The SED/CSED model implemented in the FRAPTRAN code tends to give more conservative predictions of fuel failures. Figure 4-10 gives the prediction of errors of failure enthalpy. Enthalpy at failure is generally under estimated by the MIT failure model. That is because the model actually predicts the onset of crack growth rather than the final loss of integrity of the cladding. The crack growth in the remaining ligament is not calculated Thus the calculated failure enthalpy is generally 20-30 cal/g lower than the experimental data.

Also, the crack may be arrested in the inner cladding ligament as the temperature is higher and Zry properties tend to be more ductile. Then failure should be driven by the plastic collapse rather than the crack growth. Figure 4-11 to Figure 4-13 show

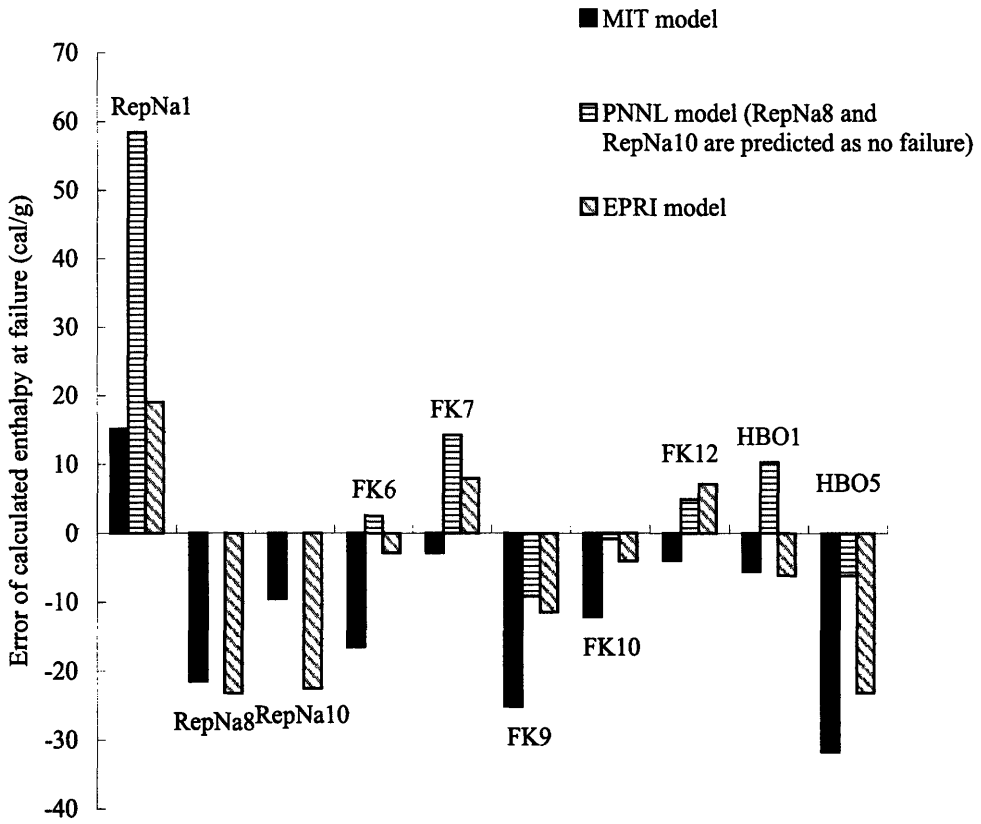

Figure 4-10: Errors for prediction of failure enthalpy

the enthalpy rise and parameter J and critical value of J. The J is compared with J_{IC} at each time step to determine whether failure would occur. When failure occurs, the enthalpy at failure time is recorded as failure enthalpy. Although the difference between the measured failure enthalpy and calculated failure enthalpy can be as large as more than 20 cal/g, the time interval is only 2-3 ms.

4.3.2 Discussion

- Flaw size effects

  Figure 4-14 show the sensitivity study of flaw size for cases RepNa1, RepNa8,

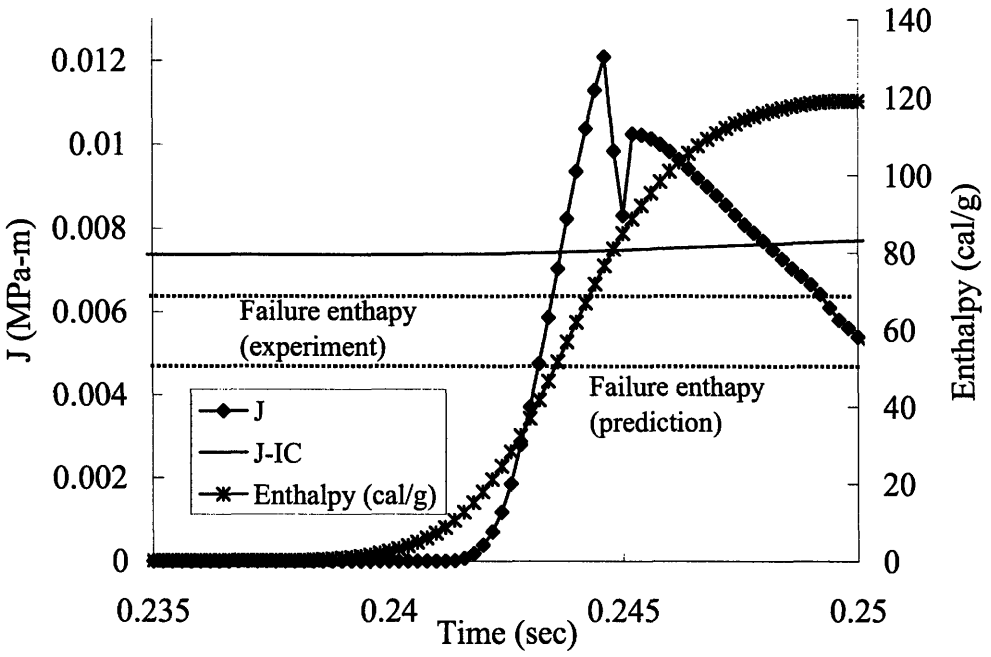

Figure 4-11: Enthalpy rise and J vs. time for case FK6

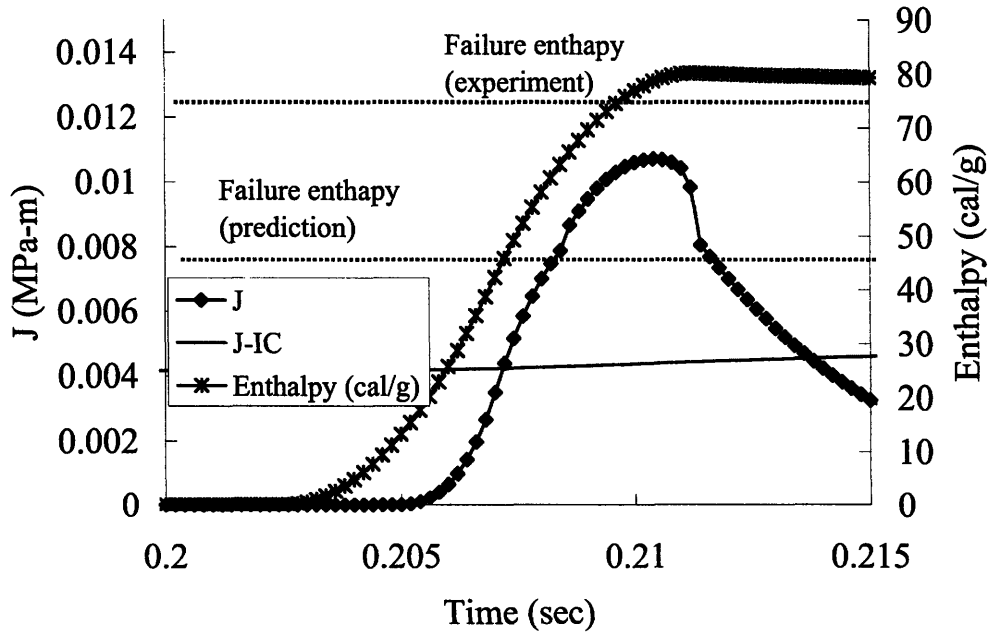

Figure 4-12: Enthalpy rise and J vs. time for case HBO5

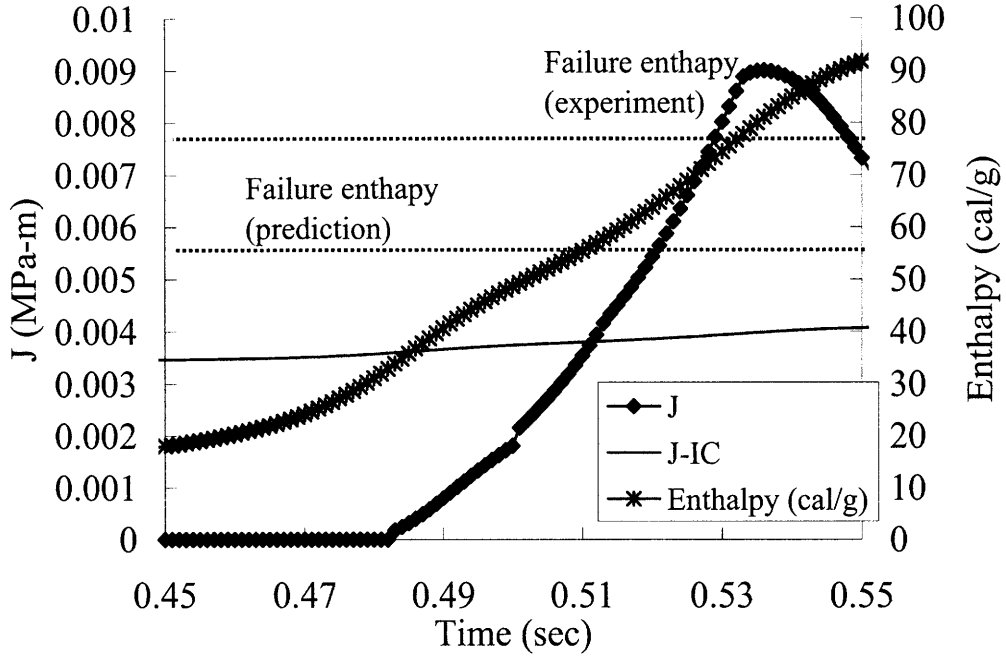

Figure 4-13: Enthalpy rise and J vs. time for case RepNa8

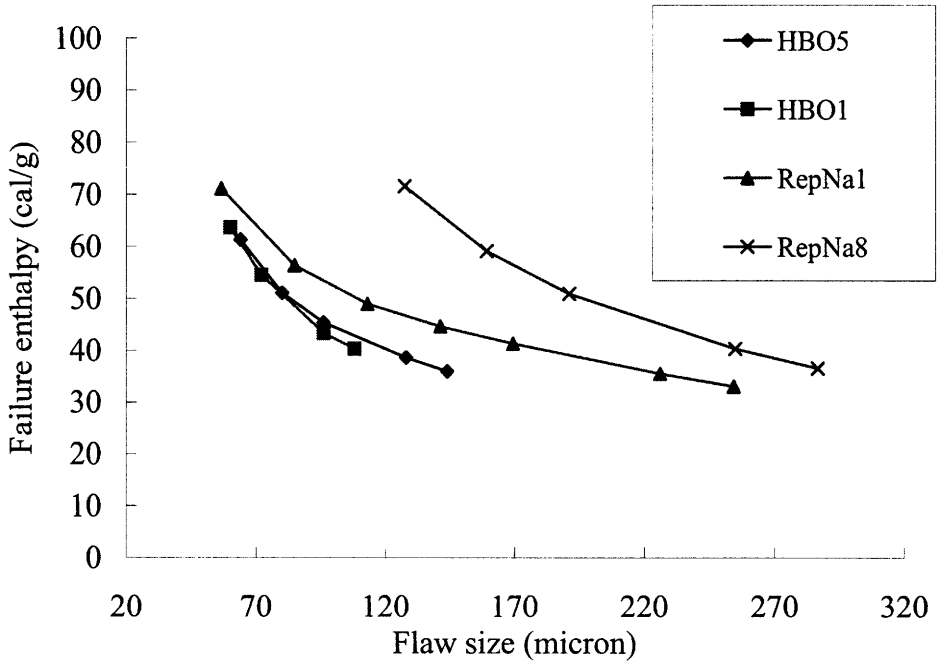

Figure 4-14: Sensitivity to flaw size

HBO1 and HBO5. All the test cases show the decreasing trend of failure enthalpy as flaw size increases. This decrease of failure enthalpy tends to change abruptly at small flaw size but change gradually at a larger flaw size. The flaw size would affect directly the stress intensity factor K_I and thus J_I, which is the parameter to characterize the stress field at the crack tip. Increasing flaw size tends to shorten the time to reach the onset of crack growth, and decrease the amount of enthalpy deposit to fail the cladding. The driving force during the PCMI is the displacement load from pellet. Certain amount of enthalpy is required for the thermal expansion and swelling of pellet to close the gap and to form the initial crack with plastic deformation in the matrix around the hydride platelet. This amount of enthalpy deposit might be less dependent on the flaw size. That explains the gradual decrease of enthalpy deposit at large flaw size. On the other hand, the larger the flaw size, the more extensive the corrosion would be in the cladding alloy. This tends to decrease fracture toughness of the cladding, and may lead to the unstable crack propagation. In such a scenario, Eq 4.38 is closer to the failure condition. It implies the enthalpy deposit can be very low, around 40 cal/g, with extensive corrosion in the cladding.

- Comparison with scaling analysis

  Table 4.5 summarizes the scaling analysis by NRC [46]. By changing the coolant condition to PWR HZP condition and power pulse width and magnitude to make it more representative of the PWR condition, the failure enthalpies for PWR conditions based on CABRI cases RepNa7, RepNa8 and RepNa10 are reduced. The failure enthalpies for NSRR cases: HBO1 and TK2 are increased more than 20 cal/g as the power pulse is changed from 5 ms to 10 ms and coolant condition changed from CZP to HZP. To compare with the scaling analysis, test cases HBO1, RepNa8 and RepNa10 are changed to PWR HZP conditions in the same way as done in Table 4.5. The failure model is applied to those three cases at both test conditions and PWR HZP conditions. Table 4.6 to Table 4.8 show the failure prediction. As can be seen, the NSRR case HBO1 which features

Table 4.5: Summary of scaling analysis by NRC [46]

	Test conditions				PWR conditions			
Test No.	Temp. (°C)	Pulse width (ms)	Failure stress, strain	Enthalpy change at failure (cal/g)	Temp. (°C)	Pulse width (ms)	Enthalpy change at failure (cal/g)	Scaling (cal/g)
RepNa10	280	31	230 MPa	59	280	13	57	-2
RepNa8	280	75	130 MPa	63	280	16	54	-9
RepNa7	280	40	0.49%	97	280	12	78	-19
HBO1	18	4.4	0.52%	57	277	10	80	23
TK2	25	4.4	0.58%	59	277	11	86	27

narrow power pulse, doesn't fail when extrapolated to PWR HZP condition. It seems more likely due to the temperature change. At the test condition of room temperature with almost adiabatic power pulse, the cladding surface temperature remains very low, at time of failure 342 K, which is lower than the ductile to brittle transition temperature. At HZP with wider power pulse, the cladding temperature reaches 774 K at maximum J/J_{IC}, thus cladding becomes more ductile to prevent failure. For CABRI cases RepNa8 and RepNa10, the power pulse however is more narrow when extrapolated from the test condition to HZP condition. The initial cladding temperature is same. Therefore, failure occurs at even lower enthalpy deposit. The trend for failure enthalpy change is the same as the analysis by Meyer [91] when the test conditions are changed to PWR conditions. Although the model is conservative in predicting the enthalpy at failure, it also demonstrates that there is a large safe margin in the ductility change. The extent of corrosion in the cladding of HBO1 though cause the failure at test conditions may not be able to fail at a wider power pulse and higher temperature. The maximum oxide layer thickness measured in HBO1 is 50 micron, still much lower compared to the CABRI test cases: 130 micron for RepNa8 and 80 micron for RepNa10. Another similar test HBO7 conducted at NSRR with higher enthalpy than HBO1 but slightly less corrosion (peak oxide layer thickness is 45 micron) didn't fail, indicating that the failure of HBO1 is

marginal.

Table 4.6: Analysis of HBO1 extrapolated to PWR HZP condition

	Test condition	PWR condition
Peak fuel enthalpy increase (cal/g)	82.6	82.6
Failure	Y	N
Failure time (sec)	0.2017	-
Enthalpy increase at failure (cal/g)	54.23	-
Cladding avg. temperature at failure (K)	342	774 [a]

[a]Temperature at max(J/J_{IC})

Table 4.7: Analysis of RepNa8 extrapolated to PWR HZP condition

	Test condition	PWR condition
Peak fuel enthalpy increase (cal/g)	79.4	79.1
Failure	Y	Y
Failure time (sec)	0.5075	0.5286
Enthalpy increase at failure (cal/g)	37.6	27.5
Cladding avg. temperature at failure (K)	662	589

Table 4.8: Analysis of RepNa10 extrapolated to PWR HZP condition

	Test condition	PWR condition	
		(a)	(b)
Peak fuel enthalpy increase (cal/g)	78.9	88.7	66.0
Failure	Y	Y	Y
Failure time (sec)	0.4513	0.4440	38.0
Enthalpy increase at failure (cal/g)	50.6	38.0	38.0
Cladding avg. temperature at failure (K)	682.6	628.1	628.1

When case RepNa10 is extrapolated to PWR HZP condition, it is found that the peak fuel enthalpy increase is sensitive to change of power magnitude. For the case of PWR condition with peak fuel enthalpy of 66.0 cal/g, DNB doesn't happen, but for the case with peak fuel enthalpy of 88.7 cal/g, film boiling occurs. Thus, when DNB happens, there is a jump of the peak fuel enthalpy increase due to the deterioration of heat transfer at cladding surface, which prevents the fuel from cooling, thus allowing larger enthalpy inside fuel rod. Enthalpy increase at failure however doesn't change in spite of the change of peak fuel enthalpy deposit.

4.4 Summary and conclusions

PCMI failure of high burnup fuel cladding is modeled based on fracture mechanics. Model is implemented in the FRAPTRAN code. A flaw size sub-model is set forth to capture effects of a hydride rim on the failure of a clad. A fracture toughness sub-model describes the fracture toughness as a function of hydrogen content. A DBTT is introduced to differentiate the fitting curves at different temperature and account for the high strain rate effects. A conservative failure criterion assumes that when the condition for onset of crack growth is satisfied, failure would occur. Despite its conservative assumption, the model has a very good capability to differentiate between failed and non-failed rods capturing a wide range of test database including CABRI and NSRR test rods with different burnup levels, corrosion extent and fuel enthalpy deposition.

The model generally under-estimates the enthalpy at failure. This could be due to the assumptions made in the models, which

1. neglect the crack growth in axial direction,

2. neglect the crack growth in the remaining ligament, and

3. doesn't account for the plastic collapse failure.

Applying this model to PWR conditions of test fuel rods reveals that for a wider power pulse, a higher threshold of the enthalpy is required for PCMI failure. The failure of NSRR test case HBO1 seems unlikely to materialize at PWR HZP condition with larger ductility.

Chapter 5

Fuel failures at LWR conditions

5.1 Introduction

Previous chapters described models of fission gas release and swelling, heat transfer and PCMI failure during simulated RIA test conditions. This chapter will apply these models to LWR conditions to analyze the high burnup fuel rod behavior and to determine the failure conditions of LWR fuels during RIA.

LWR accidents to be explored in this chapter include the HZP conditions of PWRs and CZP conditions of BWRs. In a PWR, as the hypothetical RIA is triggered by a control rod ejection, HZP rather than at power conditions are investigated as the largest reactivity insertion would occur at such condition. Similarly, the control blade drop down accident of a BWR at CZP condition is investigated since it is the worst scenario for a BWR as far as reactivity insertion is concerned.

The difference between test conditions and LWR conditions are listed in Table 5.1. As can be seen from Table 5.1, coolant conditions in CABRI differ largely from LWR conditions. The NSRR test conditions can best represent the BWR CZP. However, no test data is available at high system pressure conditions. The test rods are short refabricated rods as compared to the full length rod in LWRs. NSRR test rods have uniform axial power while CABRI test rods have non-uniform axial power distributions. They are able to represent the local condition of a PWR or BWR fuel rod. The range of filling gas quantity and composition in the tests is not significantly dif-

Table 5.1: Difference between test conditions and LWR conditions

	CABRI	NSRR	PWR HZP	BWR CZP
Coolant type	Flowing sodium	Stagnant water	Stagnant water	Stagnant water
Coolant pressure (MPa)	0.5	0.1	15.5	0.1
Coolant Temp. (°C)	280	20	280	20
Fuel rod	Refabricated	Refabricated	Full length	Full length
Filling gas	He	He or fission gas	He and fission gas	He and fission gas
Power pulse width (ms)	10-70	5	10-40	>20

ferent from the LWR conditions, although most test rods are filled with helium while the gas composition in LWR fuel rods is largely affected by the fission gas released during base irradiation. Most of the tests used to validate models are conducted at narrow power pulse conditions. A few wide power pulse cased in CABRI extend the capability to represent the LWR conditions.

The impacts of these differences on models presented in Chapter2-Chapter5 are summarized below:

- Model of fission gas release and swelling

  Burst gas release is related to the fuel temperature change, stress field in the fuel, cracking of grain boundary, and micro-structure evolution in the rim region. These parameters are unlikely to be affected by the coolant conditions. Refabricated fuel rode can have different void to fuel ratio but that doesn't affect the fraction of fission gas release.

- Model of heat transfer

  The model is developed for room temperature and stagnant flow condition. This is only applicable to BWR CZP condition. For PWR HZP, the original heat transfer model in FRAPTRAN is used. This neglects oxidation effects on the heat transfer.

- Model of PCMI failure

PCMI failure of high burnup fuel is more likely to be affected by the ductility change as a function of temperature, fluence, corrosion and strain rates. These parameters are also covered in test data. This mechanistic model doesn't depend on the geometry of fuel rod thus is able to predict the failure at PWR HZP and BWR. High system pressure at LWR conditions may change the initial stress and strain of cladding but this is not in conflict with any model assumptions.

Therefore the mechanistic models developed in the thesis extrapolated into LWR conditions should be able to give a good prediction in spite of the differences listed in Table 5.1.

5.2 PWR HZP

Typical parameters for a high burnup fuel rod in a PWR are listed in Table 5.2. Corresponding base irradiation input file is prepared and run by FRAPCON to provide the initial conditions at various burnup levels from 30 to 56 MWd/kgU. The width of power pulse is taken as 10 ms. The power pulse magnitude varies in the simulation to achieve different enthalpy deposit level. Generally, the shape of the power pulse depends on the neutronic characteristic of the reactor. Power pulse width tends to have an inverse relationship with both the control rod worth and maximum fuel pellet enthalpy increase. The simulations by PARCS showed that the pulse width for an REA ranges from 65 ms to 10 ms for peak fuel enthalpy changes from 15 cal/g to 100 cal/g [92].

A narrower power pulse features high strain rate and strong PCMI when the cladding remains cold. Thus, it is more dangerous for the PCMI failure as the ductility of the cladding tends to be low for a narrow power pulse. Therefore, we choose a conservative value for the power pulse width as 10 ms. This value is close to the scaling analysis given by Meyer [46].

The failure of high burnup fuel depends largely on the corrosion, which is not necessarily to be a linear function of burnup. By assuming a linear dependence of power on time, we change the slope of power history curve, the peak node hydrogen

content is calculated by the FRAPCON code. The dependence on the slope of a linear power history is shown in Figure 5-1. High linear power at the end of life would cause high temperature drop across the oxide layer, high fuel temperature due to thermal conductivity degradation. We select the power history with peak to average ratio of 1.8 as shown in Figure 5-2 as the base irradiation case for the simulation of RIA.

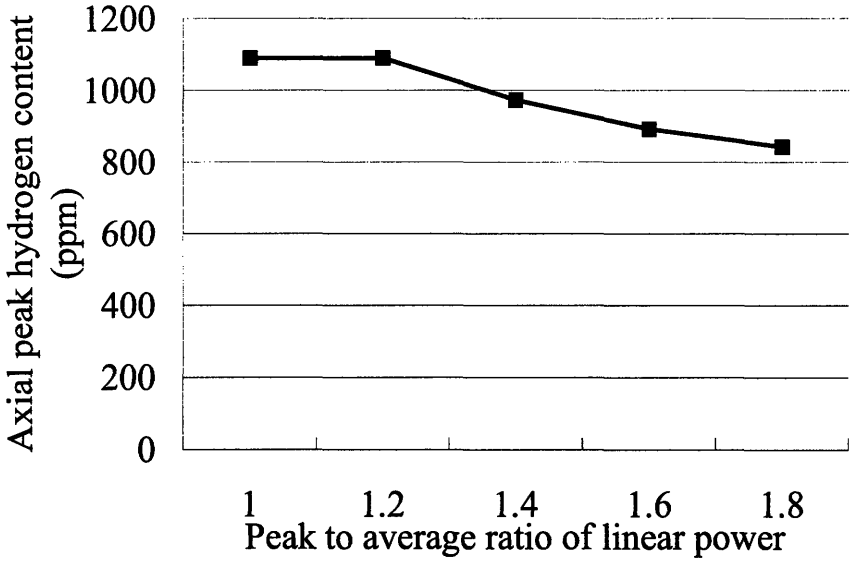

Figure 5-1: Effect of power history on the corrosion of high burnup fuel

The maximum oxide layer thickness vs. burnup for the simulated PWR rod is shown in Figure 5-3. The bounding curve by EPRI [75] is also shown in the figure for comparison. Below 50 MWd/kg, the simulated case using the oxidation model in FRAPCON can give a best estimate oxidation rate. Above 50 MWd/kg, it exceeds the EPRI fitting curve. Maximum hydrogen content vs. burnup shown in Figure 5-4 is also obtained by the corrosion model in the FRAPCON code. The hydrogen content is in general higher than that measured in most test cases. Calculations for peak fuel enthalpy at various burnup levels are conducted for simulated RIA cases with different power pulse magnitude and with three different failure model options:

1. strain-based failure model by PNNL

2. SED/CSED model by ANATECH/EPRI and

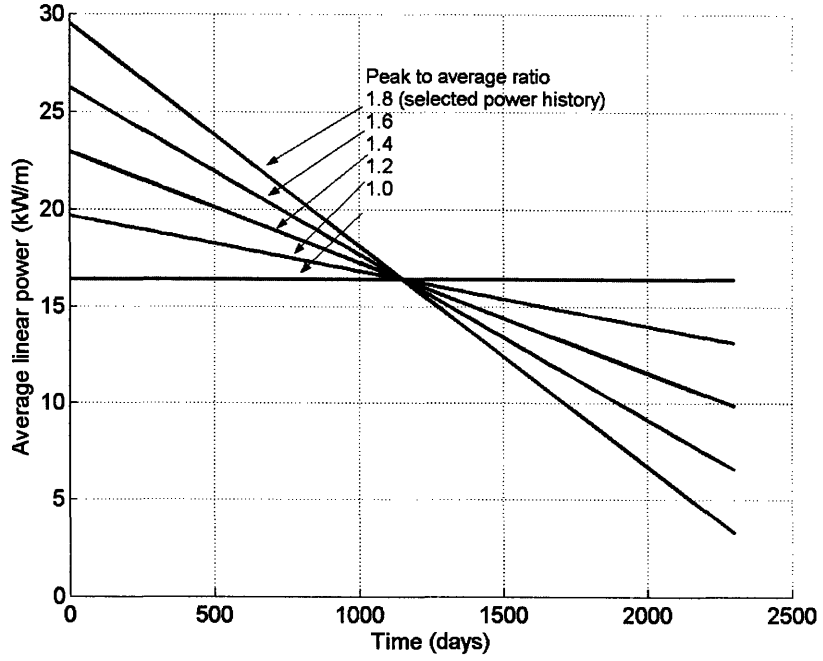

Figure 5-2: Linear power of PWR rod

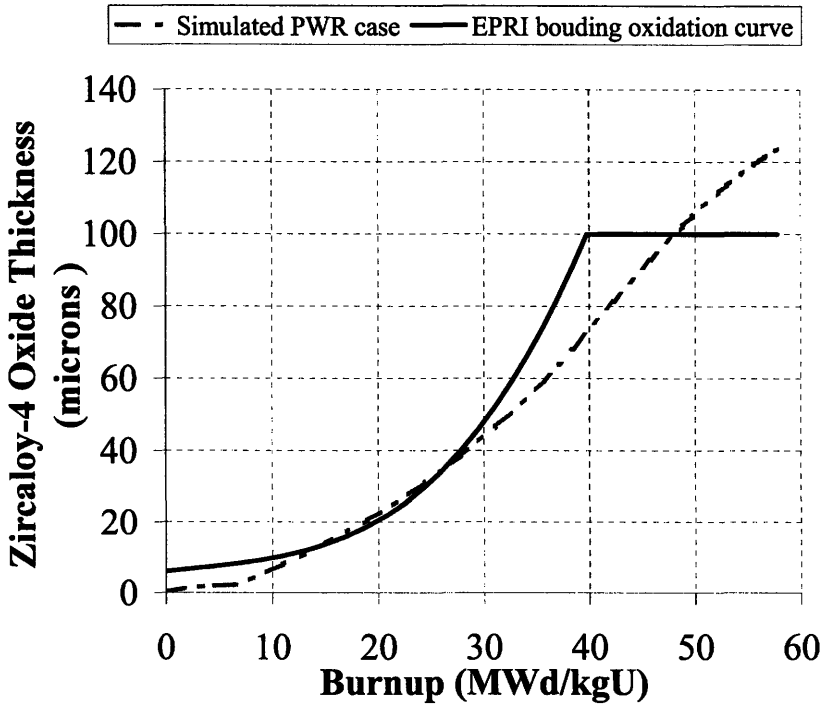

Figure 5-3: Buildup of oxide layer as a function of burnup for simulated PWR rod

Table 5.2: Parameters for simulated PWR RIA at HZP

Parameter	Unit	Value
Design		
Cladding Type		Zry-4
Cladding OD	mm	10.9
Cladding Thickness	mm	0.673
Fuel OD	mm	9.388
Fuel Stack Length	m	3.505
Pellet Height	mm	10.2
Fill Gas		He
Fill Gas Pressure	MPa	3.5
Fuel Density	%	95
Fuel Enrichment	%	4.5
Internal Void Volume	cm^3	27.9
Base irradiation		
Peak Linear Power	kW/m	16.4
Irradiation Time	day	2200
Reactor Type		PWR
Coolant Pressure	MPa	15.5
Coolant Inlet Temperature	°C	293
Mass Flow Rate	kg/m^2-s	3570
Burnup	MWd/kg	56
Cladding Corrosion	micron	150
Fission Gas Release	%	3
Transient		
Power Pulse Width	ms	10
Coolant Temperature	°C	278
Coolant Pressure	MPa	15.5

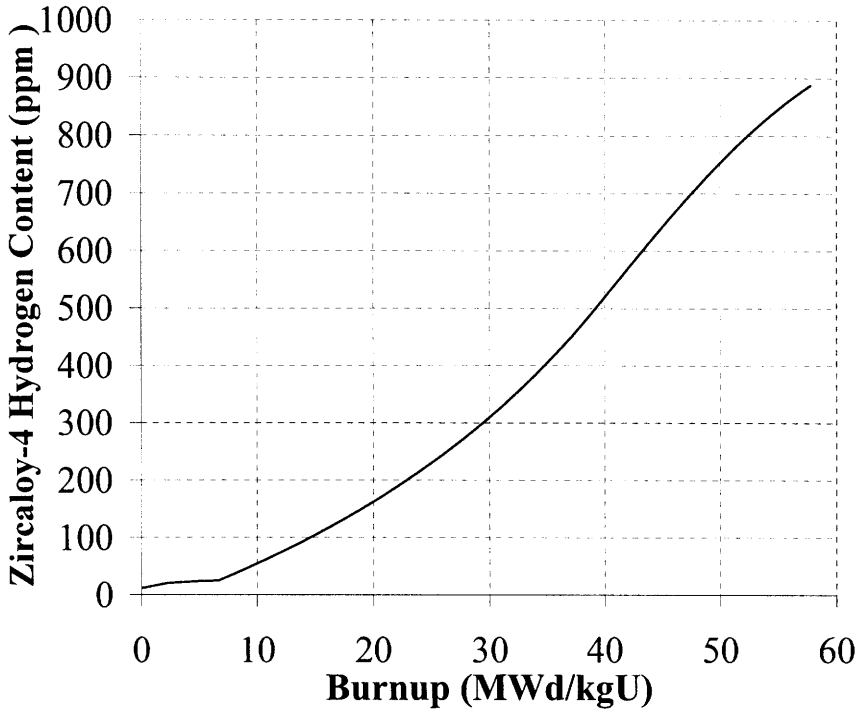

Figure 5-4: Hydrogen content vs. burnup for simulated PWR rod

3. the fracture mechanics model developed in the thesis.

By examining the calculation results of all those simulated cases, a threshold failure case is selected from the test cases at a given burnup and corresponding peak fuel enthalpy vs. burnup for different models are shown in Table 5.3 and Figure 5-5.

Table 5.3: Peak fuel enthalpy of failure for PWR HZP

Burnup (MWd/kg)	Hydrogen (ppm)	PNNL	MIT	EPRI
24.5	220.97	N	N	138.5
32.2	357.71	N	N	79.2
37.4	451.02	N	N	49.7
41.3	545.51	N	N	45.5
51.6	783.39	141.6	100.8	43.3
56.8	877.23	127.4	78.8	45.4

The MIT model using fracture mechanics shows that the result of failure enthalpy vs. burnup is between that predicted by SED/CSED model and by strain based failure model. The SED/CSED model prediction seems much lower. It indicates the

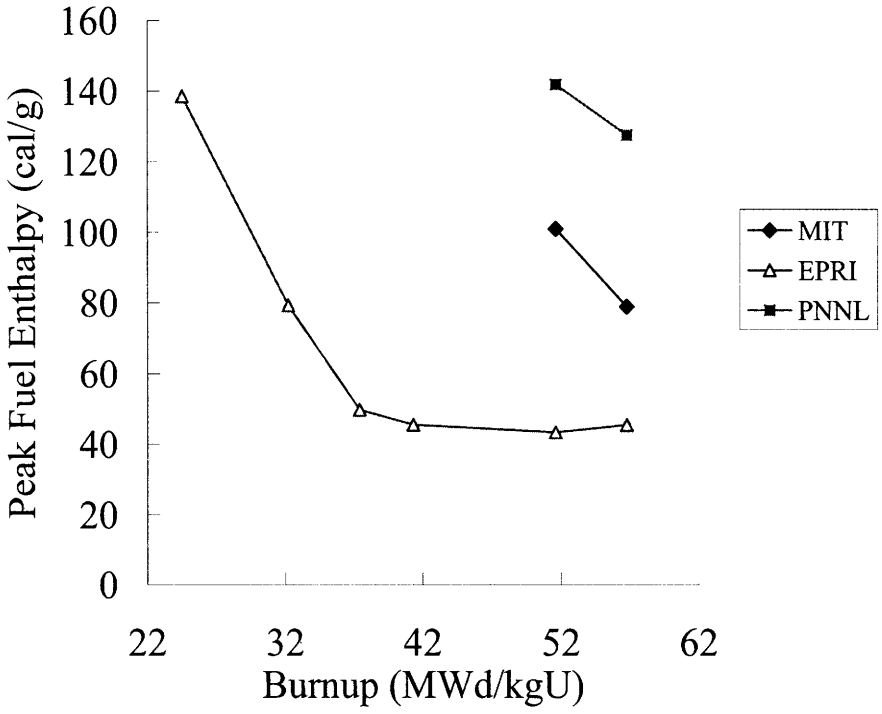

Figure 5-5: Peak fuel enthalpy vs. burnup for PWR failure cases

SED/CSED model needs to be benchmarked in the FRAPTRAN code as the SED calculation by the two codes FRAPTRAN and FALCON are not necessarily to be same. The HZP condition with higher operating temperature than the cold power condition doesn't provide sufficient ductility to keep the fuel from failure during PCMI for oxidation above 70 micron. At HZP condition, the reduced gap might result in a strong PCMI in the early phase of RIA. The system pressure is small as compared to the interface pressure.

However as the power pulse width changed, the dependence of peak fuel enthalpy on burnup also changed. The failure enthalpy vs. hydrogen absorption at different pulse widths are calculated and shown in Figure 5-6. The failure enthalpy increases at a wider power pulse due to mitigated PCMI loading and increased ductility of the cladding with higher cladding temperature. This is a more pronounced effect at a lower burnup with smaller hydrogen absorption. At higher burnup with total hydrogen absorption greater than 1000 ppm, the extensive hydride network would decrease the ductility greatly. This makes the power pulse effects less obvious: the

enthalpy only increases 6 cal/g when the power pulse width is changed from 10 ms to 40 ms.

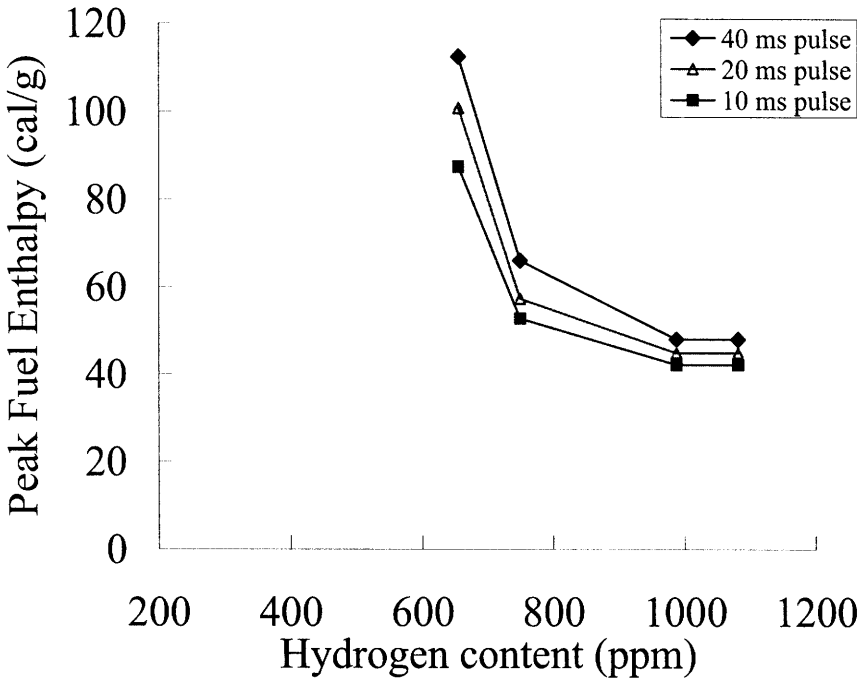

Figure 5-6: Effects of power pulse width on failure

5.3 BWR CZP

Typical parameters for a high burnup fuel rod in a BWR are listed in Table 5.4. A corresponding base irradiation input file was prepared and run by FRAPCON to provide initial conditions at various burnup levels from 30 to 54.3 MWd/kgU. The width of power pulse is selected to be 20 ms. This is a recommendation by GNF as a conservative power pulse width [93]. Figure 5-7 is the linear power history for the simulated BWR rod. Figure 5-8 and Figure 5-10 give the maximum oxide layer thickness and hydrogen content vs. burnup respectively. Although the hydrogen content is lower than that of PWR fuel, the hydride might be more detrimental to the cladding as a certain fraction of radially orientated hydride tend to more easily crack under the hoop stress. This difference has been empirically reflected in Eq 4.29.

Table 5.4: Parameters for simulated BWR RIA at CZP

Parameter	Unit	Value
Design		
Cladding Type		Zry-2
Cladding OD	mm	11.18
Cladding Thickness	mm	0.711
Fuel OD	mm	9.55
Fuel Stack Length	m	3.71
Pellet Height	mm	12.7
Fill Gas		He
Fill Gas Pressure	MPa	0.1
Fuel Density	%	95
Fuel Enrichment	%	4.31
Fuel Rod Pitch	mm	14.3
Base irradiation		
Peak Linear Power	kW/m	25
Irradiation Time	day	2192
Reactor Type		BWR
Coolant Pressure	MPa	7.14
Coolant Inlet Temperature	°C	278.2
Mass Flow Rate	kg/m^2-s	1649
Burnup	MWd/kg	54.3
Cladding Corrosion	micron	28
Fission Gas Release	%	1.86
Transient		
Power Pulse Width	ms	20
Coolant Temperature	°C	20
Coolant Pressure	MPa	0.1

Figure 5-9 shows various parameters during the base irradiation history. At EOL,

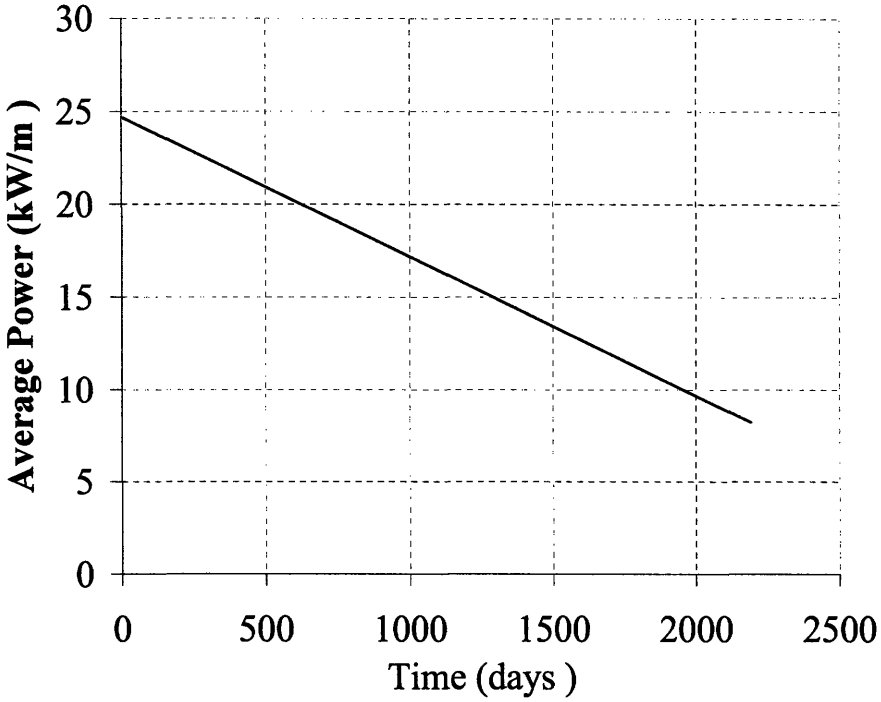

Figure 5-7: Linear power of BWR rod

cumulative FGR is around 1.8%, which contributes mainly to the plenum pressure above 1 MPa. After 1000 power days, the gap starts to close because of fuel swelling and relocation, initial creep down of cladding come to be counteracted by the PC contact pressure. At EOL, the gap contact pressure is 25 MPa and the cladding is still in compression.

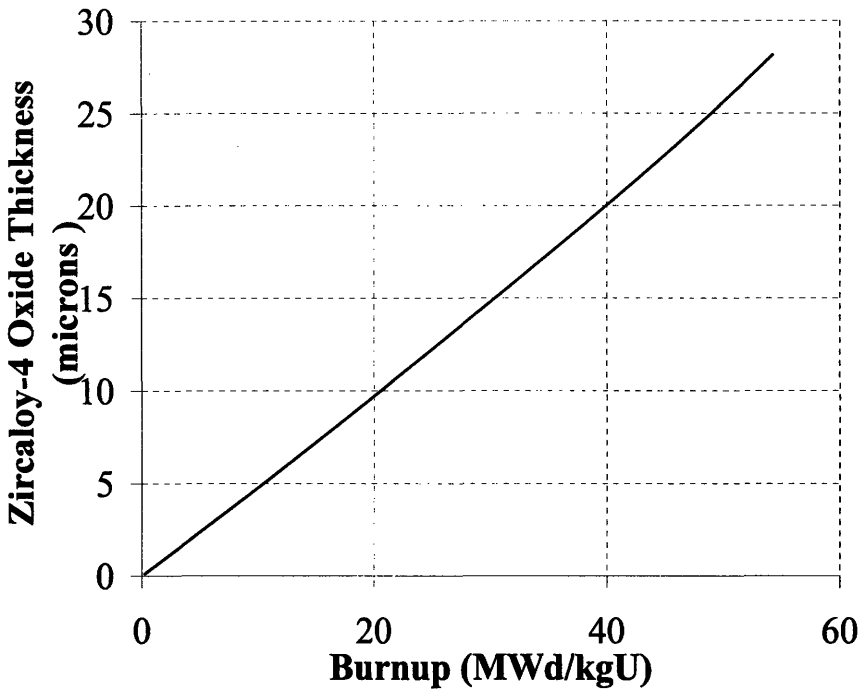

Figure 5-8: Oxide vs. burnup for simulated BWR rod

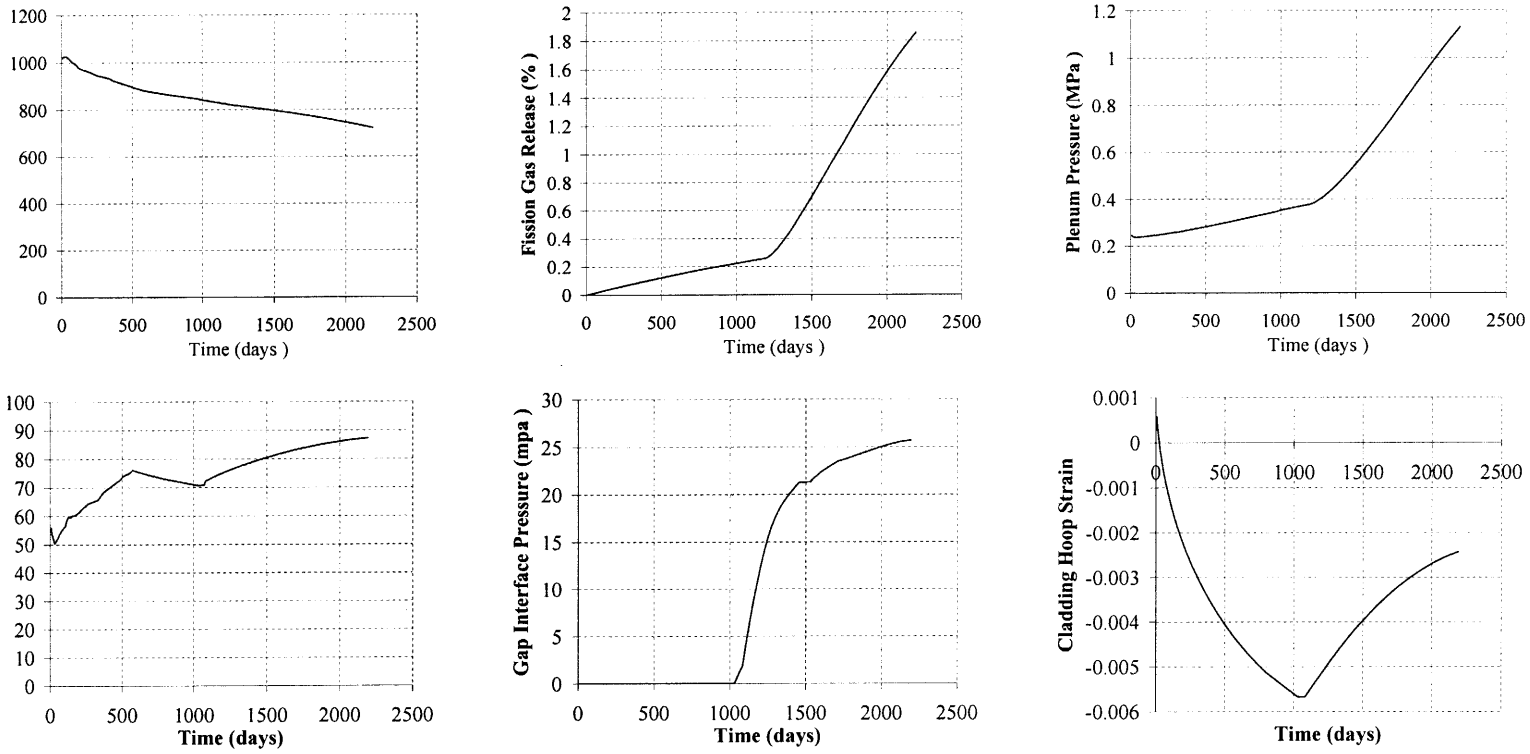

Figure 5-9: FRAPCON simulation of irradiation of a BWR case up to 54.3 MWd/kgU

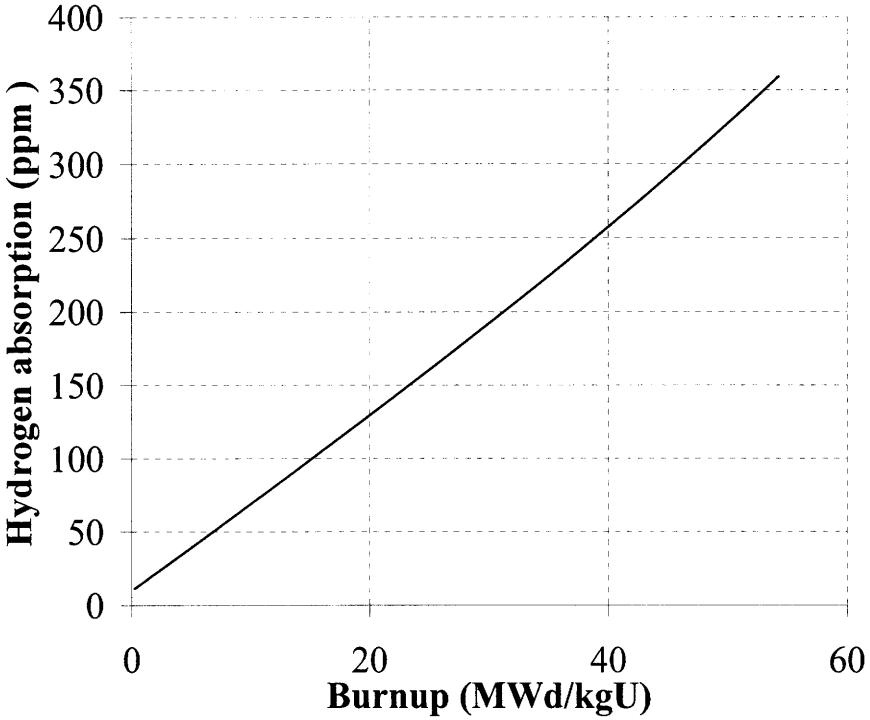

Figure 5-10: Hydrogen content vs. burnup for simulated BWR rod

The same procedure as done for the PWR fuel is conducted here. One failure case at burnup level above 54.3 MWd/kgU is identified with a peak fuel enthalpy at 146 cal/g as shown in Table 5.5 and Figure 5-11. Using the strain-based failure model by PNNL however doesn't show any failure up to 54.3 MWd/kgU. The SED/CSED model was not applied to the BWR case as the model has not been validated against the BWR Zry-2 cladding. Figure 5-12 shows the response of a BWR fuel rod

Table 5.5: Peak fuel enthalpy vs. burnup for BWR CZP

Burnup (MWd/kg)	Hydrogen (ppm)	PNNL	MIT
30.8	196.95	N	N
42.1	272.21	N	N
51.8	342.18	N	N
54.3	358.97	N	146

with the reference power pulse width of 20 ms. Figure 5-13 gives the response of BWR fuel rod with the narrower power pulse width of 10 ms. Although the peak fuel

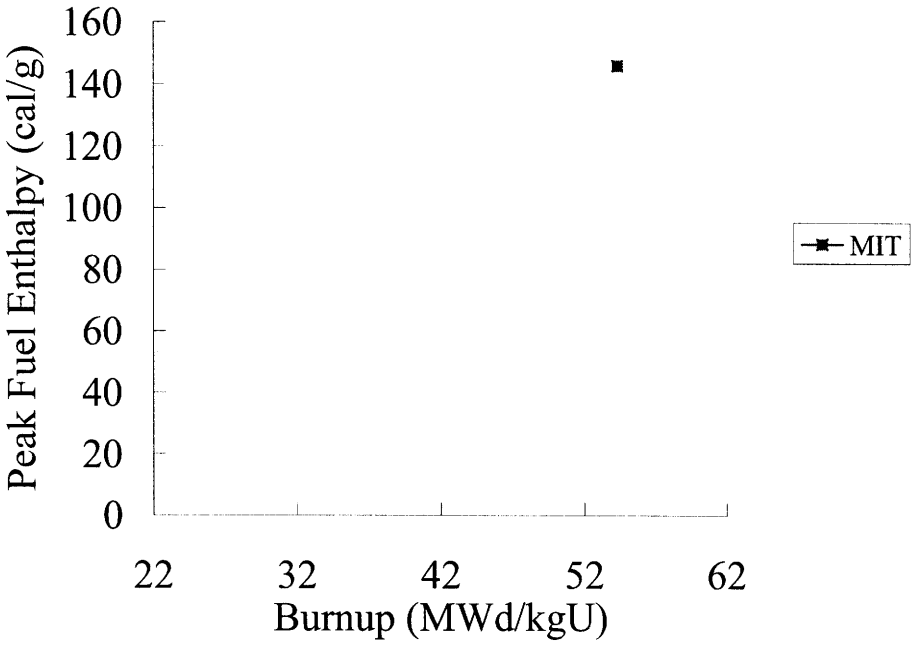

Figure 5-11: Peak fuel enthalpy vs. burnup for BWR failure cases

enthalpy deposit deposit is the same. Failure is predicted by the model for the narrow power pulse case. No failure is predicted by the model for the reference case. For a wider pulse, some amount of heat transferred out to the coolant and the temperature redistribution in the pellet during the power pulse may mitigate the loading force. As can be seen from Figure 5-12 and Figure 5-13, the peak hoop stress is higher for the narrow power pulse case. The stress intensity as a function of hoop stress would decrease for the wider power. As a result, the driving parameter for failure by J-integral increases. Since 20 ms is a conservative estimation of BWR, it is expected that the PCMI loading of BWR CRDA should be even smaller. Also, initial lager gap and smaller creep down of BWR fuel can accommodate some amount of deformation during PCMI. However, the inner bonding of pellet and cladding is not accounted for in the current analysis, which occurs at a burnup about 50 MWd/kg [2]. Both Figure 5-12 and Figure 5-13 show large plastic deformation as DNB has occurred for both cases indicating a possible ductile failure mode, which can't be predicted by the failure model developed particularly for brittle failures.

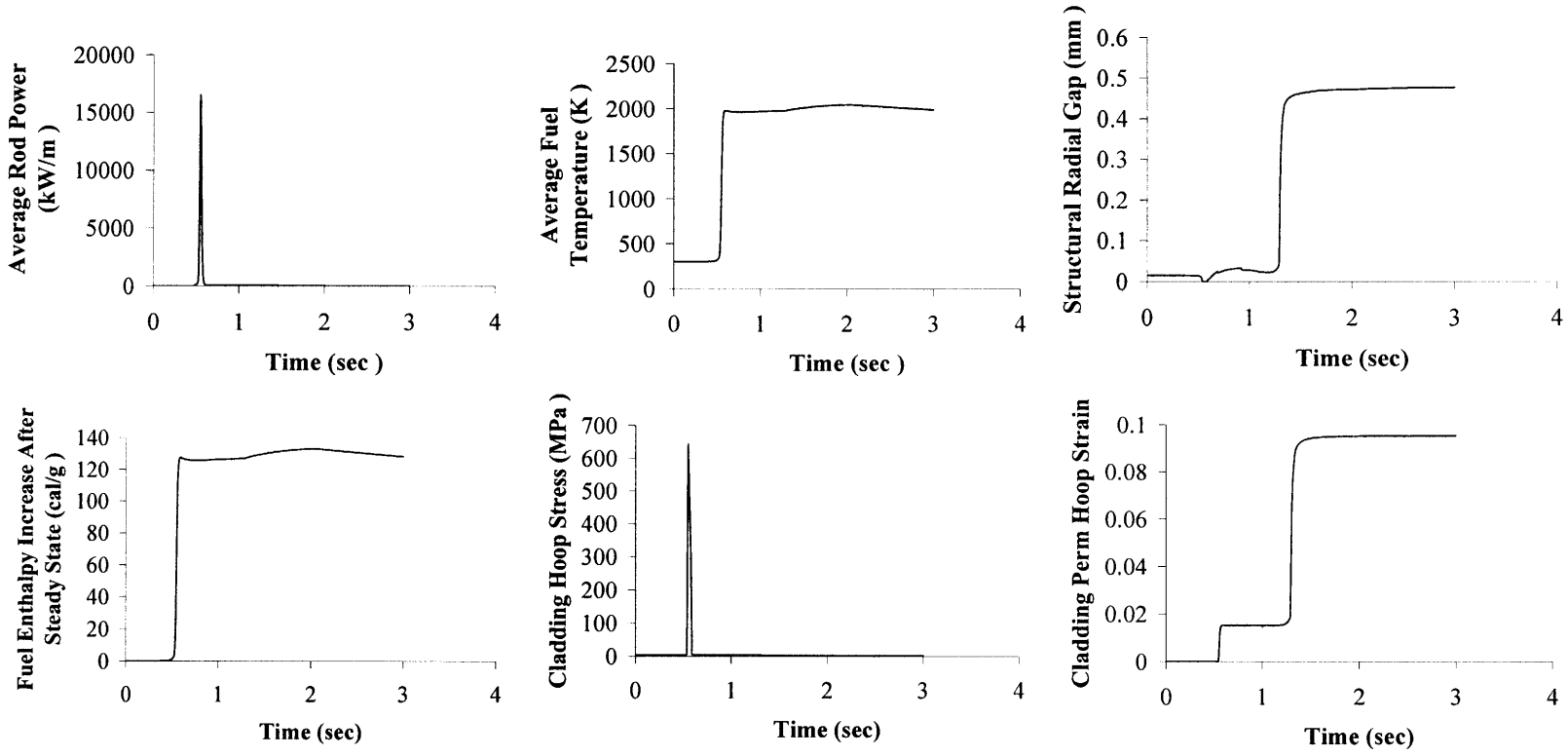

Figure 5-12: RIA transient at burnup 51.8 MWd/kgU with power pulse width of 20 ms

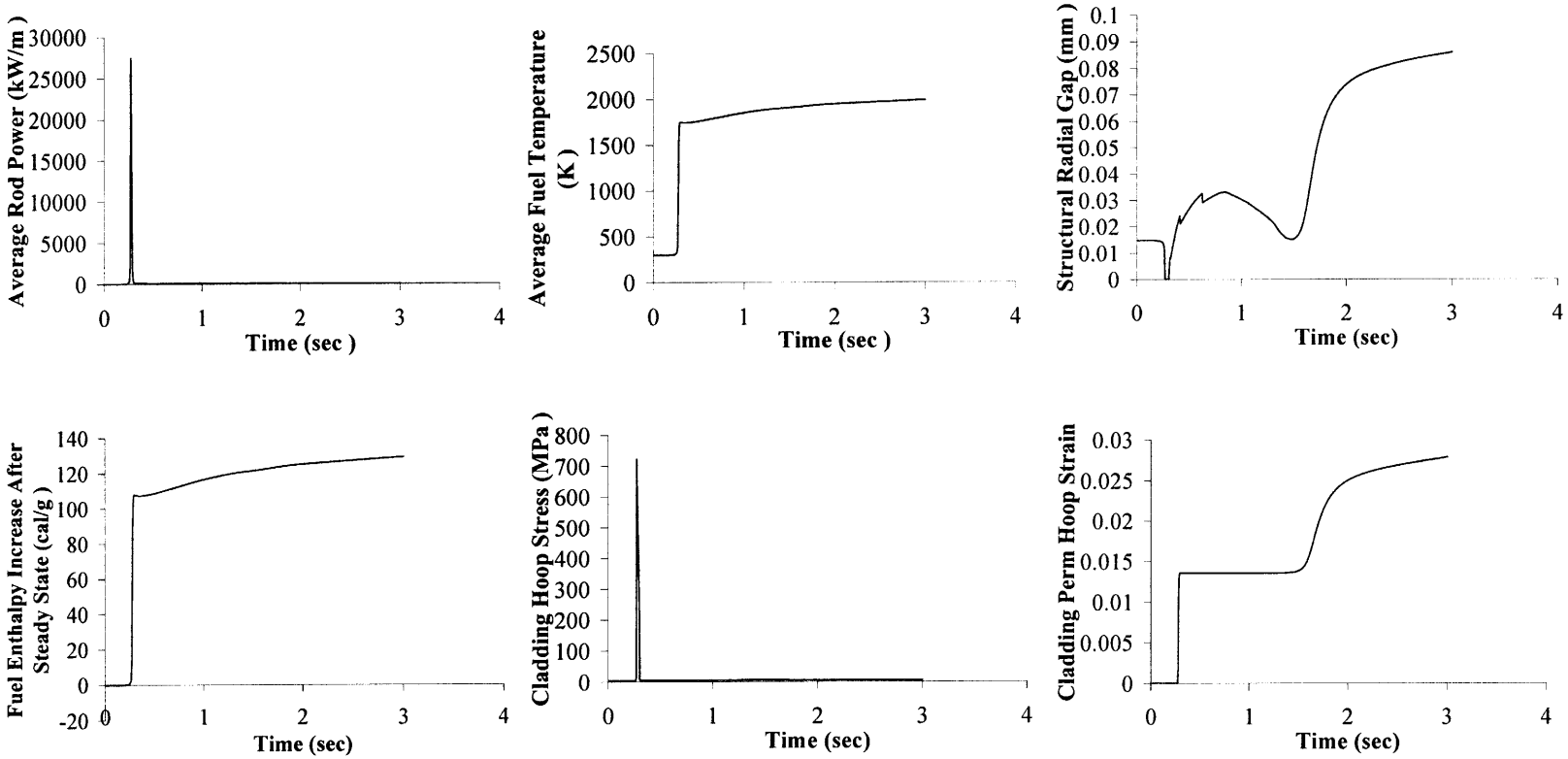

Figure 5-13: RIA transient at burnup 51.8 MWd/kgU with power pulse width of 10 ms

5.4 Summary and conclusions

In this chapter, a typical PWR fuel rod and a BWR fuel rod are simulated to be irradiated up to 56 MWd/kg by the FRAPCON code. Subsequently, the response of the PWR and BWR fuel rods to a Reactivity-Initiated Accident are evaluated using the FRAPTRAN code with models developed in the thesis. The RIA is simulated with various level of enthalpy deposit at each given burnup level. Threshold peak fuel enthalpy vs. burnup is determined by using fracture mechanics model in the thesis. The failure threshold prediction by combining stress and strain shows less safety margin than that predicted by strain-based failure model by PNNL. The computation results reveal effects of power pulse width: a wider pulse width generally increases failure threshold, however this effect is less obvious for highly corroded cladding. Since the ductility change of cladding is closely related to the hydrogen content, which are mechanistically modeled in the paper taking into account of temperature effects and non-uniform distribution of hydride, it would be a better approach to judge the failure than using only oxide layer of the cladding.

Chapter 6

Summary, conclusions and recommendations

6.1 Summary and conclusions

This thesis developed and improved the mechanistic models to address issues pertinent to high burnup fuel during Reactivity Initiated Accident including:

1. Enhanced fission gas release
2. Fission gas induced swelling
3. Embrittlement of cladding with hydrides
4. Cladding oxidation

These models are incorporated into fuel performance code FRAPTRAN and compared to experiments conducted at CABRI, NSRR and BIGR test facilities. These models extend the capability of fuel code to simulate high burnup fuel behavior during transients.

This thesis modeled fission gas release (FGR) and swelling systematically to quantify gaseous loading effects. The grain boundary fission gas inventory is simulated prior to the transient using a diffusion model in FRAPCON 3.3 code. The restruc-

turing of high burnup fuel in rim region is described in terms of porosity, pore size distribution, fission gas concentration, and pore overpressure.

The model assumes the fragmentation of fuel upon the separation of grain boundary or when a threshold temperature is exceeded in the rim region. The fission gas in fragmented fuel is assumed to release instantaneously to the free volume when the fuel expansion and swelling creates sufficient pellet-clad gap. The relaxation of rim pore at rapid temperature increase and the thermal expansion of fission gas in fragmented fuel are considered as additional loads on the cladding besides the contact force due to fuel thermal expansion. An analytical approximation is made to calculate the clad radial displacement subjected to fission gas expansion accounting for the constraint of the cladding on the fission gas which would otherwise be neglected in a rigid pellet model FRACAS-I in the FRAPTRAN code.

In comparison to the measured FGR from CABRI, NSRR and BIGR test facilities, this mechanistic model can reasonably predict fission gas release fraction for most of the test cases covering a burnup range of 26-64 MWd/kgU and enthalpy deposit of 37-200 cal/g. It reveals the effects of burnup and enthalpy deposit on the fission gas release: burnup is an important parameter affecting fission gas inventory and fuel micro-structure evolution during base irradiation; enthalpy deposit is directly connected to the availability of fission gas release via the grain boundary separation by the intergranular bubble over-pressurization. The accuracy to predict the fission gas release is dependent on not only the capability of the fuel code to simulate the fission gas retention and release during the base irradiation but also on the detailed distributions in the fuel micro-structures. Analysis of the fission gas radial profile is made with the aid of the neutronic code MCODE (A code coupling the transport code, MCNP, and isotope generation/depletion code, ORIGEN) to validate the fission gas release from the rim of UO_2 fuel. The analysis indicates fission gas release is partly from the rim region and the majority of fission gas release is from grain boundaries for burnup up to 50 MWd/kgU. Fission gas induced hoop strain is predicted to be less than 0.3% in the early phase of RIA with peak fuel enthalpy less than 145 cal/g. The fission gas induced deformation in the early phase of RIA is not significant as

expected even in the presence of rim structure and large amount of fission gas at grain boundaries for high burnup fuel. Thus, a simple pellet expansion model is still considered as effective in analyzing the PCMI failure of fuel pins. However at high level of enthalpy deposit, when clad yield strength is decreased at escalated temperature due to film boiling, the fission gas either released into the plenum or retained in the fuel pellet might strain more the cladding. This is observed in the large deformation of the cladding in some test cases in NSRR and BIGR due to pressure load.

This thesis selected a new set of heat transfer correlations and implemented them in the FRAPTRAN code to model the cladding-coolant heat transfer of high burnup fuel at room temperature and atmospheric pressure condition. This new set of correlations addressed the effects of subcooling and oxidation on the heat transfer characteristics at pool boiling conditions. They reflect the increase of rewetting temperature and increase of Critical Heat Flux (CHF) due to subcooling. They account for oxidation effects on the transition and film boiling regime and heat conduction through thick oxide as the oxidation is considered as a prominent feature of surface condition change of high burnup fuel. In addition to high burnup fuels tested in NSRR, several fresh fuel tests with different degree of subcooling and a few separate-effects RIA tests are also included to validate the applicability of this set of correlations. For fuel enthalpy up to 190 cal/g and oxidation up to 25 micron, the predicted peak cladding temperature (PCT) and duration of DNB achieves generally good agreement with the experimental data.

The analysis of high burnup fuel heat transfer reveals that the surface oxidation could cause an early rewetting of high burnup fuel or suppression of DNB. Surface oxidation can delay the heat conducting to the surface while keeping the surface heat transfer in the effective nucleate boiling regime. It also raises the minimum stable film boiling temperature by lowering the interface temperature during liquid-solid contact resulting from vapor breaking down. Implementation of the heat transfer models into the fuel performance code provide the basis for predicting cladding temperature of high burnup fuel, thus help to characterize the failure belonging to ductile or brittle

mode.

This thesis modeled Pellet-Cladding Mechanical Interaction (PCMI) failure of irradiated and hydrided cladding based on fracture mechanics. The hydride rim accumulated at outer clad is assumed to cause the crack initiation. The fracture toughness of irradiated and hydrided cladding is fitted with experimental data at different temperature range. The model sets forth a simple criterion for failure associated with crack growth based on the J integral approach. The simplification is that for the thin clad, failure is assumed to occur at the onset of crack tip growth.

In comparison to CABRI and NSRR test results and other failure models, the model shows a good capability to separate the failure cases from non-failure cases. Application of the model shows that, at high burnup (and therefore high hydride levels in the clad), the failure enthalpy is smaller than at low burnup. The pulse width is an important parameter in the burnup up to 50 MWd/kg, but starts to become less important for higher burnup with highly corroded cladding. Since the ductility change of cladding is directly related to the hydrogen content, which are mechanistically modeled in this work taking into account of temperature effects and non-uniform distribution of hydrides, it would be a better approach to judge the failure than using the oxide layer of the cladding , and has been adopted thus far.

6.2 Recommendations for future work

6.2.1 Improvement of models

Extensive work has been done to model the behavior of high burnup fuel during RIA. Models can be improved and need to be updated as more relevant experimental data on high burnup become available and the numerical solution scheme is refined. A list of recommendations on potential improvement is given as follows:

- Prediction of the fission gas inventory

  Fission gas release model depends largely on the fission gas inventory in the base irradiation. Current fission gas release model in steady state focused mainly

on predicting the fraction of fission gas release rather than on the detailed distribution of fission gas. Developing a model that can characterize well the fission gas retained in the fuel as well as fission gas released will be a more challenging task given the current knowledge on fission gas behavior in the irradiated fuel. It is expected that the accuracy of transient fission gas release can be increased should the understanding and experimental technique on the fission gas in irradiated fuel is improved.

- Kinetics of fission gas release

  A simple instantaneous fission gas release is assumed for the fast transient of RIA due to lack of measurement data to validate the kinetics during the transient. When measured data on gas kinetics during transient becomes available, the model can to be updated. The program of separate effects of fission gas release, SILENE, is undergoing to obtain a better quantification of the kinetic aspects of fission gas under RIA transients [35], which may provide some relevant data to update the model.

- Gap conductance of high burnup fuel

  Gap conductance plays a role as important as the clad outer surface heat transfer in affecting the temperature prediction during transient. The influences of inner oxidation of cladding, chemical bonding, fuel fragmentation, and rim structure on the gap conductance are not well understood for high burnup fuel. Information regarding these influences may help to improve the gap conductance model.

- Minimum stable film boiling temperature

  The minimum stable film boiling temperature is a parameter that strongly affect the rewetting of high burnup fuel. Measurement so far were only done on fresh fuel. It is worth to conduct a measurement of this parameter for clad of high burnup fuel with oxidized surface and crud deposition to provide a good foundation for developing post-DNB heat transfer correlations.

6.2.2 Analysis of advanced cladding alloys

Besides the traditional cladding alloy Zry-2 and Zry-4, advanced cladding alloys have also been tested in recent RIA experiments. The test results for those advanced cladding materials are summarized in Table 6.1.

Table 6.1: Summary of test for advanced cladding alloy

Test No.	RepNa-11	CIP0-1	CIP0-2	OI-10	OI-11	OI-12	VA-1
Test Facility	CABRI	CABRI	CABRI	NSRR	NSRR	NSRR	NSRR
Cladding type	M5 [a]	Zirlo [b]	M5	MDA [c]	Zirlo	NDA [d]	MDA
Burnup (MWd/kg)	60	75	77	60	58	61	78
Oxide thickness (μm)	20	80	20	27	28	41	81
Peak fuel enthalpy (cal/g)	92	90	81	104	157	143	127
Pulse width (ms)	30.8	32	28	5.6	4.4	4.4	4.4
Failure	No	No	No	No	Yes	No	Yes

[a]Developed by AREVA
[b]Developed by Westinghouse
[c]Developed by Mitsubishi Heavy Industries, Ltd.
[d]Developed by Nuclear Fuel Industries, Ltd. and Sumitomo Metal Industries, Ltd.

Among those test cases, only two failures were found in the NSRR tests. The failure of test case OI-11 is still under investigation as cracking occurred along a position where thermal couples were welded on the surface of the cladding indicating possible initiation of cracking from welding position [7]. This case has the highest enthalpy deposit among all those irradiated LWR fuel tested in NSRR. The oxide thickness of VA-1 is comparable to those failure cases with traditional cladding alloy indicating the failure is also caused by PCMI. The alloy elements for traditional cladding alloy Zry-4 as well as those advanced cladding alloy are listed in Table 6.2. Improvement of these advanced cladding alloy with respect to the Zry-2 and Zry-4 is mainly the capability of corrosion resistance. For example, Zirlo shows decreased oxide thickness: the average peak oxide of Zirlo is 30% that of conventional Zry-

Table 6.2: Chemical composition for various Zircaloy cladding

Alloy elements	Zry-4	Low tin Zry	E110	MDA	NDA	ZIRLO	M5
Sn (wt. %)	1.2-1.7	1.28-1.31	0.9-1.1	0.8	1.0	0.96-0.98	
Fe (wt. %)	0.18-0.24	0.22-0.23	<500 ppm	0.3	0.27	0.094-0.105	
Cr (wt. %)	0.07-0.13	0.11-0.12	<200 ppm	0.1	0.16	79-83 ppm	
O (ppm)	900-1400	0.125-0.133%	<1000			900-1200	0.11-0.17 %
N (ppm)	<65		<60			22-30	
Nb(wt. %)			1	0.5	0.1	1.02-1.04	0.8-1.2
C (ppm)	150-400		<200			60-80	
Ni(wt. %)					0.01		

4 at BU= 38MWd/kg [94]. The hydrogen pickup fraction for Zirlo was reduced from the 15% derived for Zry-4 to 12.5%. The hydrogen pickup fraction for M5 was reduced from the 15% derived for Zry-4 to 7.5%. These features will greatly reduce the propensity to failure as compared to the conventional alloys. In the future, as mechanical property data for those alloys become available, these test cases can be incorporated into the analysis of RIA.

6.2.3 Other transients of concern

This thesis focuses mainly on the reactivity-initiated accidents scenario. Besides RIA, other types of transients that are particularly important for high burnup fuel are LOCA and power oscillations of BWRs. Safety criteria regarding LOCA and BWR ATWS need to be revised as these criteria are mainly based on fresh fuel with experiments conducted in 1960s and 1970s. For high burnup fuel, the existing oxidation of cladding and enhanced fission gas release might get exacerbated during transients and corresponding safety margin would be reduced. Many recent simulated LOCA experiments in-pile and out-of-pile are undergoing. Coupling of the fuel performance code and single channel thermal hydraulics code has been attempted to model the

heat transfer during LOCA. Power oscillation of BWRs are recently simulated by repeated pulse irradiation tests. They may share some similarities with the RIA test. Models on heat transfer and fission gas release is expected to be applicable to such situation with minor revision.

Appendix A

RIA test data

Table A.1: Parameters of PWR fuel HBO series in NSRR RIA tests

Parameter	Unit	HBO1	HBO2	HBO3	HBO4	HBO5	HBO6	HBO7
Local Burnup (GWd/tU)	MWd/kgU	50.4	50.4	50.4	50.4	44	49	49
Enrichment	%	3.2	3.2	3.2	3.2	3.2	3.2	3.2
Oxide thickness	micron	40-48	30-40	20-25	15-20	35-60	20-30	35-45
Pretest fill gas (He) pressure	MPa	0.1	5	0.1	0.1	0.1	0.1	0.1
Average linear heat rate	W/cm	161	161	161	161	-	152	-
Energy deposition	J/g	390	215	397	279	420	420	420
Peak fuel enthalpy	cal/g	73	37	74	50	80	85	88
Pulse width	ms	4.4	6.9	4.4	5.4	4.4	4.4	4.4
Coolant		stagnant water @ 20 °C, 0.1MPa						
Cladding permanent axial strain	%	-	-	-	-	-	0.05	-
Cladding permanent hoop strain	%	-	0.41	1.5	0.17	-	1.2	2.23
Fission gas release	%	-	17.7	22.7	21.1	-	10	8.5
Xe/Kr		-	10.35	11.75	11.7	-	10.38	10.5
Base irradiation FGR	%	-	-	-	-	-	0.78	-
Failure		Yes	No	No	No	Yes	No	No
Failure enthalpy	cal/g	60	-	-	-	70	-	-
Peak Cladding surface temperature	°C	-	115	400	110	180	150	-

Table A.2: Parameters of PWR fuel OI, MH and GK series in NSRR RIA tests

Parameter	Unit	OI1	OI2	MH1	MH2	MH3	GK1	GK2
Local Burnup	MWd/kgU	39.2	39.2	38.9	38.9	38.9	42	42
Fuel enrichment	%	3.2	3.2	2.6	2.6	2.6	3.4	3.4
Oxide thickness	micron	15	15	4	4	4	10	10
Pretest fill gas (He) pressure	MPa	0.1	0.1	0.1	@ 0.1	4.6	4.7	0.1
Average linear heat rate	W/cm	207	207	198	198	198	201	201
Energy deposit	cal/g	136	139	63	72	87	121	117
Peak fuel enthalpy	cal/g	106	108	47	54	67	93	90
Coolant		water at 20 °C 0.1MPa						
Cladding permanent axial strain	%	-	3.2	-	-	0.36	0.15	-
Cladding permanent hoop strain	%	1.49	4.8	0.02	0.05	1.6	2.23	1.05
Fission gas release	%	-	10.2	3.5	-	4	12.8	7
Base fission gas release	%	-	1	-	-	0.15	0.4	-
Failure		No	No	No	No	No	No	No
Failure enthalpy	cal/g	-	-	-	-	-	-	-
Active length	mm	133	133	121.6	121.6	121.6	121.6	121.6
Peak Cladding surface temperature	°C	450	390	105	100	200	305	300

Table A.3: Parameters of BWR fuel TS series in NSRR RIA tests

Parameter	Unit	TS1	TS2	TS3	TS4	TS5
Local Burnup	MWd/kgU	26.6	26.6	26.6	26.6	26.6
Fuel enrichment	%	2.79	2.79	2.79	2.79	2.79
Oxide thickness	micron	6	6	6	6	6
EOL pressure	MPa	1.1	1.1	1.1	1.1	1.1
Pretest fill gas pressure	MPa	1.1 (77.9% Xe, 11.3%Kr, 10.8%He)	1.1 (77.9% Xe, 11.3%Kr, 10.8%He)	1.1 He	1.1 (77.9% Xe, 11.3%Kr, 10.8%He)	1.1 (72% Xe, 9.3%Kr, 18.7%He)
Average linear heat rate	W/cm	330	330	330	330	330
Energy deposit	cal/g	70	82	109	110	117
Peak fuel enthalpy	cal/g	55	66	88	89	98
Pulse width	ms	5.8	5.2	4.6	4.3	4.8
Coolant		water at 20 °C 0.1MPa				
Peak coolant temperature	°C	40	35	41	42	82
Fuel rod internal pressure increase	MPa	-	0.98	0.95	-	1.5
Peak stack elongation	mm	-	-	0.71	0.71	-
Cladding elongation	mm	-	0.26	0.05	0.51	0.55
Cladding permanent axial strain	%	-	-	-	-	0
Cladding permanent hoop strain	%	0	0.4	0.5	0.4	0
Fission gas release	%	NM	12	10	15	8
Base irradiation FGR	%	19.7	19.7	19.7	19.7	19.7
Failure		No	No	No	No	No
Failure enthalpy	cal/g	-	-	-	-	-
Active length	mm	126	126	126	126	126
Peak cladding surface temperature	°C	110	110	120	150	170

Table A.4: Parameters of BWR fuel FK series in the NSRR RIA tests

Parameter	Unit	FK1	FK2	FK3	FK4	FK5	FK6	FK7	FK8	FK9	FK10	FK12
Local burnup	MWd/kgU	45	45	41	56	56	61	61	61	61	61	61
Maximum oxide thickness	micron	21.5	24.0	25.8	15	15	27	27	27	27	27	27
Maximum hydrogen content	ppm	72	72	72	82	82	220	220	159	159	220	220
Effective diametral gap thickness	micron	190	190	190	85	85	60	60	60	60	60	60
Initial diametral gap thickness	micron	240	240	240	200	200	200	200	200	200	200	200
EOL pressure	MPa	0.42	0.42	0.35	1.2	1.2	1.5	1.5	1.5	1.5	1.5	1.5
Pretest fill gas pressure	MPa	0.3	0.3	0.3	0.5	0.5	0.1	1.5	1.5	1.5	1.4	1.4
Peak linear heat rate	W/cm	228	228	209	350	350	350	350	350	350	350	350
Energy deposit	cal/g	167	95	186	180	100	168	166	90	119	135	118
Peak fuel enthalpy	cal/g	129.52	69.8	144.5	139.5	69.8	130.5	128.6	64.8	89.8	102.4	88.8
Pulse width	ms	4.5	7	4.5	4.3	7.3	4.3	4.3	7.3	5.7	5.2	5.5
Initial coolant temperature @ 0.1 MPa	°C	20	20	20	20	20	20	20	20	20	80	85
Peak cladding surface temperature	°C	350	-	620	625	100	-	96	620	-	-	
Peak stack elongation	%	1.4	0.78	-	3.9	0.45	-	-	-	-	-	-
Cladding axial strain	%	1.1	0.3	0.9	0.8	0.36	-	-	-	-	-	-
Cladding permanent axial strain	%	0.3	0	0.2	0.5	0	-	-	0	-	-	-
Cladding hoop strain	%	-	-	-	-	-	-	-	-	-	0.33	0.37
Cladding permanent hoop strain	%	0.85	0	1.5	1.25	0	¡0.1	¡0.1	¡0.02	-	-	-
Fission gas release	%	8.2	3.1	4.7	15.7	9.6	16.9	17	11.3	16.6	16.1	17.8
Base irradiation FGR	%	1.5	1.5	0.35	12.5	12.5	14.2	14.2	12	12	14	14
Failure		No	No	No	No	No	Yes	Yes	No	Yes	Yes	Yes
Failure enthalpy	cal/g	-	-	-	-	-	70	62		86	80	72

Table A.5: Parameters of PWR fuel in the CABRI RIA tests

Parameter	Unit	RepNa1	RepNa2	RepNa3	RepNa4	RepNa5	RepNa8	RepNa10
Local burnup	MWd/kgU	63.8	33	52.8	62.3	64.3	60	62
Enrichment	%	4.5	6.85	4.5	4.5	4.5	4.5	4.5
Oxide thickness	micron	80	4	40	80	20	130	80
Pretest fill gas pressure at 20 °C	MPa	He@0.1	He@ 0.3	He@ 0.3	He@ 0.3	He@ 0.3	He@ 0.3	He@ 0.3
Energy deposit	cal/g	111	207	122	95	104	103	108
Peak fuel enthalpy	cal/g	114	210	125	88	108	98	98
Pulse width	ms	9.5	9.5	9.5	64	9	75	31
Coolant		flowing sodium @ 280 °C, 0.5MPa						
Peak cladding elongation	mm	-	-	6	4	6.5	-	-
Cladding permanent axial strain	%	-	-	0.8	0.07	0.35	-	-
Cladding permanent hoop strain	%	-	3.5	2	0.4	1.1	-	-
Fission gas release	%	-	5.54	13.7	8.3	15.1	-	-
Base irradiation FGR	-	-	-	1.48	1.84	1.84	-	-
Failure		Yes	No	No	No	No	Yes	Yes
Failure enthalpy	cal/g	30	-	-	-	-	78	81

Table A.6: Parameters of VVER fuel in the BIGR RIA tests

Parameter	Unit	RT1	RT2	RT3	RT4	RT5	RT6	RT7	RT8	RT9	RT10	RT11	RT12
Local burnup	MWd/kgU	48.3	48	47.5	60.1	48.6	47.8	60.5	60	59.8	46.9	47.2	47.3
Enrichment	%	4.4	4.4	4.4	4.37	4.4	4.4	3.6	4.37	4.37	4.4	4.4	4.4
Oxide thickness	micron	4	4	4	4	4	4	4	4	4	4	4	4
Hydrogen content	ppm	50	50	50	70	50	50	-	70	70	50	50	50
EOL pressure	MPa	1.26	1.26	1.26	1.26	1.26	1.26	1.08	1.26	1.26	1.26	1.26	1.26
Pretest fill gas (He)pressure at 20 °C	MPa	2.1	2.1	2.1	2.1	2.1	2.1	2	2	0.1	2	2	0.1
Energy deposit	cal/g	174	143	168	152	178	187	165	202	201	207	237	198
Peak fuel enthalpy	cal/g	142	115	138	125	146	153	134	164	165	164	188	155
Pulse width	ms	2.6	2.6	2.6	2.6	2.6	2.6	2.6	2.6	2.6	2.6	2.6	2.6
Initial coolant temperature @ 0.1 MPa	°C	20	20	20	20	20	20	20	20	20	20	20	20
Maximum cladding permanent hoop strain	%	4.07	0.85	3.4	5.5	4.2	6.0	3.5	11.1	9.6	18.9	8.31	5.78
Average cladding permanent hoop strain	%	2.2	0.63	2.0	3.7	2.7	3.2	2.07	6.08	6.27	8.94	5.45	4.35
Fission gas release	%	22.8	16.1	21.3	-	26	26.5	26.8	-	-	-	-	22.7
Base irradiation FGR	%	2.85	2.85	2.85	2.82	4.46	2.41	1.15	2.82	2.82	2.08	2.08	2.08
Failure		No	No	No	No	No	No	No	No	Yes	Yes	Yes	Yes
Fuel stack length	mm	153	151	45	155	153	142	153.1	150	149	152	152	152.6
Clad outer diameter	mm	9.06	9.06	9.06	9.08	9.06	9.07	9.062	9.09	9.07	9.072	9.08	9.066
Central hole diameter	mm	2.46	2.46	2.46	1.65	2.5	2.5	1.65	1.65	1.65	2.5	2.5	2.5
Free gas volume	cm^3	6.13	6.12	6.08	5.54	6.07	6.03	5.75	5.93	5.88	6.1	6.23	6.11
Average clad thickness	mm	0.72	0.72	0.72	0.73	0.69	0.7	-	0.73	0.73	0.69	0.69	0.69
Fuel outer diameter	mm	7.57	7.57	7.57	7.61	7.66	7.62	7.68	7.61	7.61	7.66	7.66	7.66
Fuel inner diameter	mm	2.46	2.46	2.46	1.7	2.5	2.5	1.65	1.7	1.7	2.5	2.5	2.5
Radial gap thickness	micron	25	25	25	0	17	32	3	3	1	23	18	12
Rim size	micron	60	60	60	175	60	60	-	175	175	60	60	60

Appendix B

Computer codes

B.1 Subroutine for FGR and swelling

```
*deck gastore
      subroutine gastore(buradv, bufrad, nbuq,
     &  nring, naxn, dvoid, dfs, FuelRodLength,
     &  IBuprf, prodgas)

      implicit real (a-h, o-z)

      include 'FgRlsSwl.h'
      include 'FgRlsSwli.h'

      dimension    buradv(51, 25), bufrad(51, 25),
     &  tradv(51, 25), tfrad(51, 25),
     &  gpradv(25, 51), gprad(25, 51), gbradv(25,51), gbrad(25,51),
     &  ggradv(25, 51), ggrad(25, 51), bnradv(25,51), bnrad(25,51),
     &    gfcradv(25,51), gfcrad(25,51)

      dimension    poregas(50), Rimsize(50),
     &         buk(50), bukr(50), brn(50),
```

```
&          tempk(50), tempkr(50), trn(50), trnhot(50),
&       gbk(50), gbkr(50), gbrn(50),                          20
&          ggk(50), ggkr(50), ggrn(50),
&          gpk(50), gpkr(50), gprn(50),
&          bnk(50), bnkr(50), bnrn(50),
&          gfck(50), gfckr(50), gfcrn(50)

      data trn /50*0.0d0/, brn /50*0.0d0/, poregas /50*0.0d0/,
&          poroavg /50*0.0d0/, porepresscoef/50*0.0d0/,
&          trnhot/50*0.0d0/,
&          gbk /50*0.0d0/, gbkr/50*0.0d0/, gbrn/50*0.0d0/,
&          ggk /50*0.0d0/, ggkr/50*0.0d0/, ggrn/50*0.0d0/,    30
&          gpk /50*0.0d0/, gpkr/50*0.0d0/, gprn/50*0.0d0/,
&          bnk /50*0.0d0/, bnkr/50*0.0d0/, bnrn/50*0.0d0/,
&          gfck /50*0.0d0/, gfckr/50*0.0d0/, gfcrn/50*0.0d0/

c     Gpore          fission gas  in pores   (mol)
c                    the rim size is so small that the pore gas is assumed
c                    to be uniformly distributed in the rim zone
c                    with the same temperature and porosity
c     Gbubble        fission gas in grain boundary bubbles (mol)
c     Buavg          average burnup (MWd/kg)                    40
c     burim          the burnup in rim zone
c     buradv         radial burnup values
c     bufrad         fuel radius for radial burnup values
c     nbuq           number of radial bu pairs
c     tradv          radial temperature values
c     tfrad          fuel radis for raidal temperature values
c     ntempq         nubmer of radial temperature pairs
c     nring          number of rings
```

```
c       naxn            number of axial node
c       dvoid           pellet inner diameter                                   50
c       dfs                     pellet outer diameter
c       FuelRodLength
c                               length of fuel rod      (m)
c       IBuprf          = 1 if Burn up profile availabe
c                               = 0 otherwise
c       poroavg
c                               average porosity in the rim zone
c
c       brn                     ring specific burnup values
c       trn                     ring specific temperature values                60
c       buk                     raidial burnup at aixal region k
c       tempk           raidial temperature at axial region k
c       rpore           radius of pore in rim zone (m)
c       esurface        surface tension energy of bubble and pore(J/m^2)
c       fna                     Avogadro constant
c       fkb                     Boltzmann constant
c       B                       van der waals constant for xenon atom
c       d2, d3          pore size distribution parameter
c                               assume it's a log-normal distribution
c                               d2 = log(rpore_median), d3 = variance           70
c                               rpore (m)
c       rporemin        minimum pore radius (m)
c       rporemax        maximum pore radius (m)
```

esurface = 0.6

pi = 3.14159

d2 = −14.27

d3 = 0.1457

```
      rporemin = 0.25e-6
      rporemax = 2.0e-6                                                  80
c     avg pore size
      avp = (4.*pi/3.)* 2.0 * sqrt(d3) * exp(3*d2 + 4.5*d3)* sqrt(pi/2)
      rpore0 = (avp*3.0/ (4.0*pi) )** 0.333
c     threshold bu for xe depletion
      bu0 = 52.0

c     Start - ring volume calculation
      fmxrim = 0.1
      nring1 = nring/3
      nDiv = nring1                                                      90
      nring2 = nring - nring1
      fnreg1 = float(nring1)
      fnreg2 = float(nring2)
      ansda1 = dfs*dfs*(1 - 0.9*0.9)/4./fnreg1
      ansda2 = (dfs*dfs*0.81 - dvoid*dvoid)/4./fnreg2
      routr = dfs/2
      do 10 i1 = 1, nring1
      routr2 = routr*routr
      ansr(i1) = sqrt(routr2 - ansda1/2.)
      FineRadialBound(i1) = routr                                        100
      ansdia = ansr(i1)*2
      if(i1.eq.nring1) go to 10
      routr = sqrt(routr2 - ansda1)
10    continue

      routr = (1.0 - fmxrim)*dfs/2
      do 11 i1 = nring1+1, nring
      routr2 = routr*routr
```

```
      ansr(i1) = sqrt(routr2 - ansda2/2.)
      FineRadialBound(i1) = routr                                    110
      ansdia = ansr(i1)*2
      if(i1.eq.nring) go to 11
      routr = sqrt(routr2 - ansda2)
11    continue
c     End - ring volume calculation

c     Start - rim size calculation
      do 61 k = 1, naxn
      if(rsize(k) .eq. 0.0) rsize(k) = RimsizeFit(Buavg(k), 1)
c     determine the ring index for the rim region                    120
      nrimidx(k) = 0
      rrsize = dfs/2. - rsize(k)
      do 60 j3 = 1, nring1
      if( (rrsize .gt. ansr(j3+1)) .AND. (rrsize .le. ansr(j3)) ) then
      nrimidx(k) = j3
      if ( (ansr(j3+1) - rrsize).le.(rrsize - ansr(j3)) )
     &  nrimidx(k) = j3+1
      go to 62
      endif
60    continue                                                       130
62    continue

      call    PorosityFit(ansr, nrimidx(k), dfs, Buavg(k), porok)
      poroavg(k) = porok
61    continue
c     End - rim size calculation

      deltHeight = FuelRodLength/float(naxn);
```

```
      deltV1 = deltHeight * ansda1 *pi
      deltV2 = deltHeight * ansda2 *pi                                  140
      V0 = deltHeight*pi*(dfs*dfs - dvoid*dvoid)/4.0

      ntempq = itempq /2/naxn
      ngp    = igp/2/naxn
      ngg    = igg/2/naxn
      ngb    = igb/2/naxn
      ngbn = igbn/2/naxn
      ngfc  = igbfc/2/naxn

      icnt = 1                                                          150
      do 15 k=1, naxn
            do 15 j=1, ntempq
c     radial temperature values
            tradv(k,j) = Tempeol(icnt)
c     fuel radius for raidal temperature values
            tfrad(k,j) = Tempeol(icnt+1)
            icnt = icnt +2
15    continue

      icnt = 1                                                          160
      do 16 k=1, naxn
            do 16 j=1, ngb
            gbradv(k,j) = gb(icnt)
            gbrad(k,j) = gb(icnt+1)
            icnt = icnt + 2
16    continue

      icnt = 1
```

```
      do 17 k=1, naxn
            do 17 j=1, ngg                                          170
            ggradv(k,j) = gg(icnt)
            ggrad(k,j) = gg(icnt+1)
            icnt = icnt + 2
17    continue

      icnt = 1
      do 18 k=1, naxn
            do 18 j=1, ngp
            gpradv(k,j) = gp(icnt)
            gprad(k,j) = gp(icnt+1)                                 180
            icnt = icnt + 2
18    continue

      icnt = 1
      do 19 k=1, naxn
            do 19 j=1,ngbn
            bnradv(k,j) = bbnumden(icnt)
         bnrad(k,j) = bbnumden(icnt+1)
      icnt = icnt +2
19    continue                                                      190

      icnt = 1
      do 21 k=1, naxn
            do 21 j=1,ngfc
            gfcradv(k,j) = gbfc(icnt)
         gfcrad(k,j) = gbfc(icnt+1)
      icnt = icnt +2
21    continue
```

```
c       Iteration for each axial region                                  200
        do 20 k = 1, naxn
        do 30 j1 = 1, nbuq
        buk(j1) =       buradv(k, j1)
        bukr(j1) = bufrad(j1, k)
30      continue

        do 32 j1 = 1, ntempq
        tempk(j1) = tradv(k, j1)
        tempkr(j1) = tfrad(k, j1)
32      continue                                                         210

        do 33 j1 = 1, ngb
        gbk(j1) = gbradv(k,j1)
        gbkr(j1) = gbrad(k,j1)
33      continue

        do 34 j1 = 1, ngg
        ggk(j1) = ggradv(k,j1)
        ggkr(j1) = ggrad(k,j1)
34      continue                                                         220

        do 35 j1 = 1, ngp
        gpk(j1) = gpradv(k,j1)
        gpkr(j1) = gprad(k,j1)
35      continue

        do 36 j1 = 1,ngbn
        bnk(j1) = bnradv(k,j1)
```

```
      bnkr(j1) = bnrad(k,j1)
36    continue                                                    230
      do 37 j1 = 1,ngfc
      gfck(j1) = gfcradv(k,j1)
      gfckr(j1) = gfcrad(k,j1)
37    continue

      do 50 j2 = 1, nring
      if(nbuq .gt. 0) brn(j2) = terp(ansr(j2), bukr, buk, nbuq)/1000.0
      if(ntempq .gt. 0) then
      trnhot(j2) = terp(ansr(j2), tempkr, tempk, ntempq)
      end if                                                      240

      trn(j2) = 290.0
      if(ngb .gt. 0)  gbrn(j2) = terp(ansr(j2), gbkr, gbk, ngb)
      if(ngg .gt. 0)  ggrn(j2) = terp(ansr(j2), ggkr, ggk, ngg)
      if(ngp .gt. 0)  gprn(j2) = terp(ansr(j2), gpkr, gpk, ngp)
      if(ngbn .gt. 0) bnrn(j2) = terp(ansr(j2), bnkr, bnk, ngbn)
      if(ngfc .gt. 0) gfcrn(j2) = terp(ansr(j2), gfckr, gfck, ngfc)

50    continue
                                                                  250

c     If no burnup profile is defined,
c     using rim average burnup instead
      if (IBuprf .eq. 0) then
      do 51 j2 = 1, nrimidx(k)
      brn(j2) = Buavg(k)*1.33
51    continue
      do 52 j2 = nrimidx(k)+1, nring
```

```
      brn(j2) =
     & (Buavg(k) - Buavg(k)*1.33* fmxrim*                                  260
     & float(nrimidx(k))/float(nring1) ) / (1.0 - fmxrim)

52    continue
      end if

c     calculate gas storage in each ring at axial node k
      Gfmax = 0.0d0
      do 70 j2 = 1, nring
c     theta = 0.8727
c     Fcover = 0.6;                                                         270
c     Ftheta = (1 - 3*cos(theta)/2 + (cos(theta))^3/2)/(sin(theta))^2 * Fcover;
      Ftheta = 0.1724
      deltV = deltV1

      if( j2 .gt. nring1) deltV = deltV2
      Gbubble(k, j2) = deltV * gbrn(j2)
      Ggrain(k, j2) = deltV * ggrn(j2)
      Gproduct(k,j2) = deltV * gprn(j2)
      Gnumden(k,j2) = bnrn(j2)
      Gfc(k,j2) = gfcrn(j2)                                                 280
      if(Gfc(k,j2) .gt. Gfmax) Gfmax = Gfc(k,j2)

70    continue

      do 90 j2=1, nring
      Gfc(k,j2) = Gfc(k,j2) / Gfmax
90    continue
```

```
c       calculate pore gas storage
        if(nrimidx(k) .eq. 0) go to 20                                    290
        call PoreGasConcentration(bu0,brn,poroavg(k),nrimidx(k),poregas)
        do 80 j2 = 1, nrimidx(k)
c       if negative pore gas is found, the rim size is forced to be zero
        if(poregas(j2) .lt. 0.0) nrimidx(k) = 0
        if(poregas(j2) .lt. 0.0) rsize(k) = 0.0
        Gpore(k, j2) = poregas(j2) * deltV1
        rporeold(j2, k) = rpore0
80      continue

c       pore excess pressure                                              300
        call Porepressure(poregas, poroavg(k), nrimidx(k),
     & pcoef, d2, d3)

        porepresscoef(k) = pcoef
20      continue
        if(Iprint .eq. 1) then
c       Total gas storage
        TotalBubbleGas = 0.0d0
        TotalPoreGas = 0.0d0
        Totalprogas = 0.0d0                                               310
        TotalGraingas = 0.0d0

        do 8000 igas = 1, naxn
              do 8000 jgas = 1, nring
                    TotalBubbleGas = TotalBubbleGas + Gbubble(igas, jgas)
                    TotalPoreGas = TotalPoreGas + Gpore(igas, jgas)
                    Totalprogas    = Totalprogas + Gproduct(igas, jgas)
                    Ggrain(igas, jgas) = Ggrain(igas, jgas) - Gpore(igas,jgas)
```

```
                    TotalGraingas = TotalGrainGas + Ggrain(igas, jgas)
                                                                        320
8000   continue
       write(30, '                                          ')
       write(30, 8001) Totalprogas
8001 format('Total gas production  ', 12X, E15.8, ' (mole)')
       write(30, 8002) TotalBubbleGas
8002 format('Total gas in grain boundary ', 12X, E15.8, ' (mole)')
       write(30, 8003) TotalPoreGas
8003 format('Total gas in rim pores ', 12X, E15.8, ' (mole)')
       write(30, 8004) TotalGraingas
8004   format('Total gas in grains    ', 12X, E15.8, ' (mole)')          330

       write(30, 8005) TotalBubbleGas *100.0 / Totalprogas
8005   format('Grain boundary gas fraction ', 12X, E15.8, ' %')
       write(30, 8006) TotalPoreGas *100.0 / Totalprogas
8006   format('Rim pore gas fraction ', 12X, E15.8, ' %')
       write(30, 8007) TotalGraingas *100.0/ Totalprogas
8007   format('Grain gas fraction     ', 12X, E15.8, ' %')

       do 8050 igas = 1, naxn
       write(30, 8051) igas, rsize(igas), dfs/2.0, 1.0-rsize(igas)*2/dfs   340
8051 format('Axial node=', i5, 2x, 'rim =', e10.4, 2x,
     &    'radius=', e10.4, 2x, 'radius(div)=', e10.4)
8050   continue
       write(30,*)'Fission gas distribution at start time'
       do 8100 igas = 1, naxn
              do 8100 jgas = 1, nring
                 deltV = deltV1
                    if (jgas .gt. nring1) deltV = deltV2
```

```
                write(30, 9001) igas, ansr(jgas),
     &      Gbubble(igas, jgas)/deltV, Gpore(igas, jgas)/deltV,
     &      Ggrain(igas, jgas)/deltV,
     &          Gproduct(igas, jgas)/deltV

9001  format(2x, 'axial node=', i5, 2x, 'r =', e10.4, '(m)' 2x,
     &   'Gbubble=', e10.4, 2x,
     &   'Gpore=', e10.4, 2x,
     &   'Ggrain=', e10.4, 2x,
     & 'Gproduct=', e10.4)

8100  continue
      end if
      return
      end
c*********************************************************
c     function RimsizeFit(buavg, mtype)
c
c     Fitting the rim size at given average burnup (buavg)
c     and burnup in rim zone (bus)
c
c     buravg  MWd/kg
c     mtype   model type
c
c     RimsizeFit              m
c*********************************************************
      function RimsizeFit(buavg, mtype)

      implicit real (a-h, o-z)
      ffit = 1.0
```

```
      burim = 1.33*buavg*ffit
                                                                      380
      if(mtype .eq. 0) then
            RimsizeFit =(5.28*burim - 178)*1.0e-6
      else
            RimsizeFit = (3.55*burim - 185)*1.0e-6
      end if
      end

c*****************************************************************
c     subroutine     PorosityFit(ansr, nring, dfs, buavg, flocalporo)
c                                                                     390
c     calculate the porosity at the relative pellet radius
c     and the given avg. burnup
c
c     ansr,          radius
c     nring,         ring number
c     dfs,           pellet outer diameter
c     buavg,         average burnup
c     poroavg,       average porosity in rim region
c*****************************************************************
                                                                      400
      subroutine   PorosityFit(ansr, nring, dfs, buavg, poroavg)

      implicit real (a-h, o-z)
      dimension    ansr(50), flocalporo(50)

      p1 = 0.001144
      p2 = -0.02287
      p3 = 1.05
```

```
      p4 = -100.6
      p5 = -1.057                                                    410
      p6 = 99.01
      a = p1 *buavg + p2
      b = p3 *buavg + p4
      c = p5 *buavg + p6

      poroavg = 0
      if(nring .le. 0.0d0) go to 110
      do 100 i=1, nring

      flocalporo(i) = a + exp(b + c*ansr(i)*2.0d0/dfs)                420
      poroavg = poroavg + flocalporo(i)
100   continue
      poroavg = poroavg / float(nring)
110   continue

      end
c*****************************************************************
c     subroutine PoreGasConcentration(brn, poroavg, nring, poregas)
c
c     brn,          ring specific burnup (MWd/kg)                    430
c     nring,        ring number
c     poroavg,      average porosity
c     poregas,      pore gas concentration (mole /m^3 fuel), return value
c
c     bu0,          burnup threshold (MWd/kg)
c     fdensity,     fuel theoretical density (g/cm^3)
c*****************************************************************
```

```
      subroutine PoreGasConcentration(bu0, brn, poroavg, nring, poregas)
                                                                      440
      implicit real (a-h, o-z)
      dimension    brn(50), poregas(50)

c     theoretical density of UO2 g/m^3
      fdensity = 10.96e6
      fmxe = 134.
      a = 0.0584
      c = 1.46e-2

      do 200 i=1, nring                                               450
      poregas(i) = c*brn(i) -
     & c * (1/a + (bu0 -1/a)*exp(-a*(brn(i)-bu0)) )
      poregas(i) = poregas(i)*0.01 * fdensity /fmxe
200   continue

      end
c*****************************************************************
c     subroutine Porepressure(poregas, poroavg, trn, nring, porepresscoef
c                             d1, d2, d3)
c                                                                     460
c     poregas,        poregas concentration (mol/m^3)
c     poroavg,        average porosity in rim region
c     nring,          ring number
c     porepresscoef (return value J/m^2)
c                             pore pressure coefficient,
c                             pore press = press0 + coeff/rp
c     d1,d2,d3        pore size distribution parameter
c
```

```
c
c*****************************************************************  470

      subroutine 0Porepressure(poregas, poroavg, nring,
     &                porepresscoef, d2, d3)

      implicit real (a-h, o-z)
      dimension    poregas(50)

      fna = 6.02e23
      fkb = 1.38e-23
      B = 8.5e-29                                                    480
      pi = 3.14159
      rpv = 0.74e-6
      Trim   = 800.0

      avp = (4.*pi/3.)* 2.0 * sqrt(d3) * exp(3*d2 + 4.5*d3)* sqrt(pi/2)
      d1 = poroavg / (avp * sqrt(2.*pi*d3))
      F = d1*(4.*pi/3.)* 2.0 * sqrt(d3) * exp(2.*d2 + 2.*d3) *sqrt(pi/2)
      porepresscoef = 0.0

      do 300 i=1, nring                                              490
      phi = poregas(i) * fna * fkb * Trim /F
      porepresscoef = porepresscoef +
     &        phi /( 1. - B* phi/(rpv *fkb * Trim ))

300   continue
      porepresscoef = porepresscoef / float(nring)
      end
*deck  GBSwelling
```

```
      subroutine    GBSwelling(Fueltemp,
     &  TimeIncrement, FGSwl, nring, naxn, igpnod, ncladi,
     & nmesh, Igapclose, Irls)

      implicit real (a-h, o-z)

      include 'FgRlsSwl.h'
      include 'FgRlsSwli.h'
      include 'dyna.h'
      include 'FissionGasRelease.h'
      include 'Oxidation.h'
      include 'Debug.h'

      dimension     Fueltemp(51, 25), FGSwl(51), Ph(51),
     &              Igapclose(26), Irls(26), ev(51,50), epswellpore(51)

      data          fR /8.31/, B /8.5e-29/, pi /3.14159265/,
     &              ftom /0.3048d0/, fna /6.02e23/, fkb/1.38e-23/
      data          eVcrit/0.3/, TempCrack1 /1600/
     data           ffitswl/1.0/
c     Input variables
c     Fueltemp  is to be got from the calculation in FRAPTRAN
c     Gpore         pore gas quantity       (mol)
c     Ph                    Hydrostatic pressure (Pa)
c     Igapclose     1 for closed gap, 0 for open gap
c     Irls          1 for gas released, 0 for no release
c     Time          current time
c     naxn          number of axial node
c     igpod         radial index for pellet surface
c     ncladi        radial index for inner surface of cladding
```

```
c       nmesh          radial index for outer surface of cladding
                                                                      530
c       Output variables
c       FGSwl          Fission gas induced swelling factor

        ndebug = 0
      if(Time .ge. DebugTime .and. Time .le. DebugTimeStop) ndebug = 1
        do 10 k=1, naxn
              Ph(k) = (TerfacePres(k) + Gaspress(k))*6894.757

c       rim region
c       pore relaxation model is tripped on by IPoreSwl = 1             540
              do 11 j=1, nrimidx(k)
              deltV = deltV1
              if(Fueltemp(j,k) .ge. TempCrack ) then
                    IsFreeGas(k,j) = 1
              end if
              dVp = 0.0d0
              epswellpore(k) = 0.0d0
              if(IPoreSwl.eq.1) then
                    call PoreSwelling(Fueltemp, k, Ph(k), dVp)
                    epswellpore(k) = dVp / ( deltV * poroavg(k))/3.0d0  550
              end if

11            continue

c       calculate  volume of intergranular bubbles

              do 12 j=nrimidx(k)+1, nring
```

```
            deltV = deltV1
            if (j .gt. nDiv) deltV = deltV2                                  560

          gasbubble = Gnumden(k,j)

            tempk = Fueltemp(j,k)
            IIntergasSwl = 0
c       bypass  the bubble expansion model
            if ( IIntergasSwl .eq. 1) then
c                   calculate bubble radius
                    call bubbleradius(gasbubble, tempk, Ph(k), rb)
                    rbubble0(k,j) = rb                                       570
                    Teff    = tempk + B *(2*esurface/rb) /fkb
     VGBGasNew(k,j)= fR*Gbubble(k, j)* Teff
     &              /(Ph(k) + 2*0.6/rb)

                    if(Time.eq. 0) VGBGasOld(k,j) = VGBGasNew(k,j)

                    ev(k,j) = ( VGBGasNew(k,j) - VGBGasOld(k,j) )
     &        / ( deltV + VGBGasOld(k,j))
                    if(ev(k,j) .ge. eVcrit) then
                        IsFreeGas(k,j) = 1                                   580
                    endif
            else
                    if(Time .eq. 0) then
                        call bubbleradius(gasbubble, tempk, Ph(k), rb)
                        rbubble0(k,j) = rb
                        Teff    = tempk + B *(2*esurface/rb) /fkb
                        VGBGasOld(k,j)= fR*Gbubble(k, j)* Teff
     &                  /(Ph(k) + 2*0.6/rb)
```

```
                endif
c               grain boundary cracking model                          590
                fc = Gfc(k,j)
                call gbcracking(gasbubble, tempk, Ph(k),
     &          fstress, Ftheta, esurface, fc, rbubblec,
     &          Ph_low, fcmultifactor, icrack)

                if( icrack .eq. 1) then
                    IsFreeGas(k,j) = icrack
                VGBGasNew(k,j)= fR*Gbubble(k, j)* Fueltemp(j,k)/Ph(k)
     &                          + Gbubble(k,j) * B * fna
                                                                       600
                endif
                end if
12              continue

      if(IPoreSwl.eq.1) then
                FGSwl(k) =
     &(rsize(k)*epswellpore(k) + FineRadialBound(1))/FineRadialBound(1)
      else
                FGSwl(k) = 1.0
      endif                                                            610

c     Bypass the swelling if IFGR .ne. 2
      if(IFGR .ne. 2) goto 10
c     open gap, bypass the swelling
      if(GapIndex(k) .eq. 0) goto 10
      if(Time.eq. 0) goto 10
      VGBGasNewc = 0.0
      VGBGasOldc = 0.0
```

```
      gpr              = 0.0
                                                                    620
      do 20 j=1, nrimidx(k)
      if (IsFreeGas(k,j) .ne. 1) go to 20
            VGBGasNewc = VGBGasNewc +
     &      (fR * Gpore(k, j)* Fueltemp(j,k)) / Ph(k)
            VGBGasOldc = VGBGasOldc + poroavg(k)* deltV1
            gpr = gpr + fR*Gpore(k, j)*Fueltemp(j,k)

20    continue

      gpri = 0.0d0                                                  630
      VGBGasNewi = 0.0d0
      VGBGasOldi = 0.0d0
      gvi  = 0.0d0

      do 22 j=nrimidx(k)+1, nring
            if (IsFreeGas(k,j) .ne. 1) goto 22
            VGBGasNewi = VGBGasNewi + VGBGasNew(k,j)
            VGBGasOldi = VGBGasOldi + VGBGasOld(k,j)
            gpri = gpri + fR*Gbubble(k, j)*Fueltemp(j,k)
            gvi      = gvi + Gbubble(k,j) * B * fna               640

22    continue
      gpr = gpr + gpri

40    continue

      Pext = CoolPress(k)*6894.757
      rf0      = RadialBound(igpnod)*ftom
```

```
      ri0 = RadialBound(ncladi)*ftom
      hRod = AxialNodLen(k)*ftom                                        650

      rm0 = (RadialBound(ncladi)+RadialBound(nmesh))*ftom/2.0d0
      cthk0 = (RadialBound(nmesh) - RadialBound(ncladi))*ftom
      sigz     = CldStress(k, 2)*6894.757
      sigtheta = CldStress(k, 1)*6894.757

      tcf = CladAveTemp(k)
      tck = tfk(CladAveTemp(k))

c     e: elastic modulus of cladding in Pa                              660
      e = celmod (tck, EffFastFluStrenCoef(k),
     &          EffColdWkStrenCoef(k) ,OxygenConcenAve(k), CladType)

c     v:      Poission's ratio
      v = (celmod (tck, EffFastFluStrenCoef(k),
     &    EffColdWkStrenCoef(k), OxygenConcenAve(k), CladType)
     &    /(2.d0 * cshear(tck, EffFastFluStrenCoef(k),
     &    EffColdWkStrenCoef(k), OxygenConcenAve(k), CladType)))- 1.0d0

      sm    = (sigtheta + sigz)/3.0d0                                   670
      stheta = sigtheta - sm
      sz     = sigz - sm
      sr         = -sm
      cldeffstress = sqrt(0.5d0 * ((sigtheta - sigz)**2 + (sigz
     &                  -0.0d0)**2 + (0.0d0 - sigtheta)**2))

      edot1 = FuelSrfStrRat(k)
      edot2 = EDotFZ(k)
```

```
 edot3 = - edot1 - edot2
   depp1 = edot1 * TimeIncrement                                        680
 depp2 = edot2 * TimeIncrement
 depp3 = edot3 * TimeIncrement
 depnew = 0.4714d0 * sqrt((depp1 - depp2)**2 + (depp2 - depp3)**2
&         + (depp3 - depp1)**2)
 edot1 = depnew/TimeIncrement
   edot2 = 0.0d0
   edot3 = 0.0d0

 zero = 0.0
   cep = EffStrain(k)                                                   690

   call stress (olsigf, cep, zero, tcf, edot1,
&              edot2, edot3, WorkSpaceTCMx(k),
&              coldw, k, CladType)

 deldep = 0.0001d0
 call stress (dsigf, cep, deldep, tcf, edot1,
&              edot2, edot3, WorkSpaceTCMx(k),
&              coldw, k, CladType)
                                                                      700
   slope = (dsigf - olsigf)/deldep * 6894.757

   pslope = (1/e + cthk0*v/2/e/rm0)
   pslope = pslope + (stheta**2.0 - stheta*sr*cthk0/2/rm0)
&                  * (3/2/cldeffstress)**2.0 /slope
   pslope = rm0 * (ri0 / cthk0) * pslope
   go to 800
```

```
c       variation of axial strain is zero
        a11 = 1.0 + 0.5 * v * cthk0/rm0                                    710
        a12 = v * (0.5 * cthk0 / rm0 - 1.0)
        a21 = -v
        a22 = 1.0

        fmu1  = a11 / (a11*a22 - a12*a21)
        fmu2  = a21 / (a11*a22 - a12*a21)
        flamd1 = a22 / (a11*a22 - a12*a21)
        flamd2 = a12 / (a11*a22 - a12*a21)

        e2 = slope                                                         720
        stheta = 1.5*stheta/cldeffstress
        sz     = 1.5*sz/cldeffstress

        c11 = 1.0 + flamd1 * (e*cthk0/2.0/rm0 + e)*stheta**2.0/e2
     &            + flamd1 * e*cthk0/2.0/rm0 *stheta*sz/e2
     &            - flamd2 * e/e2 * stheta * sz
        c12 = flamd1 * (e*cthk0/2.0/rm0 + e)*stheta*sz/e2
     & + flamd1 * e * cthk0/2.0/rm0 * sz**2.0 /e2
        c21 = -fmu1*(e*cthk0/2.0/rm0 + e)*stheta**2.0/e2
     &   -fmu2*e*cthk0/2.0/rm0 *stheta*sz/e2                               730
     &   +fmu1*e/e2 * sz * stheta
        c22 = 1.0 - fmu2*(e*cthk0/2.0/rm0 + e)*stheta**2.0/e2
     &            - fmu2*e*cthk0/2.0/rm0 *sz**2.0/e2
     &            + fmu1 *(e/e2)*sz**2.0
        pslope = ri0/cthk0 * (c11*c22 - c21*c12)/(flamd1*c22 + fmu2*c12)
     &         *rm0 / e
800     continue
```

```
      swlold = gpr/(3*pi*rf0**2.0*hRod)/Ph(k)
      flamda = gpr/(3*pi*rf0*hRod)                                    740
      swlnew = pslope*0.5*(-Ph(k) + sqrt(Ph(k)**2.0 + 4*flamda/pslope))
     & /rf0

      fgswlnew = 1 + swlnew
      FGSwl(k) = FGSwl(k) * fgswlnew
      if(k .eq. 5) then
      nndebug = 1
      else
      nndebug = 0
      endif                                                           750
      nndebug = 0
      if(nndebug .eq. 1)    write(6,900) Time, k, pslope, pslope1,
     &  swlold, swlnew, edot01, edot1, slope, slope1
900   format('Time =', e14.6, ' du_vs_p slope (',i2,')=', e10.4,
     &      ' pslope1 = ', e10.4' oldswl=', e10.4, ' newswl=', e10.4
     &      ' edot01 = ', e10.4 ' edot1=', e10.4,
     &    ' slope = ', e10.4 ' slope1=', e10.4)

10    continue
      end                                                             760


c*********************************************************************
c     subroutine bubbleradius(gasbubble, tempk, press, rb)
c
c     gasbubble,      mole gas per bubble
c     tempk,          bubble temperature (K)
c     press,          hydrostatic pressure
```

```
c
c       rb,                     bubble radius (m)                       770
c*****************************************************************
        subroutine bubbleradius(gasbubble, tempk, press, rb)

        implicit real (a-h, o-z)

        rb0 = 0.5e-6
        eps = 1.0e-6
        ftheta = 0.2874
        pi      = 3.1415926
        R       = 8.314                                                 780
        A       =       4*pi*ftheta/3.0*press/(R * tempk)
        C       =       4*pi*ftheta/3*2*0.6/(R * tempk)

        rbnew = rb0
1000    continue
        rbold = rbnew
        rbnew = rbold - (A * rbold**3.0 + C * rbold**2.0 - gasbubble)/
     &          (3*A*rbold**2.0 + 2 * C * rbold)

        if(abs(rbnew - rbold)/rbold .ge. eps ) goto 1000                790
        rb = rbnew

        end


c*****************************************************************
c subroutine gbcracking(gasbubble, tempk, press, fstress, Ftheta, esurface, icrack)
c
```

```
c       gasbubble,      mole gas per bubble
c       tempk,          bubble temperature (K)                          800
c       press,          hydrostatic pressure (Pa)
c
c       icrack,         index for grain boundary cracking
c*****************************************************************
      subroutine gbcracking(gasbubble, tempk, press,
     & fstress, Ftheta, esurface, fc, rbubblec, Ph_low,
     &   fcmultifactor, icrack)

      implicit real (a-h, o-z)
                                                                      810
      fna = 6.02e23
      fkb = 1.38e-23
      B = 8.5e-29
      pi = 3.14159
      icrack = 0.0
      gasbubble = 2.0e-17

      Pb = gasbubble * fna * fkb * tempk
     &  / (4.0*pi/3.0*rbubblec**3.0 - gasbubble * fna * B)
                                                                      820
      Ps  = 2*esurface/rbubblec

      if(press .lt. Ph_low) then
            Phstress = Ph_low
      else
            Phstress = press
      end if
```

```
      if (((Pb - Ps)*1.0*fc*fcmultifactor - Phstress)
     & .ge. (1-fc*fcmultifactor)*fstress ) then                    830
       icrack = 1.0
      endif
      end


*deck FGRelease
      subroutine FGRelease(GRelease, Grlsp, Grlsb,
     & nring, naxn, Igapclose, Ioldgapclose, Irls, Time)

      implicit real (a-h,o-z)                                      840

      include 'FgRlsSwl.h'
      include 'FgRlsSwli.h'

      dimension    Igapclose(26), Irls(26), Ioldgapclose(26)

      data   ffitgas /1.0/, IRctrl/0/

c     Iteration for each axial node
      GRelease = 0.0                                               850
      Grlsp = 0.0
      Grlsb = 0.0

      do 10 k=1, naxn
      if(IRctrl .eq. 1 ) goto 10
      if(Iprint .eq. 1) then
      if(Igapclose(k) .eq. 1 .and. Ioldgapclose(k) .eq. 0) then
      write(30, 8002) k, Time
```

```
8002  FORMAT('Onset of gap closure at node', I3, 8X, E15.8, ' (sec)')
      end if                                                          860

      if(Igapclose(k) .eq. 0 .and. Ioldgapclose(k) .eq. 1) then
      write(30, 8003) k, Time
8003 FORMAT('Onset of gap opening at node', I3, 8X, E15.8, ' (sec)')
      end if
      end if


      If (Igapclose(k) .eq. 1.0) go to 10
      do 20 j=1, nrimidx(k)                                           870
      if(IsFreegas(k,j) .eq. 0) go to 20
c     release the fission gas in GasRls
      GasRls(k,j) = Gpore(k,j)
      Gpore(k,j) = 0.0
      Grlsp   = Grlsp + GasRls(k,j)
      GRelease = GRelease + GasRls(k,j)
      GasRls(k,j) = 0.0
20    continue

      do 30 j=nrimidx(k)+1, nring                                     880
      if(IsFreegas(k,j) .eq. 0) go to 30
c     release the fission gas in GasRls
      GasRls(k,j) = Gbubble(k,j)*ffitgas
      Gbubble(k,j) = 0.0
      Grlsb   = Grlsb + GasRls(k,j)
      GRelease = GRelease + GasRls(k,j)
      GasRls(k,j) = 0.0
30    continue
```

```
10      continue                                                        890
        end
*deck   PoreSwelling
        subroutine  PoreSwelling(Fueltemp, k, Pin, dV)

        implicit real (a-h, o-z)

        include 'FgRlsSwl.h'
        include 'FgRlsSwli.h'
        include 'dyna.h'
                                                                        900
        dimension   Fueltemp(51, 25)
c       Input variablesc
c       Fueltemp    Temperature distribution of fuel pellet(K)
c       Gpore       pore gas quantity      (mol)
c       k                   axial node
c       Pin                 Hydrostatic pressure (Pa)

c       Output variables
c       dV                  Volume Increment(m^3)
                                                                        910
        fkb = 1.38e-23
        B = 8.5e-29
        fNa = 6.02e23
        fR = 8.31
        pi = 3.14159
        burgers = 0.39e-9

c       calculate the initial equivalent pore radius and pore gas volume
```

```
      TotalVGBGasNew = 0.0d0                                              920
      TotalVGBGasOld = 0.0d0

      do 10 j=1, nrimidx(k)
      if(IsFreegas(k,j) .eq. 1) go to 10
      rrporek = rporeold(j, k)
      avp = (4.*pi/3.)* rpore0**3.0
      tporenum = poroavg(k)/avp * deltV1

c     fission gas in each pore (mole)
      fmole = Gpore(k,j)/tporenum                                         930
      pressnew1 = XeEquationOfState(Fueltemp(j, k), rrporek, fmole)
30    continue

      presseq = porepresscoef(k) / rrporek + Pin

      if (pressnew1 .ge. presseq) then
      rporenew = rrporek *(1.0 + 3./4. *burgers/rrporek)**0.333
      pressnew1 = XeEquationOfState(Fueltemp(j, k), rporenew, fmole)
      rrporek = rporenew
      go to 30                                                            940

      end if


      TotalVGBGasNew = TotalVGBGasNew + tporenum * (4.*pi/3.)
     & *rrporek**3.0
      TotalVGBGasOld = TotalVGBGasOld + tporenum * (4.*pi/3.)
     & *rpore0**3.0
```

```
10      continue
                                                                    950
        dV = TotalVGBGasNew - TotalVGBGasOld
        rporeold(j, k) = rrporek
        end


        function XeEquationOfState(T, R, fmole)

        implicit real (a-h, o-z)

        fkb = 1.38e-23                                              960
        fna = 6.02e23
      sig = 0.445e-9
        T0 = 231.2
        pi = 3.1415926

      d = sig * (0.8542 - 0.03996 * log(T / T0))
      V = 4.0 / 3.0 * pi * R * R * R
      y = pi * d * d * d / 6.0 * (fmole*fna) / V
      Z = (1 + y + y * y) / (1 - y) / (1 - y) / (1 - y)
        p = Z * (fmole*fna*fkb) * T / V;                            970
        XeEquationOfState = p
        end
```

B.2 Subroutine for PCMI failure

```
*deck fracstrain
c
      subroutine fracstrain (ncladi, nmesh, naxn, Time)
```

```
c
      implicit real (a-h,o-z)
c
c     this is the executive subroutine for calculation of failure
c     cladding due to PCMI

                                                                      10
      include 'dyna.h'
      include 'fracstrain.h'
      include 'Oxidation.h'
      include 'FgRlsSwli.h'
      include 'FgRlsSwl.h'
      include 'FissionGasRelease.h'

      data pi /3.1415926/, ftom /0.3048d0/, DBTT /500/, flambda /6.0/

                                                                      20
      do 10 k=1, naxn

      tck = tfk(CladAveTemp(k))
      if( tck .le. DBTT) then
       igtdbtt = 0
      else
       igtdbtt = 1
      end if

                                                                      30
      ch = cexh2a(k)
      ri = RadialBound(ncladi)*ftom
      ro = RadialBound(nmesh)*ftom
```

```
      hthk = hydridethk(ch, ri, ro)
      if (ICladType .eq. 1) then
        flambda = 6.0
      else
            flambda = 11.0
      end if                                                    40

      a = hthk*fcracksize*flambda
      call fractoughness (fKc, ch, igtdbtt)

c     Elastic modulus in Pa
      E = celmod (tck, EffFastFluStrenCoef(k),
     &          EffColdWkStrenCoef(k) ,OxygenConcenAve(k), CladType)
      E = E/1.0e6

      v = (celmod (tck, EffFastFluStrenCoef(k),                 50
     &  EffColdWkStrenCoef(k), OxygenConcenAve(k), CladType)
     &  /(2.d0 * cshear(tck, EffFastFluStrenCoef(k),
     &  EffColdWkStrenCoef(k), OxygenConcenAve(k), CladType)))- 1.0d0

      edot = CldStrnRat(k,1)
      call ckmn (tck, OxygenConcenAve(k), EffFastFluStrenCoef(k),
     &                EffFastFluStrnHardExp(k), EffColdWkStrenCoef(k),
     &                EffColdWkStrnHardExp(k), edot, ak, an, am)

      ak = ak/1.0e6                                             60
c     Yield stress in MPa
      sigma0 = CladYieldStress(k)*6894.757/1.0e6
```

```
c       Yield stress less than 0 (unknown reasons), skip the calculation
        if(sigma0 .le. 0.0) go to 10
c       Hoop stress in MPa
        sigma = CldStress(k, 1)*6894.757/1.0e6
        if(sigma .le. 0.0) sigma = 0.0

        delt = a/(EOSRad(nmesh, k)*ftom - EOSRad(ncladi,k)*ftom)        70
        sigman = sigma/ (1.0 - delt )

        F = 1.12 - 0.231*delt + 10.55*delt**2
     & - 21.72*delt**3 + 30.39*delt**4


        fKe = F * sigma * sqrt(pi* a)
        ae      = a

        alpha = sigma0 **(1/an -1)*E/ ak**(1/an)                        80
        fK      = fKe * sqrt(1.0 + alpha * (sigman/sigma0)**(1.0/an - 1.0))


        fstrain(k)  = alpha* sigma0 *
     &          (((fKc/fKe)**2 - 1)/alpha)**(1/(1-an))/E


        fJic(k)     = fKc**2.0 *(1 - v**2.0) / E
        fJe(k)      = fKe**2.0 *(1 - v**2.0) / E                        90
        fJp1(k)     = fJe(k) * alpha * (sigman/sigma0)**(1.0/an - 1.0)
        eps0        = sigma0 / E
        an_inverse = 1.0/an
```

```
      fJp2(k)    = 1.21* 3.1415926 * an_inverse **0.5 * alpha *eps0* a*
     &                  (3.0**0.5/2.0 * sigman )**(an_inverse+1)
     &                        / sigma0**an_inverse


      epsplastic1     = (sigma/ak)**(1/an)
      epsplastic2 = CldPermHoopStrn(k)                                  100

      if(epsplastic1 .gt. epsplastic2) epsplastic1 = epsplastic2

      if(sigma .le. 0.0) then
      epse = 0.001
      else
      epse            = (sigma/E)
      endif

      fJp1(k)         = fJe(k)* epsplastic1 / epse / (an)**0.5          110
      fJ       = fJe(k) + fJp1(k)
      fstrain(k) = fJ/fJic(k)

      if(fJ .ge. fJic(k)) then
      if (IPCMIfailure .eq. 1) goto 10
      IPCMIfailure = 1
      write(6,*)'PCMI failure at time = ',Time
      write(6,*)'Axial node = ', k
      write(6,*)'Damage factor = ', fstrain(k)
      if (Iprint .eq. 1) then                                           120
      write(30,*)'PCMI failure at time = ',Time
      write(30,*)'Axial node = ', k
      write(30,*)'Damage factor = ', fstrain(k)
```

```
      end if
      return

      end if

10    continue
                                                                    130
      end
*deck hydridethk
c
      function hydridethk(ch, ri, ro)
c
      implicit real (a-h,o-z)
c
c     this is the executive subroutine for calculation of thickness
c       of hydride rim
                                                                    140
c       ch:                     hydrogen content (wtppm)
c       ri:                     inner radius of cladding (m)
c       ro:                     outer radius of cladding (m)
c       hydridethk:         hydride rim thickness (m)
c
c       Note:  since majority hydrogen precipitated as hydrides,
c       hydrogen in alpha-phase is neglected in calculating
c       the thickness of hydride rim. Otherwise, the temperature distribution
c       during base irradiation should be an input to account for the hyrogen
c       dissioved in Zr.                                            150
c

      data  cdh /16000.0/, pi /3.14159/
```

```
      v0 = pi*(ro**2.0 - ri**2.0)

      v1 = v0*ch/cdh

      hydridethk = (ro - sqrt(ro**2.0 - v1/pi))
      end                                                    160
*deck fractoughness
c
      subroutine fractoughness (fKc, ch, igtdbtt)
c
      implicit real (a-h,o-z)
c
c     this is the executive subroutine for calculation of hydrided
c     cladding fracture toughness
c       suitable for hydrogen content < 4000ppm
c                                                            170
c       Kc:                    fracture toughness of hydrided cladding
c                (returen value, (Mpa)^(1/2)*m )
c       ch:                    hydrogen content (wtppm)
c       igtdbtt:          1  temperature > DBTT
c                              0  otherwise


      if ( igtdbtt .eq. 1) then

      if ( ch .lt. 411.297) then                             180
       fKc = 116.9 - 0.00782*ch
      else if ( ( ch .ge. 411.297) .AND. (ch .lt. 806.093) ) then
       fKc = 855.3*exp(-0.005*ch)
```

```
      else if ( ch .ge. 806.093) then
       fKc = 19.38 - 0.00257*ch
      end if

      else
      if ( ch .lt. 532.35) then
       fKc = 42.64*exp(-0.001619*ch)                                    190
      else if ( ch .ge. 532.35) then
       fKc = 19.38 - 0.00257*ch
      end if
      end if

      return
      end
*     deck csed
      subroutine csed(ncladi, nmesh, naxn, time, ispalled)
                                                                        200
      implicit real (a-h, o-z)

      include 'dyna.h'
      include 'fracstrain.h'
      include 'Oxidation.h'
      include 'FgRlsSwli.h'
      include 'FgRlsSwl.h'
      include 'FissionGasRelease.h'

      data pi /3.1415926/, ftom /0.3048d0/, DBTT /550/,                 210
     &     iwarning /0.0/
```

```
      do 10 k=1, naxn

      tck = tfk(CladAveTemp(k))
      if( tck .le. DBTT) then
       igtdbtt = 0
      else
       igtdbtt = 1                                                    220
      end if


      ri = RadialBound(ncladi)*ftom
      ro = RadialBound(nmesh)*ftom

      Rox = oxideod(k) / (ro - ri)


      if(igtdbtt .eq. 0) then                                        230
            crsed =        15.67 * exp(-7.19*Rox)
      else
            if(ispalled .eq. 0) then
c     none-spalled cladding, 0.03 < Rox < 0.23
                  crsed = 41.5*exp(-6.6*Rox)
                  if(Rox .ge. 0.23) iwarning=1.0
                  if(Rox .le. 0.03) iwarning=1.0
            else
c     spalled cladding, 0.1 < Rox < 0.23
                  crsed = 0.371* Rox**(-1.24)                        240
                  if(Rox .ge. 0.23) iwarning=1.0
                  if(Rox .le. 0.1)  iwarning=1.0
            end if
```

```
      end if

      fstrain(k) = SEDEPRI(k) / crsed

      if(SEDEPRI(k) .ge. crsed) then
      if (IPCMIfailure .eq. 1) goto 10
      IPCMIfailure = 1                                                    250
      write(6,*)'PCMI failure at time = ',Time
      write(6,*)'Axial node = ', k
      write(6,*)'Damage factor = ', fstrain(k)
      write(30,*) 'CSED (MJ/m^3) = ', crsed
      if (iwarning .eq. 1) then
      write(6,*) 'Warning: Rox is out of range ', Rox
      end if

      if (Iprint .eq. 1) then
      write(30,*)'PCMI failure at time = ',Time                           260
      write(30,*)'Axial node = ', k
      write(30,*)'Damage factor = ', fstrain(k)
      write(30,*) 'CSED (MJ/m^3) = ', crsed
      if (iwarning .eq. 1) then
      write(30,*) 'Warning: Rox is out of range ', Rox
      end if

      end if
      return
                                                                          270
      end if

10    continue
```

```
      end
```

B.3 Subroutine for heat transfer

```
*deck qqdot
c
      subroutine qqdot (a, b, cpf, cpg, cp, rf, rg, r, MassFlowRate,
     &                  Quality, hd, hf, hg, CoolPress, qcrit, qq, tbulk,
     &                  ts, tsat, tsur, ih, j, l, tempcm, zroxid, dh,
     &                  aflow, dr, beta)
c
c     qqdot calculates surface temperature, flux, and h.t. coefficient,
c     given a specific heat transfer correlation and conduction values.
c                                                                       10
      implicit real (a-h,o-z)
c
c     aasth stores water property table
c
      include 'ftblcm.h'
        include 'FgRlsSwl.h'
        include 'FgRlsSwli.h'
c
      real MassFlowRate, Quality
c     prop stores input and output arguments to water property          20
c     subroutines
      include 'CoolProperties.h'
c     Debug is for use in controling debug output by setting DebugTime
      include 'Debug.h'
c     new heat trans props, from tkcon, visc, steam tables. 7/74 gaj
```

```
c     a, b   = coefficients from the conduction solution in
c              the form qq = a*tsur + b
c     cpf    = specific heat capacity for saturated liquid
c     cpg    = specific heat capacity for saturated gas
c     cp     = specific heat capacity for single phase                    30
c     rf     = density for saturated liquid, lbm/ft**3
c     rg     = density for saturated gas
c     r      = single phase density
c     MassFlowRate = coolant flow rate
c     Quality= volume average quality
c     hd     = hydraulic diameter, ft
c     hf     = saturation liquid enthalpy  (btu/lb)
c     hg     = saturation gas enthalpy
c     CoolPress  = volume pressure
c     qcrit = critical heat flux  (btu/hr-ft2)                            40
c     qq     = surface heat flux (btu/hr-ft2)     output
c     tbulk = bulk coolant temperature (F)
c     ts     = surface temperature (F)            output
c     tsat   = saturation temperature (F)
c     tsur   = surface temperature guess          input
c     ih   = heat transfer mode -
c              1 = forced convection to liquid
c              2 = nucleate boiling
c              3 = forced convection vaporization
c              4 = flow transition boiling                                50
c              5 = flow film boiling
c              6 = pool film boiling
c              7 = pool transition boiling
c              8 = forced convection to gas
c              9 = dougall-rohsenow for low pressure flow film boiling
```

```
c     j       = indicator for film boiling correlation
c               0 = use groeneveld 5.9 for mode 5
c               1 = use groeneveld 5.7 for mode 5
c               2 = use dougall-rohsenow for mode 5
c               3 = combined tong-young (mode 4) and condie-bengston        60
c                   (mode 5)
c     l   = type of pool boiling, used only for modes, ih = 6 and 7
c           1 = transition pool boiling                    output
c           2 = laminar pool boiling
c     tempcm = peak clad temperature (F)
c     zroxid = oxide layer thickness
c     dh     = equivalent heated diameter (ft)
c
c     aflow = cross-sectional flow area (ft**2)
c                                                                          70
c     dr     = cladding outer diameter (ft)
c
c     beta = thermal coefficient of expansion of sat. vapor phase (1/F)
c           beta is only defined if ih=6
c
      dimension reyn(30) , fsup(26)
      logical err
      data dp01 ,  dp023 ,  dp072
     & /  0.01d0 , 0.023d0 , 0.072d0 /
c         goeneveld 5.9 coefficients                                       80
      data gr9a,     gr9b,      gr9c,     gr9d
     & / 0.00327d0, 0.901d0,  1.32d0,  −1.50d0 /
c         groeneveld 5.7coefficients
      data gr7a,     gr7b,      gr7c,     gr7d
     & / 0.052d0 ,  0.688d0,   1.26d0,  −1.06d0 /
```

```
      data xgrmx /0.950d0/
c     condie - bengston coefficients  (11 dec 74)
      data cba, cbb, cbc, cb0, cb1, cb2, cb3, cb4, cb5, cb6, cb7/
     & 42011.23d0, 659.91d0, -16.04d0, -0.5d0, 0.2007d0, 0.0483d0,
     & 0.7441d0, 3.6155d0, 1000.0d0, 0.2771d0, 10.8450d0/                  90
      data dp1 /0.1d0/, dp4 /0.4d0/
      data dp8 /0.8d0/, one /1.0d0/
      data five /5.0d0/
      data        d400 , d800  , d1200 , d1260
     &    /        400.0d0 , 800.0d0  , 1200.0d0 , 1260.0d0/
c     d19800 is 99 per cent of d20000 for mode 6 test
      data sigma /1.73d-09/
      data n1, n2 /1, 2/
      data fthun, prhi /1500.0d0, 0.8695652174d0/
      data xx, yy, zz /979.2d0, 1180.8d0, 1501.2d0/                        100
      data ftor /459.67d0/, tradcb /1800.0d0/
      data xminty /0.05d0/
      data hmin /0.01d0/, ft /12.0d0/, gravc /4.173d+8/
      data sipr /6894.76d0/, encp/ 2.388458966d-4/
      data sisvol /6.24279606d-2/
      data pi /3.141592654d0/
c
c     define reynolds # factor table for chen correlation for nucleate
c     boiling
      data reyn / 1.07d0, 0.1d0, 1.21d0, 0.2d0,  1.42d0,  0.3d0,           110
     &            1.63d0, 0.4d0,  2.02d0, 0.6d0,  2.75d0,  1.0d0,
     &            4.30d0, 2.0d0,  5.60d0, 3.0d0,  6.75d0,  4.0d0,
     &            9.10d0, 6.0d0, 12.10d0,10.0d0, 22.00d0, 20.0d0,
     &           44.70d0,50.0d0, 76.00d0,100.0d0, 200.00d0,400.0d0/
      data nreyn /15/, ireyn/1/
```

```
c
c     define suppression factor for chen correlation for nucleate boil.
      data fsup /1.000d0,1.0d+3,
     &          0.893d0,1.0d+4, 0.793d0,2.0d+4, 0.703d0,3.0d+4,
     &          0.629d0,4.0d+4, 0.513d0,6.0d+4, 0.375d0,1.0d+5,                120
     &          0.213d0,2.0d+5, 0.142d0,3.0d+5, 0.115d0,4.0d+5,
     &          0.093d0,6.0d+5, 0.083d0,1.0d+6, 0.000d0,1.0d+8/
      data nfsup /13/, ifsup/1/
c
      ndebug = 0
      if(Time .ge. DebugTime .and. Time .le. DebugTimeStop) ndebug = 1
      if(ndebug .eq. 1) write(6,905) Time, ih, Quality, MassFlowRate
     &                              ,CoolPress, j
  905 format(' QDOT: Time = ',e10.4,' ih = ',i3, ' Quality = ',e10.4,
     &       ' MassFlowRate = ',e10.4, ' CoolPress = ',e10.4,' j = ',i3)     130
c
      go to (100,200,300,400,500,600,600,800,890), ih
c
      write(6,*) ' execution terminated in qdot.'
      stop

c     mode 1 subcooled forced convection dittus-boelter
  100 continue
c       bypass forced convection goto natural convection
        go to 1000                                                           140

      tkf = thcon (n1, tbulk, r)
c     compute liquid viscosity using relap5 function
      pressi = CoolPress * 6.896552d+3
      tbulkk = tfk(tbulk)
```

```
      rhosi = r/0.0624279606d0
      tsatk = tfk(tsat)

      viscsi = viscol (pressi, tbulkk, rhosi, tsatk)
                                                                    150
      vsf = viscsi * 2419.09d0
      prf = cp * vsf/tkf
      ref = MassFlowRate * hd/vsf
      hc = (dp023 * tkf/hd) * ref**dp8 * prf**dp4
      if(hc .lt. five) hc = five
      ts = (b + hc * tbulk)/(hc - a)
      qq = hc * (ts - tbulk)
      go to 900

c     mode 2 subcooled nucleat boiling     Thom                     160
  200 continue
  300 continue
c       by pass the flow subcooled nucleat boiling and go to pool nucleat boiling
        go to 1200
      itn = 1
c     heat transfer modes 2 and 3 are combined together and modeled by
c     the chen correlation
c
c     first compute the required water properties
c                                                                    170
      tkf = thcon (n1, tsat, r)
c     if liquid subcooled, use relaps viscosity subroutine
      if(Quality .gt. 0.0d0) go to 206
      pressi = CoolPress * 6.896552d+3
      tbulkk = tfk(tbulk)
```

```
      rhosi = r/0.0624279609d0
      tsatk = tfk (tsat)
      viscsi = viscol (pressi, tbulkk, rhosi, tsatk)
      vsf = viscsi * 2419.09d0
      go to 208                                                    180
  206 continue

      vsf = visc (n1, tsat, r)
  208 continue
c
      call surten (tsat, sig)
      prf = cpf * vsf/tkf
      ref = MassFlowRate * hd/vsf
      vsg = visc (n2, tsat, rg)
c     check to see if subcooled or saturated                       190
      if(Quality .gt. 0.0d0) go to 220
c     subcooled. reynolds number factor = 1.
      freyn = 1.0d0
      go to 230
  220 continue
c
c     compute gamma for input argument to reynolds number table
c
      xgam = Quality
      if(xgam .gt. 0.99d0) xgam = 0.99d0                           200
      gamma = ((xgam/(1.0d0 - xgam))**0.9d0)
     &        * ((rf/rg)**0.5d0) * ((vsg/vsf)**0.1d0)
      if(gamma .gt. 0.1d0) go to 222
      freyn = 1.07d0
      go to 230
```

```
 222 continue
     if(gamma .lt. 400.0d0) go to 224
     freyn = 200.0d0
     go to 230
 224 continue                                                    210
     freyn = polate (reyn, gamma, nreyn, ireyn)
 230 continue

c    compute suppression factor
     fsupin = ref * freyn**1.25d0
     if(fsupin .gt. 1.0d+3) go to 232
     fsupf = 1.0d0
     go to 240
 232 continue
     if(fsupin .lt. 1.0d+8) go to 234                            220
     fsupf = 0.0d0
     go to 240
 234 continue
     fsupf = polate (fsup, fsupin, nfsup, ifsup)
 240 continue

c    compute material property factors for hmic and hmac
     fmic = 0.00122d0 * (((tkf**0.79d0) * (cpf**0.45d0) * (rf**0.49d0)
    &       * (gravc**0.25d0))/((sig**0.5d0) * (vsf**0.29d0)
    &       * ((hg-hf)**0.24d0) * (rg**0.24d0))) * fsupf          230
     hmac = 0.023d0 * (tkf/hd) * (prf**0.4d0) * (ref**0.8d0) * freyn

c    compute vapor pressure at cladding surface temperature

 241 continue
```

```
      tsurk = tfk(tsur)
c     limit temperature to critical temperature
      if(tsurk .ge. 640.0d0) tsurk = 640.0d0
c
      call sth2x0 (tsurk, psatsi, err)                                  240
c
      if(.not.err) go to 244
      write(6,242) tsurk, psatsi
  242 format(//' error in call to sth2x0 in qdot for nucleate',
     &        ' boiling heat transfer. program stopped: tsurk = '
     &        ,e10.4,' psatsi = ',e10.4)
      stop
c
  244 continue
c                                                                       250
c**** convert psat from pa to psia
      psatw = 0.000145d0 * psatsi

c     since tsat was evaluated at pressure CoolPress,
c     psat(tsat), dpsat has units of lbf/ft**2
      dpsat = (psatw - CoolPress) * 144.0d0
      if(dpsat .lt. 0.0d0) dpsat = 0.0d0
      dtsat = tsur - tsat
      if(dtsat .lt. 0.0d0) dtsat = 0.0d0
      hmic = fmic * (dtsat**0.24d0) * (dpsat**0.75d0)                   260
c
c     check to see if subcooled or saturated
      if(Quality .gt. 0.0d0) go to 250
      twall2 = (b + hmic * tsat + hmac * tbulk)/(hmic + hmac - a)
      go to 260
```

```
c
  250 continue
      twall2 = (b + (hmic + hmac) * tsat)/(hmic + hmac - a)
  260 continue
      if(ndebug .eq. 1) write(6,942) itn,tsur,twall2,hmic,hmac,dtsat          270
  942 format(' QDOT for mode 2, itn = ',i5,' tsur = ',e12.6,
     &       ' twall2 = ',e12.6,' hmic = ',e10.4,' hmac = ',e10.4,
     &       ' dtsat = ',e12.6)
      if(abs(twall2 - tsur) .lt. 0.1d0) go to 280
      if(itn .gt. 1) go to 262
      tin1 = twall2
      twgs = twall2
      go to 278
c
  262 continue                                                                280
      if(itn .gt. 2) go to 263
      tin2 = twall2
      tout1 = tin2
      twgs = twall2
      go to 278
c
  263 continue
      if(abs(tin2 - tin1) .lt. 1.0d-5) go to 280
      tout2 = twall2
c     get improved guess of surface temperature using method of newton        290
      dtidto = (tout2 - tout1)/(tin2 - tin1)
      twgs = (tout1 - dtidto * tin1)/(1.0d0 - dtidto)
      tout1 = tout2
      tin1 = tin2
      tin2 = twgs
```

```
      if(ndebug .eq. 1) write(6,944) itn, twgs, tout2, tin2, tout1, tin1
  944 format(' QDOT for mode 2, itn = ',i5,' twgs = ',e12.6,
     &       ' tout2 = ',e12.6,' tin2 = ',e12.6,' tout1 = ',e12.6,
     &       ' tin1 = ',e12.6)
  278 continue                                                          300
      tsur = twgs
      itn = itn + 1
      if(itn .lt. 100) go to 241
      write(6,277) twall2, tsur
  277 format(////,' iteration on cladding surface temperature in '
     &,'qdot for nucleate boiling mode did not converge. ',
     & 'program stopped.', /,' twall2 = ',e12.6,' twall1 = ',e12.6)

      twall2 = 0.5d0 * (twall2 + tsur)
                                                                        310
c     iteration converged
  280 continue
      ts = twall2
      if(ts .lt. tsat) ts = tsat
      qq = a * ts + b
      go to 900
c
                                                                        320
c     mode 4 transition boiling       mcdonough,milich, and king
c      or combined tong-young (transition) and condie-bengston (stable)

  400 continue
c       by pass flow transtion boiling, go to pool transition boiling
```

```
        go to 600
      if(j .eq. 3) go to 450
      if(j .eq. 4) go to 450
      twdnb = tsat + dp072 * exp(-CoolPress/d1260) * sqrt(qcrit)
      if(CoolPress .gt. d1200) go to 410                                  330
      s = yy + (zz - yy) * (d1200 - CoolPress)/d400
      go to 420
c
  410 continue
      s = yy - (yy - xx) * (CoolPress - d1200)/d800
  420 continue
      ts = (qcrit - b + s * twdnb)/(a + s)
      qq = qcrit - s * (ts - twdnb)
      if(ndebug.eq.1) write(6,915) qq, qcrit, s, ts, twdnb
  915 format(' for mcdon, qq = ',e10.4,' qcrit = ',e10.4,             340
     &       ' s = ',e10.4,' ts = ',e10.4,' twdnb = ',e10.4)
      if(qq .gt. qcrit) qq = qcrit
      if(qq .le. dp01) qq = dp01
      go to 900
c     combined tong-young and condie-bengston


  450 continue
      xe = Quality
      if(xe .lt. xminty) xe = xminty
      itn = 0                                                             350
c     q = q(dnb) * exp(cty) + q(c-b)
c
c     first evaluate cty using guess of wall temperature


      twall = tsur
```

```
 455 continue
     itn = itn + 1
     if(twall .lt. (tsat + 1.0d0)) twall = tsat + 1.0d0
     dtsat = twall - tsat
     qcty = a * twall + b                                          360
     if(qcty .ge. 1.0d0) go to 456
     cty = 0.0d0
     go to 458
c
c      dr and aflow are converted from feet to inches
c
 456 continue
     denom = (qcty/(MassFlowRate * (hg - hf)))
    &        * (pi * 12.0d0 * dr/(144.0d0 * aflow))
     cty1 = 0.666666667d0                                          370
     cty2 = 1.0d0 + 0.0016d0 * dtsat
     cty = ((0.001d0 * xe**cty1)/denom) * (dtsat/100.0d0)**cty2
c
c     compute stable film boiling heat transfer coefficient using
c     condie-bengston correlation
c
c     compute density and specific heat of vapor phase at wall
c     temperature

 458 continue                                                      380
     if(cty .lt. 0.0d0) cty = 0.0d0
     twallk = tfk(twall)
     if(twallk .gt. 1800.0d0) twallk = 1800.0d0
     prop(1) = twallk
     prop(2) = CoolPress * sipr
```

```
c
      if(ndebug .eq. 1) then
        write(6,912) qcty, twall, tsat
  912   format(' QDOT for ty-cb, qcty = ',e10.4,' twall = ',
     &         e10.4,' tsat = ',e10.4)                                  390
        write(6,913) cty, aflow, dr
  913   format(' after stat 458, cty = ',e10.4,' aflow = ',e10.4,
     &         ' dr = ',e10.4)
      endif
c
      call sth2x3 (aasth, prop, itn, err)
c
      if(.not.err) go to 460
      write(6,461)
  461 format(///,' failure in call to sth2x3 from qdot ')               400
      write(6,468) twall, CoolPress
  468 format(' twall = ',e10.4,' CoolPress = ',e10.4)
      call fabend
c     cp = specific heat of vapor at wall temperature (btu/lb-F)
  460 continue
      cp = prop(8) * encp
c
c     r= vapor density at wall temperature (lb/ft**3)c
      r = sisvol/prop(3)
c                                                                      410
c     compute thermal conductivity of vapor at wall temperaturec
      tk = thcon (n2, twall, r)
c
c     compute viscosity of vapor phase at wall temperature
      vs = visc (n2,twall,r)
```

```
c
c     compute prandtl number at wall temperature
      prw = cp * vs/tk
      if(cp .ge. 0.0d0) go to 462
  459 continue                                                    420
      write(6,911) cp, vs, tk, prw, r, twall
  911 format(' QDOT for c-b, cp = ',e10.4,' vs = ',e10.4,' tk = ',
     &       e10.4,' prw = ',e10.4,' r = ',e10.4,' twall = ',e10.4)
      stop
c
  462 continue
      if(vs .ge. 0.0d0) go to 463
      go to 459
c
  463 continue                                                    430
      if(tk .gt. 0.0d0) go to 464
      go to 459
c
  464 continue
c
c     compute thermal conductivity of saturated gas
      tkg = thcon (n2, tsat, rg)

c     compute viscosity of saturated gas
      vsg = visc (n2, tsat, rg)                                   440

c     compute reynolds number of saturated gas
      reg = MassFlowRate * hd/vsg
      cbh1 = tkg**0.4376d0
      if(prw .ge. 1.0d-10) go to 465
```

```
      cbh2 = 0.0d0
      go to 467
c
  465 continue
      cbh2 = prw**2.3070d0                                          450
  467 continue
      cbh3 = reg**(0.6004d0 + 0.2456d0 * log(1.0d0 + xe))
      cbh4 = hd**0.7842d0
      cbh5 = (1.0d0 + xe)**2.59028d0
      hcb = 0.04487d0 * (cbh1 * cbh2 * cbh3/(cbh4 * cbh5))

c     compute wall temperature neglecting radiation heat transfer
      if(cty .gt. 50.0d0) cty = 50.0d0
      qtyng = qcrit * exp(-cty)
c                                                                   460
      if(ndebug .eq. 1) write(6,914) qtyng
  914 format(' qtyng= ',e10.4)
      twall2 = -qcrit * exp(-cty)/(hcb - a) + hcb * tsat/(hcb - a)
     &         + b/(hcb - a)
      if(ndebug .eq. 0) go to 470
      write(6,981) itn, twall, twall2, qcrit, cty, hcb
  981 format(' QDOT, itn = ',i5,' twall = ',e12.6,' twall2 = ',e12.6,
     &       ' qcrit = ',e10.4,' cty = ',e10.4,' hcb = ',e10.4)
  470 continue
      if(twall2 .lt. (tsat + 1.0d0)) twall2 = tsat + 1.0d0          470
      if(itn .gt. 1) go to 472
      tin1 = twall2
      twgs = twall2
      go to 490
c
```

```
 472 continue
     if(itn .gt. 2) go to 474
     tin2 = twall2
     tout1 = tin2
     twgs = twall2                                                    480
     go to 490
c
 474 continue
     if(abs(tin2 - tin1) .lt. 1.0d-5) go to 496
     tout2 = twall2
     if(abs(tout2 - tin2) .lt. 1.0d0) go to 496
c
c    get improved guess of twall using method of newton
c
     dtidto = (tout2 - tout1)/(tin2 - tin1)                           490
     twgs = (tout1 - dtidto * tin1) / (1.0d0 - dtidto)
     if(twgs .lt. (tsat + 1.0d0)) twgs = tsat + 1.0d0
     tout1 = tout2
     tin1  = tin2
     tin2  = twgs
     if(ndebug .eq. 1) write(6,983) itn, twgs, tout2, tin2, tout1,
    &                               tin1, Time
 983 format(' itn = ',i5,' twgs =',e12.6,' tout2 =',e12.6,' tin2 = ',
    &       e12.6,' tout1 = ',e12.6,' tin1 = ',e12.6,' Time = ',e12.6)
 490 continue                                                         500
     twall = twgs
     if(itn .lt. 100) go to 455
     write(6,477) itn, twall2, tin1
 477 format(///' iteration on wall temperature in qdot with combined',
    &       '   tong-young + condie-bengston. program stopped.'/
```

```
     &          ' itn=',i5,' twall2 = ',e12.6,' twall = ',e12.6)
      if(twall .lt. twall2) twall2 = twall
c
c     iteration converged.
c                                                                    510
  496 continue
      ts = twall2
      if(ts .lt. tsat) ts = tsat
      qq = a * ts + b
      go to 900
c
c     mode 5  film boiling
  500 continue
      if(j .eq. 3) go to 450
      if(j .eq. 4) go to 450                                         520
c
c     if j=3 or 4, combined tong-young & condie-bengston used
c
      itn = 0
      xsave = Quality
      if(j .eq. 2) go to 5200
      xsave = Quality
      if(Quality .lt. dp1) Quality = dp1
      yyy = one - dp1 * ((one - Quality) * (rf/rg - one))**dp4
      if(yyy .lt. dp1) yyy = dp1                                     530
      tp1 = Quality + (one - Quality) * rg/rf
      Quality = xsave
      tkg = thcon (n2, tbulk, rg)
      vsg = visc (n2, tbulk, rg)
```

```
c   prandtl no. eval. at wall temp.
      if(tsur .gt. fthun) go to 540
      tk = thcon (n2, tsur, r)
      vs = visc (n2, tsur, r)
      prw = cp * vs/tk                                          540
      go to 550
c
  540 continue
      prw = prhi
  550 continue
      reg = MassFlowRate * hd/vs
c     choice of groeneveld version
      if(j .gt. 0) go to 570
      hc = (gr9a * tkg/hd) * (reg * tp1)**gr9b * prw**gr9c * yyy**gr9d
      go to 580                                                 550
c
  570 continue
      hc = (gr7a * tkg/hd) * (reg * tp1)**gr7b * prw**gr7c * yyy**gr7d
c
  580 continue
      if(hc .lt. five) hc = five
      hgroen = hc
      if(xsave .ge. xgrmx) go to 5200
      ts = (b + hc * tsat)/(hc - a)
      qq = hc * (ts - tsat)                                     560
      go to 900
c
c     dougall-rohsenow film boiling correlation
 5200 continue
      xsave = Quality
```

```
      if(Quality .lt. dp1) Quality = dp1
      tp1 = Quality + (one - Quality) * rg/rf
      tkg = thcon (n2, tsat, rg)
      vsg = visc (n2, tsat, rg)
      prg = cpg * vsg/tkg                                          570
      reg = MassFlowRate * hd/vsg
      hc = (dp023 * tkg/hd) * (reg * tp1)**dp8 * prg**dp4
      if(hc .lt. five) hc = five
      Quality = xsave
c     if groeneveld specified, but quality greater than groeneveld
c     quality cutoff, interpolate between groeneveld and dougall rohse-
c     now
      if(j .le. 1 .and. Quality .ge. xgrmx)
     & hc = hgroen + ((Quality - xgrmx)/(1.0d0 - xgrmx)) * (hc - hgroen)
c     see if radiation heat transfer needs to be included          580
      if(tsur .gt. tradcb) go to 5250
      ts = (b + hc * tsat)/(hc - a)
      qq = hc * (ts - tsat)
      go to 900
c
 5250 continue
c
      call void (Quality, rf, rg, hd*ft, sr, alpha)
      call emssf1 (tempcm, alpha, zroxid, fe)
      rk = fe * sigma                                              590
      c1 = (hc - a)/rk
      tts = tfr (tsat) * tfr (tsat)
      c2 = -(tts * tts + (hc * tfr(tsat) + b - ftor * a)/rk)
      call root1 (c1, c2, tfr(tsur), ts)
      ts = ts - ftor
```

```
      qq = a * ts + b
      go to 900
c     pool film boiling. modified bromley if void fraction less than .6,
c     free convection if void fraction greater than 0.6
  600 continue                                                        600
c
      call void (Quality, rf, rg, hd*ft, sr, alpha)
      itn = 1
c     free convection plus radiation
  650 continue
      betav = beta
      if(tsur .lt. (tsat + 1.0d0)) tsur = tsat + 1.0d0
      tfilm = 0.5d0 * (tsur + tsat)
                                                                      610
      vsf = visc (n2, tfilm, r)
      vsg = visc (n2, tsat , rg)
      ckf = thcon (n2, tfilm, r)

c     first compute heat flux to the vapor phase
c     update free convection correlation

      prf = cp * vsf/ckf
      dtsat1 = tsur - tsat
      if(dtsat1 .lt. 0.0d0) dtsat1 = 0.0d0                            620
      hfree = 0.4d0 * (ckf/hd) * (((hd/2.0d0)**3) * gravc * betav
     &        * ((rg/vsg)**2) * dtsat1 * prf)**0.2d0
c     if low cladding temp, ignore radiation
      if(tsur .gt. (tsat + 250.0d0)) go to 651
      hrad = 0.0d0
```

```
      go to 655
c
  651 continue
c
c     compute radiation htc                                          630
      call emssf1 (tempcm, alpha, zroxid, fe)

c     assume configuration factor equals one

      hrad = fe * sigma * ((tfr(tsur))**4 - (tfr(tsat))**4)
     &       /(tsur - tsat)
  655 continue
      qvapor = (hfree + hrad) * (tsur - tsat) * alpha
      if(ndebug .eq. 1) write(6,985) itn, tsur, hfree, ckf, hd, hrad,
     &                               qvapor                          640
  985 format(' QDOT for free convection, itn = ',i4,' t1 = ',e12.6,
     & ' h = ',e12.6,' ckf = ',e10.4,' hd = ',e12.6,' hrad = ',e10.4,
     & ' qvapor = ',e10.4)
      if(itn .gt. 1) go to 646

      call surten (tsat, sig)
c
      al = 2.0d0 * pi * sqrt(sig/(rf - rg))
      tkg = thcon (n2, tsat, rg)
                                                                     650
c     compute film boiling term
  646 continue
      dtsat = tsur - tsat

c       Frederking
```

```
      hfb_4 = 0.2 * ((( (tkg**2) *rg*(rf - rg)*hfg1*gravc )
     &  / (vsg*dtsat1) )**0.333d0)

c     Modified Bromley
      hfg1 = hfg*(1+0.5*cpg*(tsur - tsat)/hfg)                    660
      hfb_5 = 0.62d0 * ((hd/al)**0.172d0) *
     &     ((( (tkg**3) * rg * (rf - rg) * hfg1 * gravc)
     &     /(hd*vsg * dtsat1))**0.25d0)

      fsubc = 1.d0 + 0.1d0 * ((rf/rg)**0.75) * (cpf * (tsat - tbulk)
     &          /(hg - hf))
      fsubcool = fsubc * ffhtc
      hfb = hfb_4*fsubcool

c     compute tranistion boiling and film boiling                 670
      if(ITmin .le. 1) then
      thkf = thcon(n1, tsat, rf)
      Tref = tfk(tsat)
      iIter = 1
      nItermax = 500
      Tmin  =       Tref + 1.0

      do while((abs(Tref - Tmin) > 0.1) .AND. (iIter < nItermax))

      Tref = Tmin                                                 680
      call Wallthprop(tkw, cpw, rw, Iszry, Tref)
      Ra = thkf*cpf*rf/(tkw*cpw*rw)
      dp = 3203.6 - CoolPress
      Tnh = 705.44 - 4.722e-2*dp +
     &  2.3907e-5*dp**2.0 - 5.8193e-9*dp**3.0
```

```
      Tmin = Tnh + (Tnh - tbulk)*Ra**0.5
      iIter = iIter + 1
      end do
                                                                    690
      Tmink = tfk(Tmin)
      Tmin = tcf(Tmink + Tminshift +
     &  3.3*(tfk(tsat)- tfk(tbulk)) - 273.15)
      elseif( ITmin .eq. 2) then
c     NSR-77
      Tmin = tfk(tsat) + 350 + 5.1*(tfk(tsat) - tfk(tbulk))
      if(Iszry .eq. 0) Tminshift = Tminshift + 160
      Tmin = Tmin + Tminshift
      Tmin = tcf(Tmin - 273.15)
      endif                                                         700

c     compute Tchf using rosenhow correlation
      cs = 0.013
      fn = 1.7
      call surten(tsat, sigrsh)
c     viscosity in [lbm/hr-ft]
      viscf = visc (n1, tsat, rf)
      tkf = thcon (n1, tsat, rf)
      prf = cpf * viscf/tkf
      hfg = hg - hf                                                 710
      alrsh = sqrt(sigrsh/(rf - rg))

      fsubc = 1.d0 + 0.1d0 * ((rf/rg)**0.75) * (cpf * (tsat - tbulk)
     &        /(hg - hf))
```

```
      Tchff = (qcrit/(fsubc*fqcritm)*alrsh/(viscf*hfg))**0.333
     & *(cs*hfg*prf**fn)/cpf + tsat
      zeta = ((tsur - Tmin)/(Tchff - Tmin))**2

c     calculate qmin                                                    720
      hfg1min = hfg*(1+0.5*cpg*(Tmin - tsat)/hfg)
      hfb5min = 0.62d0 * ((hd/al)**0.172d0) *
     &     ((( (tkg**3) * rg * (rf - rg) * hfg1min * gravc)
     &     /(hd*vsg * (Tmin - tsat)))**0.25d0)
c

      hfb4min = 0.2 * ((( (tkg**2) *rg*(rf - rg)*hfg1min*gravc )
     &  / (vsg*(Tmin - tsat)) )**0.333d0)

      hfbmin = hfb4min * fsubcool                                       730

      prf = cp * vsf/ckf
     hfreemin = 0.4d0 * (ckf/hd) * (((hd/2.0d0)**3) * gravc * betav
     &       * ((rg/vsg)**2) * (Tmin - tsat) * prf)**0.2d0
     if(Tmin .gt. (tsat + 250.0d0)) go to 1651
     hrad = 0.0d0
     go to 1655
c
 1651 continue
c                                                                       740
c     compute radiation htc at Tmin
      call emssf1 (tempcm, alpha, zroxid, fe)
c     assume configuration factor equals one
      hradmin = fe * sigma * ((tfr(Tmin))**4 - (tfr(tsat))**4)
     &     /(Tmin - tsat)
```

```
1655    hmin = (hfbmin + hfreemin + hradmin)

        qmin = hmin*(Tmin - tsat)                                    750

        if (tsur .lt. Tmin) then
              qtot = zeta * qcrit + (1 - zeta)*qmin
        else
              qtot = (hfb + hfree + hrad)*(tsur - tsat)
        end if
c       from conduction equation, a*tsur + b = qtot
c       solve above equation for new surface temperature
c
        if(dtsat1 .lt. 0.1d0) dtsat1 = 0.1d0                         760
        htot = qtot/dtsat1
        twall2 = (b + htot * tsat)/(htot - a)
        if(abs(twall2 - tsur) .lt. 1.0d0) go to 669
        if(twall2 .lt. (tsat+2.0d0)) go to 669
        if(itn .gt. 1) go to 662
        tin1 = twall2
        twgs = twall2
        go to 668
c
  662 continue                                                       770
        if(itn .gt. 2) go to 663
        tin2 = twall2
        tout1 = tin2
        twgs = twall2
        go to 668
```

```
c
  663 continue
      if(abs(tin2 - tin1) .lt. 1.0d-5) go to 669
      tout2 = twall2
c     get improved guess of surface temperature using method of newton        780
c
      dtidto = (tout2 - tout1)/(tin2 - tin1)
      twgs = (tout1 - dtidto * tin1)/(1.0d0 - dtidto)
      tout1 = tout2
      tin1 = tin2
      tin2 = twgs
      if(ndebug .eq. 1) write(6,987) itn, twgs, tout2, tin2, tout1, tin1
  987 format(' itn = ',i4,' twgs = ',e10.4,' tout2 = ',e12.6,
     &       ' tin2 = ',e12.6,' tout1 = ',e12.6,' tin1 = ',e12.6)
  668 continue                                                                790
      tsur = twgs
      itn = itn + 1
      if(itn .lt. 100) go to 650
      write(6,649) twall2, tsur
  649 format(///' iteration on cladding surface temperature in qdot'
     &       ' for low flow film boiling did not converge. program'/
     &       ' stopped twall2= ',e10.4,' twall1= ',e10.4)
      write(6,647) Time
  647 format(' Time = ',e12.6)
      write(6,648)                                                            800
  648 format(' temperature set to upper bound value ')
      if(tsur .gt. twall2) twall2 = tsur

c     iteration converged
```

```
669 continue
      ts = twall2
      if(ts .lt. tsat) ts = tsat
      qq = a * ts + b
      l = 2                                                    810
      go to 900
c
c     mode 8 forced convection to vapor
800 continue
c
      tk = thcon (n2, tbulk, r)
c
      vs = visc (n2, tbulk, r)
c
      prn = cp * vs/tk                                         820
      if(tbulk .gt. fthun) prn = prhi
      re = MassFlowRate * hd/vs
      hc = (dp023 * tk/hd) * re**dp8 * prn**dp4
      if(hc .lt. hmin) hc = hmin

c     if radiation switch turned on, assume fuel rod surrounded by
c     annular flow shroud made of zircaloy with inside temperature
c     of tbulk. assume radiation if 0.9hd> dh
      if((hd/dh) .lt. 0.9d0) go to 860
      ts = (b + hc * tbulk)/(hc - a)                           830
      qq = hc * (ts - tbulk)
      go to 900
c
860 continue
      alpha = 1.0d0
```

```
c**** assume maximum shroud surface temp. = tbulk
      tshrd = tbulk
      toxshr = 2.5d-7
c
      call emssf1 (tshrd, alpha, toxshr, fe)                    840
c
      rk = fe * sigma
      c1 = (hc - a)/rk
      tts = tfr(tbulk) * tfr(tbulk)
      c2 = - (tts * tts + (hc * tfr(tbulk) + b - ftor * a)/rk)
c
      call root1 (c1, c2, tfr(tsur), ts)
c
      ts = ts - ftor
      qq = a * ts + b                                           850
      go to 900
c
  890 continue
c     mode 9  dougall-rohsenow
      xsave = Quality
      if(Quality .lt. dp1) Quality = dp1
      tp1 = Quality + (one - Quality) * rg/rf
      tkg = thcon (n2, tsat, rg)
      vsg = visc (n2, tsat, rg)
      prg = cpg * vsg/tkg                                       860
      reg = MassFlowRate * hd/vsg
      hc = (dp023 * tkg/hd) * (reg * tp1)**dp8 * prg**dp4
      if(hc .lt. five) hc = five
      ts = (b + hc * tsat)/(hc - a)
      qq = hc * (ts - tsat)
```

```
      Quality = xsave
c
  900 continue
      if(ndebug .eq. 1) write(6,999) ts, qq
  999 format(' QDOT: surface temperature = ',e10.4                    870
     &       ,' surface heat flux = ',e10.4)
c
      return
c       mode 1a subcooled natural convection
 1000   continue
c       compute Pr number
      thkf = thcon (n1, tbulk, r)
      pressi = CoolPress * 6.896552d+3
        tbulkk = tfk(tbulk)
      rhosi = r/0.0624279606d0                                        880
      tsatk = tfk(tsat)
      viscsi = viscol (pressi, tbulkk, rhosi, tsatk)
      vsf = viscsi * 2419.09d0
      prf = cp * vsf/thkf

c       compute Gr number
        dtwall = ts - tbulk

        if(dtwall .lt. 0.0d0) dtwall = 0.0d0
        betaf = 3.293e-3                                              890
      grf = dh**3 * gravc * betaf
     &       * ((rf/vsf)**2) * dtwall

c       heat transfer correlation
        if( grf*prf .lt. 1.0e9) then
```

```
            hc = 0.59*thkf/dh *(grf*prf)**0.25
          else
            hc = 0.10*thkf/dh *(grf*prf)**0.333
          end if
                                                                    900
        if(hc .lt. five) hc = five

          ts = (b + hc * tbulk)/(hc - a)
        qq = hc * (ts - tbulk)

          go to 900

c       mode 2a nucleat boiling at pool condition Rosenhow correlation

1200    cs = 0.013                                                  910
          fn = 1.7
          call surten(tsat, sig)

c       viscosity in [lbm/hr-ft]
        viscf = visc (n1, tsat, rf)
          tkf = thcon (n1, tsat, rf)
          prf = cpf * viscf/tkf
          hfg = hg - hf

          twall2 = tsur                                             920
          itn = 0

          al = sqrt(sig/(rf - rg))
          qwsat = a*tsat + b
```

```
1250   qrosenhow = viscf*hfg/al*
     & (cpf*(twall2 - tsat)/(cs*hfg*prf**fn))**3

      fsubc = 1.d0 + 0.1d0 * ((rf/rg)**0.75) * (cpf * (tsat - tbulk)
     &          /(hg - hf))                                          930

        qrosenhow = qrosenhow * fsubc * fqcritm

        qwall = a*twall2 + b
        twallnew = twall2 - (qrosenhow - qwall)*(twall2 - tsat)
     &                    /(3*qrosenhow - qwall + qwsat)
        itn = itn + 1
        if(abs(twallnew - twall2) .lt. 1.0d-3 ) goto 1350

        twall2 = twallnew                                           940
        if( itn .lt. 100) go to 1250

        write(6,1300) twall2, tsur
1300 format(////,' iteration on cladding surface temperature in '
     &,'qdot for nucleate boiling mode did not converge. ',
     & 'program stopped.', /,' twall2 = ',e12.6,' twall1 = ',e12.6)
        stop

1350   continue
       ts = twall2                                                  950
       if(ts .lt. tsat) ts = tsat
       qq = a * ts + b
       go to 900
        end
c*****************************************************************
```

```
c       subroutine  Wallthprop(tkw, cpw, rw, iszry, Tref)
c
c       tkw,    thermal conductivity of wall (btu/ft-hr-F)
c       cpw,    specific heat of wall (btu/lbm-F)
c       rw,             density of wall (lbm/ft**3)                    960

c       iszry,  1 (ziraloy), 0 (zirconia)
c       Tref,   temperature (K)
c*****************************************************************
        subroutine Wallthprop(tkw, cpw, rw, iszry, Tref)

        implicit real (a-h, o-z)
        if(iszry .eq. 0)  goto 100
c       Zry
c       http://www.insc.anl.gov/matprop/zircaloy/zirck.pdf             970
c       (300-1800K)
        tkw = 7.51 + 2.09e-2*Tref - 1.45e-5*Tref**2.0 + 7.67e-9*Tref**3.0

c       W/m-K -> btu/ft-hr-F
        tkw = tkw * 0.5778

c        (273-1100K)
        if(Tref .le. 1100) then
        cpw = 255.66 + 0.1024*Tref
                                                                       980
        elseif ( (Tref .gt. 1100) .and. (Tref .le. 1213.8) ) then
        cpw = 255.66 + 0.1024*Tref + 1058.4*exp(-(Tref-1213.8)**2/719.61)

        elseif ( (Tref .gt. 1213.8) .and. (Tref .le. 1320) ) then
        cpw = 597.1 - 0.4088*Tref + 1.565e-4*Tref**2.0 +
```

```
     & 1058.4*exp(-(Tref-1213.8)**2/719.61)

       elseif ( Tref .gt. 1320 ) then
       cpw = 597.1 - 0.4088*Tref + 1.565e-4*Tref**2.0
       endif                                                    990

c      J/kg-K -> btu/lbm-F
       cpw = 2.388e-4*cpw
c      <1800
       if(Tref .le. 1083) then
       rw = 6595.2 - 0.1477*Tref

       elseif((Tref .gt. 1083) .and. (Tref .le. 1144)) then
       rw = 6435.24 + (Tref - 1083)*(6477.788 - 6435.24)/(1144 -1083)
                                                                1000
       elseif(Tref .gt. 1144) then
       rw = 6690.0 - 0.1855*Tref
       endif
c      kg/m**3 -> lbm/ft**3
       rw = 6.2475e-2*rw
       return
100    continue
c      zirconia
c      tkw = zotcon(Tref)
       tkw = 0.835 + 1.81e-4 * Tref                             1010

c      W/m-K -> btu/ft-hr-F
       tkw = tkw * 0.5778

c      specific heat (valid <2000K)
```

```
      if( Tref .le. 1478.0) then
      cpw = 565 + 6.11e-2*Tref -1.14e7/Tref**2.0
      elseif ( Tref .gt. 1478.0) then
      cpw = 604.5
      endif                                                    1020
c     J/kg-K -> btu/lbm-F
      cpw = 2.388e-4*cpw

c     density (valid <2973K)
      rw0 = 5800.0
      if(Tref .le. 1478.0) then
      eps0 = 7.8e-6*Tref - 2.34e-3
      elseif( Tref .gt. 1478.0) then
      eps0 = 1.302e-5*Tref - 3.38e-2
      endif                                                    1030

      rw = rw0*(1 - 3*eps0)
c     kg/m**3 -> lbm/ft**3
      rw = 6.2375e-2*rw
      end
```

Appendix C

A user manual for FRAPTRAN_MIT

FRAPTRAN_MIT keeps all the functionalities of FRATPRAN 1.3. Besides the input files for FRAPTRAN code, a file named *hbmodel.dat* must be provided including information shown in Table C.1-Table C.3 to use the model in this thesis. Variables concerning the grain boundary gas inventory (GG, GP, GB, BBNUMDEN and GBFC) can be obtained from an output file named *fgstore.txt* by running the modified version of FRAPCON code.

Table C.1: Input variables for PCMI data block

Variable(type)	Description	Units	Default Value
IPCMI (I)	Option to model PCMI failure. IPCMI = 1, MIT model is turned on; IPCMI = 2, PNNL model is turned on; IPCMI = 3, EPRI CSED model without oxdie spallation is turned on; IPCMI = 4, EPRI CSED model with oxide spallation is turned on; IPCMI = 0 model is off.	-	0
FCRACKSIZE (I)	Multiplication factor for initial flaw size	-	1.0
ICLADTYPE (I)	Cladding alloy type. ICLADTYPE = 1 for Zry-4. ICLADTYPE = 2 for Zry-2.	-	1
IABORT (I)	Option to abort calculation when PCMI failure occurs. IABORT = 1 to stop the execution of code when PCMI occurs. IABORT = 0 to continue the execution of code after PCMI occurs.	-	0

Table C.2: Input variables for FGR data block

Variable(type)	Description	Units	Default Value
IFGR (I)	Model option for fission gas release and swelling. IFGR = 2, both FGR model and swelling model is turned on; IFGR = 1, only FGR model is turned on; IFGR = 0, model is turned off.	-	1
IPORESWL (I)	Model option for pore swelling. IPORESWL = 1 for pore swelling; IPORESWL = 0, pore swelling is neglected.	-	0
FSTRESS (F)	Fracture stress of UO2 grain boundary.	MPa	50
PH_LOW (F)	Threshold pressure to suppress grain boundary cracking	MPa	20
RBUBBLEC (F)	Radius of intergranular bubbles	m	9.0e-8
TEMPCRACK (F)	Threshold temperature for rim fragmentation	K	1400
GG (F)	Radial profile of gas concentraion in grain for each axial node. Input pairs of gas concentraion value and radius for bottom axial node, from fuel centerline to edge, and then continue for each axial node. Limit for the array size is 1260.	Mol/m^3,-m	
GP (F)	Radial profile of gas concentraion production for each axial node. Input pairs of gas concentraion value and radius for bottom axial node, from fuel centerline to edge, and then continue for each axial node. Limit for the array size is 1260.	Mol/m^3,-m	
GB (F)	Radial profile of gas concentraion in grain boundary for each axial node. Input pairs of gas concentraion value and radius for bottom axial node, from fuel centerline to edge, and then continue for each axial node. Limit for the array size is 1260.	Mol/m^3,-m	
BBNUMDEN (F)	Radial profile of intergranular bubble number density for each axial node. Input pairs of bubble number density and radius for bottom axial node, from fuel centerline to edge, and then continue for each axial node. Limit for the array size is 1260.	$/m^3$, m	-
GBFC (F)	Radial profile of grain boundary surface coverage for each axial node. Input pairs of grain boundary surface coverage and radius for bottom axial node, from fuel centerline to edge, and then continue for each axial node. Limit for the array size is 1260.	-, m	-
BUAVG (F)	Radial average burnup for each axial node. Input from bottom node to top axial node. Limit for the array size is 51.	MWd/kg	
RSIZE (F)	Rim size for each axial node. Input from bottom node to top axial node. Limit for the array size is 51.	m	

Table C.3: Input variables for heat transfer data block

Variable(type)	Description	Units	Default Value
IDNB (I)	Model option for cladding surface heat transfer calculation. IDNB = 1 heat transfer model is turned on (validated for BWR CZP); IDNB = 2, default heat transfer model in FRAPTRAN is used; IDNB = 0, model is turned off.	-	1
FQCRITM (F)	Multiplication factor for critical heat flux	-	1.0
FFHTC (F)	Multiplication factor for film boiling heat transfer coefficient.	-	1.0
TMINSHIFT (F)	Temperature shift for minimal stable film boiling temperature.	K	0.0
ITMIN (I)	Model option for calculating Tmin. ITMIN = 1 for Henry correlation; ITMIN = 2 for NSR-77 correlation.	-	1
IFILM (I)	Model option for film boiling heat transfer. Not implemented.	-	1
ISZRY (I)	Surface condition. ISZRY = 1 for fresh cladding; ISZRY = 0 for oxidized cladding.	-	0
FGAPHTC (F)	Multiplication factor for gap heat transfer coefficient.	-	1.0

Bibliography

[1] D. D. Lanning, C. E. Beyer, and C. L. Painter. FRAPCON-3: Modifications to Fuel Rod Material Properties and Performance Models for High-Burnup Application. Technical Report NUREG/CR-6534 Vol 1, PNNL-11513, 1997.

[2] Nuclear Fuel Safety Criteria Technical Review. Technical report, OECD Nuclear Energy Agency, 2001.

[3] W. Wiesenack. Assessment of UO_2 Conductivity Degradation based on In-pile Temperature Data. In *Proceedings of the 1997 International Meeting on LWR Fuel Performance*, pages 507–511, Portland, Oregon, United States, March 2-6, 1997.

[4] P. E. MacDonald, S. L. Seiffert, Z. R. Martinson, and R. K. McCardell. Assessment of Light-Water-Reactor Fuel Damage During a Reactivity-Initiated Accident. *Nuclear Safety*, 21(5):582–602, 1980.

[5] T. Fuketa, F. Nagase, K. Ishijima, and T. Fujishiro. NSRR/RIA Experiments with High-burnup PWR Fuels. *Nuclear Safety:Technical Progress Journal*, 37(4):328–342, 1996.

[6] J. Papin, M. Balourdet, F. Lemoine, F. Lamare, J. M. Frizonnet, and F. Schmitz. French Studies on High-burnup Fuel Transient Behavior under RIA Conditions. *Nuclear Safety:Technical Progress Journal*, 37(4):289–327, 1996.

[7] T. Fuketa, T. Sugiyama, H. Sasajima, and F. Nagase. NSRR RIA-simulating Experiments on High Burnup LWR Fuels. In *Proceedings of the 2005 International Meeting on LWR Fuel Performance*, Kyoto, Japan, Oct 2-6, 2005.

[8] V. Asmolov and L. Yegorova. Russian RIA Research Program: Motivation, definition, execution, and results. *Nuclear Safety:Technical Progress Journal*, 37(4):343–371, 1996.

[9] L. Yegorova, K. Lioutov, and N. Jouravkova et al. Experimental Study of Narrow Pulse Effects on the Behavior of High Burnup Fuel Rods with Zr-1%Nb Cladding and UO2 Fuel (VVER Type) under Reactivity-Initiated Accident Conditions: Test Conditions and Results. Technical Report NUREG/IA-0213 Vol 1, IRSN/DPAM 2005-275, NSI RRC KI 3230, 2006.

[10] L. Yegorova, K. Lioutov, and N. Jouravkova et al. Experimental Study of Narrow Pulse Effects on the Behavior of High Burnup Fuel Rods with Zr-1%Nb Cladding and UO2 Fuel (VVER Type) under Reactivity-Initiated Accident Conditions: Test Conditions and Results. Technical Report NUREG/IA-0213 Vol 2, IRSN/DPAM 2005-275, NSI RRC KI 3230, 2006.

[11] Y. Long, M. S. Kazimi, R. G. Ballinger, and J. E. Meyer. Modeling The Performance of High Burnup Thoria and Urania PWR Fuel. Technical Report MIT-NFC-TR-044, July 2002.

[12] M. E. Cunningham, C. E. Beyer, F. E. Panisko, P. G. Medvedev, and G. A. Berna. FRAPTRAN: A Computer Code for the Transient Analysis of Oxide Fuel Rods. Technical Report NUREG/CR-6739, Vol 1, PNNL-13576, 2001.

[13] SCDAP/RELAP5-3D Code Development Team. SCDAP/RELAP5-3D Code Manual Volume 4: Matpro - A Library of Materials Properties for Light-Water-Reactor Accident Analysis. Technical Report INEEL/EXT-02-00589-V4-R2.2, 2003.

[14] Z. Xu, M. J. Driscoll, and M. S. Kazimi. Design Strategies for Optimizing High Burnup Fuel in Pressurized Water Reactors. Technical Report MIT-NFC-TR-053, July 2003.

[15] L. C. Bernard, J. L. Jacoud, and P. Vesco. An Efficient Model for the Analysis of Fission Gas Release. *Journal of Nuclear Materials*, 302(2-3):125–134, 2002.

[16] J. Spino, D. Papaioannou, and I. Ray. Rim Formation and Fission Gas Behaviour: Some Structure Remarks, 2000.

[17] Y. Koo, J. Oh, B. Lee, and D. Sohn. Three-dimensional Simulation of Threshold Porosity for Fission Gas Release in the Rim Region of LWR UO_2 Fuel. *Journal of Nuclear Materials*, 321(2-3):249–255, 2003.

[18] J. Spino, D. Papaioannou, and J. P. Glatz. Comments on the Threshold Porosity for Fission Gas Release in High Burn-up Fuels. *Journal of Nuclear Materials*, 328:67–70, 2004.

[19] P. Losonen. On the Behaviour of Intragranular Fission Gas in UO_2 Fuel. *Journal of Nuclear Materials*, 280(1):56–72, 2000.

[20] A. H. Booth. A Method of Calculating Fission Gas Diffusion for UO_2 Fuel and its Application to the X-2-f Loop Test. Technical Report AECL 496, 1957.

[21] M. V. Speight. A Calculation of the Migration of Fission Gas in Material Exhibiting Precipitaion and Re-solution of Gas Atoms under Irradiation. *Nuclear Science and Engineering*, 37:180–185, 1969.

[22] R. J. White and M. O. Tucker. A New Fission Gas Release Model. *Journal of Nuclear Materials*, 118(1):1 – 38, 1983.

[23] F. Forsberg and A. R. Massih. Diffusion Theory of Fission Gas Migration in Irradiated Nuclear Fuel UO_2 . *Journal of Nuclear Materials*, 135(2-3):140–148, 1985.

[24] Y. Kim. Theoretical Analysis of Two-stage Fission Gas Release Processes: Grain Lattice and Grain Boundary Diffusion. *Journal of Nuclear Materials*, 326(2-3):97–105, 3/15 2004.

[25] Y. Koo, B. Lee, and D. Sohn. Analysis of Fission Gas Release and Gaseous Swelling in UO_2 Fuel under the Effect of External Restraint. *Journal of Nuclear Materials*, 280(1):86–98, 6 2000.

[26] P. Hermansson and A. R. Massih. An Effective Method for Calculation of Diffusive Flow in Spherical Grains. *Journal of Nuclear Materials*, 304(2-3):204–211, 2002.

[27] D. D. Lanning, C. E. Beyer, and K. J. Geelhood. FRAPCON-3 Updates, Including Mixed-Oxide Fuel Properties. Technical Report NUREG/CR-6534 Vol 4, PNNL-11513, 2005.

[28] D. D. Lanning, C. E. Beyer, and G. A. Berna. FRAPCON-3: Integral Assessment. Technical Report NUREG/CR-6534 Vol 3, PNNL-11513, 1997.

[29] D. R. Olander. *Fundamental Aspects of Nuclear Reactor Fuel Elements.* Technical Information Center, Office of Public Affairs Energy Research and Development Administration, Springfield, Virginia, 1976.

[30] J. A. Turnbull and M. O. Tucker. The Release of Fission Gas from Nuclear Fuels during Temperature Transients. *Journal of Nuclear Materials*, 50(1):53–61, 1974.

[31] S. Kashibe and K. Une. Fission Gas Release From Externally Restrained Uranium Dioxide Fuel. *Journal of Nuclear Science and Technology*, 37(6):530 – 535, 2000.

[32] P. V. Uffelen. *Contribution to the Modelling of Fission Gas Release in Light Water Reactor Fuel.* Ph.d. dissertation blg-907, 2002.

[33] F. Lemoine. High Burnup Fuel Behavior related to Fission Gas Effects under Reactivity Initiated Accidents (RIA) Conditions. *Journal of Nuclear Materials*, 248:238–248, 1997.

[34] W Hering. The KWU Fission Gas Release Model for LWR Fuel Rods. *Journal of Nuclear Materials*, 114(1):41–49, 1983.

[35] F. Lemoine, J. Papin, J. M. Frizonnet, B. Cazalis, and H. Rigat. The Role of Grain Boundary Fission Gases in High Burn-up Fuel under Reactivity Initiated Accident Conditions, 2000.

[36] C. T. Walker, D. Staicu, M. Sheindlin, D. Papaioannou, W. Goll, and F. Sontheimer. On the Thermal Conductivity of UO_2 Nuclear Fuel at a High Burn-up of around 100 MWd/kgHM. *Journal of Nuclear Materials*, 350(1):19–39, 2006.

[37] Y. Koo, B. Lee, J. Cheon, and D. Sohn. Pore pressure and swelling in the rim region of lwr high burnup uo2 fuel. *Journal of Nuclear Materials*, 295(2-3):213–220, 2001.

[38] K. Lassmann, C. T. Walker, J. van de Laar, and F. Lindstrom. Modelling the High Burnup UO_2 Structure in LWR Fuel. *Journal of Nuclear Materials*, 226(1-2):1–8, 1995.

[39] H. Matzke and J. Spino. Formation of the Rim Structure in High Burnup Fuel. *Journal of Nuclear Materials*, 248:170–179, 1997.

[40] P. G. Lucuta, Hj Matzke, and I. J. Hastings. A Pragmatic Approach to Modelling Thermal Conductivity of Irradiated UO_2 Fuel: Review and Recommendationsa. *Journal of Nuclear Materials*, 232(2-3):166–180, 1996.

[41] C. Ronchi, M. Sheindlin, D. Staicu, and M. Kinoshita. Effect of Burn-up on the Thermal Conductivity of Uranium Dioxide up to 100.000 $MWdt^{-1}$. *Journal of Nuclear Materials*, 327(1):58–76, 2004.

[42] K. Ohira and N. Itagaki. Thermal Conductivity Measurements of High Burnup UO_2 Pellet and a Benchmark Calculation of Fuel Center Temperature. In *Proceedings of the 1997 International Meeting on LWR Fuel Performance*, pages 541–549, Portland, Oregon, United States, March 2-6, 1997.

[43] B. Lee, Y. Koo, and D. Sohn. Rim Characteristics and their Effects on the Thermal Conductivity in High Burnup UO_2 Fuel. *Journal of Nuclear Science and Technology*, 38(1):45 – 52, 2001.

[44] M. Kinoshita, T. Sonoda, and S. Kitajima et al. High Burnup Rim Project: (III) Properties of Rim-structured Fuel. In *Proceedings of the 2004 International Meeting on LWR Fuel Performance*, pages 207–213, Orlando, U.S., Sep 19-22, 2004.

[45] K. Nogita and K. Une. Irradiation-induced Recrystallization in High Burnup UO_2 Fuel. *Journal of Nuclear Materials*, 226(3):302–310, 1995/11.

[46] R. O. Meyer. An Assessment of Fuel Damage in Postulated Reactivity-initiated Accidents. *Nuclear Technology*, 155(3):293 – 311, 2006.

[47] W. Liu, A. Romano, and M. S. Kazimi. Modeling High-Burnup LWR Fuel Fission Gas Released and Swelling During Fast Transients. In *Proceedings of the 2004 International Meeting on LWR Fuel Performance*, Orlando, U.S., Sep 19-22, 2004.

[48] M. Amaya, T. Sugiyama, and T. Fuketa. Fission Gas Release in Irradiated UO_2 Fuel at Burnup of 45 GWd/t during Simulated Reactivity Initiated Accident (RIA) Condition. *Journal of Nuclear Science and Technology*, 41(10):966 – 972, 2004.

[49] T. Sugiyama, T. Nakamura, K. Kusagaya, H. Sasajima, F. Nagase, and T. Fuketa. Behavior of Irradiated BWR fuel Under Reactivity-Initiated-Accident Conditions - Results of Tests FK-1,-2 and -3. Technical Report JAERI-Research 2003-033, 2004.

[50] T. Nakamura, K. Kusagaya, T. Fuketa, and H. Uetsuka. High-burnup BWR Fuel Behavior under Simulated Reactivity-initiated Accident Conditions. *Nuclear Technology*, 138(3):246–259, 2002.

[51] N. Ohnishi, K. Ishijima, and S. Tanzawa. Study of Subcooled Film-boiling Heat Transfer under Reactivity-initiated Accident Conditions in Light Water Reactorsa. *Nuclear Science and Engineering*, 88(3):331–341, 1984.

[52] U. Rohde. The Modeling of Fuel Rod Behaviour under RIA Conditions in the Code DYN3D. *Annals of Nuclear Energy*, 28(13):1343–1363, 2001.

[53] T. Nakamura et al. Evaluation of Burnup Characteristics and Energy Deposition During NSRR Pulse Irradiation Tests on Irradiated BWR Fuels. Technical Report JAERI-Research 2000-048, 2000.

[54] T. Sugiyama and T. Fuketa. Effect of Cladding Surface Pre-oxidation on Rod Coolability under Reactivity Initiated Accident Conditions. *Journal of Nuclear Science and Technology*, 41(11):1083–1090, 2004.

[55] S. K. Roy Chowdhury and R. H. S. Winterton. Surface Effects in Pool Boiling. *International Journal of Heat and Mass Transfer*, 28(10):1881–1889, 1985.

[56] J. W. Westwater, J. J. Hwalek, and M. E. Irving. Suggested Standard Method for Obtaining Boiling Curves by Quenching. *Industrial & Engineering Chemistry, Fundamentals*, 25(4):685–692, 1986.

[57] R. E. Henry, D. J. Quinn, and E. A. Spleha. Experimental Study of the Minimum Film Boiling Point for Liquid-liquid Systems. *Int Heat Transfer Conf, 5th, Proc*, pages 101–104, 1974.

[58] H.J. Ivey and D.J. Morris. Critical Heat Flux of Saturation and Subcooled Pool Boiling in Water at Atmospheric Pressure. In *Proceedings of 3rd International Heat Transfer Conference*, volume 3, pages 129–142, 1966.

[59] J. G. Coiler and J. R. Thome. *Convective boiling and condensation.* Oxford University Press, New York, 1994.

[60] L. S. Tong. *Boiling Crisis and Critical Heat Flux.* USAEC, Washington, D.C., 1972.

[61] V. Bessiron. Main Outcomes from the PATRICIA Program on Clad to Coolant Heat Transfer during RIAs. In *Colloquim on High Burnup Fuels for LWRs.* MIT, Cambridge, 2003.

[62] W. M. Rohsenow, J. P. Hartnett, and Y. I. Cho. *Handbook of Heat Transfer.* McGraw-Hill, New York, 1998.

[63] L. S. Tong and Y. S. Tang. *Boiling Heat Transfer and Two-phase Flow.* Taylor & Francis, Washington, D.C., 1997.

[64] T. H. K. Frederking, Y. C. Wu, and B. W. Clement. Effects of Interfacial Instability on Film Boiling of Saturated Liquid Helium I above a Horizontal Surface. *AIChe Journal*, 12(2):238–244, 1966.

[65] J. W. Spore, J. S. Elson, and S. J. Jooly-Woodruf et al. TRAC-M/FORTRAN90 (Version3.0) Theory Manual. Technical Report LA-UR-00-910, 2000.

[66] S. G. Kandlikar, M. Shoji, and V. K. Dhir. *Handbook of Phase Change : Boiling and Condensation.* Taylor & Francis, Philadelphia, PA, 1999.

[67] H. Auracher and W. Marquardt. Heat Transfer Characteristics and Mechanisms along Entire Boiling Curves under Steady-state and Transient Conditions. *International Journal of Heat and Fluid Flow*, 25(2):223–242, 2004.

[68] T. Torimaru, T. Yasuda, and M. Nakatsuka. Changes in Mechanical Properties of Irradiated Zircaloy-2 Fuel Cladding due to Short Term Annealing. *Journal of Nuclear Materials*, 238(2-3):169–174, 1996.

[69] C. Pan, J. Y. Hwang, and T. L. Lin. The Mechanism of Heat Transfer in Transition Boilinga. *International Journal of Heat and Mass Transfer*, 32(7):1337–1349, 7 1989.

[70] L. S. Tong and J. Weisman. *Thermal Analysis of Pressurized Water Reactors.* American Nuclear Society, Illinois USA, 1996.

[71] V. Bessiron. Realiability of TC Measurement in NSRR Experiments. In *FSRM Tokai*, 2006.

[72] T. Nakamura et al. High Burnup (41-61GWd/tU) BWR Fuel Behavior under Reactivity Initiated Accident Conditions. Technical Report JAERI-Research 2001-054, 2001.

[73] T. Nakamura, M. Yoshinaga, M. Takahashi, K. Okonogi, and K. Ishijima. Boiling Water Reactor Fuel Behavior under Reactivity-initiated-accident Conditions at Burnup of 41 to 45 GWd/tonne U. *Nuclear Technology*, 129(2):141–151, 2000.

[74] K. J. Geelhood, C. E. Beyer, and M. E. Cunningham. Modifications to FRAP-TRAN to Predict Fuel Rod Failures due to PCMI During RIA-type Accidents. In *Proceedings of the 2004 International Meeting on LWR Fuel Performance*, Orlando, U.S., Sep 19-22, 2004.

[75] Topical Report on Reactivity Initiated Accident: Bases for RIA Fuel and Core Coolability Criteria. Technical Report 1002865, 2002.

[76] M. Kuroda, S. Yamanaka, F. Nagase, and H. Uetsuka. Analysis of the Fracture Behavior of Hydrided Fuel Cladding by Fracture Mechanics. *Nuclear Engineering and Design*, 203(2):185–194, 2001.

[77] L. O. Jernkvist, A. R. Massih, and P. Rudling. A Strain-based Clad Failure Criterion for Reactivity Initiated Accidents in Light Water Reactors. Technical Report Dnr 14.6-011070:02149, 2003.

[78] F. Nagase and T. Fuketa. Investigation of Hydride Rim Effect on Failure of Zircaloy-4 Cladding with Tube Burst Test. *Journal of Nuclear Science and Technology*, 42(1):58–65, 2005.

[79] J. Bai et al. Effects of Hydrides on the Ductile Brittle Transition in Stress-Relieved, Recrystallized and β-Treated Zr-4. In *Proceedings of International Topical Meetingg on LWR Fuel Performance*, pages 379–400. Avignon, France, American Nuclear Society, La Gragen Park, IL, 1991.

[80] A. M. Garde. Influence of Cladding Microstructure on the Low Enthalpy Failures in RIA Simulation Tests. *ASTM Special Technical Publication*, (1354):234–255, 2000.

[81] M. Kuroda, K. Yoshioka, and S. Yamanaka et al. Influence of Precipitated Hydride on the Fracture Behavior of Zircaloy Fule Cladding Tube. *Journal of Nuclear Science and Technology*, 37(8):670–675, 2000.

[82] G. Domizzi, R. A. Enrique, J. Ovejero-Garca, and G. C. Buscagliaet. Blister Growth in Zirconium Alloys: Experimentation and Modeling. *Journal of Nuclear Materials*, 229(2):36–47, 1996.

[83] A. Sawatzky. The Diffusion and Solubility of Hydrogen in the Alpha-Phase of Zircaloy. *Journal of Nuclear Materials*, 2(1):62, 1960.

[84] S. B. Wisner and R. B. Adamson. Combined Effects of Radiation Damage and Hydrides on the Ductility of Zircaloy-2. *Nuclear Engineering and Design*, 185(1):33–49, 1998.

[85] A. Sawatzky and B. J. S. Wilkins. Hydrogen Solubility in Zirconium Alloys Determined by Thermal Diffusion. *Journal of Nuclear Materials*, 22(3):304, 1967.

[86] K. Edsinger, J. H. Davies, and R. B. Adamson. Degraded Fuel Cladding Fractography and Fracture Behavior. *ASTM Special Technical Publication*, (1354):316–339, 2000.

[87] V. Grigoriev, B. Josefsson, and B. Rosborg. Fracture Toughness of Zircaloy Cladding Tubes. In *Proceedings of the 1995 11th International Symposium on Zirconium in the Nuclear Industry, Sep 11-14 1995*, ASTM Special Technical Publication, pages 431–446, Garmisch-Partenkirchen, Ger, 1996. Studsvik Material AB, Nykoping, Sweden, ASTM, Conshohocken, PA, USA.

[88] P. H. Kreyns et al. Embrittlement of Reactor Core Materials. In *Proceedings of the 1995 11th International Symposium on Zirconium in the Nuclear Industry,*

ASTM Special Technical Publication, pages 758–782, Garmisch-Partenkirchen, Ger, 1996. Studsvik Material AB, Nykoping, Sweden, ASTM, Conshohocken, PA, USA.

[89] T. Nakamura, T. Fuketa, T. Sugiyama, and H. Sasajima. Failure Thresholds of High Burnup BWR Fuel Rods under RIA Conditions. *Journal of Nuclear Science and Technology*, 41(1):37–43, 2004.

[90] N. E. Dowling. *Mechanical Behavior of Materials Engineering Methods for Deformation, Fracture and Fatigue.* Prentice Hall, Englewood Cliffs, New Jersey, U.S., 1993.

[91] R. O. Meyer, R. K. McCardell, H. M. Chung, D. J. Diamond, and H. H. Scott. Regulatory Assessment of Test Data for Reactivity-initiated Accidents. *Nuclear Safety:Technical Progress Journal*, 37(4):271–288, 1996.

[92] D. Diamond. Studies of the Rod Ejection Accident in a PWR. Technical Report W-6382 1/22/02, 2002.

[93] GE Energy Global Nuclear Fuel. BWR Control Rod Drop Accident. In *NRC Workshop on RIA/RDA*, 2006.

[94] G. P. Sabol, R. J. Comstock, R. A. Weiner, P. Larouere, and R. N. Stanutz. In-reactor Corrosion Performance of ZIRLO and Zircaloy-4. In *Proceedings of the 1994 10th International Symposium on Zirconium in the Nuclear Industry*, pages 724–744, 1994.